The kinematics of intra-salt layers during salt tectonics

Hamood Al-Habsi

Submitted in partial fulfilment of the requirements for the degree of PhD

Cardiff University

June 2016

DECLARATION

This work has not been submitted in substance for any other degree or award at this or any other university or place of learning, nor is being submitted concurrently in candidature for any degree or other award.

Signed   **HAMOOD AL-HABSI**   (candidate) Date …**25 JUNE 2016**…

STATEMENT 1

This thesis is being submitted in partial fulfilment of the requirements for the degree of ……… **PhD** …………(insert MCh, MD, MPhil, **PhD** etc., as appropriate)

Signed   **HAMOOD AL-HABSI**   (candidate) Date …**25 JUNE 2016**…

STATEMENT 2

This thesis is the result of my own independent work/investigation, except where otherwise stated.

Other sources are acknowledged by explicit references. The views expressed are my own.

Signed   **HAMOOD AL-HABSI**   (candidate) Date …**25 JUNE 2016**…

STATEMENT 3

I hereby give consent for my thesis, if accepted, to be available online in the University's Open Access repository and for inter-library loan, and for the title and summary to be made available to outside organisations.

Signed   **HAMOOD AL-HABSI**   (candidate) Date …**25 JUNE 2016**…

STATEMENT 4: PREVIOUSLY APPROVED BAR ON ACCESS

I hereby give consent for my thesis, if accepted, to be available online in the University's Open Access repository and for inter-library loans **after expiry of a bar on access previously approved by the Academic Standards & Quality Committee.**

Signed   **HAMOOD AL-HABSI**   (candidate) Date …**25 JUNE 2016**…

Acknowledgements

Abstract

The structures and dynamics of intra-salt layers have received limited study in comparison with the external shape of salt structures. Our limited understanding of the behaviour of intra-salt layers generally comes from salt mines, outcrops, analogue, and numerical modelling where the full three-dimensionality of intra-salt layers is barely observed. To understand the internal dynamics of giant salt structures and the response of their intra-salt layers during regional tectonics, this thesis provides detailed interpretation and analysis of intra-salt layers from the Silverpit Basin, in the Southern North Sea Basin, and the Birba Area, in the South Oman Salt Basin.

These two locations provide unique natural laboratories where driver mechanisms for salt tectonics are investigated using high-resolution, high-quality three-dimensional (3D) seismic reflection data. The Silverpit Basin is a buckled basin formed during the Mid Eocene to Late Oligocene, while the Birba Basin was affected by massive sediment loading, which generated differential loading from the Early Cambrian to the Late Permian. Differential loading of the basin caused down-building and influenced the growth of diapirs and minibasins, which later led to intense deformation and fragmentation of the intra-salt carbonate stringers.

In the Silverpit Basin, regional salt anticlines encapsulated a 23–63 m-thick intra-salt layer known as the Z3 Stringer. Lithologically, the Z3 Stringer is composed of anhydrite, and it represents a strong seismic marker across the Southern North Sea Basin. Relative to regional anticlines and synclines at the Top Salt level, the Z3 Stringer deformed in a ductile manner comparable in geometry and attitude to the regional salt structure. Non-cylindrical stringer folds, which vary from gentle to isoclinal, are related to the intensity of the regional-scale structure, whereby tighter

stringer folds are observed under well-developed Top Salt anticlines and synclines. Synclines at the Top Salt level include long-wavelength gentle folds. Extreme thinning of the Zechstein by the downward displacement of the Top Salt causes the stringers to extend and finally break laterally in a mode-1 tensile fracture mechanism.

This thesis highlights the complexity of intra-salt deformation and forms a good large-scale case study for the analysis of the kinematics and rheology of competent material enclosed within an incompetent medium. Understanding the complexities and attitudes of intra-salt layers and their encasing salt structures has broader implications for regional tectonic history, hydrocarbon prospectivity, and industrial applications.

Table of Contents

List of Figures

List of Tables

Chapter 1: Introduction and literature review

1.1   Rationale for the study

Rock salt is considered to be the weakest sedimentary rock. Due to its rheology, low strength, low density, and incompressibility, rock salt is an inherently unstable and unique rock type (Hudec and Jackson 2007). Most of the regional subsurface knowledge of salt deformation, including external and internal structures and geometries, is based on three-dimensional (3D) seismic data. However, seismic data provide limited information on the subtle details of the internal deformation of salt structures compared with salt mine and outcrop data (Schléder et al. 2008; Reuning et al. 2009), because of the general lack of internal reflectivity within the deformed salt layer.

Although the top and base salt reflectors of deformed salt layers are commonly well-imaged, it is rare to find comparably well-imaged examples of continuous marker layers inside the salt. Instead, deformed salt layers are always characterised by a seismically opaque, featureless, or incoherent seismic facies (Hudec and Jackson 2007). Where there are sufficiently thick, interbedded layers of anhydrite, limestone, dolomite, or shale, these layers can produce a coherent and well-imaged seismic reflection within the salt, but these have only rarely been described to date.

These internal layers within the salt are known as "stringers", "rafts", and "floaters" (Peters et al. 2003; Al-Siyabi 2005). Examples of seismically imaged intra-salt layers are the Z3 Stringer in the Zechstein salt in the North Sea (van Gent et al. 2011), the carbonate Ara stringers in Oman Salt Basins (Al-Siyabi 2005), the multi-layered Messinian evaporites in the Eastern Mediterranean (Cartwright et al. 2012), and the layered evaporite sequences in the Santos Basin (Fiduk and Rowan 2012; Jackson et al. 2015).

At the seismic scale, these intra-salt reflections give the most reliable indication of the intra-salt deformation, and analysing their geometry can provide a better understanding of the internal dynamic of deformed salt bodies, be they diapirs, salt-cored folds, or salt sheets. In contrast, information from surface-piercing salt domes and observations from salt mines generally only provide a two-dimensional (2D) view of the internal salt structure. However, the 3D internal structure of the salt is well known to be complex, and most of the fold structures are non-cylindrical; thus, the 2D sectional display will only show very limited information on the true deformational history inside the salt (van Gent et al. 2011; Strozyk et al. 2012).

Nevertheless, the 3D description and the kinematic evolution of the internal salt structures during salt tectonics have received only limited attention in the literature on salt tectonics (Strozyk et al. 2014). Although some numerical and analogue studies have introduced the kinematics and structural styles of the competent materials that are embedded within an incompetent matrix, the details of the geometrical evolution are still poorly understood. A summary of the kinematic evolution and structural styles of internal salt structures based on the regional driving mechanisms (e.g., tectonics derived by shortening, differential loading, and extension) and the mechanical properties of the stringers has not been undertaken. Although some numerical and analogue experimental studies have discussed the behaviour of the internal layering of competent layers and incompetent materials by changing the mechanical properties of those two (e.g., Koyi 2001; Dooley et al. 2008; Li et al. 2012a; Abe et al. 2013), the results of these models and their application to real seismic examples need to be further addressed.

1.2   Research question

The regional-scale kinematic evolution of the internal salt layers during salt tectonics has received only limited attention in the literature, and it has rarely been observed and described using seismic data. The main research question addressed in this thesis is how the internal salt layers behave and deform during salt tectonics under variable regional driver mechanisms (e.g., differential loading, gravitational spreading, and compression) underneath regional salt structures (i.e., minibasins, diapirs, diapir flanks, and salt anticlines and synclines) with variable internal salt stratigraphies (i.e., pure salt, layered evaporites, evaporitic stringers, and carbonate stringers).

This research project aims to summarise the 3D deformation of intra-salt layers to understand their kinematic evolution. This aim will be achieved by analysing intra-salt layers using seismic data from two different basins and with different variables, including stringer mechanical properties, salt stratigraphy, regional driver mechanisms, and the degree of tectonics (early, intermediate, or late). Understanding the kinematic evolution of the intra-salt stringers will help to constrain and explain the flow regime inside the salt. Additionally, understanding when and how these rock bodies deform is of practical importance for understanding the elements of petroleum systems, which include structural traps, source rocks, reservoirs, seals, maturation, and migration.

1.3 Previous works on internal salt structures

Internal salt structures have been studied using salt mine and borehole observations (e.g., Borchert and Muir 1964; Kupfer 1968; Richter-Bernburg 1980; Schwerdtner and Van Kranendonk 1984; Talbot and Jackson 1987; Jackson et al. 1990; Jackson 1995; Geluk 2000; Behlau and Mingerzahn 2001; Schléder et al. 2008), observations from salt outcrops and surface-piercing salt domes (e.g., Kent 1979; Peters et al. 2003; Al-Siyabi 2005; Talbot and Aftabi 2004; Reuning et al. 2009), seismic data (Al-Siyabi 2005; Kukla et al. 2011; van Gent et al. 2011; Cartwright et al. 2012; Fiduk and Rowan 2012; Strozyk et al. 2012; Strozyk et al. 2014), and numerical and analogue modelling data (Jackson and Talbot 1989; Koyi 2001; Zulauf and Zulauf 2005; Chemia et al. 2008; Zulauf et al. 2009; Li et al. 2012a; Abe et al. 2013).

1.3.1 Salt mine and borehole observations (millimetre-to-metre scale)

Salt mine and borehole observations of intra-salt structures display a variety of deformation structures of shear zones, boudinage, and complex fold structures over a wide range of scales from millimetres to tens of metres (Richter-Bernburg 1980; Geluk et al. 1997). Various fold styles have been observed in the internal inclusions within the Zechstein salt in the Morsleben radioactive waste repository (Behlau and Mingerzahn 2001). Isoclinal folded halite and anhydrite layers (Fig. 1.1a) and isoclinal similar folds of halite and clay layers (Fig. 1.1b) have been described within the Zechstein-1 rock salt in the Neuhof salt mine (Schléder et al. 2008). Examples of inclined to overturned isoclinal folds of continuous anhydrite layers within the salt have also been observed (Fig. 1.1c). In addition, thrusts within recumbent folds and

fractured isoclinal folds have been identified in clay layers within the Ara Group evaporites in Oman salt domes (Fig. 1.1d) (Reuning et al. 2009). Core samples from the Zechstein show an intensive folding of anhydrite and halite layers with secondary veins sealed by large euhedral to subhedral halite grains (Fig. 1.1e) (Schléder et al. 2008). From these observations, it can be summarised that the internal salt structures are intensively folded on a millimetre-to-metre scale and that continuous intra-salt layers can experience a high grade of folding with no significant brittle deformation (Fig. 1.1a,b,c). Similarly, the intra-salt inclusions can exhibit both folding and more brittle deformation (Fig. 1.1d,e).

1.3.2 Intra-salt from regional outcrop examples (kilometre scale)

1.3.2.1   Gorleben salt dome

The Gorleben salt dome in the Lüchow-Dannenberg district in Germany is about 3300 m high and 10 km wide (Bornemann 1991; Bäuerle et al. 2000) (Fig. 1.2a). The internal stringers (Z3HA and Z4RT in Fig. 1.2a) in the core of the dome are characterised by rotated geometries and steeply inclined to vertical fold axes. These have been interpreted as constrictional folds on 3D seismic data (van Gent et al. 2011) and curtain folds in salt outcrops (Talbot and Jackson 1986). However, such descriptions cannot be applied to the 2D cross-section. The folds of the internal layers in the NW side of the dome are clearly large-scale folds (1–2 km) verging away from the source layer. Thin layers belonging to am1 and Z3OSM are folded with a higher degree of shortening than the thicker Z3HA (Fig. 1.2a). The Z3 Stringer below the thinned salt area in the SE side of the dome displays very large wavelength gentle folds reflecting lesser degrees of shortening (Fig. 1.2a).
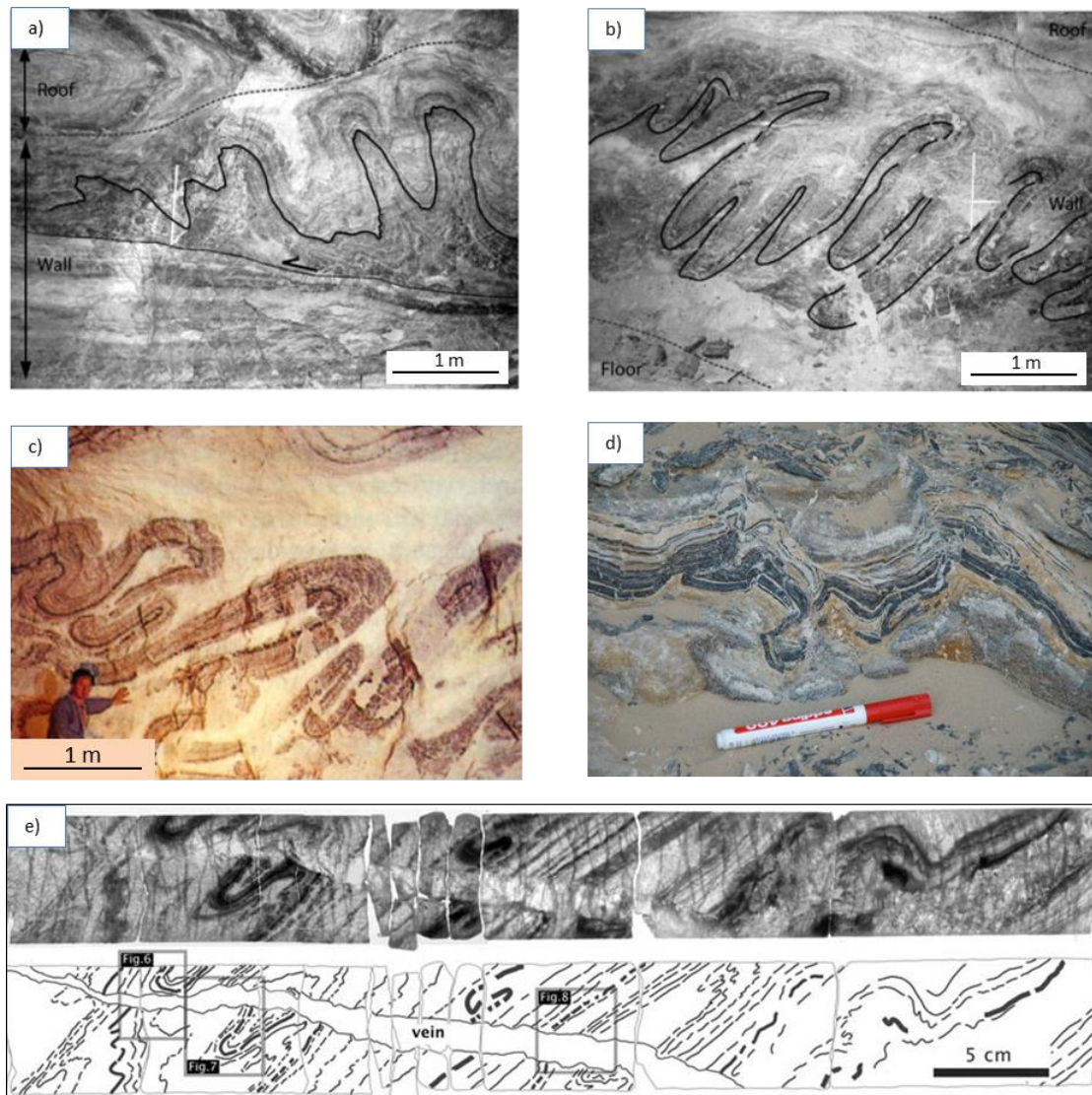
Fig. 1.1: (a) Tight to isoclinal anhydrite and halite folds with vertical to inclined folds axes. (b) Isoclinal tight folds of halite and clay minerals (Schléder et al. 2008). (c) Organic-rich layer within halite shows isoclinal tight folding (middle) and thrusted recumbent fold (left); from Jabal Majayiz, Oman (Reuning et al. 2009). (d) Inclined isoclinal fold structures within the Zechstein salt, with complex deformations at the bottom (Kukla et al. 2011). (e) Top: A scanned image of a core sample shows folded halite layers (light) and anhydrite layers (dark). Bottom: Trace interpretation of the anhydrite layers (black lines); after Schléder et al. (2008).

1.3.2.2   Surface-piercing Zechstein salt

A sketch of the Z3 Stringer within a salt dome by Seidl (1921) shows complex folding with very high amplitude isoclinal, upright, and inclined folds associated with thickened hinges and thinned limbs (Fig. 1.2b). The folds below the flanks of the salt dome are inclined and verge away from the thinned source layer, while upright and less inclined folds are concentrated in the middle of the dome. The profile also shows that the tightness of the folds decreases downward to open and gentle folds in the lower layers. Such complexity and variability of the intra-salt deformations can be used to understand the salt behaviour and to predict the expected internal deformation at every part of the salt structure. However, such continuity of the Z3 Stringer is not found in the carbonate stringers in the South Oman Salt Basin (Peters et al. 2003; Al-Siyabi 2005; Reuning et al. 2009).

1.3.2.3   Salt domes in Oman

Carbonate rocks of Late Precambrian age are well exposed within six salt domes that crop out in the desert of the interior of North Oman, thus allowing detailed field observations of intra-salt carbonate stringers (Peters et al. 2003). Field work in the Qarn Nihayda salt dome in the Ghaba Salt Basin revealed intensive deformation and fragmentation of the stringers, as well as chaotic architecture, folding, and random strikes of the stringers in the middle of the dome, and consistent strikes of steeply dipping stringer parts that are parallel to the dome axis distributed near the dome margins (Fig. 1.2c).
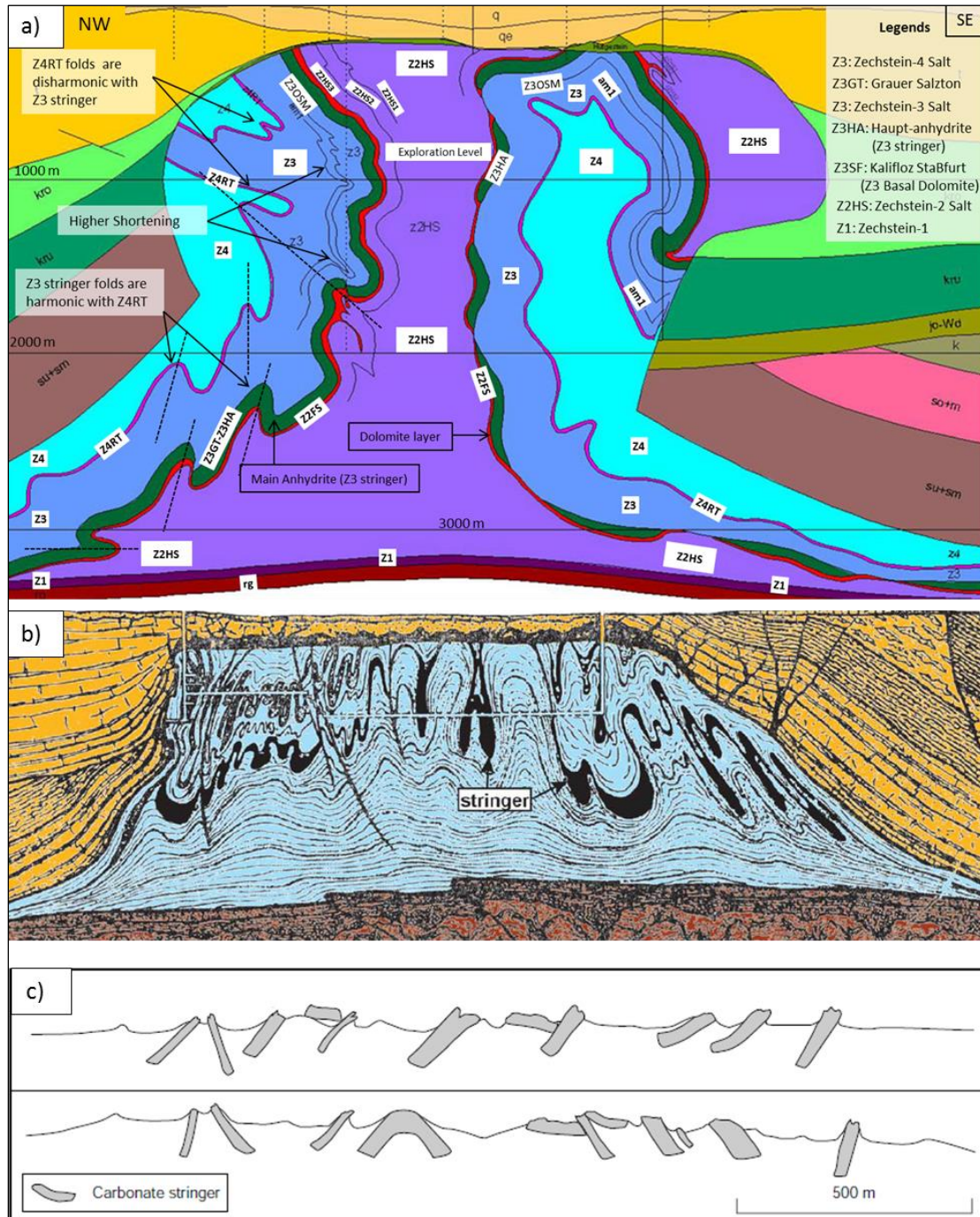
Fig. 1.2: Examples of regional salt structures from outcrops. (a) Profile of the Gorleben salt dome, NW Germany. The dark green layer is the Z3 anhydrite Stringer (after Bornemann 1991). (b) The Z3 Stringer deformation (thick black) with other intra-salt layers within a Zechstein salt dome (Seidle 1921). (c) Two cross-sections through the Qarn Nihayda salt dome, North Oman (after Peters et al. 2003).

1.3.3 Intra-salt structures from seismic data

On seismic data, salt-related structures are commonly studied by focusing on the external salt layers (base and top salt), with the evaporites shown as structureless bodies (e.g., Vendeville and Jackson 1992a; Rowan 1995; Hudec et al. 2009). This lack of imaging within the salt contrasts markedly with the prominence of internal structure of salt bodies observed in outcrops and salt mines. The base salt and top salt layers are generally well-imaged and well-studied on seismic data. However, it is rare to find and hard to map lateral continuous markers within the salt, because salt, in many cases, is featureless and expressed on seismic data as an incoherent seismic facies (Cartwright et al. 2012). Some seismic case studies were able to image the internal geometry of the salt structure, such as the intra-salt Zechstein-3 anhydrite layer (known as the Z3 Stringer) in Northern Europe (Kukla et al. 2011; van Gent et al. 2011; Strozyk et al. 2012; van Gent et al. 2012; Strozyk et al. 2014), the multi-layered Messinian evaporites in the Levant Basin (Cartwright et al. 2012), the layered evaporites in the Santos Basin (Fiduk and Rowan 2012; Jackson et al. 2015), and the carbonate stringers in the South and North Oman Salt Basins (Al-Siyabi 2005; Li et al. 2012a).
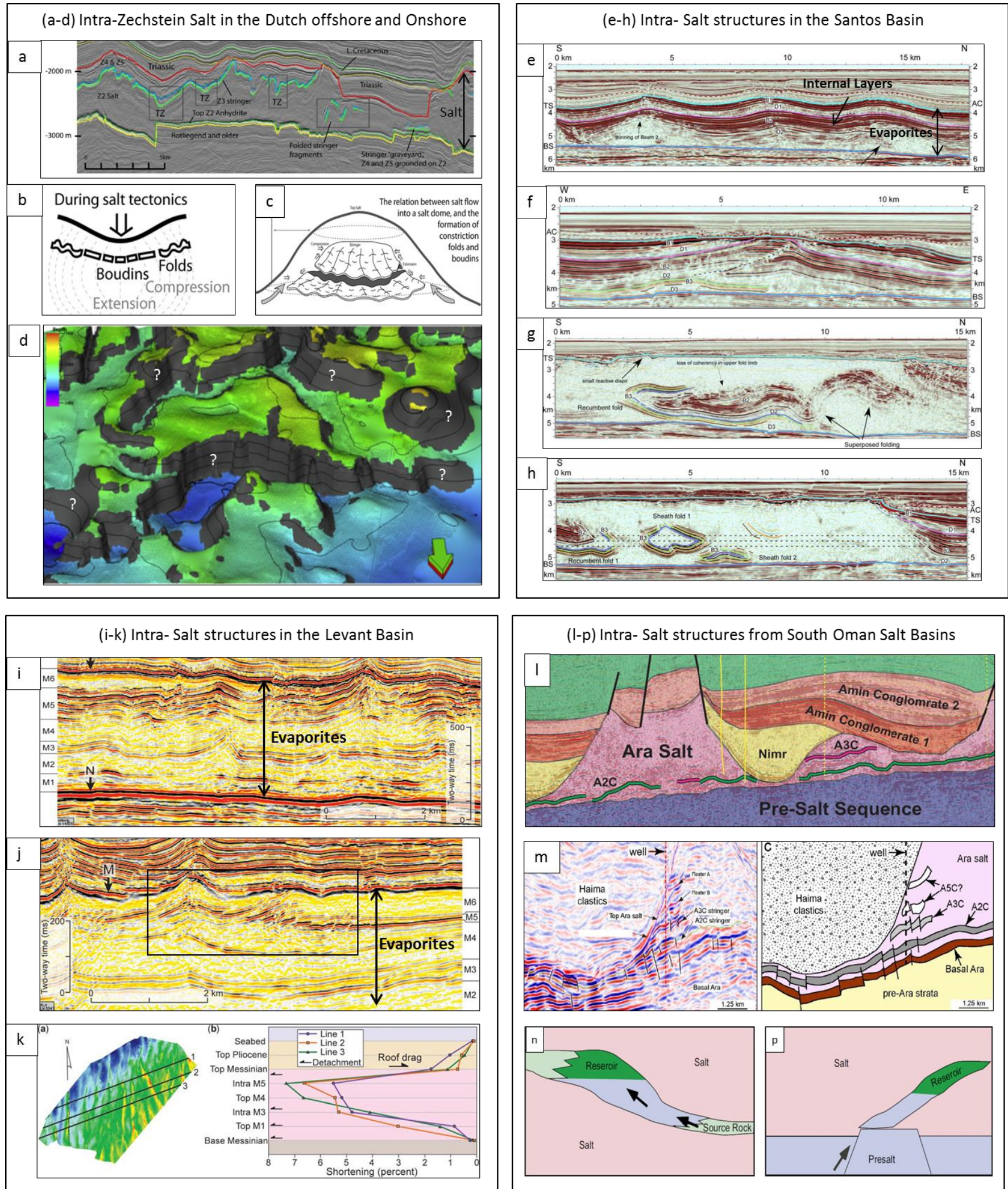
Fig. 1.3: Intra-salt seismic studies. (a–d) Intra-salt structures of the Zechstein from the Dutch offshore and onshore (van Gent et al. 2011). (a) Seismic section across the Zechstein salt shows boudinage and fold structures of the Z3 Stringer. (b) Areas of layer-parallel extension (boudinage) form below subsidence and shortening (folds) in pillows. (c) The formation of folds and boudins during salt flow into the salt dome. (d) Areas of non-imaged steep stringer parts marked with question marks. (e–h) Intra-salt structures from the Santos Basin (Fiduk and Rowan 2012). (e) Open upright folds. (f) Inclined thrusted fold. (g) Recumbent isoclinal fold. (h) Sheath folds. (i–k) Internal salt structure of the Messinian evaporites in the Levant Basin (Cartwright et al. 2012). (i) Evaporite successions composed of competent units (M3 and M5) and incompetent halite-rich units (M1, M2, and M4) show an upward increase in fold structures. (j) Imbricate fore-thrusts in the upper part of the evaporite (k) shortening identified on three seismic profiles show that shortening increases upward within the evaporites and is sharply reduced in the overburden. (l–p) Intra-salt structures from South Oman Salt Basins. (l) Interpreted seismic line shows the creation of salt diapirs and minibasins driven by differential loading (Li et al. 2012a). (m) A diapir flank shows significant deformation of faulting of the intra-salt stringers (Al-Siyabi 2005). (n) The petroleum system of the Ara carbonate stringers shows the self-charging, migration, and trapping. (p) Structural welding and grounding of the stringer allows hydrocarbon migration from the sub-salt section (Al-Siyabi 2005).

Seismic studies of the Z3 Stringer from the Dutch onshore and offshore show

the presence of large-scale brittle and fold structures (Fig. 1.3a) (van Gent et

al. 2012; Strozyk et al. 2014). The study concluded that the regional salt

structures are divided into areas of layer-parallel extension, and boudinage

structures form in areas of top salt subsidence (Fig. 1.3b), while folding

(sometimes associated with boudinage) forms in salt pillows (Figs. 1.3b,c).

Analysis of recent seismic studies in the northern Netherlands suggests that

the Z3 Stringer is frequently broken during the early stages of the deformation

and shows kilometre-sized, sub-parallel to parallel gaps (Strozyk et al. 2014).

The structural complexities of the intra-salt Z3 Stringer lead to several seismic

imaging problems that require further seismic processing and careful seismic

interpretation. Imaging limitations within the salt are either related to the

frequency content and noise level of the seismic data or to the presence of

steeply dipping and thin stringers (Sleep and Fujita 1997; van Gent et al.

2011). One of the most common limitations of the seismic method is its

inability to image steeply dipping stringer inclusions (Fig. 1.3d, van Gent et al.

2011; Strozyk et al. 2012).

Studies of intra-salt deformation from the Santos Basin revealed large-scale

upright open folds (Fig. 1.3e), inclined thrusted folds (Fig. 1.3f), isoclinal

recumbent folds (Fig. 1.3g), and sheath folds (Fig. 1.3h), all interpreted to be

formed primarily by bulk shortening of the whole salt section (Fiduk and

Rowan 2012).

Based on the interpretation of recent seismic studies in the Levant Basin of

the thick multi-layered Messinian evaporites with competent and incompetent

layers (named M1–M6) (Fig. 1.3i), Cartwright and Jackson (2008) and Clark

and Cartwright (2009) have proposed that the evaporites are at an early stage

of salt tectonics and are deformed by gravity-spreading, which has been

driven by the progradation of the Nile Cone and the tilting of the Levant

margin. The internal structure of the evaporites varies vertically from upright

detachment buckle folds in the form of narrow anticlines in the lower part of

the evaporites (M1) (Fig. 1.3i) to high shortening structures of kinked

asymmetric folds and thrust-ramp folds in the top of the evaporites (Fig. 1.3j)

(Cartwright et al. 2012). Shortening of the evaporites varies vertically from 1–

2% near the base of the evaporites to 7% in the upper part, with sharp

reduction in shortening in the overburden indicating asymmetric Poiseuille

flow within the evaporites, where the downdip salt flow is faster than the

overburden translation (Fig. 1.3k).

The Ara Group in Oman is a thick salt succession that contains five to six

hydrocarbon-bearing carbonate platforms known as A1C-A6C stringers and

are completely sealed by halite (Al-Siyabi 2005). These stringers underwent

significant fragmentation, faulting, and folding during halokinesis by differential

loading (Fig. 1.3l and 1.3m) (Al-Marjeby and Nash 1986; Heward 1990).

Understanding the kinematic evolution of these carbonate stringers is of

practical importance for understanding their reservoir distributions, reservoir

quality, hydrocarbon charge (Fig. 1.3n), migration (Fig. 1.3p), and maturity

(Terken and Frewin 2000; Al-Siyabi 2005).

1.3.4 Analogue and numerical modelling

Analogue and numerical modelling in salt tectonics and intra-salt structures

are a rapidly developing area of research (see section 1.4). The numerical

techniques allow incorporating complex geometries, realistic rheologies, and

boundary conditions, and are especially useful for sensitivity analyses to

explore the dependence of the system on various variables and parameters.

Analogue modelling is also an effective tool in the understanding and testing

of brittle/ductile deformation systems in 3D with variable geological boundary

conditions (Vendeville and Jackson 1992b). The results of several analogue

and numerical models simulating similar conditions of competent inclusions

embedded within a salt body (viscous Newtonian or non-Newtonian matrix)

have shown the development of brittle and ductile deformations for the

competent inclusion with purely ductile deformations of the viscous matrix

(e.g., Koyi 2001; Goscombe and Passchier 2003; Goscombe et al. 2004;

Zulauf and Zulauf 2005; Chemia et al. 2008; Dooley et al. 2007; Zulauf et al.

2009; Li et al. 2012a; Abe et al. 2013).

Simultaneous formation of folds and boudinage was also observed by

inclusion of anhydrite within rock salt (Zulauf and Zulauf 2005). Analogue

modelling simulating gravity-driven salt tectonics of competent layers encased

within a ductile incompetent matrix shows the formation of two regional

provinces (Fig. 1.4a): (1) an extensional domain in areas where the evaporites

are thinned and where the competent layer is laterally fragmented and

displaced, similar to boudinage structures and (2) a compressional domain in

areas where the evaporites are thickened and the internal competent layer

forms open to isoclinal, upright to recumbent folds (Cartwright et al. 2012;

Fiduk and Rowan 2012).

Similar brittle extensional zones of boudinage were found in numerical

experiments by modelling a viscous salt section with a single competent non-

Newtonian carbonate layer and exposed to progressive downward subsidence by top salt (Li et al. 2012a). The experiment shows that relying only on top salt subsidence, the stringer breaks below the subsided regions into single isolated fragments and boudins (Fig. 1.4b). The study also introduced the velocity gradient of the salt flow pattern, which allows the prediction of future breaks within the stringer (Fig. 1.4c). A strong horizontally diverging flow pattern in the upper ductile section between the stringer and top salt is generated during subsidence, whilst low salt flow in the lower ductile layer between the stringer and the basement suggested an expected Couette flow type (Fig. 1.4c). Layer-parallel extension of the inclusions within a subsided and thinned salt section also has been recorded by differential loading experiments during diapir build-up (Koyi 2001) (Fig 1.4d). Some of these separated inclusions were carried upward with the rising diaper and rotated to vertical positions or overturned (Fig. 1.4d).

However, most of these experiments are based on 2D modelling boundary conditions. The 2D models show limited information and do not show the full story of the deformational pattern; thus, much is still unknown about the 3D geometry of intra-salt structures.

Three-dimensional mechanical experiments of a single competent layer of anhydrite embedded in a ductile incompetent rock salt matrix that has been subjected to perpendicular bulk flattening (Fig 1.4f) has resulted in the formation of tablet-shaped boudins of the competent anhydrite (Zulauf et al. 2011) (Fig 1.4e,g). A similar result was found in numerical modelling when applying the isotropic strain ratio of the two strain components ($\varepsilon_x = \varepsilon_y$) which resulted in polygonal fracture patterns (Abe et al. 2013) (Fig 1.4h). However,

when rocks with the same mechanical properties as those reported by Zulauf et al. (2011) were subjected to bulk constriction instead of bulk flattening, the competent anhydrite layer revealed intensive fracturing and boudinage with less folded structures (Zulauf et al. 2009). This lack of fold development in constrictional systems is in contrast to what has been observed in nature, where constrictional folds in salt pillows (van Gent et al. 2011), curtain folds in salt diapirs (Talbot and Jackson 1987; Zirngast 1996), and open to isoclinal folds in salt walls (Cartwright et al. 2012; Fiduk and Rowan 2012) are common structures within shortened salt provinces.

In contrast to the aforementioned experiments involving bulk flattening and bulk constriction, analogue experiments of a layer of brittle-cohesive material overlaying a viscous layer of honey (Fig 1.4i) subjected to lateral gravitational spreading show that the brittle layer deforms by uniaxial, tensile, brittle extensional deformations (elongated boudins) (Kettermann 2009) (Fig 1.4j). This uniaxial fracturing of the brittle layer has also been generated using numerical modelling by applying a uniaxial strain ratio of 1:0 between the ε_x and ε_y strain components (Abe et al. 2013) (Fig 1.4k). Such a relationship between the strain ratio and the orientation, shape, and degree of the fractures and boudins can be applied in real seismic examples to constrain the deformation history of intra-salt stringers where salt flow is complicated and spatially heterogeneous (e.g., van Gent et al. 2011).
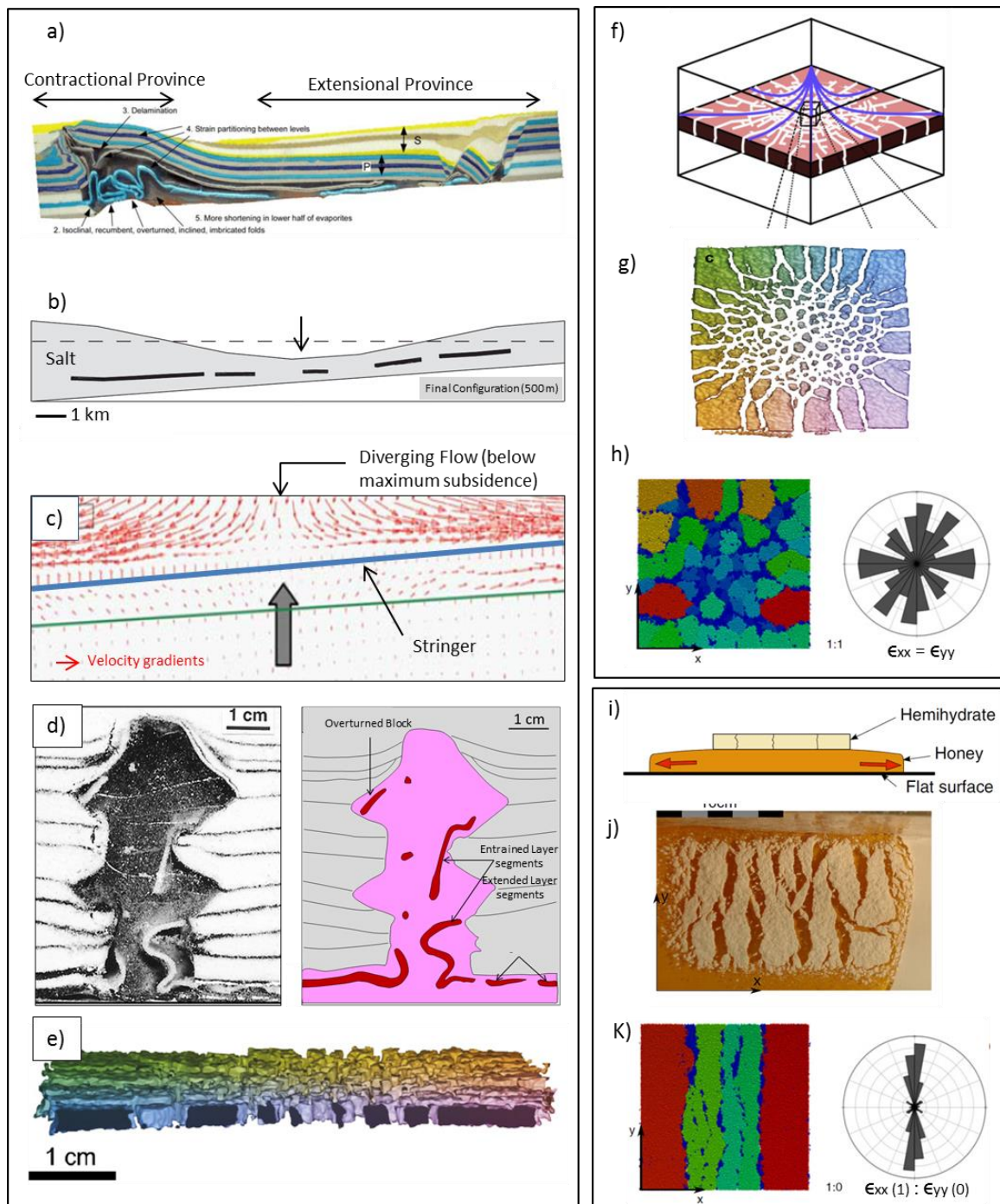
Fig. 1.4: (a) Analogue modelling of a gravitational spreading system (Cartwright et al. 2012). (b) Down-building by top salt subsidence (Li et al. 2012a). (c) Velocity gradient of the salt flow pattern within the salt (Li et al. 2012a). (d) Analogue model simulating an anhydrite layer embedded within salt and subjected to differential loading (Koyi 2001). (f–g) Anhydrite exposed to pure flattening resulted in tablet-shaped boudins (Zulauf et al. 2011). (h) Polygonal-shape pattern of a competent layer subjected to an isotropic strain ratio (Abe et al. 2013). (i–j) Analogue experiments of brittle layer (top) and viscous layer (bottom) exposed to lateral gravitational spreading show uniaxial extensional fractures (Kettermann 2009). (k) Subparallel fractures alignments in uniaxial extension ($\epsilon_y=0$), after Abe et al. (2013).

1.4   Structural evolution and conceptual models of intra-salt layers

Most structural and conceptual models of the intra-salt stringers are constructed based on the final configuration of a given structure (e.g., Talbot and Jackson 1987; Reuning et al. 2009; van Gent et al. 2011) or based on numerical and analogue experiments (e.g., Koyi 2001; Chemia et al. 2008; Dooley et al. 2008; Zulauf et al. 2009; Cartwright et al. 2012; Li et al. 2012a). Talbot and Jackson (1987) suggested that the internal structural styles of a salt layer flowing laterally within a thinned source layer into a diapir are characterised by the formation of recumbent and sheath folds in the source layer which refold as the bed flows towards the centre of the stock of the diapir (Fig.1.5a). The internal layers in the upper part of the source layer are characterised by anti-clockwise rotations of highly inclined and recumbent folds with boudinage, while those in the lower part form clockwise recumbent folds (Fig. 1.5b). The stem of the diapir is characterised by folds with vertical fold axes, known as curtain folds (Fig.1.5a).

In interpreting an anhydrite stringer within the Zechstein salt, van Gent et al. (2011) suggested the combination of boudinage and folding within the salt dome. The flow inside the dome creates vertical extension of the steeply inclined stringer and leads to tensile failure, while coeval horizontal compression creates constrictional folds with steeply inclined axes (Fig.1.5e).

The structural evolution of the intra-carbonate stringers within a salt diapir that derived from down-building of differential loading has been interpreted from field observations of six outcropping salt domes in Oman (Reuning et al. 2009). The structural evolution model suggested the presence of flat undeformed stringers during and after deposition, followed by rotation, uplift,

and fragmentation of the stringers during down-building (Fig.1.5d). However, the details of each stage of diapirism are still poorly understood. Integration of seismic examples from salt basins in Oman with these field observations will enable the building of a more accurate and complete model of the geometrical evolution of the stringers from the early salt flow to the late diapirism stage.

For a salt layer that has been subjected to downward subsidence, numerical modelling of a single carbonate stringer exposed to the progressive downward displacements of top salt, similar to the down-building process, shows lateral extensional deformations of the stringer repeated and propagated laterally with more subsidence by top salt (Fig. 1.5c).

Recently, the structural evolution of the Z3 Stringer has been interpreted using seismic data from the northern Netherlands (Strozyk et al. 2014). These authors suggest (1) early rupturing and extensional deformations of the stringer during syn-depositional salt flow with the development of small-amplitude folds; followed by (2) rotation of the stringers parallel to top salt during the subsidence of the basin, with the formation of bigger-amplitude folds within pillow structures; and finally (3) significant fragmentation in the subsided region and the development of large-amplitude folds below the thick salt sections (Fig. 1.5f).

Such variations in the structural evolution of the intra-salt structures need to be further classified based on key variables such as the stratigraphy of the salt section (e.g., pure halite, multi-layered evaporites), the stringer rock type (e.g., anhydrite, carbonate, clastic), the driver mechanism of salt tectonics (e.g., lateral gravity spreading, differential loading, compressional tectonics),

the stage or the degree of tectonics and halokinesis, and the provinces or locations of each of the structures based on the regional salt structure (e.g., below subsided regions, within salt diapirs, in salt pillows, below diapir flanks).
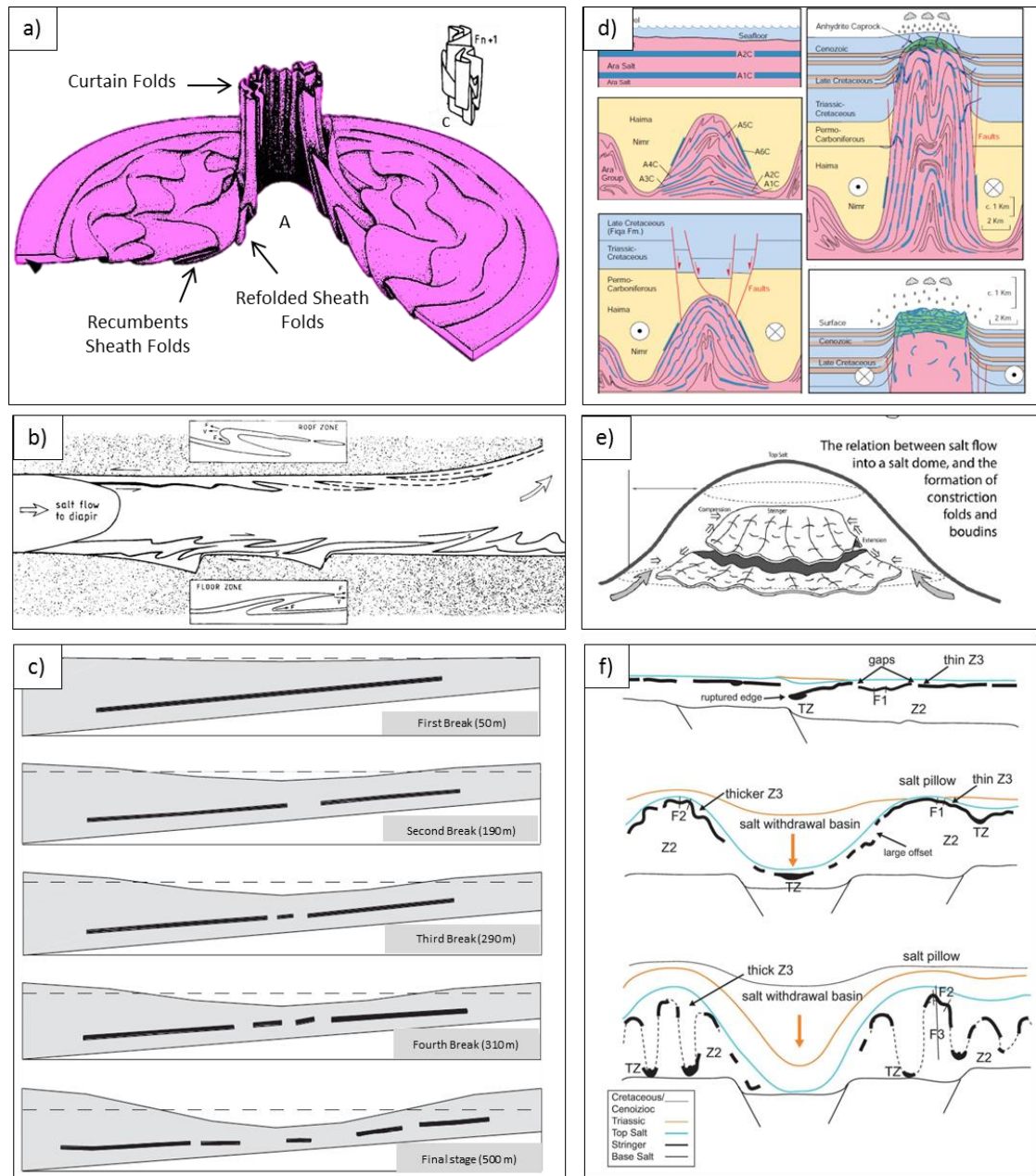
Fig. 1.5: Conceptual models of intra-salt structures. (a) Single layer within a source layer and a diapir (after Talbot and Jackson 1987). (b) Salt flowing from the source layer into the diapir (Talbot and Jackson 1987). (c) Numerical evolution of a single competent stringer within salt exposed to progressive top salt subsidence (Li et al. 2012a). (d) Intra-salt evolution during diapir build-up (Reuning et al. 2009). (e) Z3 Stringer structural style within a salt dome (van Gent et al. 2011). (f) Z3 Stringer structural style and evolution from northern Netherlands (Strozyk et al. 2014).

1.5   Regional salt tectonics: Driver mechanisms

The onset of salt tectonics can be triggered by variable mechanisms such as density inversion or buoyancy (Talbot 1992), stratigraphy by differential depositional loading (Trusheim 1960; Hodgson et al. 1992; Jackson and Vendeville 1994; Koyi 1996; Ge et al. 1997; Gaullier and Vendeville 2005; Vendeville 2005; Warsitzka et al. 2013), tectonics by either contraction (e.g., Humphris 1979; Rowan 2002; Rowan and Vendeville 2006; Ings and Beaumont 2010) or extension (e.g., Vendeville and Jackson 1992a,b; Vendeville 2005), and thermal loading (Talbot and Jackson 1987; Talbot 1998).

1.5.1   Density-driven salt tectonics

This mechanism suggests that salt will start sinking if the average density of post-salt sediments is greater than that of the salt (e.g., Talbot 1992; Podladchikov et al. 1993; Van Keken 1993; Kaus and Podladchikov 2001) (Fig. 1.6a). However, the model suggests that salt cannot sink until the sediment accumulation is denser than salt. The average density of non-pure salt is about 2200 kg/m^3 (Hudec et al. 2009). Most siliciclastic rocks can only reach the required density and generate the density inversion between the salt and the overburden only after the accumulation of 2.3 km of sediments (Hudec et al. 2009). An average sediment density of 2700 kg/m^3 is able to drive instability of the salt layer after the deposition of 1600 m of sediments, while a minimum of 2300 m of sediment accumulation is required to initiate sinking over the salt if the average density of the overburden is 2600 kg/m^3. However, observations of salt tectonics triggered by differential loading suggest that salt starts sinking when only a few hundred metres of sediment

had accumulated (Hudec et al. 2009). This suggests that there are other mechanisms that trigger salt tectonics and that buoyancy is not the only process that leads to salt movements. However, the model is still considered to be valid in situations that experience sediment loading where no significant extension or contraction exists and there is no significant surface or basal slope (Fig. 1.6b), as for example in some intracontinental basins such as the Ara Group in the South Oman Salt Basin (Al-Marjeby and Nash 1986; Li et al. 2012a) and the Zechstein of the Central North Sea (Hodgson et al. 1992) and North Germany (Trusheim 1960).

1.5.2 Salt tectonics driven by sedimentary topographic loading

Variable overburden thickness that overlies a weak salt layer induces pressure gradients and causes the salt to flow and subside (Kehle 1988; Warsitzka et al. 2013). This process does not require density inversion and is considered to be much more powerful than buoyancy (Hudec et al. 2009). The most common example is when a prograding sediment wedge in updip areas accumulates over a salt layer and causes the salt to subside and evacuate (Gemmer et al. 2004; Ings et al. 2004) (Fig. 1.6c). Differential loading in intracratonic basins can also induce instability in the salt layer, which will lead to the formation of minibasins and diapirs (Fig. 1.6b).

Since the salt behaves almost like a fluid, gravitational loading effects have been simplified by using the concept of hydraulic head, which states that the fluid will flow from zones of high head to zones of lower head (Kehle 1988; Hudec and Jackson 2007) (Figs. 1.6d,e,f). In this case, salt can flow either by variable overburden thickness with no elevation head gradient (Fig. 1.6d), by

conformable overburden thickness but with a dipping salt layer (Fig. 1.6e), or by the combination of these two.

1.5.3 Salt tectonics driven by shortening (compression)

Many compressional or transpressional salt basins in passive margins are the results of downslope salt flow from an updip extension (Wu et al. 1990; Demercian et al. 1993; Cartwright et al. 2012) (Fig. 1.6c). Alternatively, compressional related salt structures are derived from regional buckling of the basin (Figs. 1.6g,h). During shortening, salt is squeezed laterally by the inward movement of one or both sidewalls, forcing the salt to rise upward (Hudec and Jackson 2007). Salt may flow and penetrate the surface and grow as a passive diapir by pressurization of the salt body due to contractional tectonics forces even if the salt layer is not buoyant with the overburden sediments (Hudec and Jackson 2007) (Fig.16g). The upward movement of the salt may sometimes result in the roof of the overburden being pierced by crestal normal faulting (Fig. 1.6h).
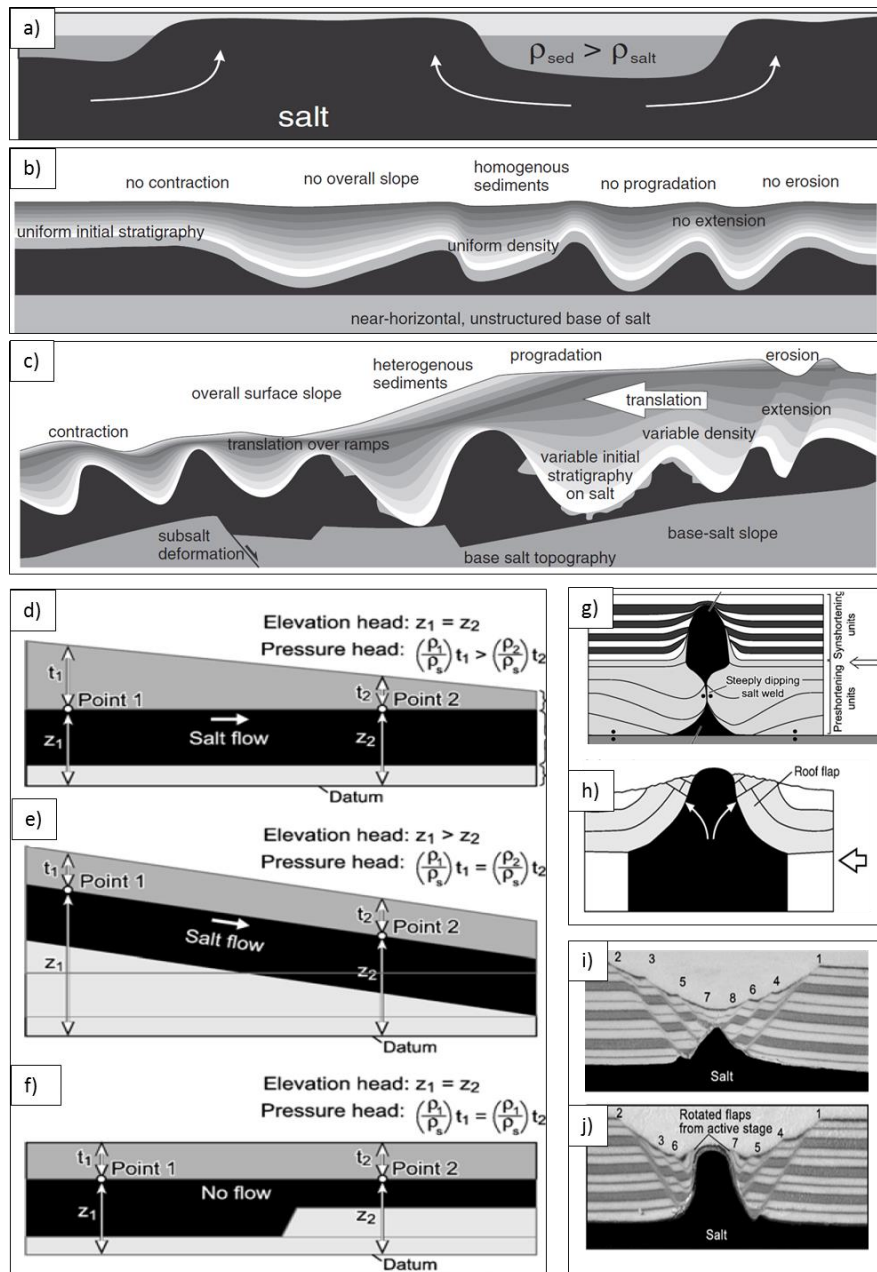
Fig. 1.6: Regional salt tectonics driver mechanisms. (a) Buoyancy or density inversion between salt and overburden. (b) Sediment differential loading with the absence of regional extension and regional compression. (c) Complex passive margin settings. Extension in the updip areas leads into salt flow and translation of the overburden and the formation of a contraction province in the downdip. (d–f) Examples of hydraulic head-gradient analysis in salt tectonics (after Hudec and Jackson 2007). (d) A pressure head gradient is generated by overburden thickness variation. (e) An elevation head gradient produced by an inclined salt layer with uniform overburden thickness. (f) An equilibrium state reached by a flat salt layer above conformable overburden thickness. (g–h) Diapirism during shortening (Hudec and Jackson 2007). (i–j) Reactive diapirism in an extension system (Vendeville and Jackson 1992b).

1.5.4 Salt tectonics driven by extension

Extensional-related salt diapirism is the opposite of compression. In this case, the overburden is stretched and displaced by extensional faults, which allows the salt to rise either by buoyancy or by the pressure created by the differential loading between the flanks of the rifted area and the weak faulted zone in the middle. If the overburden is broken by extensional faults, an initial small reactive diapir can develop in the weakest faulted crust (grabens or footwalls) (Fig.1.6i), which later propagates upward when the pressure of the salt is enough to penetrate the graben roof and to form a passive diapir (Vendeville and Jackson 1992b) (Fig.1.6j).

1.5.5 Thermal loading

The influence of temperature on salt behaviour is not widely documented in the literature. If salt is considered a fluid, then the temperature has an important effect on salt (just as it has on any other type of fluid) by changing its dynamics and viscosity. Thermal loading is defined as the change in the volume of salt due to the change in its temperature (Hudec and Jackson 2007). Because salt is a good thermal conductor, if its volume increases, salt layers become more buoyant and intra-salt thermal convection results (Talbot and Jackson 1987; Talbot 1998).

1.6   Patterns of salt flow

The terms "salt withdrawal" and "salt expulsion" refer to the flow of the salt from where it has been deposited into the salt structure (Hudec and Jackson 2007). On a geological timescale, salt flows similarly to an incompressible fluid under applied stress (Davison et al. 1996). The salt body can deform by Poiseuille flow, Couette flow, or a combination of these two (Jaeger and Cook

1979; Weijermars et al. 1993; Rowan et al. 2004). Very few studies have demonstrated the flow regime within the salt on a regional seismic scale (Cartwright et al. 2012). The main salt flow profiles are summarised in Fig. 1.7a–e (Davison et al. 1996).

1.6.1 Poiseuille flow

In a confined salt layer, a viscous salt layer flows as a Poiseuille profile, where the highest velocity is concentrated in the middle, similar to the flow of a viscous liquid through a pipe (Fig. 1.7a) (Vendeville et al. 1993; Weijermars et al. 1993; Davison et al. 1996). The displacement is almost zero along the upper and lower boundaries, where the salt layer experiences friction and flow resistance; thus, no lateral translation of the overburden is required for this type of flow (Davison et al. 1996; Cartwright et al. 2012). A Poiseuille flow commonly forms when the salt flows into a salt structure during the building of a salt diapir (Davison et al. 1996).

Numerical modelling shows that differential sediment loading on a viscous salt layer leads to a pressure-driven Poiseuille flow (Fig. 1.7f, g) (Gemmer et al. 2005). Analogue modelling of multi-layered evaporites exposed to gravitational spreading shows the formation of an asymmetrical Poiseuille flow in the incompetent layers (Dooley et al. 2008; Cartwright et al. 2012) (Fig. 1.7h). Shortening analysis of the competent seismic markers in the Messinian evaporites (M1, M3, and M5 in Fig. 1.3i) has been used to generate salt flow profiles (Fig. 1.3k) (Cartwright et al. 2012). The results indicate asymmetrical Poiseuille flow profiles where the upper part of the evaporites is shortened more than the middle and the lower part, indicating that the flow velocity is higher at the top of the evaporites during the gravity spreading of the basin

(Fig. 1.3k). This also means that the greatest shear-strain gradient is in the uppermost Messinian, indicating that it is the main detachment of the salt flow (Cartwright et al. 2012). Since the overburden has larger shortening than the sub-salt section (Fig. 1.3k), the base of the overburden is interpreted to have been dragged with the upper evaporites but at a slower velocity.

1.6.2 Couette flow

When the overburden is influenced by extension or compression where the upper salt layer is dragged with the overburden movement, the salt flow profile is a Couette flow (Fig. 1.7b). In a non-inverted Couette flow, the maximum drag and flow of the salt is in the upper part (Fig. 1.7i), while in an inverted Couette flow, the maximum drag and flow of the salt is in the lower part (Fig.1.7j). A Couette flow involves simple shearing within the salt layer as the overburden is laterally translating (Vendeville et al. 1993). Unlike in a Poiseuille flow, the salt layer in a Couette flow neither thins nor thickens. The overburden displacement rate is directly proportional with the thickness of the salt and the shear stress applied (Davison et al. 1996). The combination of a Couette flow and a Poiseuille flow results in an asymmetric Poiseuille flow (Fig. 1.7c).

1.6.3 Multi-layer flow

Salt stratigraphy is sometimes complex, and multiple Poiseuille and Couette flows result when sedimentary layers are present within the salt (Fig. 1.7d). Such flow is relatively slower than the pure Poiseuille flow because of the drag effect between the salt and the rigid layers (Davison et al. 1996). The layers behave individually during lateral flow, but act together during vertical flow (Fig. 1.7e).
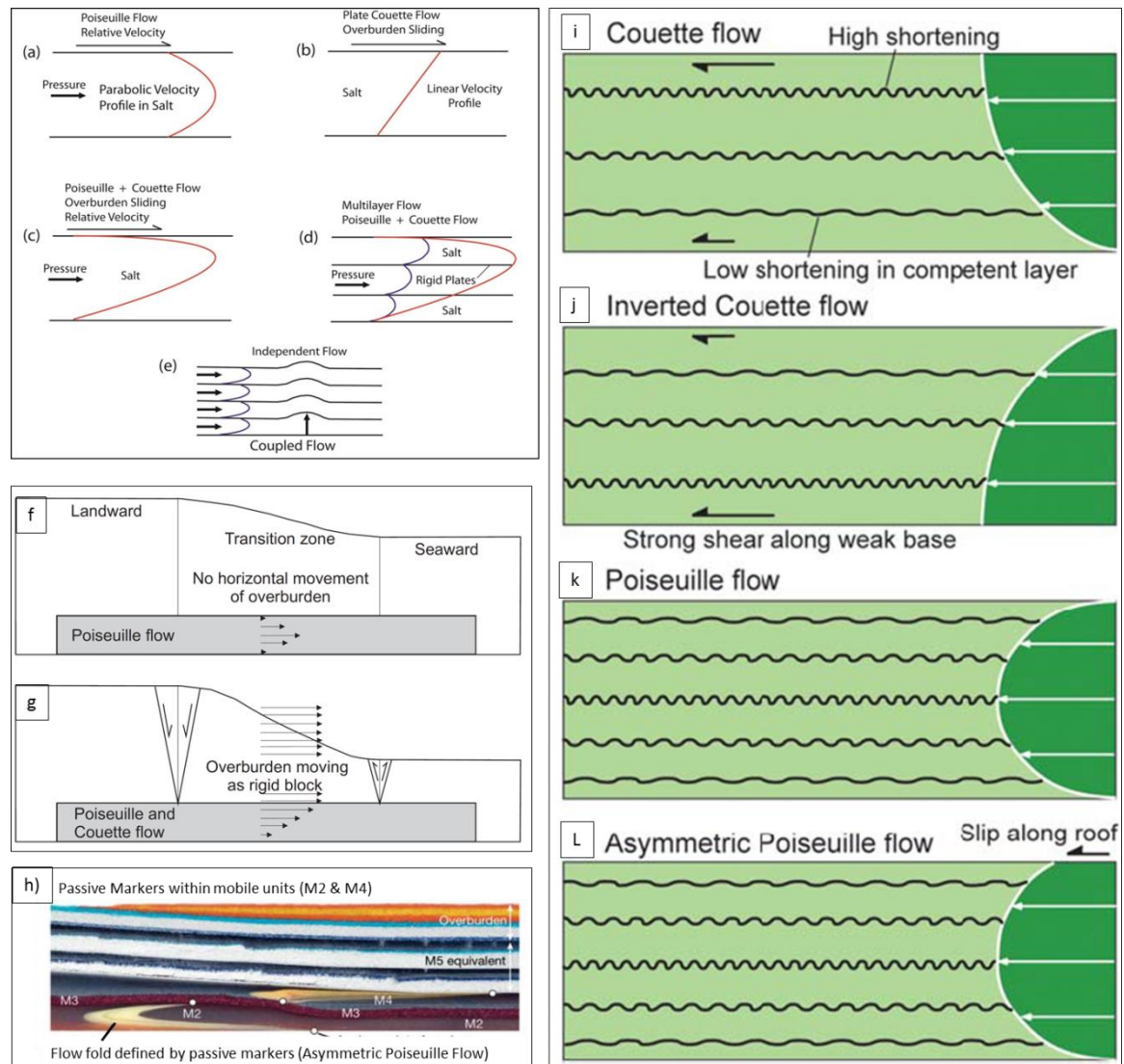
Fig. 1.7: (a–e) Salt flow profiles (modified after Davison et al. 1996). (f) Differential loading of the overburden induces a pressure-driven Poiseuille flow. (g) Differential loading and extension of the overburden generates Poiseuille and Couette flows in the viscous layer (Gemmer et al. 2005). (h) Analogue model of multi-layered evaporites shows the formation of an asymmetric Poiseuille flow within the ductile mobile units (Cartwright et al. 2012) (i) Sketch shows shortening analysis of buckled folded competent layers (black) within the evaporites (green) used to create four salt flow profiles (Cartwright et al. 2012).

1.7   The properties of evaporite facies

Evaporites are generally the weakest lithology in sedimentary basins (Hudec and Jackson 2007; Urai et al. 2008; Davison 2009). Salt layers sometimes contain other evaporitic rocks (e.g., anhydrite or gypsum) or any non-evaporitic rocks such as clastic or volcanic intrusions (Jackson 1995; Urai et al. 2008). Halite rock (NaCl) is generally the most common chloride facies in evaporites. Due to its low density, low creep strength, low porosity, and low permeability, halite rock exerts a significant influence on basin structure and evolution through salt tectonics movements and fluid trapping (Urai et al. 2008). The physical properties of salt in general are low density, very low permeability, low effective viscosity, high solubility, very low water content, and very low compressibility (Carter et al. 1993; Davison et al. 1996) (Table 1.1). The density of halite is about 2000 kg/m^3 (Koyi 2001; Urai et al 2008). Halite has a lower density and viscosity than most of the intra-salt layers, such as sandstone (2600 kg/m^3), limestone (2700 kg/m^3), dolomite (2870 kg/m^3), and anhydrite (2900–3000 kg/m^3). When they are encased within the salt, most of these rocks behave as competent materials compared with the ductile, incompetent salt. Examples include the carbonate stringers of the Infra-Cambrian Ara Group evaporites in the Oman Salt Basins (Al-Siyabi 2005; Reuning et al. 2009; Schoenherr et al. 2009; Li et al. 2012a) and the Z3 anhydrite/carbonate stringer in Northern Europe (van Gent et al. 2011). However, there are other common evaporite minerals known as the potassium–magnesium salts (K-Mg salts), that are much weaker than halite and have much lower effective viscosities, such as bischofite (1560 kg/m^3) carnallite (1570 kg/m^3), epsomite (1700 kg/m^3), and sylvite (1860 kg/m^3) (Urai

et al. 2008), (Table 1.2). These rocks act as incompetent materials within the halite salt and thus may have an impact on the internal deformation (Geluk et al. 1997; Raith et al. 2015).

Table 1.1: Key mechanical properties of some evaporites (after Davison et al. 1996)

Salt – seismic velocity	$4500 ms^{-1}$
Salt - viscosity	10^{14}-10^{19} PaS
Salt- density	2100-$2200 kgm^{-3}$ - can decrease with depth/increased temperature
Salt – thermal conductivity	6.0W/m K (surface), 4W/ m K (@ 130°C)
Salt - melting point	800°C
Salt - permeability	$10^{-20} m^2$
Salt - rate of solubility	East Flower Graben Banks – 10,700-21,700m^3 per annum
Anhydrite – density	$2980 kgm^{-3}$
Anhydrite – seismic velocity	$6500 ms^{-1}$
K rich salts (Carnalite) – Visc.	10^8 PaS

Table 1.2: The main evaporite minerals and their wireline log properties (after Urai et al. 2008).

Name	Formula	Density (kg/m^3)	GR (API)	Neutron "Porosity"	Sonic "ms/ft"
Bischofite	$MgCl_2 \cdot 6H_2O$	1560	0	>60	100
Carnallite	$KMgCl_3 \cdot 6H_2O$	1570	220	65	78
Epsomite	$MgSO_4 \cdot 7H_2O$	1710	0	>60	
Sylvite	KCl	1860	500	-3	74
Halite	NaCl	2040	0	-3	67
Kainite	$KMg(SO_4)Cl \cdot 3H_2O$	2120	245	45	
Gypsum	$CaSO4 \cdot 2H_2O$	2350	0	>60	52
Kieserite	$MgSO4 \cdot H_2O$	2590	0	38	
Calcite	$CaCO_3$	2710	0	-1	49
Polyhalite	$K_2 \cdot Ca_2$ $Mg(SO_4)_4 \cdot 2H_2O$	2790	180	15	57
Langbeinite	$K_2Mg_2 (SO_4)_3$	2820	275	0	52
Dolomite	$CaMg(CO_3)_2$	2870	0	1	44
Anhydrite	$CaSO_4$	2980	0	-2	50

31

1.7.1 The rheology of salt

The rheology of salt has been summarised by Vendeville and Jackson (1992a) and Urai et al. (2008). The occurrence of wide-scale intra-salt deformation (millimetre to kilometre scale) of folding and shear zones in both highly deformed regional salt structures (salt domes, salt diapirs, salt walls) and within flat-lying salt bodies reflects the heterogeneous rheology of rock salt (Urai et al. 2008). In a simple way, dry salt deforms as a power-law fluid (dislocation creep), whereas wet salt behaves as a Newtonian fluid (diffusion creep). Temperature is crucial in controlling the viscosity of wet salt, while stress and strain rate are less important. Wet salt, thus, has no yield strength. Therefore, faults rarely occur within salt, and if a thin salt layer has been displaced, the displacement was achieved by a ductile shear zone or by widely distributed strains (Vendeville and Jackson 1992b). This explains why most overburden faults terminate and disappear at the upper salt and the overburden displacement at the upper salt layer is high. However, fractures and faults are observed very locally in some salt domes and salt glaciers, and these have been interpreted to be controlled significantly by fluid overpressure (Davison 2009).

1.8 Importance and implications of intra-salt studies

Understanding the deformation behaviour of salt rocks is important for several purposes.

Intra-salt layers as hydrocarbon reservoirs: Hydrocarbon reservoirs have been found in the carbonate stringers in Oman Salt Basins, as well as in some stringers in Europe (Geluk et al. 1997; Peters et al. 2003; Al-Siyabi 2005; Schröder et al. 2005; Schoenherr et al. 2009; Reuning et al. 2009). In Oman, the intra-salt carbonate stringers reservoirs, which include inter-crystalline dolomite, grainstones, packstones, and stromatolitic and thrombolytic reef facies, are hydrocarbon

producers (Al-Siyabi 2005). The limited knowledge of the geometrical complexities, diagenetic history, and depositional environments of these carbonate stringers makes the prediction of reservoir quality challenging (Al-Siyabi 2005).

Sealing potential: Salt is considered to be a very good seal layer because of its low permeability and very fine grain size. However, drilled stringers in the South Oman Salt Basins indicate that the salt layer that is close to the stringer reservoir is oil-stained, suggesting that the oil flowed into the salt (Mattes and Morris 1990). Recent studies of the sealing capacity of the Ara salt conclude that the sealing capacity of rock salt is reduced and the permeability is increased by many orders of magnitude when the stringer oil pressure is more than the salt lithostatic pressure, resulting in leaking of hydrocarbons from the reservoir into the salt (Schoenherr et al. 2007). Therefore, the depth, salt lithostatic pressure, fluid overpressure of the stringers, and position of the stringers relative to the overburden are important parameters to be considered when measuring the sealing capacity of the stringer reservoirs.

Hydrocarbon migration: Proper interpretation of the discontinuities and internal fracturing of the intra-salt stringers is important for understanding hydrocarbon migration. Understanding the structural evolution and the movement history of the stringers will help clarify the migration history, for example, the hydrocarbon charge from sub-salt into the stringers, the hydrocarbon migration from one stringer into another, as well as the hydrocarbon leakage from the stringers into the overburden (Al-Siyabi 2005) (Fig.1.3n,p).

Drilling hazards: The Ara carbonate stringers in Oman, as well as the intra-Zechstein stringers in Europe, pose serious drilling hazards to the drilling campaigns and therefore need to be avoided as much as possible (Williamson et al. 1997; Koyi

33

2001; Al-Siyabi 2005; Schoenherr et al. 2007; Kukla et al. 2011). Therefore, proper interpretation of their discontinuities and complex geometries is crucial.

Radioactive waste disposal: Due to its unique physical and chemical properties (Hunsche and Hampel 1999), rock salt is also considered a good material for long-term repositories for nuclear and radioactive waste disposal. This is a very serious issue for the environment that requires careful and proper decision making. Salt is also used for different kinds of geological storage and solution mining (Coelewij et al. 1978; Bornemann 1991; Fokker et al. 1995; Evans and Chadwick 2009), and prediction of internal salt structure is of major relevance in these fields (see Bornemann 1991; Koyi 2001; Chemia et al. 2008).

1.9   Aims and objectives

This thesis is aimed at building a full understanding of the kinematic evolution of internal salt layers from the early to the late stages of salt tectonics by considering different driver mechanisms. Hence, the objectives of this thesis are (a) to investigate the role of regional tectonic processes such as lateral gravity spreading, differential loading, and compression in the kinematics of intra-salt layers and (b) to evaluate the influence of the lithology and compositional variation of intra-salt layers on their rheological behaviours during the different stages of tectonism and halokinesis.

1.10   Research case studies

To achieve the aforementioned objectives, two natural laboratories where used to study intra-salt deformation, as they have been widely documented and can be seismically imaged: the Southern North Sea (SNS) and the South Oman Salt Basins:

1. The first 3D seismic data set is from offshore Southern North Sea (Silverpit area), a classic study area for the analysis of salt tectonics. Importantly, the Zechstein Group has four to five evaporitic cycles (Z1–Z5). The anhydrite/carbonate stringer of the Z3 cycle is a seismically visible layer and well known to form complex structures within the halite media (Underhill 2009; van Gent et al. 2012).

2. The second 3D seismic data set is from the South Oman Salt Basin, where the Ediacaran to Early Cambrian Ara Group forms six carbonate to evaporite sequences (Al-Siyabi 2005; Schoenherr et al. 2007).

1.11   Thesis structure

Chapter 1 introduces and defines the main subject of the research, which is the kinematics of flow of salt multi-layers during salt tectonics. Previous work done in this field is summarised, and all the limitations that have not been addressed are listed. Finally, the aims and objectives of the study are introduced.

Chapter 2 discusses the characteristics of the seismic surveys and well data used to complete this research. The methodological steps and the workflow of some quantitative and qualitative analyses are explained.

Chapter 3 introduces the stratigraphic facies of the Upper Permian evaporitic Zechstein Group in the Silverpit Basin with an aim to understand the influence of salt layering, properties, and rheological heterogeneities on the salt deformational style. The second aim of this chapter is to understand the main regional tectonic phases and the driver mechanisms of the salt tectonics in the area.

Chapter 4 focuses on the dynamic and kinematic evolution of the intra-salt structures specifically in areas below top salt subsidence (regional synclines) by detail analysis of the intra-salt Z3 Stringer in the Silverpit area in the Southern North Sea. The main aim is to understand the kinematic evolution of the internal salt structure from the early stage of subsidence to the welding stage. The regional driver mechanism and the mechanical properties of the stringer used (Z3 Stringer) are compared with those of other salt basins that experience subsidence with different driver mechanisms and stringer properties (e.g., Ara salt in the South Oman Salt Basin). The chapter also classifies the discontinuities of the internal Z3 Stringer and provides the interpretation of seismically non-imaged stringer parts.

Chapter 5 is focused on the kinematic evolution of the intra-salt Z3 Stringer within regions of salt accumulations (anticlines) using 3D seismic surveys from the Silverpit Basin in the Southern North Sea. Classification of the internal salt structural styles within these regions is summarised. Shortening analysis of the intra-salt stringer and top salt is introduced in order to understand the internal salt flow patterns and the influence of the regional tectonics of the basin on the internal shortening within the salt.

Chapter 6 introduces the stratigraphic facies of the intra-salt Ara stringers in the South Oman Salt Basins with an aim to understand the influence of salt layering, properties, and rheological heterogeneities on the salt deformational style. The second aim is to construct tectonostratigraphic evolutional models of the basin using 2D and 3D seismic data in order to link the regional evolution of the basin with the distribution, deformation, trend, and structural styles of the intra-salt stringers. More detail is presented in chapter 7.

Chapter 7 is based on the structural interpretation of the Ara salt carbonate stringers in the South Oman Salt Basins. The aims of this chapter are (1) to develop a detailed kinematic structural evolution of the intra-salt stringers below regional salt structures (e.g., minibasins, salt domes, diapir flanks) and (2) to use the internal salt inclusions (fragments) as a tool to understand the internal salt flow patterns.

Chapter 8 discusses and summarises the key contributions of this research and highlights the major findings from chapters 3 to 7.

Chapter 2: Data and methodology

2.1   Introduction

This chapter introduces the data and methods used in this thesis: First, the Southern North Sea case study is used to interpret the Z3 Stringer, which has been discussed in the works of Strozyk et al. (2012), Underhill (2009), and van Gent et al. (2011). Second, the South Oman Salt Basin case study is used to interpret at least four intra-salt stringers (Al-Siyabi 2005). These intra-salt markers are well known in the literature to be challenging to interpret (Reuning et al. 2009). Therefore, a few methods are suggested in this thesis to overcome these challenges and to come up with more realistic and confident interpretations. The data include 3D seismic surveys and well logs. The workflow and the methods that are used for the interpretation and for the analysis of the intra-salt stringers are discussed in the following sections.

2.2   Case study 1: The Silverpit Basin in the Southern North Sea

The Silverpit Basin is located in the Southern North Sea Basin (SNS), some 125 km off the east coast of Britain (Underhill 2009). Three seismic surveys were used in this case study for qualitative and quantitative structural analyses. The Z3 Stringer within the Zechstein salt was used for the analysis of the internal salt structure (van Gent et al. 2011). In addition, wellbore data were used to calibrate the tops of the formations, examine the stratigraphy of the salt section, and understand the mechanical properties of the stringer layer.

2.2.1   Seismic data

For the structural interpretation described in this case study, three 3D seismic data sets were used: Cavendish, Trent96, and Snsj07 (Table 2.1). All sets have zero-phased, normal polarity. The Cavendish 3D survey is the largest seismic survey of the three and is located in Block 43/19a, north of the Silverpit Crater zone (Fig. 2.1a).

The water depth in the field is approximately 18.5 m. The Cavendish survey is pre-stack time migrated and covers an area of 1293 km^2. The Trent96 survey is located in the Trent Gas Field, south of the Cavendish Field (Fig. 2.1a). Both the Cavendish and Trent96 surveys are oriented in a NNW direction and were used for the 3D seismic interpretation (Fig. 2.1b). The Snsj07 survey is oriented in a NNE direction, and it merges with the southern part of the Trent96 survey (Fig. 2.1b). Due to the poor quality of the Snsj07 survey, it was only used for well calibration and 2D cross-sectional analysis. The Z3 Stringer is rarely well-imaged on the Snsj07 survey; hence, it was not used for the 3D interpretation of the intra-salt layer.

Table 2.1: The three seismic surveys used in case study 1, in chapters 3, 4, and 5.

Seismic survey	Cavendish	Trent96	Snsj07
Area (km^2)	1293 km^2	450 km^2	2400 km^2
Location	Block 43	Block 43	Block 43, 44, 48
Data available	80% of the total area	55% of the total area	25% of the total area
Z3 Stringer	Well-imaged	Well-imaged	Poorly imaged
Interpretation	3D and 2D seismic analysis	3D and 2D seismic analysis	2D analysis
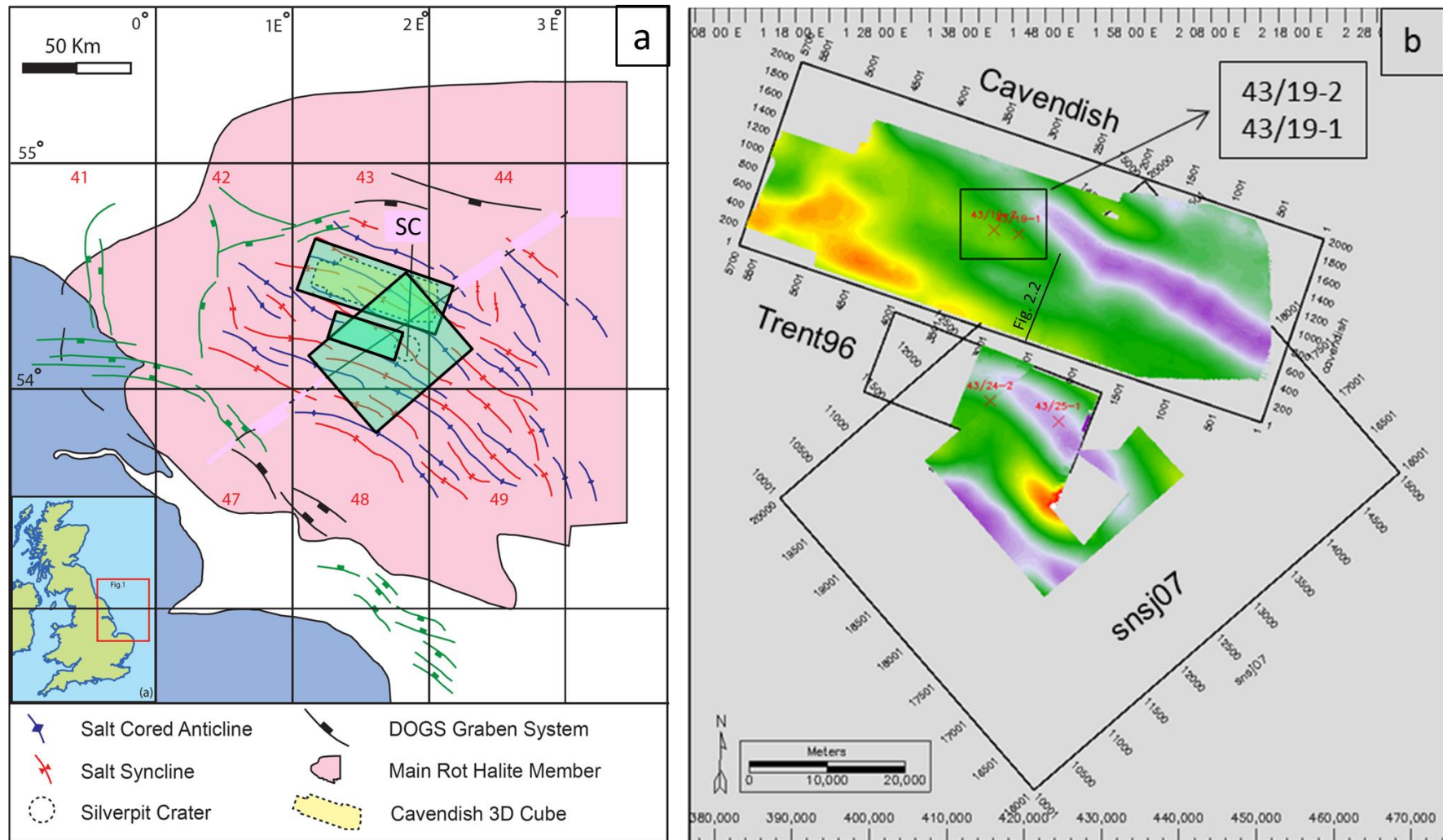
Fig. 2.1: (a) Location of the study area in the Southern North Sea Basin (after Coward and Stewart 1995). (b) The three seismic surveys in the Southern North Sea. The interpreted Top Salt surface is used to show the extent of the available data within the surveys. Non-interpreted areas inside the boxes (grey) represent the area with no data.

2.2.2. Seismic limitations

The Z3 intra-Zechstein reflector, also known as Z3 Stringer, is reasonably well-imaged because of the high density and velocity that cause a high acoustic impedance contrast between the halite and anhydrite (van Gent et al. 2011; Strozyk et al. 2012). However, where the Z3 Stringer is steep or below seismic resolution, the layer is not imaged on seismic data. The polarity of the Z3 Stringer is similar to that of the Top Salt, and both are positive reflections, indicating that the Z3 Stringer is within seismic resolution; otherwise, an inverse polarity is expected in areas where the Z3 Stringer is below the seismic resolution (Sheriff 1975; Davies et al. 2004).

Most of the seismic limitations and imaging problems of the Z3 Stringer were observed in areas of complex fold structures (Fig. 2.2). The seismic quality is strongly related to the intensity of folding. In areas where the dip of the Z3 Stringer is gentle and the layer is less deformed, it is very well-imaged. However, in areas of high-amplitude, tighter fold structures, the seismic reflector of the Z3 Stringer is always associated with seismic artefacts. The limitations of seismic data within the Zechstein salt include frequency content, noise, and migration problems (Fig. 2.2). The most common seismic artefacts can be summarised as

1. migration smiles that are vertically crossing the stratigraphy (Fig. 2.2a); these are different from faults, as they show no displacement and are easily differentiated on seismic data;

2. x-shape geometries associated with tight folds (Fig. 2.2b);

3. non-imaged steep fold limbs (Fig. 2.2c) (see also van Gent et al. 2011); and

4. high-amplitude zones at fold hinges (Fig. 2.2d).
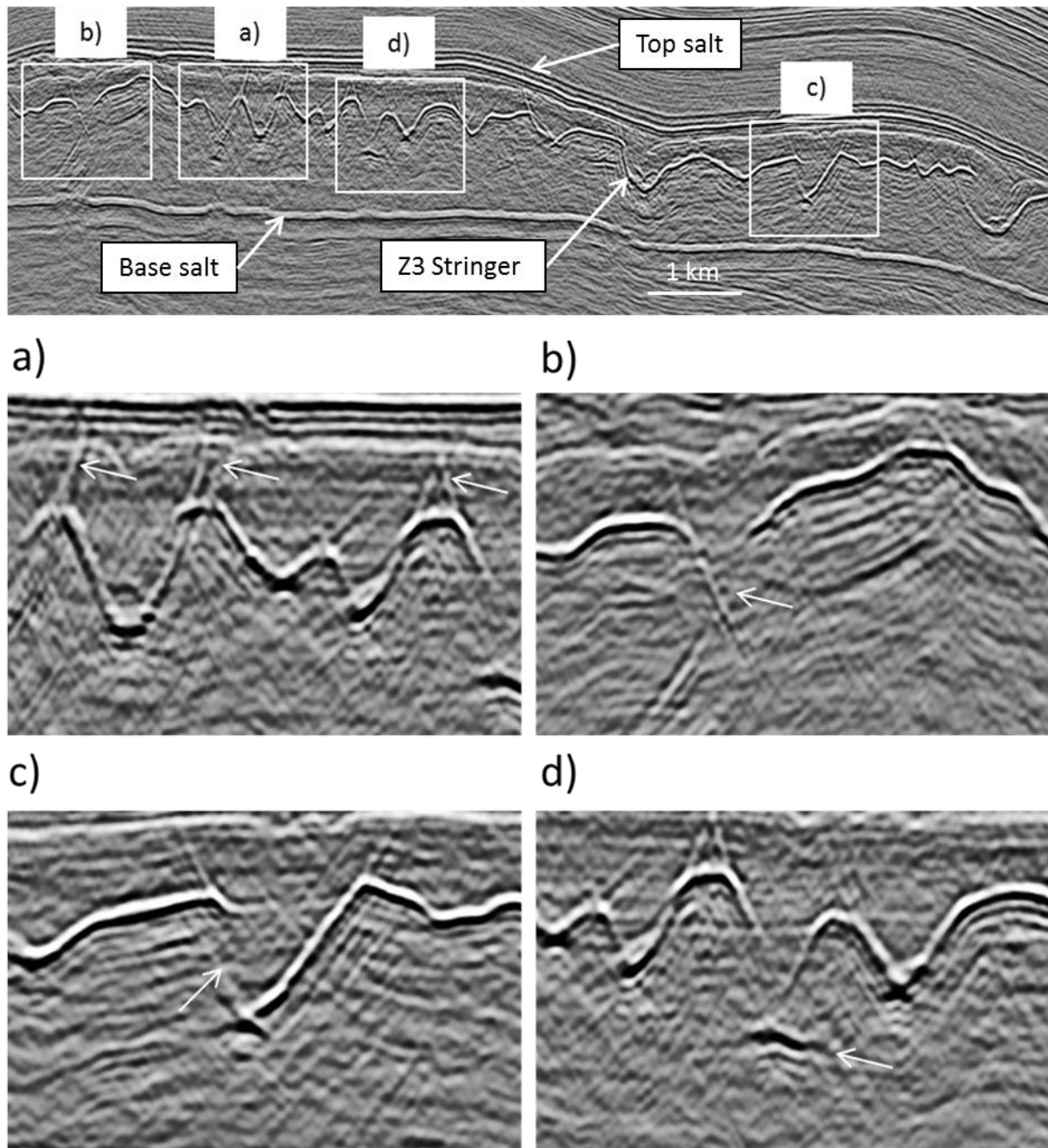
Fig. 2.2: Examples of seismic artefacts associated with the Z3 Stringer (see Fig. 2.1b for the location). (a) Migration smiles. (b) X-shape noise due to steepness or overturned styles. (c) Discontinuity of fold limb related to the steepness of the layer. (d) High-amplitude artefact form at the hinge zone of the folds.

2.2.3 Well data

Four well reports were used to examine the stratigraphy of the Zechstein salt in the Silverpit Basin:

1. well 43/19-1, located in the Cavendish survey (Fig. 2.1b);

2. well 43/19-2, located in the Cavendish survey about 3 km west of well 43/19-1 (Fig. 2.1b);

3. well 43/24-1, located in the Trent 3D survey (Fig. 2.1b); and

4. well 43/25-1, located in the Silverpit Crater syncline (Fig. 2.1b).

The well data were used for lithostratigraphic correlation across the study area. The wells in the Silverpit Basin have no wireline logs or checkshot data; therefore, manual data collection and calibration were done to define the formation tops, thicknesses, and scale.

2.3 Methods and workflow used in case study 1

2.3.1 Seismic interpretation workflow

The software that has been used for the interpretation of the seismic data from the Cavendish 3D and Trent 96 surveys includes Geoframe 2004 and Petrel 2011. Five key horizons were interpreted in this work, similarly to the interpretation of Strozyk et al. (2012), Underhill (2009), and van Gent et al. (2011). The seismically mapped horizons are the following:

1. Base Salt

2. Intra-Zechstein (Z3 Stringer)

3. Top Salt

4. Base Cretaceous Unconformity (Base Chalk)

5. Top Chalk Unconformity

The Z3 Stringer is a single continuous, hard, and positive reflector located in the middle of the Zechstein salt. The Top and Base Salt were interpreted with high confidence using a seismic grid spacing of 100, and were mapped in order to understand the sub- and post-salt regional structure and its influence on the internal salt deformation. A thickness map between the Top and Base Salt reflectors was made to examine the relationship between the internal deformation patterns and the thickness of the Zechstein. The Base and Top Chalk Unconformities were mapped to examine the timing and the mechanism driving salt tectonics, as well as to check for any salt tectonics activities that happened in the overburden.

Two-way travel time (TWTT) structural maps, amplitude, time dip, thickness maps, and curvature attributes were constructed for all of the interpreted horizons.

2.3.1.1 Z3 Stringer seismic interpretation workflow

2.3.1.1.1 Geoframe interpretation

The interpretation of the Z3 Stringer was done in Geoframe. Since this program does not allow direct 3D autotracking of the horizon, the interpretation was initiated in 2D using an inline and crossline spacing of 10 × 10 in areas of less deformation, and a seed of 5 to 1 was used in areas of complex deformation. The seeds were then autotracked in order to fill the gaps between inlines and crosslines.

2.3.1.1.2 Petrel 2011 interpretation

The seismic interpretation of the Z3 Stringer in Petrel is very useful and powerful in terms of quality and speed. Two interpretation methods were applied: (1) the classic 2D mapping of the Z3 Stringer followed by 3D autotracking (Fig. 2.3a); and (2) 3D autotracking of the Z3 Stringer. The latter technique allows snapping the horizon in all directions once clicking on the event (reflector), and the interpretation follows the targeted reflector in areas where the amplitude is continuous.

After the completion of autotracking, two techniques were applied to generate the final surfaces of the Z3 Stringer: (1) the Structural Operation technique (known as Quick Look Surface Operation) was used where the interpreted horizon is autotracked without filling the discontinuities (Fig. 2.3a,c); and (2) the Surface Generation Technique (using Petrel's Utilities tool for surface generation) was used where the discontinuities are completely filled (Fig. 2.3b,d).

The use of these two interpretation methods to differentiate between continuous non-imaged parts of the Z3 Stringer and structurally fragmented limbs is explained in detail in chapter 4.
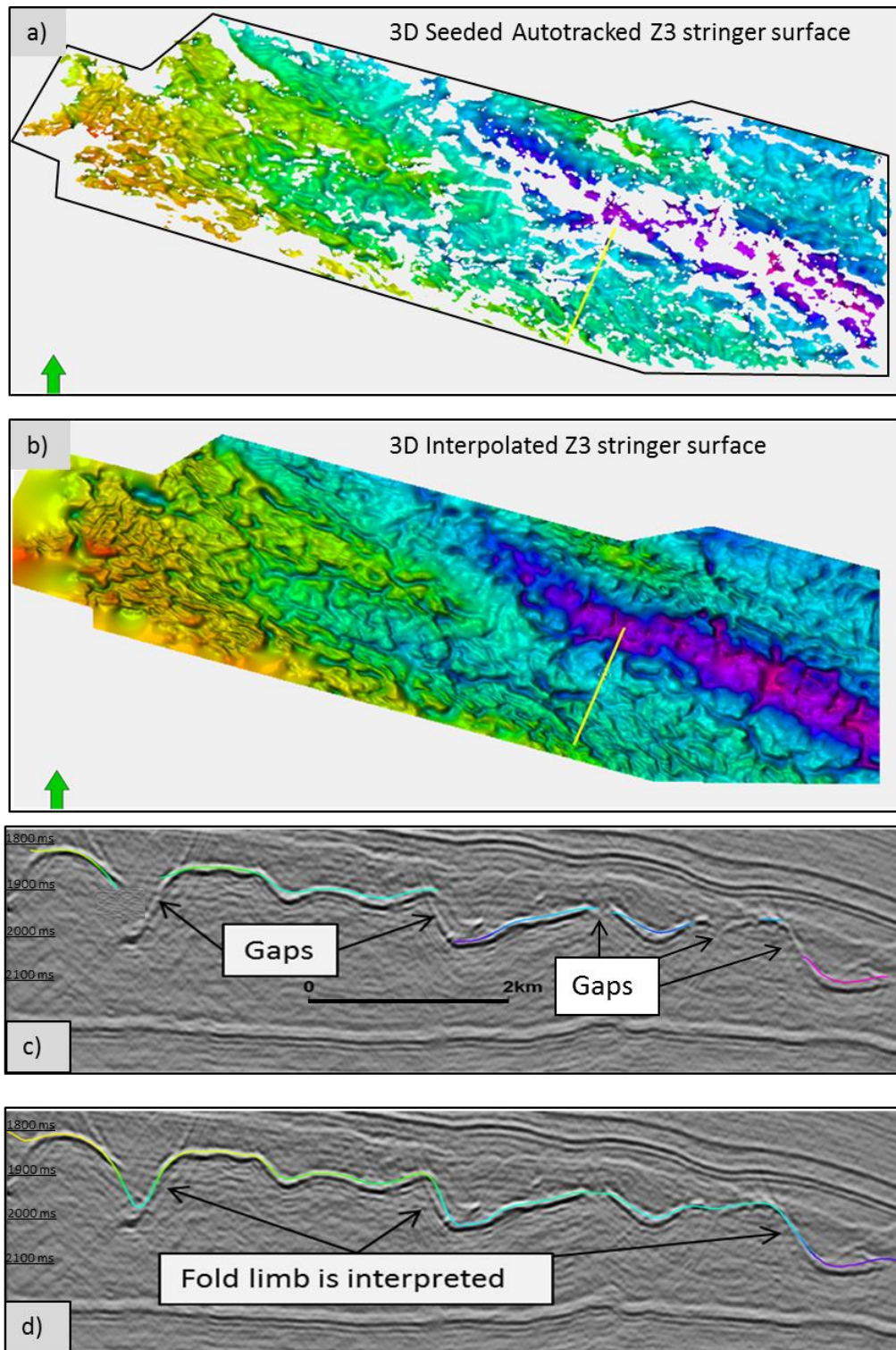
Fig. 2.3: The Z3 Stringer seismic interpretation techniques to overcome seismic limitations regarding steep stringer parts. (a) Autotracking of the Z3 Stringer surface; gaps are unfilled. (b) Interpolated surface of the Z3 Stringer where all the discontinuities are filled. (c) Interpretation of the 3D autotracked surface. (d) Petrel interpretation of interpolated surface.

2.3.2 Qualitative and quantitative methods and workflow

In addition to seismic interpretation, different techniques were applied to enhance and simplify the interpretation of the data and to analyse the Z3 Stringer. The methods applied include smoothing, datum and reference, construction of rose diagrams, and 3D seismic attribute analysis (e.g., curvature attributes, RMS attributes).

2.3.2.1   Smoothing of the Z3 Stringer surface

Smoothing of the Z3 Stringer was done in Petrel 2011 to remove smaller-scale mispicks on the intra-Z3 Stringer reflector. The concept was based on a low-pass filter where random noise and spikes were removed (Fig. 2.4 and Fig. 2.5). The smoothing filter can be controlled by determining the scale of the noise that needs to be smoothed.

Smoothing in this study was used for two purposes:

1. Removing small-scale curvatures (noise) in the Z3 Stringer reflector. This greatly enhances the results when applying curvature attributes, which are very useful for structural analysis. Examples of curvature attributes include mean curvature, Gaussian curvature, maximum curvature, and minimum curvature. These attributes were used to interpolate smaller discontinuities in the Z3 Stringer reflector, as well as to interpret the trend and pattern of the seismically undefined Z3 Stringer reflector (Fig. 2.4).

2. Analysing the Z3 Stringer folds by superimposing the unsmoothed Z3 surface with a high-grade smoothed Z3 Stringer surface. The smoothed surface is used as datum or reference to understand the variation in fold amplitudes, and to describe how harmonic the regional trend of the Z3 Stringer is with respect to Top Salt (Fig. 2.5e).
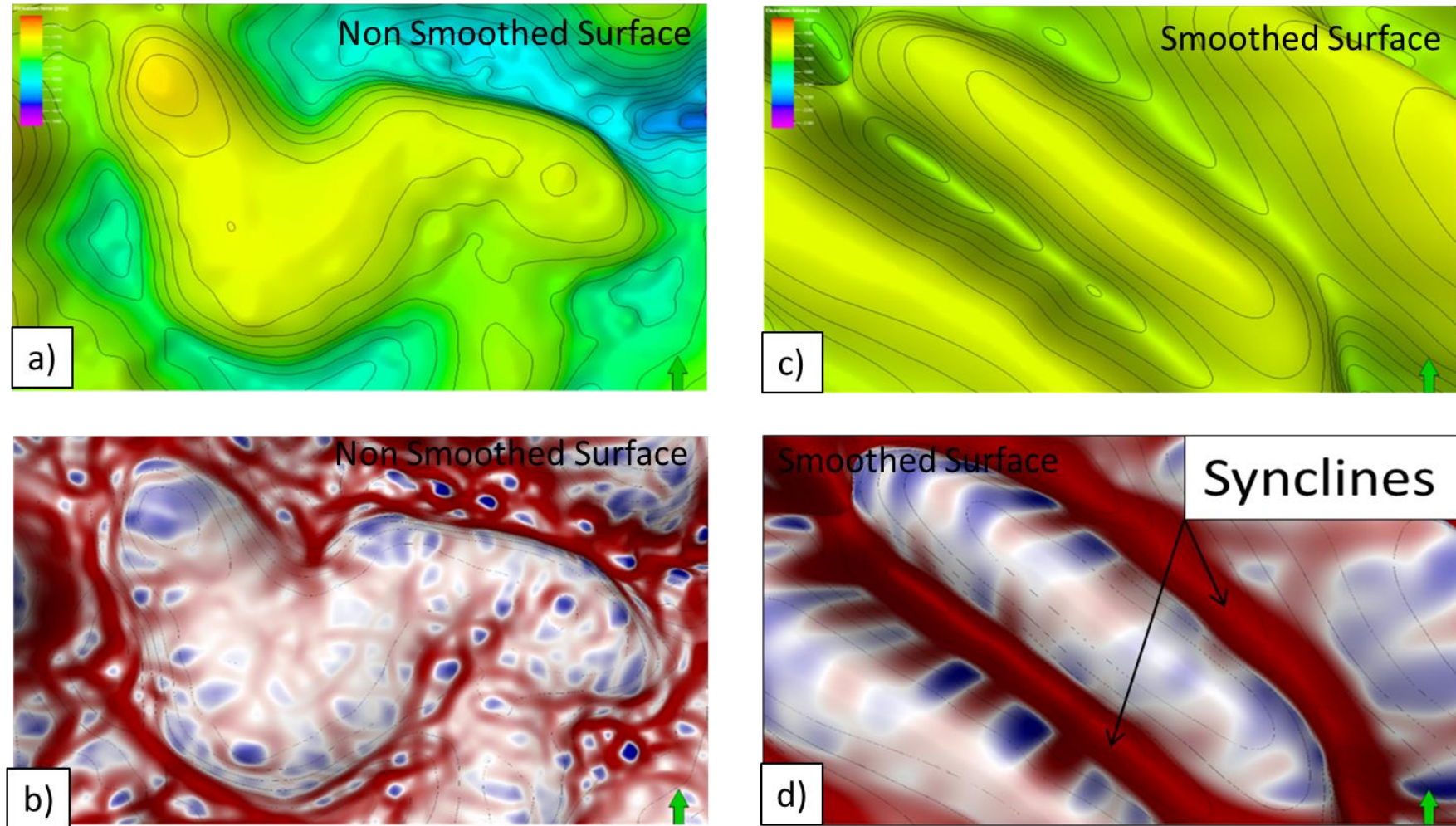
Fig. 2.4: The effect of smoothing on the Z3 Stringer surface. (a) Two-way travel time (TWT) of the non-smoothed Z3 Stringer surface. (b) Minimum curvature attributes through unsmoothed surface. Note the noise (dots) in the surface. (c) TWT smoothed Z3 Stringer surface. (d) Minimum curvature attribute through the smoothed surface. Note the clarity of synclines on the smoothed surfaces. Minimum curvature is a very useful tool to detect synclines, while maximum curvature is useful to detect anticlines.
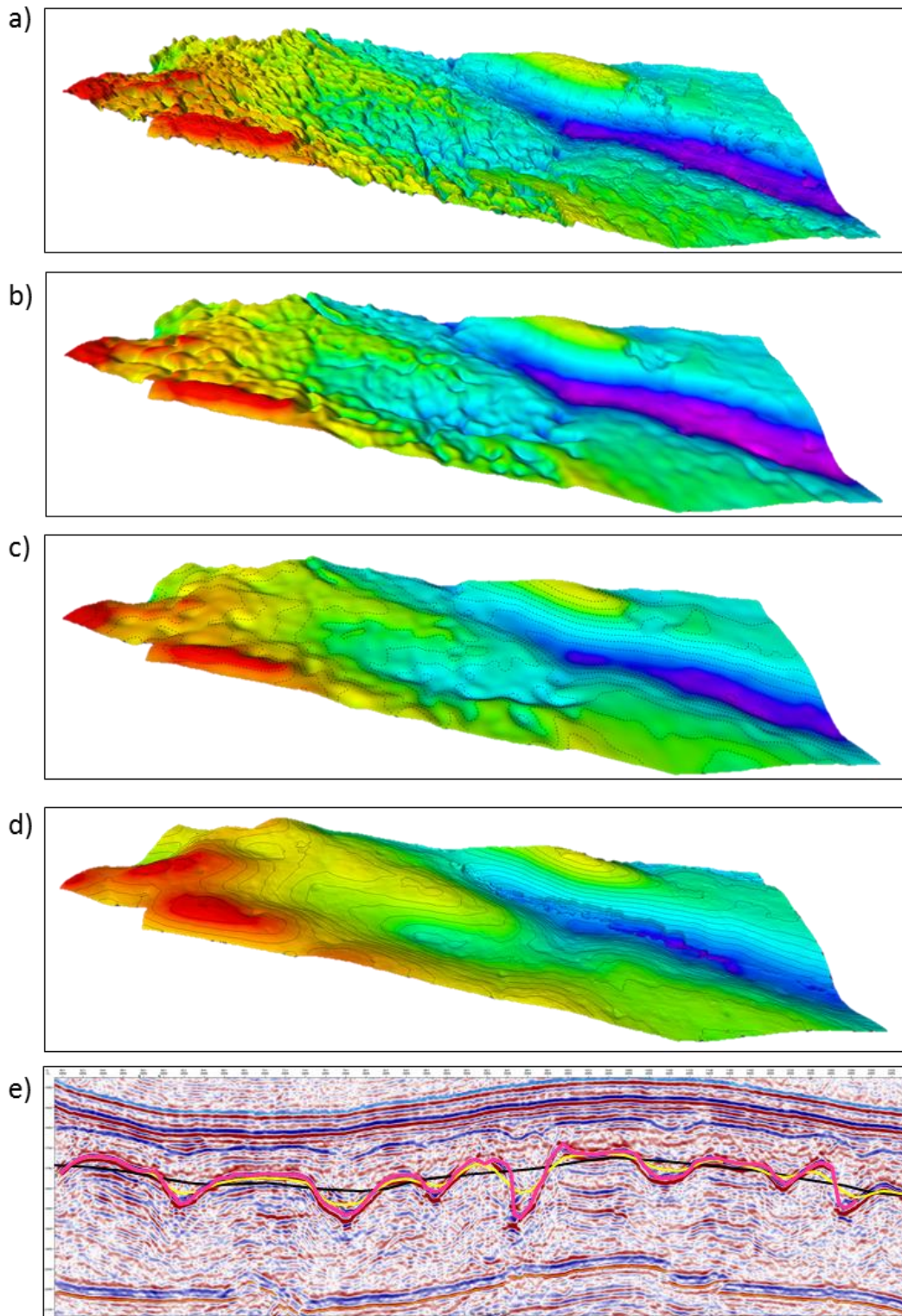
Fig. 2.5: (a, b, and c) The smoothing percentage of the Z3 Stringer surface as compared to the Top Salt time map. (d). Note that with increasing smoothing, the small features were filtered out. (e) The smoothing grades of (a, b, and c) on a seismic cross-section. The yellow and black lines are over-smoothed surfaces, which are not useful for the interpretation, while the red line is a reasonable smoothed surface, and it follows the Z3 Stringer seismic reflector. Note the close relationship of the highly smoothed Z3 Stringer surface (black line) with the Top Salt surface (blue line).

2.3.2.2   Curvature attributes

Curvature attributes were applied to classify the shapes, style, orientations, and cylindricity of the Z3 Stringer fold structures. Curvature is simply a measure of how tightly folded a surface is at a particular point (Lisle 1994). The more tightly folded a surface is, the larger its curvature. Folds appear to be well defined by the curvature attributes (Fig. 2.4c,d). In 3D, folds are not always domal in shape, and instead they contain at least two curvatures: (1) minimum curvature defines the wider radius and (2) maximum curvature is the smallest radius of the fold (Lisle and Toimil 2007).

Curvature attributes were applied to the fold structures of the Z3 Stringer in order to trace their hinge lines accurately for structural analysis by generating rose diagrams. Maximum and minimum curvatures were used to detect anticline and syncline hinges, respectively. Curvature attributes have also been used to understand the cylindricity of the fold structures. These were applied by superimposing mean curvature with Gaussian curvature (Lisle and Toimil 2007). The types of curvature attributes that were used in this thesis (i.e., minimum curvature, maximum curvature, mean curvature, and Gaussian curvature) and their applications are discussed in detail in chapter 5.

2.3.2.3   Fold orders and domains

In the Southern North Sea case study, the folds of the Top Salt are called *regional folds* or *first-order folds*, while the intra-Zechstein folds are called *second-order folds* or simply *Z3 Stringer folds*. The third-order folds refer to the smaller folds that formed within the second-order Z3 Stringer folds. To analyse the structures of the intra-salt stringer, the study area has been divided into five regional domains based on the large-scale Top Salt fold (first-order folds) and the thickness changes of the Zechstein (see chapters 4 and 5).

The borders of these domains are simply the inflection points of the first-order folds constructed from the mean curvature attributes of the Top Salt. The domains are named based on the large-scale synclines and anticlines (see methods in chapters 4 and 5).

2.3.2.4 Rose diagrams

Rose diagrams were constructed by exporting into ArcGIS the traced fold hinges that been interpreted from maximum curvature attribute (anticlines) and minimum curvature attribute (synclines) (Raharimahefa and Kusky 2009; Mogaji et al. 2011; DeVasto et al. 2012). The collection of the data was grouped based on the regional domains. The orientations of the Z3 Stringer were used to understand the effect of the regional structure trend on the intra-salt deformations and the stress applied to the Z3 Stringer in each domain.

2.3.2.5 Geobody extraction

The Geobody Horizon Probe process was used for 3D extraction of the amplitude of the Z3 Stringer from the seismic volume in Petrel 2011 (Borgos et al. 2007; Chaves et al. 2011; Paton et al. 2012). An extraction of a surface probe from an autotracked Z3 Stringer surface helps to define the discontinuities in the actual amplitude in 3D.

2.3.2.6 Fold wavelength measurements

The wavelength of the Z3 Stringer folds has been measured in each of the regional domains. The different methods for describing fold wavelengths are summarised in Adamuszek et al. (2011). The wavelength is the distance perpendicular to the fold hinge along the centre of the fold layer between two successive hinges (Marshak 2004). The Z3 Stringer folds were measured individually perpendicular to their strikes in each of the regional domains. The wavelength of the Z3 Stringer folds is

compared to the magnitude of shortening of the regional folds to test the influence of regional tectonics on internal deformation.

2.3.2.7   Fold interlimb angle measurements

The tightness of the Z3 Stringer folds is described by measuring the interlimb angles and classifying them using the Fleuty (1964) scheme. The interlimb angles of the Z3 Stringer folds were measured in all of the regional domains. Because the folds are non-cylindrical and multidirectional, the measurements were taken using profiles perpendicular to the structure of each individual fold. Using a 1:1 scale, all the interlimb angles were measured on profiles perpendicular to their fold axis.

All the workflow is summarized in Fig. 2.6.
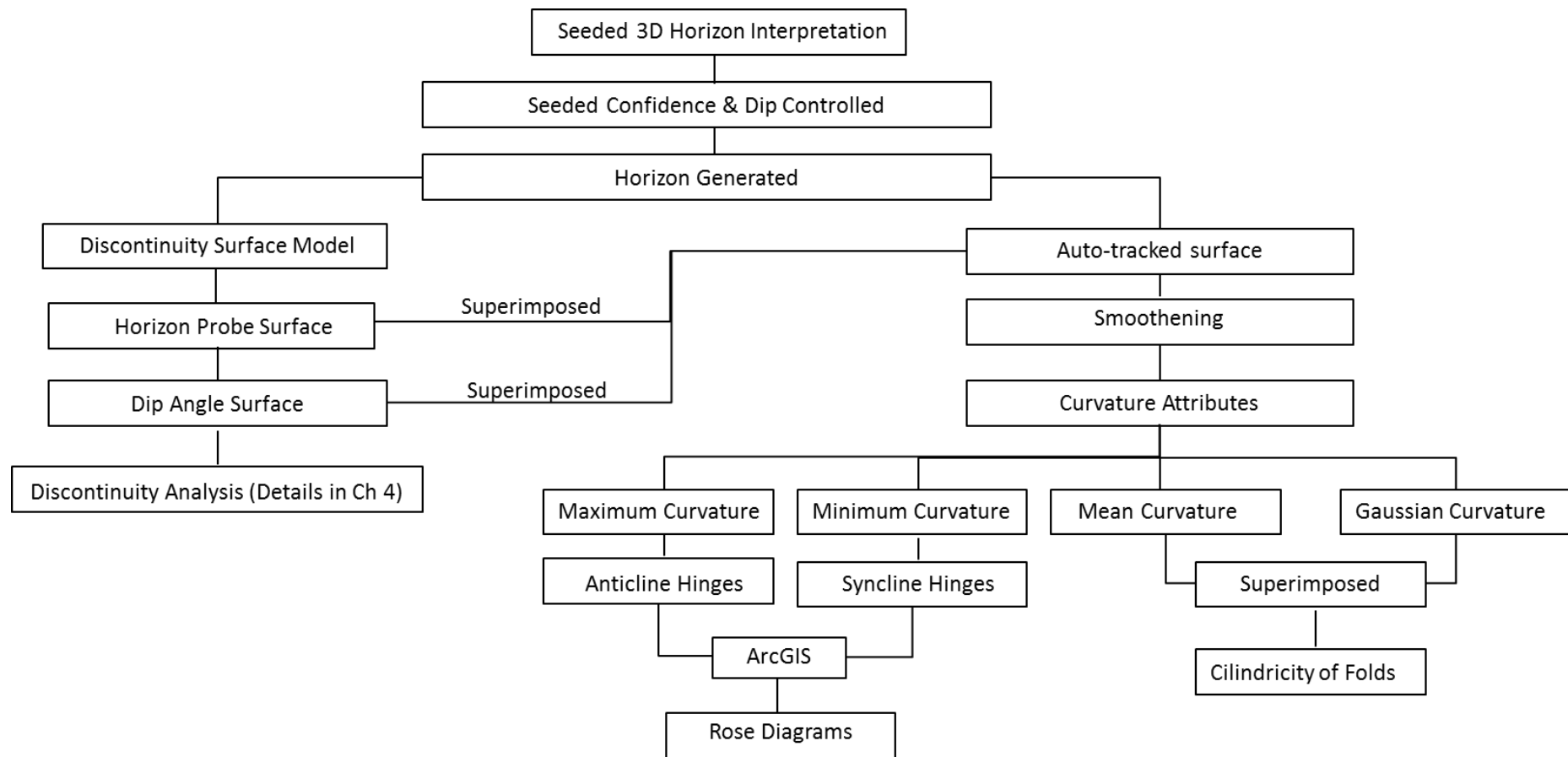
Fig. 2.6: Summary flowchart showing the workflow used for the structural analysis of the intra-salt stringer in case study 1.

2.4   Case study 2: Grater Birba in the South Oman Salt Basin

The seismic data used for the second case study is from the South Oman Salt Basin, in the Grater Birba Field (Fig. 2.7).

2.4.1 Seismic data

A 3D wide-azimuth and time-migrated survey was used to analyse the internal salt stringers in the Birba Field, South Oman Salt Basin. The survey was acquired in 2008–2009 in order to improve the imaging of the Top Ara salt, the internal Ara stringers, and Base Ara in the Birba Field (Li et al. 2012a) (Fig. 2.8 and Fig. 2.11). The seismic acquisition and processing parameters for seismic data are shown in Table 2.2.

In terms of seismic polarity, a downward increase in acoustic impedance is defined as a trough (red reflector – negative), whereas a decrease in acoustic impedance is defined as a peak (blue reflector – positive). This convention is the opposite of the SEG normal convention for a zero-phase wavelet, in which an increase in acoustic impedance is represented by a peak. Three regional 2D seismic lines crossing the greater Birba area were also used to understand the regional geology of the basin.

Table 2.2: Acquisition and seismic processing parameters of the Birba 3D WAS cube.

Receivers	25 × 200 m
Sources	50 × 50 m
Frequencies	6 to 86 Hz
Acquisition CMP	12.5 × 25 m
Processing CMP	25 × 25 m
Processing Fold	2000
In-line Offsets	±4.9875 km
X-line Offsets	±3.975 km
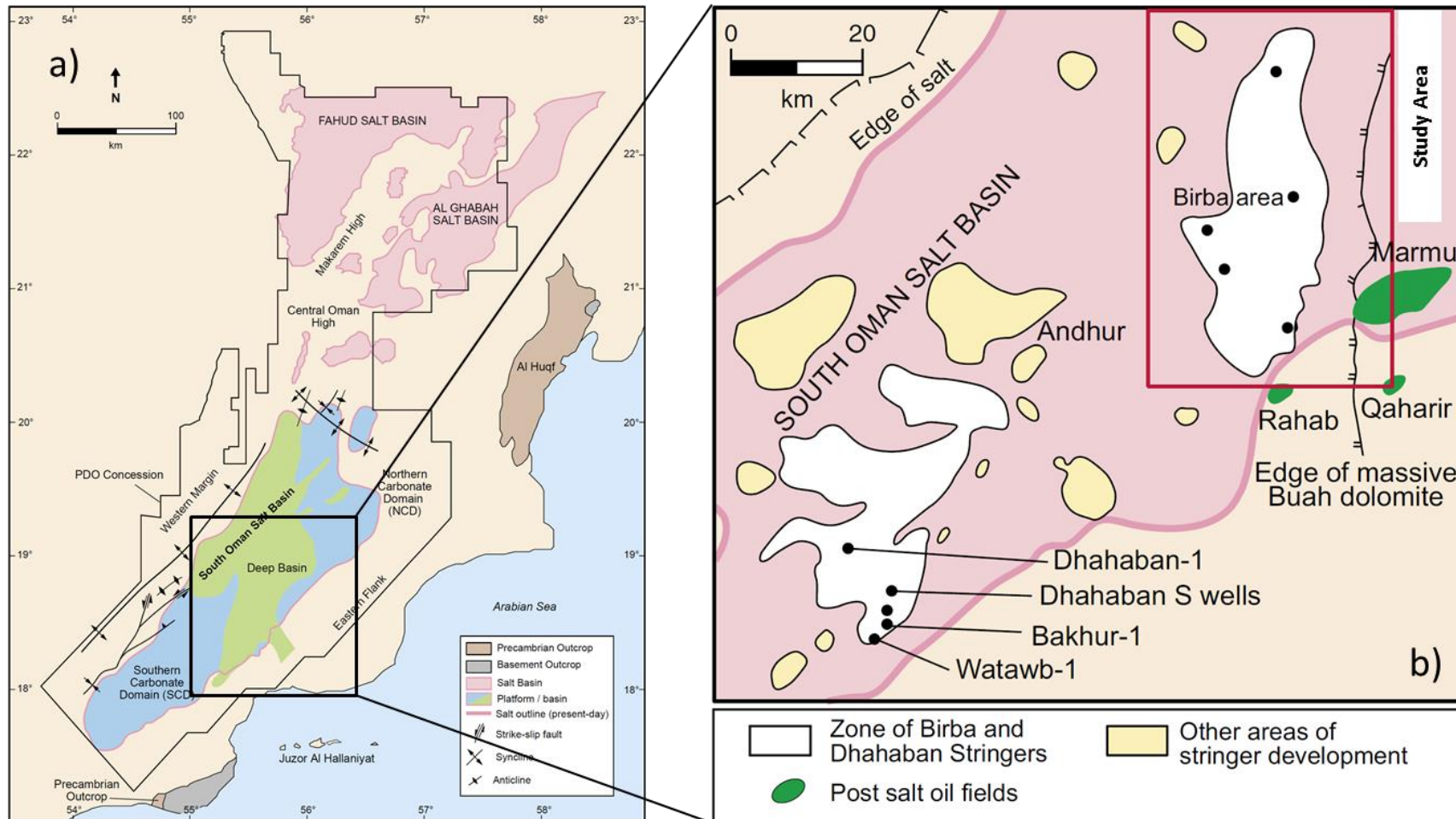
Fig. 2.7: Location and geologic map of the South Oman Salt Basin including the Birba area (after Al-Siyabi 2005).
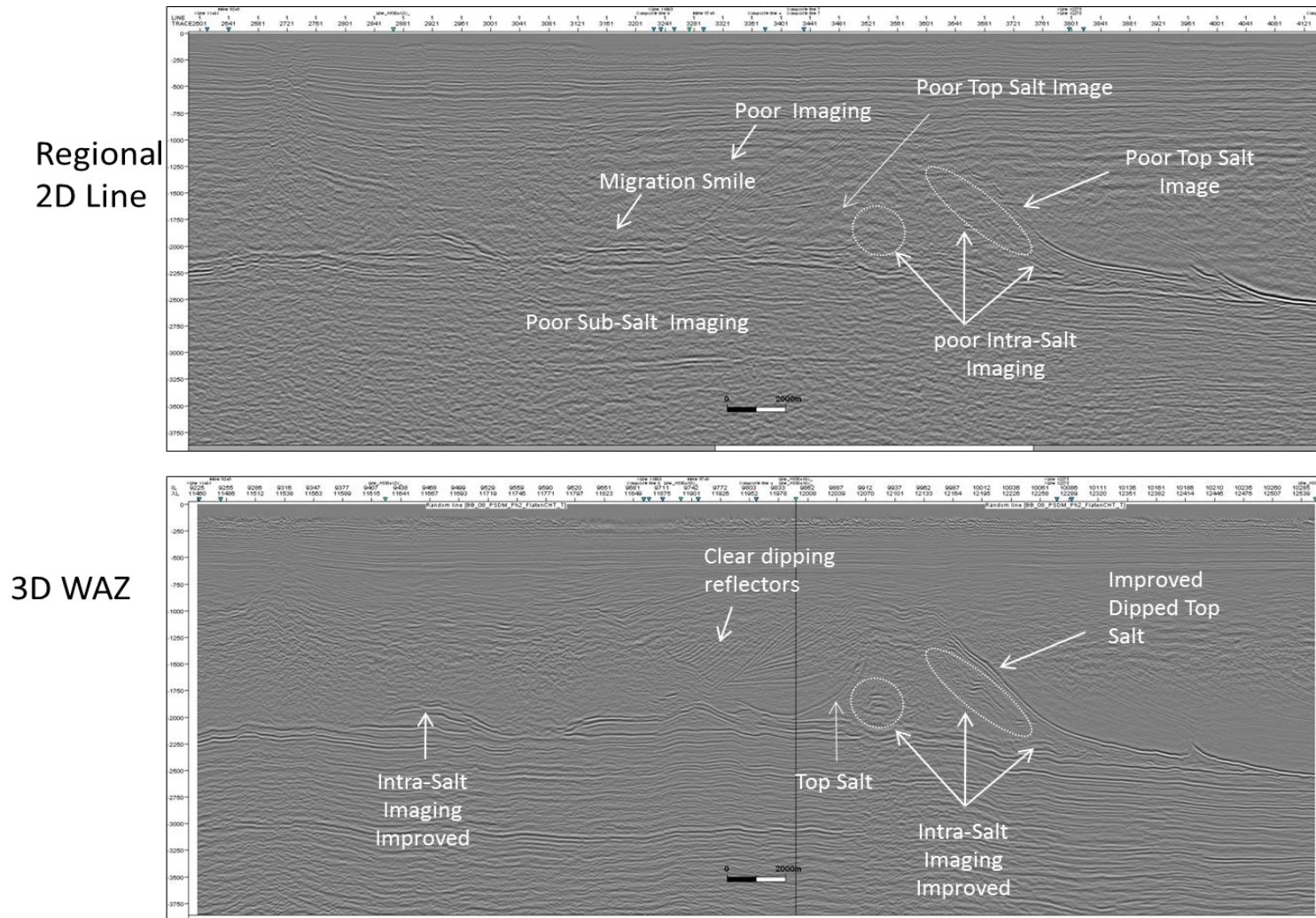
Fig. 2.8: The difference in data quality between the regional 2D and 3D seismic data (see Fig. 2.9c for the location). On the 2D seismic data, small geological features are not properly imaged as compared to the 3D seismic data (bottom). The Top Salt and intra-salt features are delineated on the 3D seismic data.

2.4.2 Seismic interpretation workflow

Petrel 2011 was used to map eight key horizons over the Birba area: Base Salt (A0C), A1C Stringer, A2C Stringer, A3C Stringer, A4C Stringer, Top Salt, Base Natih, and the Top Natih. The interpreted horizons were gridded to create time surfaces and amplitude extractions (e.g., RMS amplitude). Volume attributes were generated mostly for seismic slices, contributing to the interpretation of complex structures. Variance volume cubes and ant-tracking were generated for structural and stratigraphic detections.

2.4.2.1   Mapping of Top Salt

The Top Salt reflector was mapped initially using 50 × 50 grids (Fig. 2.9). However, in large areas, the Top Salt is not imaged on seismic data, and it is completely absent within the chaotic overburden zone. The seismic ghost curves, or facies, which allows a correlation panel or seismic overlay to be used to jump-correlate different seismic units, was used to determine the position of the Top Salt in such areas with no Top Salt reflection. In addition, the horizon autotracking tool was found applicable in these areas.

2.4.2.2   Mapping of A1C, A2C, A3C, and A4C stringers

The stringers were mostly mapped using the Petrel seeded 3D technique. Each seed grid was then autotracked over the study area in order to generate surfaces and amplitude maps. For each interpreted horizon, a two-way travel time surface was generated. An amplitude map was then extracted to highlight the variation in amplitude of the mapped seismic event across the study area. These amplitude maps help to identify the continuity of the main seismic events in the area and thus define our confidence in the mapped seismic event across the study area. The grids and surfaces generated for

each mapped lithology are illustrated in Fig. 2.9. Table 2.3 summarises the seismic character of the interpreted horizons.
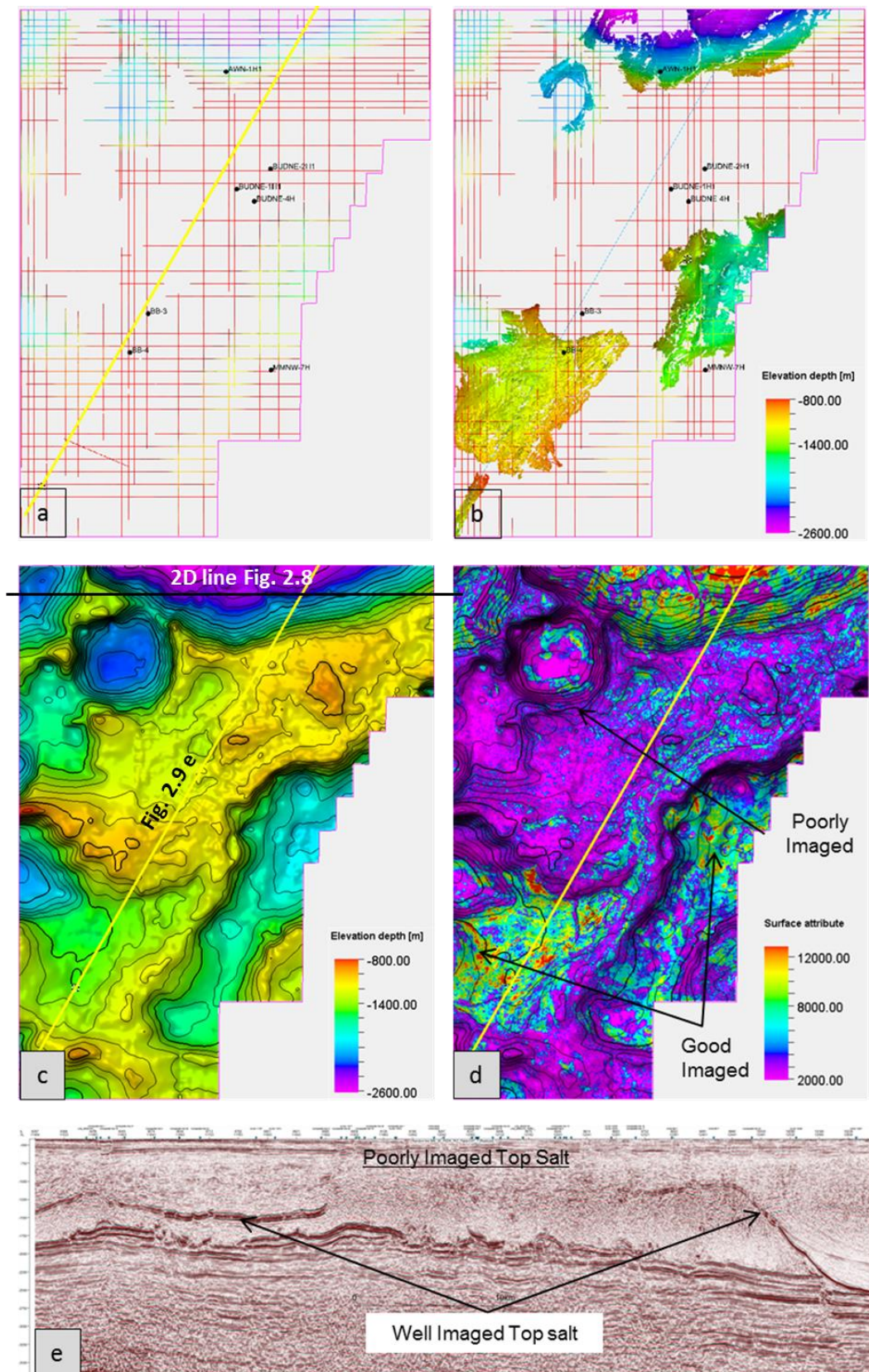
Fig. 2.9: Interpretation of the Top Salt in the Birba seismic survey. (a) Manual interpretation shows regional extent of the Top Salt. (b) Autotracked section of the seeded grid. (c) Interpolated surface. (d) RMS amplitude attribute map over the generated surface. (e) Areas of well-imaged and poorly imaged Top Salt reflector.

Table 2.3: Seismic character of the interpreted horizons in the Birba area.

Interpreted Horizon	Seismic Polarity	Colour Used on the this Study
Top Natih E	Trough (Red Polarity - Negative)	Red
Top Natih E	Peak (Blue Polarity - Positive)	Black
Top Ara Salt	Peak (Blue Polarity - Positive)	Black
Top A4C	Trough (Red Polarity - Negative)	Red
Top A3C	Trough (Red Polarity - Negative)	Red
Top A2C	Trough (Red Polarity - Negative)	Red
Top A1C	Trough (Red Polarity - Negative)	Red
Base Salt (A0C)	Peak (Blue Polarity - Positive)	Black

2.5   Well calibration workflow

Well logs are used to calibrate the age of the different geological events. In the study area, only the following eight wells have checkshot data: (a) BB-2, (b) BB-3, (c) BB-4, (d) BUD-1, (e) BUD-2, (f)   BUDNE-2, (g) BUDNE-4, and (h) AWN-1. The other wells have wireline logs, which were used for investigating the Ara stratigraphic section both vertically and laterally by doing well-to-well correlation. The checkshot data were loaded into Petrel, and a good well-to-seismic calibration was obtained to identify the stringers and to accurately map the Top Salt structure (see chapter 6).

Chapter 3: Salt tectonics in the Silverpit Basin and the stratigraphy of the Zechstein salt

Abstract

The main driver mechanisms for salt tectonics in the Silverpit Basin was investigated using high-resolution, three-dimensional seismic reflection data and four exploration wells. The study demonstrates that shortening of the basin by regional compression is the main driver mechanism for salt tectonics. Bulk shortening of the Silverpit Basin resulted in the formation of detached regional anticlines and synclines, which are simultaneously associated with intra-salt folding and extensional deformations, respectively. The study also describes the stratigraphy of the Zechstein and the Z3 Stringer. It was found that the thickness of the Z3 Stringer is laterally variable and cannot be reliably imaged in all cases on seismic data. The Z3 Stringer can be much thicker than expected due to seismic imaging problems, thus increasing the uncertainties and risk in stratigraphic prognosis and pore pressure prediction during well operations. Lithological calibration of the Z3 Stringer shows that the Z3 Stringer is represented by the Platten Dolomite Formation, which is approximately 4 m thick and is overlain by thicker anhydrite (19 m to 63 m thick). Detailed analysis of seismic stratigraphic markers in the overburden suggests that the syn-kinematic units in the Silverpit Basin were deposited during Early-Mid Eocene to Late Oligocene, a period that is coeval with salt activity and intra-salt deformation in the Silverpit Basin.

3.1   Introduction

Investigating the role of stratigraphic impurities and layering within rock salt is an important subject when discussing the internal structural styles of evaporites (Raith et al. 2015). For instance, the Messinian Evaporites in the contractional domain of the Levant Basin are composed of salt and multi-layered clastic units which were compressed into detachment folds and thrust-ramp folds at the early stage of salt tectonics (Cartwright et al. 2012). In addition, the layered evaporite sequences from the Santos Basin, offshore Brazil, mainly contain incompetent sequences of halite and competent layers, and display upright folds, thrust-related inclined folds, and recumbent, isoclinal, sheath, and superposed fold structures, which were all formed during a single regional shortening event of the basin (Fiduk and Rowan 2012). Several studies have described the internal stratigraphy and mechanical properties of the Zechstein salt (Taylor 1990; Geluk 2007; van Gent et al. 2011; Strozyk et al. 2012). Most of these studies are from the Dutch side of the Southern North Sea. In this study, the stratigraphy of the Zechstein is described at both well and seismic scales.

Understanding the mechanism that derives salt tectonics at a regional scale will help to interpret the internal deformation patterns in the Zechstein salt. Whilst both differential sediment loading and buckling mechanisms can generate salt structural low regions of synclines and minibasins and salt structural high regions of anticlines, domes, and diapirs, the influence of such structures on the internal salt deformation has not been widely discussed.

3.1.1   Aim of the chapter

The aim of this chapter is twofold: (1) understand the regional salt tectonics in the Silverpit Basin and the driver mechanism for the final basin configuration, and (2) understand the influence of evaporite stratigraphy on the internal deformation. Therefore, after discussing the stratigraphy of the Zechstein (both the ductile salt and the competent layers), a general description of the internal deformation is provided.

3.1.2   Methods

This chapter is based on structural interpretation of 3D post-stack time-migrated seismic surveys in the Silverpit Basin, Southern North Sea. Overall, three seismic surveys were used, namely Cavendish, Trent96, and Snsj07 (Fig. 3.1), with a lateral and vertical resolution of 25 m and 20 m, respectively. The Cavendish seismic survey is located in Block 43/19a around the Cavendish gas field, and has an area of 1293 km^2 (Fig. 3.1). Only the Cavendish survey was used in this study for 3D interpretation.

Four wells were used to study the stratigraphy of the Zechstein. Two of these wells (43/19-1 and 43/19-2) are located in the Cavendish survey (see Fig. 3.1 for location), while the other two (43/24-1 and 43/24-2) are located in the Trent96 survey (Fig. 3.1). The seismic interpretation of the overburden seismic markers, Top Salt, Z3 Stringer, and Base Salt is similar to that of Underhill (2009) and van Gent et al. (2011), where the Top Salt is a positive reflector and the Base Salt is a negative reflector. The seismic reflector in the middle of the salt belongs to the Z3 Stringer, and it has positive amplitude, zero phase, and normal polarity.
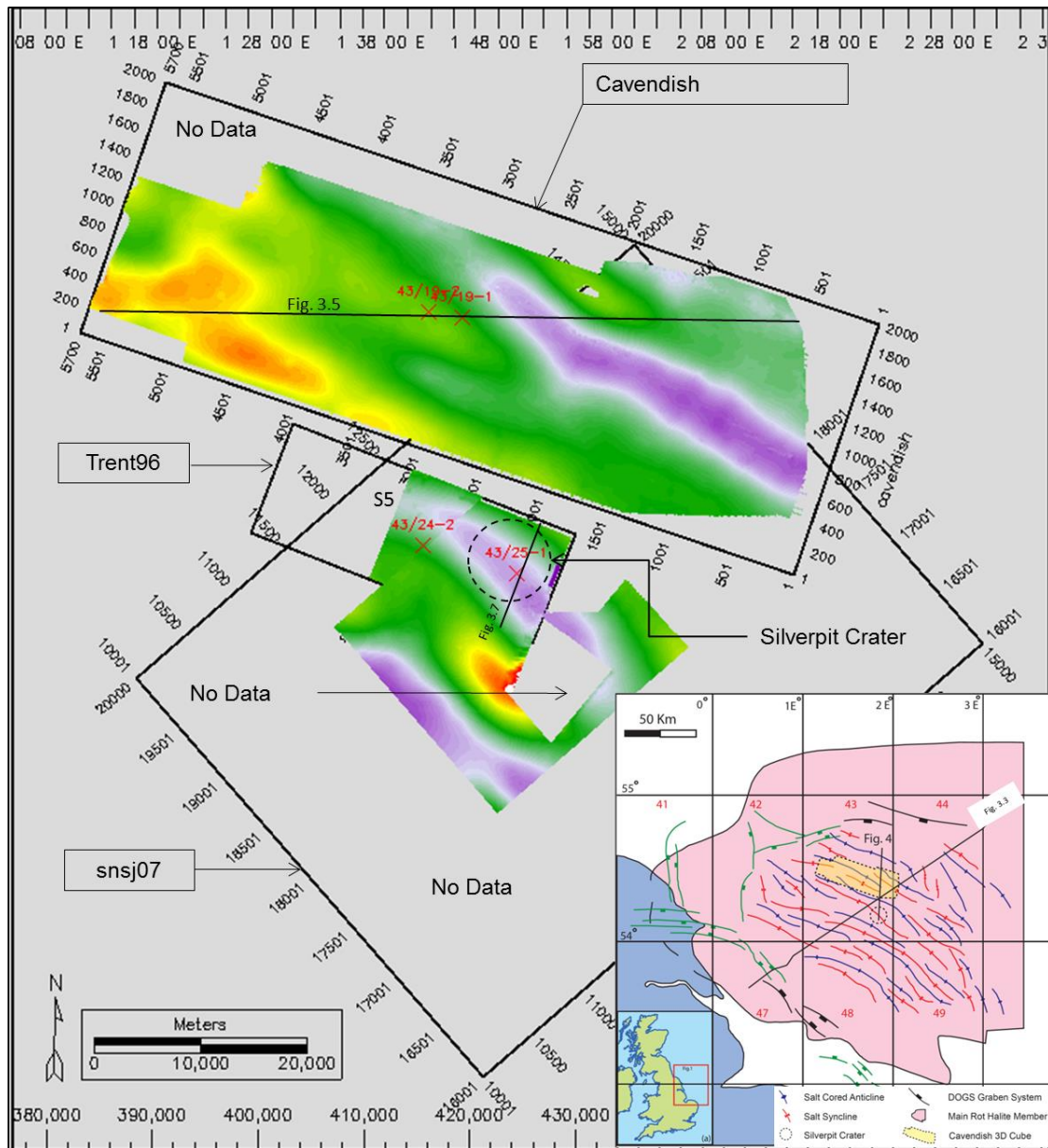
Fig. 3.1: The 3D seismic surveys: Cavendish survey, in the north, and the Trent96 merged with snsj07, in the south. The mapped horizon is the Top Salt two-way-travel-time surface. The dashed circle east of the Trent96 survey is the location of the Silverpit Crater. Well 43/25-1 passes through the syncline of the Silverpit Crater structure. The map insert shows the structural framework of the Southern North Sea. Note the location of the study area within the Cenozoic salt-cored anticlines and synclines (modified after Coward and Stewart 1995).

3.2   Regional setting

The Southern North Sea is a classic area where salt tectonics is predominant (Taylor 1990; Geluk 2000; Mohr et al. 2005; Underhill 2009; van Gent et al. 2011; Strozyk et al. 2012; van Gent et al. 2012). The study area is located in the Silverpit Basin, Southern North Sea, about 180 km to the north of Bacton on the Norfolk coast and approximately 140 km northeast of Easington on the Lincolnshire coast (Underhill 2009; Wall et al. 2010) (Fig. 3.1 and Fig. 3.2). Three distinctive regional structures were recognised in the area: (1) faulted sub-salt rock, (2) folded overburden by salt-cored anticlines and synclines, and (3) structureless conformable post-kinematic megasequences (Taylor 1990) (Fig. 3.3). These regional structures are the result of two main tectonic events in the Southern North Sea Basin: an extensional event during the Mesozoic and compressional tectonics during the Cenozoic (Coward and Stewart 1995; Stewart and Allen 2005).

The sub-salt sediments (Carboniferous and the Rotliegend) were deposited in a series of NNW trending grabens, which were reactivated during the Late Carboniferous (Stewart 2007). Consequently, the overlying Permian Zechstein salt forms an effective decoupling unit between the sub-salt and the supra-salt strata, and it is highly variable in thickness due to halokinesis (Taylor 1990; Underhill 2009). A few studies have shown that there is no connection between the sub-salt basement faults and the overlying post-salt structure (Hughes and Davison 1993). On the contrary, studies such as those of Walker and Cooper (1987) and Coward and Stewart (1995) have emphasised the decoupling character of the Zechstein salt and provided examples of decoupled pre- and post-salt structures. Furthermore, a good

connection has been found between the pre-Zechstein basement fault trends and the overlying Upper Permian Zechstein folds (Oudmayer and De Jager 1993).

On a regional scale, the Southern North Sea Basin is surrounded by Mesozoic extensional faults to the west of the basin margin, which were partly reactivated during the Cenozoic (Coward and Stewart 1995). Updip extension and regional basin tilt caused a thin-skinned gravity-driven system of detachment buckle folds in the downdip of the basin (Allen et al. 1994; Coward and Stewart 1995; Stewart and Allen 2005) (Fig. 3.1–3.3). An alternative model for the formation of the salt-cored anticlines in the Southern North Sea is the withdrawal of salt at depth due to differential loading (Underhill 2004; Thomson et al. 2005; Underhill 2009).
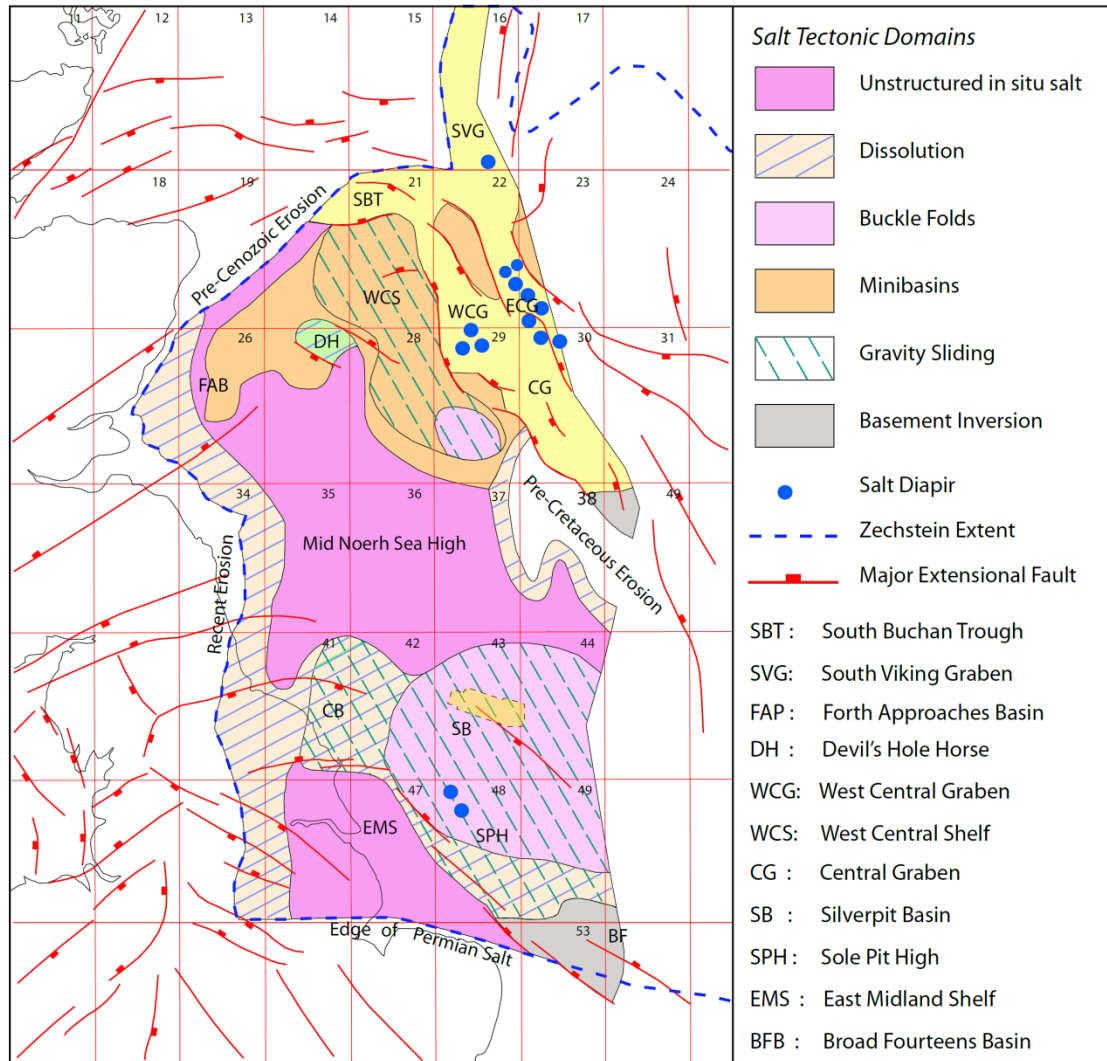
Fig. 3.2: Classification of the UK North Sea Basin structural domains based on salt structural styles. The study area is located in the Southern North Sea in Block 43, where the Zechstein salt is formed by thin-skinned shortening of detached buckle folds (modified after Stewart 2007).
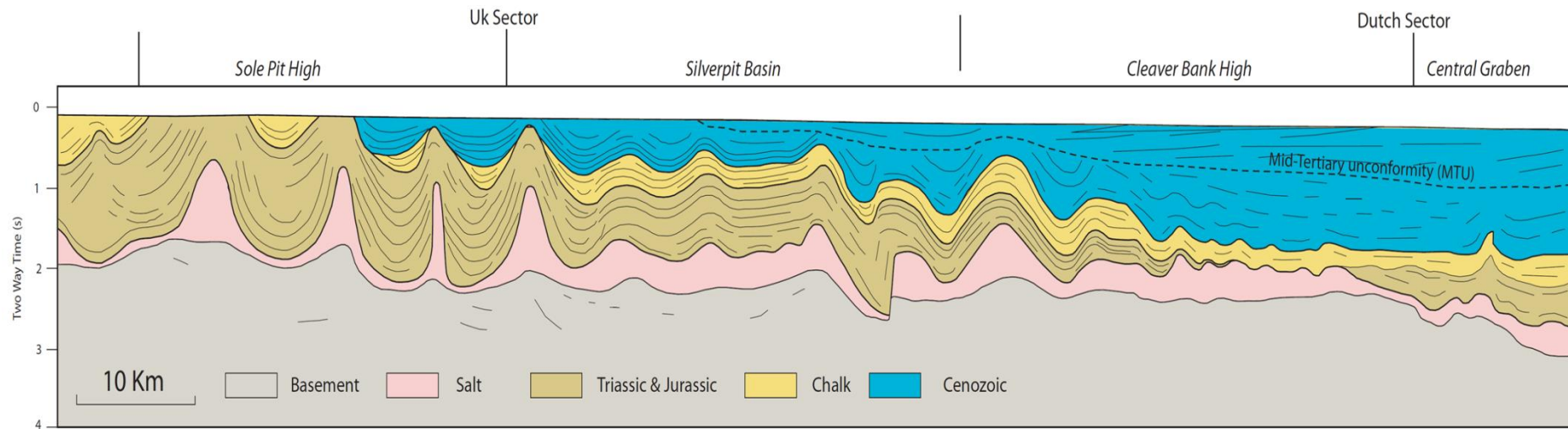
Fig. 3.3: Interpreted regional seismic line (SNST-83-10; see Fig. 3.1 for location) across the Sole Pit High, the Silverpit Basin, and the Cleaver Bank High showing important structural elements. The chalk and the Jurassic-Triassic strata are highly eroded in the Sole Pit High. However, the Cretaceous sediments are overlain by a second wedge of Early Cenozoic sediments, which thickens in the opposite direction indicating the reversal of the Jurassic basin tilt (modified after Stewart and Coward 1995).

3.3   Tectonostratigraphy of the Silverpit Basin

The stratigraphy of the Silverpit area is represented by the Carboniferous and Rotliegend sediments in the sub-salt section, the Permian Zechstein evaporite, and the Triassic to the Cenozoic in the post-salt succession (Fig. 3.4).

The tectonostratigraphy of the study area has been subdivided using seismic data into six main megasequences (Fig. 3.4). Seismic stratigraphy has been used to understand the extent and timing of the structural events that occurred in the Silverpit Basin. Several stratigraphic indicators were used:

- truncations, which indicate unconformities, or time gaps;

- onlapping reflections, which indicate progressive deposition;

- thickening of reflectors, which indicates syn-kinematic deposits;

- constant thickness with sag and bending, which indicates post-rifting or post-contraction; and

- continuous conformable reflectors, indicating a period of tectonic quiescence.

3.3.1   Carboniferous syn-rift megasequence

The base of this megasequence is hard to interpret due to the quality of the seismic data. The top of the megasequence is a clear unconformity at the base Rotliegend level (Fig. 3.5). Several half grabens with tilted and thickening packages indicate syn-extensional deposits (Fig. 3.5). The presence of folding within some of the grabens suggests post-compressional deformation and inversion (Fig. 3.5).
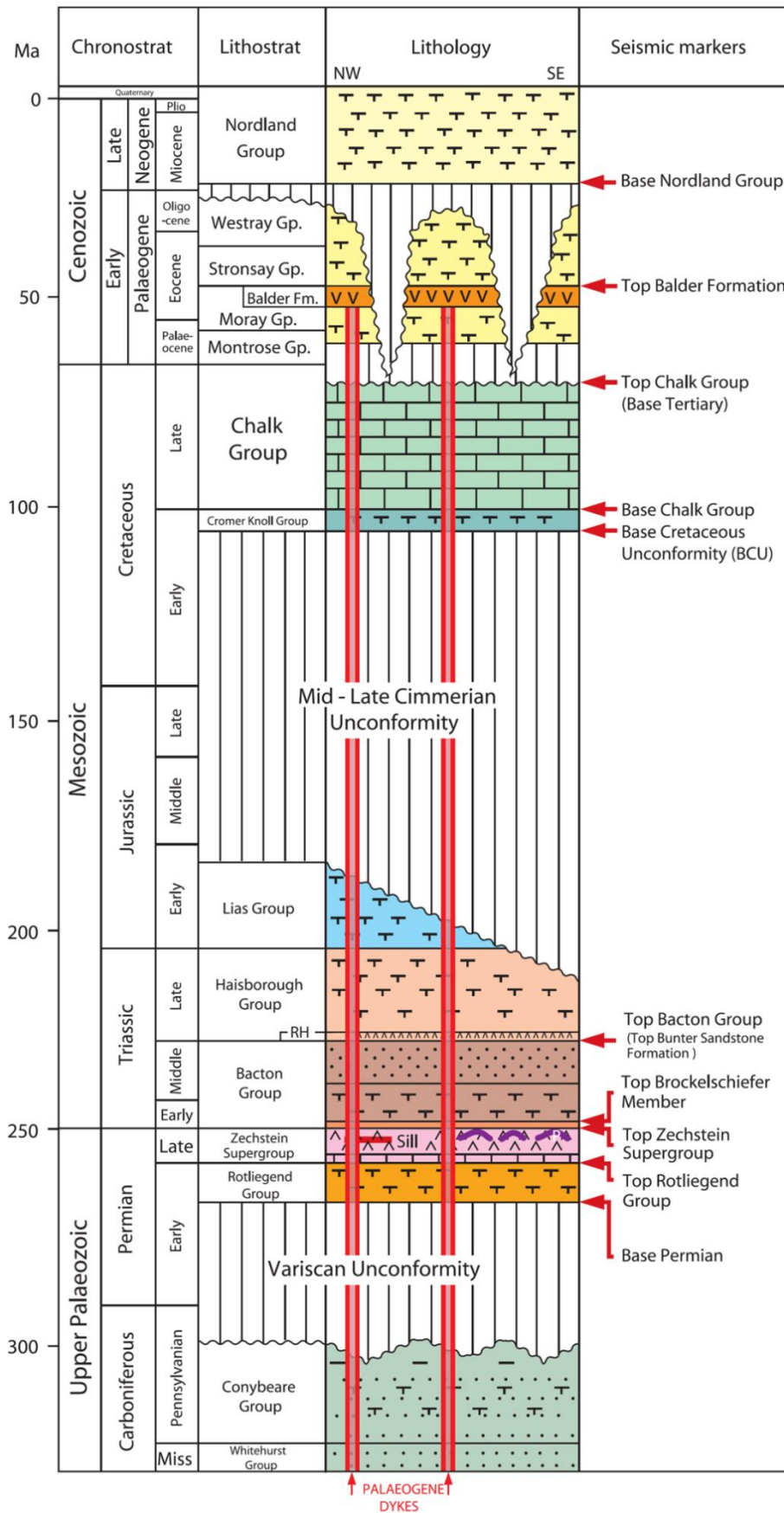
Fig. 3.4: Stratigraphy of the Silverpit Basin showing the key stratigraphic markers (after Underhill 2009).
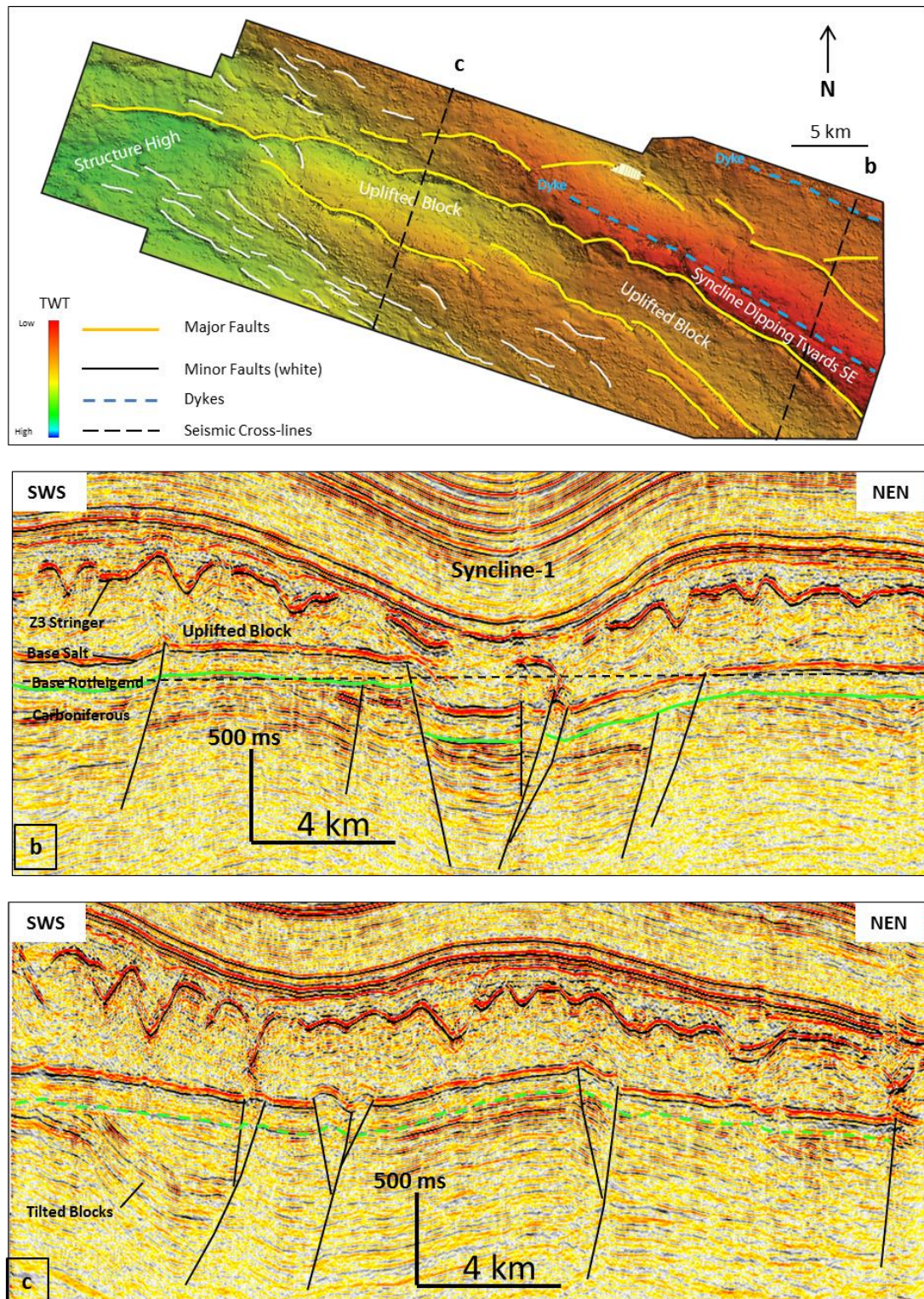
Fig. 3.5: Seismic sections showing sub-salt structural patterns. (a) Base Salt two-way-travel-time structural map showing the major and minor NW-SE trending faults. (b) Seismic section from the eastern part of the Cavendish survey passing through sub-salt normal faults. Note the decoupling character of overlying Zechstein salt. (c) Seismic line showing some reactivated normal faults (middle) due to the buckling of the basin in Late Cretaceous. The dashed green line represents the base Rotliegend unconformity. The vertical exaggeration of the seismic sections is 3.

3.3.2   Mid-Permian post-rift megasequence I

The Rotliegend above the Carboniferous is characterised by less thickening compared to the lower megasequence (Fig. 3.5). Some of the faults propagate upwards to the base of the Zechstein Group (Fig. 3.5 and Fig. 3.6). These were active after the deposition of the Permian and the Mesozoic or during the inversion of the basin during the Cenozoic (Underhill 2009).

3.3.3   Late Permian to Early Jurassic post-kinematic megasequence II

This megasequence includes the Upper Permian Zechstein, the Triassic Bacton Group, the Haisborough Group, and the Early Jurassic Lias Group (Underhill 2009). All these strata are folded and conformable, signifying that there was no thickness variation due to a period of tectonic quiescence (Fig. 3.6). The unconformity at the top of the Lias Group defines the top of this megasequence (Fig. 3.6). This unconformity is related to the uplift of the Silverpit Basin during the Late Jurassic (Stewart and Coward 1995; Stewart and Allen 2005).

3.3.4   Late Cretaceous post-kinematic megasequence III (Chalk Group)

The top of the Late Cretaceous megasequence is defined by the regional Base Cretaceous Unconformity and the overlaying Cenozoic deposits (Fig. 3.6). The megasequence displays bulk thinning towards the core of the syncline on the time profile (Fig. 3.6). This thinning has nothing to do with tectonics and is probably due to the increase in seismic velocity (Underhill 2009).
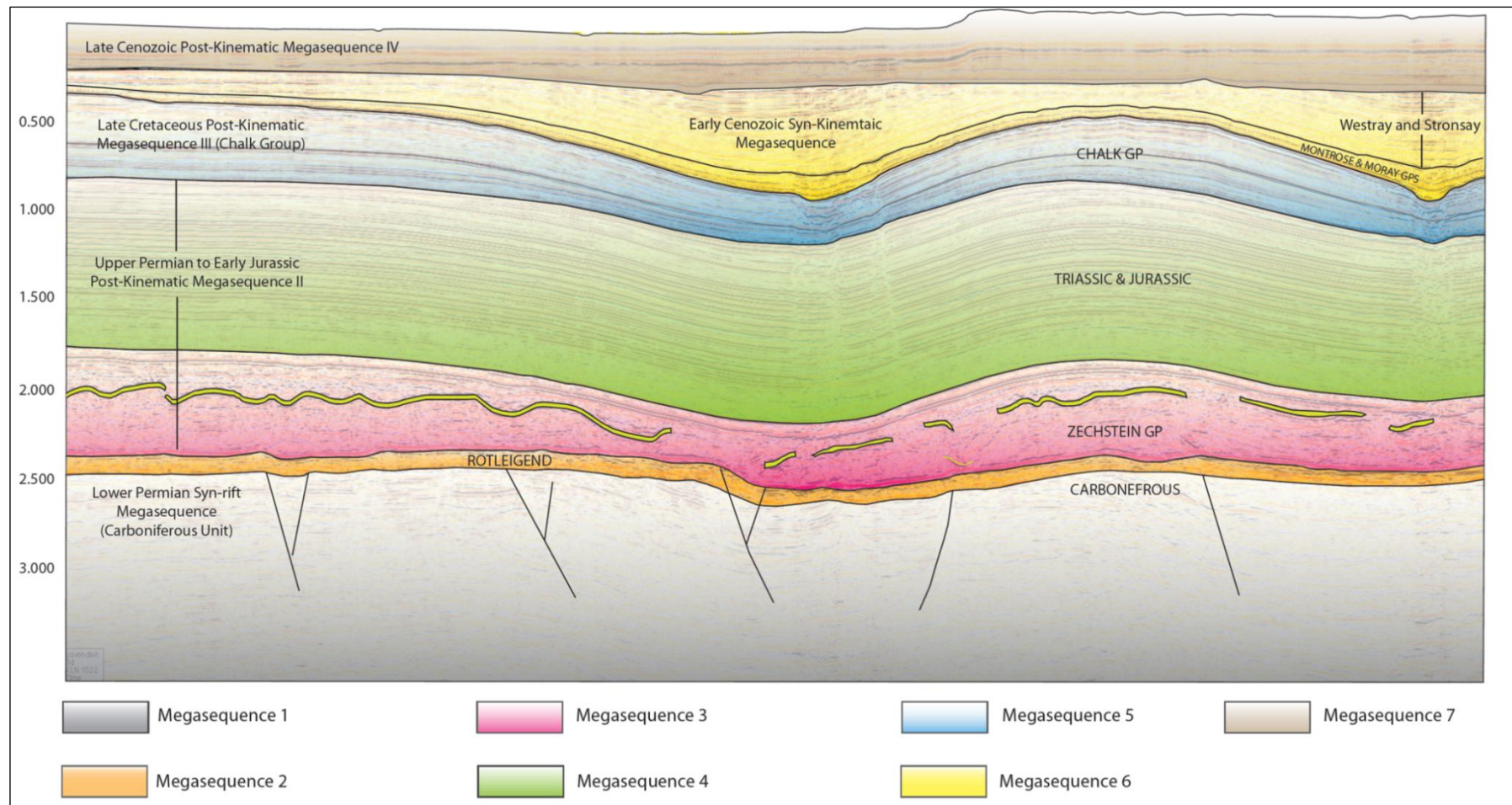
Fig. 3.6: Interpreted seismic profile from the Cavendish study area (see Fig. 3.1 for location). The main megasequences are classified based on major tectonic events and unconformities. Note the folding and displacement of the Z3 Stringer within the Zechstein salt. The vertical scale of the section is in two-way travel time (s).

3.3.5   Early Cenozoic syn-kinematic megasequence

The megasequence, which includes the Montrose, Moray, Westray, and Stronsay Groups, conformably overlies the Lower Chalk megasequence and is significantly truncated by the Oligocene-Miocene unconformity at the top (Fig. 3.6). The unconformity represents the base of the overlying Late Cenozoic megasequence (Fig. 3.6 and Fig. 3.7). The Montrose and Moray Groups belong to the Palaeocene to Early Eocene Upper Chalk Group, while the Westray and Stronsay Groups are Late Eocene to Oligocene (Underhill 2009) (Fig. 3.4). The Westray and Stronsay Groups are clearly affected by the Zechstein-cored folding, which resulted in draping, onlapping geometries, and variable thickness change from the flanks to the core of the synclines, indicating the timing of salt movement in the Early Cenozoic (Fig. 3.6 and Fig. 3.7). The upper part of the megasequence is truncated by the Oligo-Miocene angular unconformity, which marks the Base Nordland Group, indicating the end of the compressional tectonics.

3.3.6   Late Cenozoic post-kinematic megasequence IV

The Late Cenozoic megasequence is part of the Miocene to Quaternary age Nordland Group (Underhill 2009) (Fig. 3.4). This megasequence contains flat to conformable strata, which are deposited unconformably above the Early Cenozoic sediments. The seismic stratigraphic character of this megasequence indicates a period of tectonic quiescence (Fig. 3.6 and Fig. 3.7).
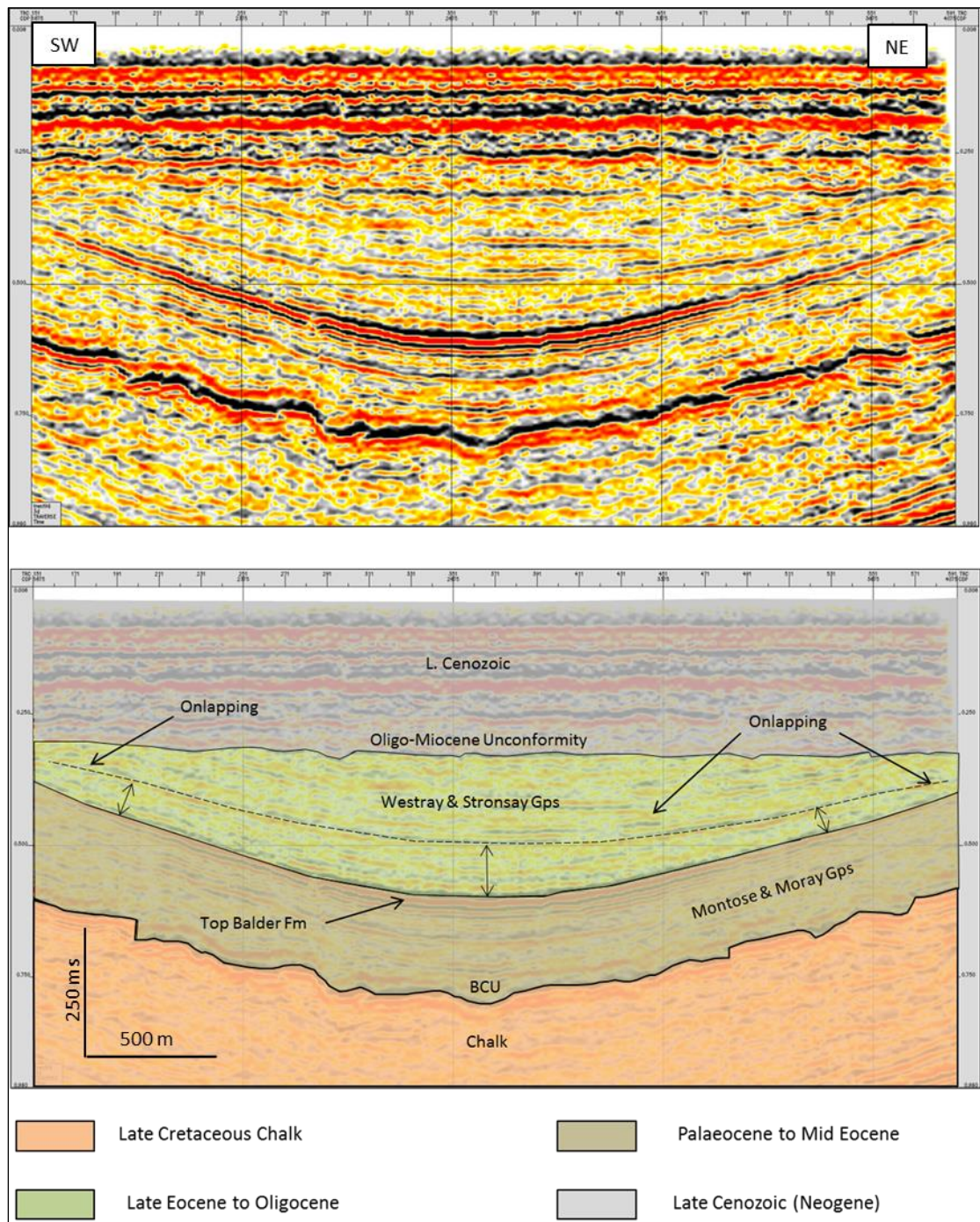
Fig. 3.7: Uninterpreted and interpreted seismic section over the syncline of the Silverpit structure (Trent 3D Survey; see Fig. 3.1 for location). The onlapping strata above the high-amplitude Balder Formation belongs to the Eocene to Oligocene Westray and Stronsay Groups. The vertical scale of the section is in two-way travel time (ms).

3.4   Regional stratigraphy of the Zechstein

Several studies on the stratigraphy of the North Sea have suggested that the Zechstein was deposited in a transgressive evaporitic marine basin with four to five evaporitic cycles (Geluk 2000). In the Norwegian-Danish sector, the Zechstein is divided into Ca-1 to Ca-2, An-1 to An-3, and Na-2 to Na-4 comprising of carbonate, anhydrite, and halite, respectively. In the Southern Permian Basin, the Zechstein is divided into Z1 to Z6 evaporitic cycles, but only the first four cycles are well-developed (Taylor 1990) (Fig. 3.8a). However, in the UK Southern North Sea and offshore Netherlands, the Zechstein is divided into five main formations: the Werra (Z1), Stassfurt (Z2), Leine (Z3), Aller (Z4), and Ohre (Z5) Formations (Fig. 3.8b). The lower part of the Zechstein (Z1–Z3) is characterised by marine successions precipitated in the classic carbonate-evaporite cycle of limestone and dolomite at the base and evaporite successions of gypsum, halite, and potassium salt in the upper part of the cycle (Geluk 2000).

In most of the Southern Permian Basin, the Z1 cycle is absent, and the lower part of the Z2 Group contains dolomite and basal anhydrite units (Wong et al. 2007). The Z2 is directly deposited on top of the Z1, forming the base brittle rock of the overlying thick ductile Z2 Stassfurt Group, which contains mostly halite with a primary thickness of 500–600 m that has strongly been modified by salt tectonics (Taylor 1990; Geluk 2000; van Gent et al. 2011; Strozyk et al. 2012). In the Northern Netherlands, significant deposits of potassium-magnesium salt characterise the top of Z2 (Geluk 2000). The base of the third Z3 Group is characterised by high gamma ray log readings caused by a thin shale layer and is overlain by a dolomite layer known as the Platten Dolomite,

with a typical thickness range of 30 m to 90 m on the shelf (Taylor 1990; Smith 1996). Progressive evaporation of the seawater resulted in the deposition of a 3 m to 45 m-thick anhydrite layer above the Platten Dolomite called Haupt Anhydrite. The Leine Halite overlies the Haupt Anhydrite, which is part of the Z3 cycle (Taylor 1990; Geluk 2000; Geluk 2007) (Fig. 3.8b). In the Groningen area, the Z3 halite interval, or the Leine Halite Formation, has a primary thickness of 200 to 300 m (van Gent et al. 2011).

In the Southern Permian Basin, the basal part of the Z3 Group that is composed of a 1 m-thick shale layer, the Platten Dolomite, and the Haupt Anhydrite unit are known as the Z3 Stringer. On seismic data, the Z3 Stringer is clearly visible in the middle of the Zechstein salt section between the Z2 Stassfurt Halite and the Leine Halite (van Gent et al. 2011). In some parts of the Southern Permian Basin, the Z3 Stringer is composed mainly of an anhydrite layer (van Gent et al. 2011). This anhydrite stringer has variable thickness either due to stratigraphic processes such as sedimentary swells and gypsum diapirism or due to tectonics during folding (Fulda 1928; Williams-Stroud and Paul 1997; van Gent et al. 2011). Some authors suggested that the transformation of gypsum to anhydrite occurred after burial and even after salt tectonics activities (Williams-Stroud and Paul 1997). The thickness range observed was between 40 m and 150 m, the latter being observed in areas where the anhydrite layer forms synclines.

The last cycles (i.e., the Aller (Z4) and Ohre (Z5) Formations) consist of sabkha deposits and are thinner than the lower Zechstein cycles (Geluk 2000). In the Southern Permian Basin, the Z6 and Z7 are not found (van Gent et al. 2011).
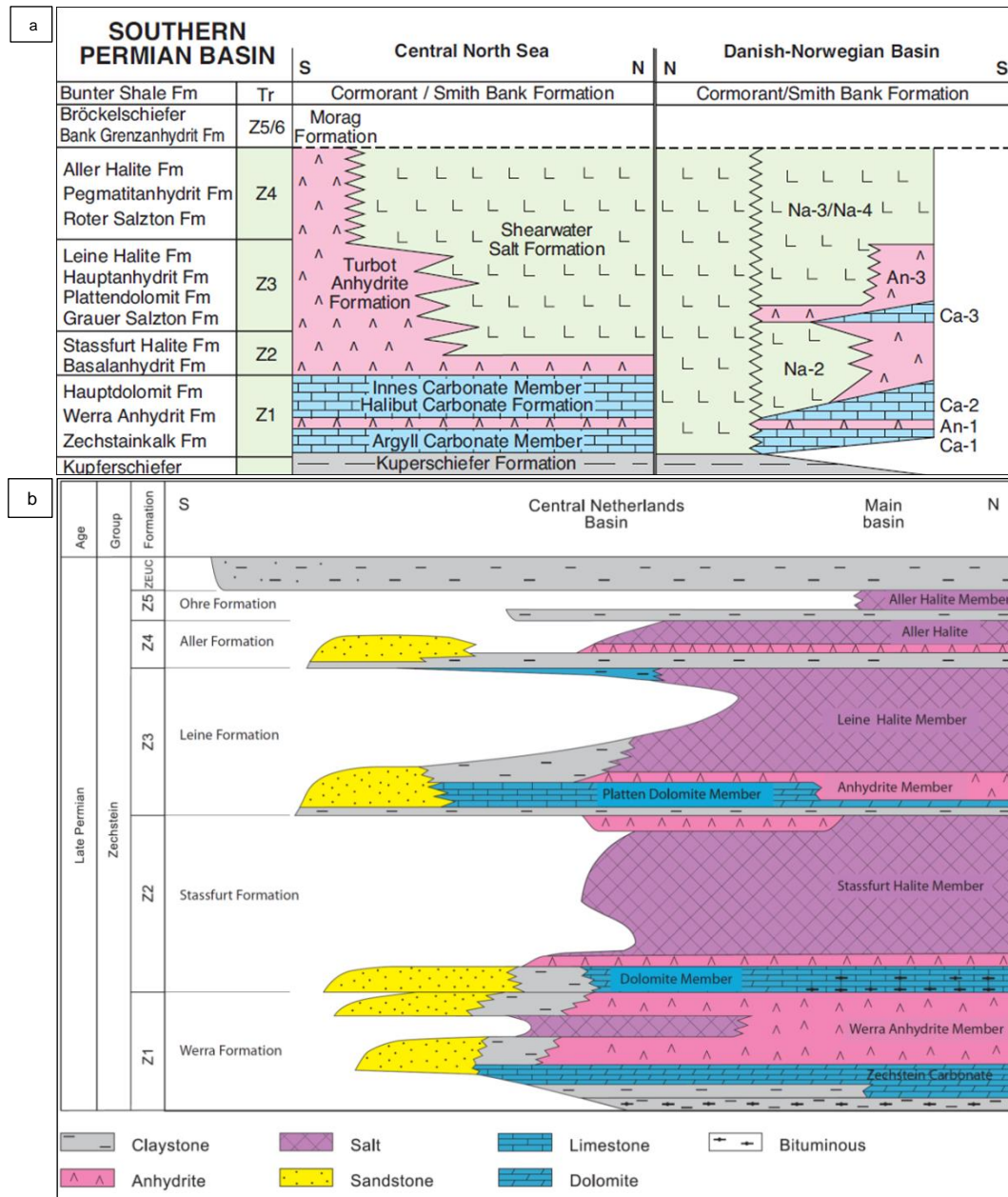
Fig. 3.8: Regional correlation of the Upper Permian Zechstein Group in the Central North Sea and the Danish-Norwegian Basin. (b) The stratigraphy of the Zechstein Group in the Netherlands. The Zechstein is divided into five cycles (Z1–Z5). Note the thick halite units in Z2 (Stassfurt Halite) and Z3 (Leine Halite) on the basin margin and the brittle rock between them (e.g., Haupt Anhydrite member, Platten Dolomite member) (modified after van Adrichem Boogaert and Kouwe 1993).

3.5   Stratigraphy of the Zechstein in the study area

3.5.1 Stratigraphic description of the Zechstein from Well reports

The stratigraphy of the Zechstein was described using well data followed by stratigraphic correlation tied to seismic facies on seismic sections. For this purpose, four wellbores were used (Fig 3.1). Two were from the Cavendish survey: well 43/19-1, a vertical well located on the flank of an anticline in the Cavendish gas field, and well 43/19-2, located 3.1 km west of well 43/19-1. The other two wells, well 43/24-2 and well 43/24-1, are from theTrent96 survey, the latter being located in the middle of the Trent 96 survey in quadrant 43, block 24 (Fig 3.1). The thickness of the Zechstein in the four wells is about 973 m, 1033 m, 570 m, and 305 m, respectively.

3.5.1.1   Zechstein 1

In well 43/19-1, the thickness of the Zechstein 1 is approximately 28 m, and it is composed of a dolomite unit at the base and an anhydrite unit at the top; the two units have thicknesses of 13 m and 15 m, respectively, ascribed to the Werra Formation (Fig. 3.9). The Zechstein 1 has similar lithology and thickness in well 43/19-2 (Fig. 3.10). However, well 43/24-2 in the south shows that the dolomite and anhydrite units are about 50 m thick (Fig. 3.11).

3.5.1.2   Zechstein-2

The Zechstein-2 cycle in well 43/19-1 is composed of anhydrite and Z2 polyhalite units with thicknesses of 13.5 m and 43 m, respectively (Fig. 3.9). A thick layer of pure halite with a thickness of 373 m overlies the Z2 Polyhalite, which belongs to the Stassfurt Halite. Above the Stassfurt Halite is a 30 m-thick unit composed of intercalations of thin potash layers. This unit belongs to

the Stassfurt Potash member. The term "potash" is a general term applied to a variety of potassium-bearing minerals. In rock salt, the mineral sylvite is the most common potassium salt (K-salt) and has a density of 1860 kg/m^3 (Urai et al. 2008) (Table 3.1). The stratigraphy of the Zechstein-2 is similar in well 43/19-2: A 10 m-thick limestone unit characterises the lower part of the cycle with 6 m of anhydrite above it, followed by 67 m of polyhalite that is interbedded with anhydrite and halite (the Z2 Polyhalite Formation). Here, the Stassfurt Halite Formation with a total thickness of 542 m overlies the Z2 Polyhalite Formation and is composed mainly of pure transparent halite capped by a 31 m-thick K-salt of the Stassfurt Potash potash member, which is the top of the carbonate-evaporite cycle of the Zechstein-2.

In well 43/24-2, the Z2 includes halite interbedded with a K-salt interval that is about 40 m thick (Fig. 3.11). The rest of the section (460 m) is halite with only 12 m of mudstone interbedded with halite and anhydrite in the middle of the interval, which is probably a fragment of the Z3 Stringer. The upper 116 m of this thick halite interval is characterised by interbedded thin K-salt, mudstone, and anhydrite.

3.5.1.3 Zechstein-3

A 10 m-thick dolomite layer ascribed to the Platten Dolomite forms the base of the Z3 evaporite cycle and is overlain by a 63 m-thick anhydrite layer that belongs to the Haupt Anhydrite (Fig. 3.9). van Gent et al. (2011) suggested that these two brittle members together form the Z3 Stringer within the ductile salt. In well 43/19-2, the Platten Dolomite member at the base of the Zechstein-3 cycle is only about 5.5 m thick, while the overlying Haupt Anhydrite is about 18 m thick.

The upper part of the Z3 cycle is characterised by a massive halite unit of 200 m above the anhydrite interval and belonging to the Leine Halite. Above this unit is a 70 m-thick unit of halite and polyhalite belonging to the Leine Potash Formation.

3.5.1.4   Zechstein-4

The thickness of the Z4 cycle is about 127 m. The lower 20 m-thick unit is composed of intercalated claystone and halite (The Roter Salzton) followed by 1.5 m of pegmatite anhydrite. Above this layer is the Aller Formation that represents the end of the Zechstein Group. The Aller Formation consists of a 108 m-thick massive halite unit with 6 m-thick dolomitic claystone and anhydrite layers in the middle part of the formation. In well 43/19-2, the lower unit comprises 28 m of mudstone interbedded with carnalite, forming the Roter Salzton Formation, followed by 10 m of anhydrite and 22 m of halite, which belong to the pegmatite anhydrite and the Aller Formation, respectively (Table 3.1). The rest of the upper part of Z4 is halite with thin units of mudstone.

Table 3.1: Petrophysical properties of evaporite minerals (Urai et al. 2008).

Name	Formula	Density	GR	Neutron "Porosity"	Sonic transit time
		kgm^{-3}	API	%	$msft^{-1}$
Bischofite	$MgCl_2 . 6 H_2O$	1560	0	> 60	100
Carnallite	$KMgCl_3 . 6 H_2O$	1570	220	65	78
Epsomite	$MgSO_4 . 7 H_2O$	1710	0	> 60	
Sylvite	KCl	1860	500	-3	74
Halite	$NaCl$	2040	0	-3	67
Kainite	$MgSO_4KCl . 3 H_2O$	2120	245	45	
Gypsum	$CaSO_4 . 2 H_2O$	2350	0	>60	52
Kieserite	$MgSO_4 \cdot (H_2O)$	2590	0	38	
Calcite	$CaCO_3$	2710	0	-1	49
Polyhalite	$K_2Ca_2Mg(SO_4)_4 \cdot 2 (H_2O)$	2790	180	15	57
Langbeinite	$K_2Mg_2(SO_4)_3$	2820	275	0	52
Dolomite	$CaCO_3 MgCO_3$	2870	0	1	44
Anhydrite	$CaSO_4$	2980	0	-2	50
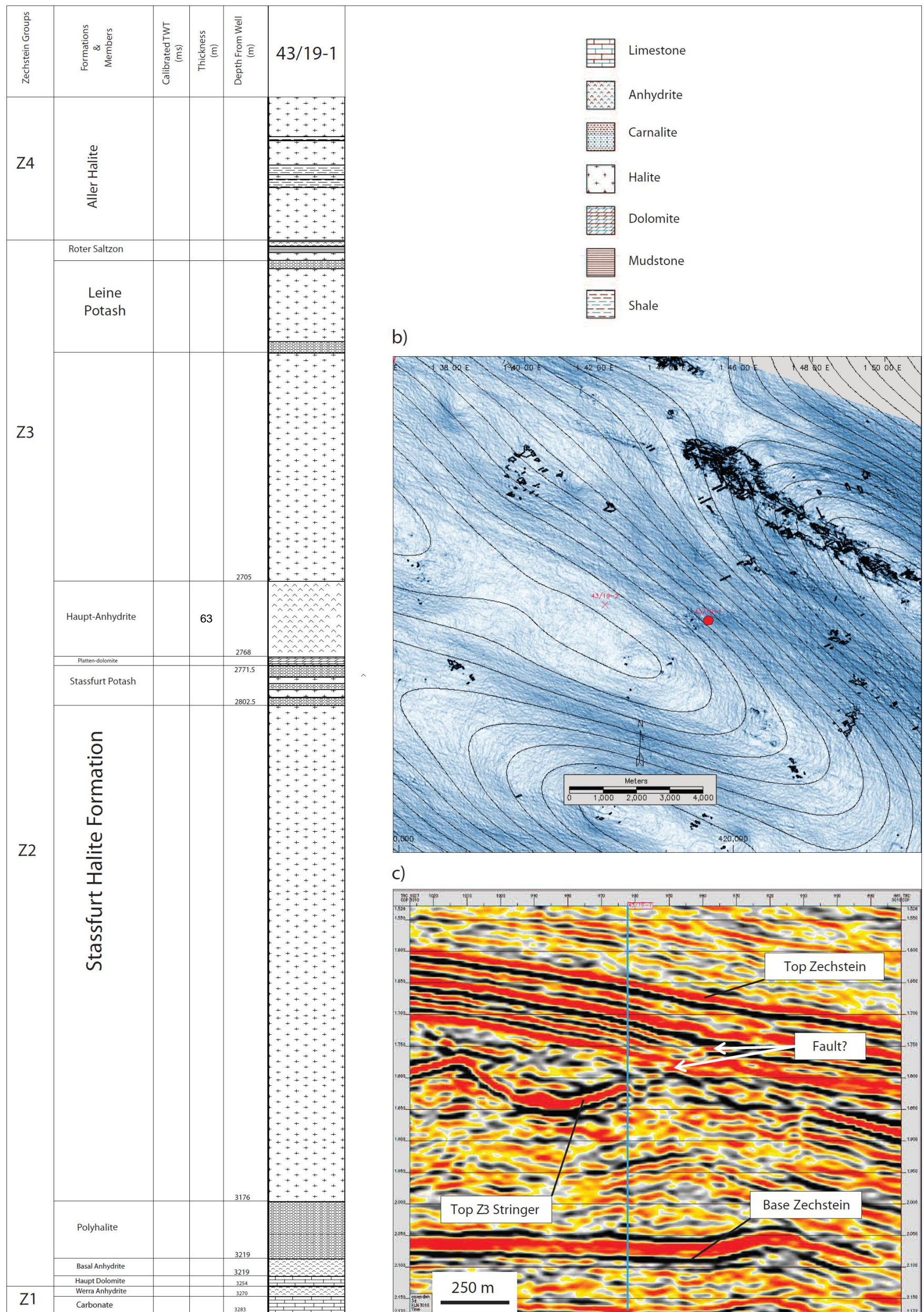
Fig. 3.9: Well 43/19-1 in the Cavendish 3D seismic survey. (a) Stratigraphic column of the Zechstein. (b) Location of the well is posted on the Top Salt dip map. (c) Position of well 43/19-1 on the seismic section passing through the Zechstein section. The top Zechstein, top Z3 Stringer, and base Zechstein are annotated. The Z3 Stringer in the well is much thicker than expected from seismic data interpretation.

a)

Zechstein Groups	Formations & Members	Calibrated TWT (ms)	Thickness (m)	Depth From Well (m)	43/19-2
Z5? Z6?	Aller Potash	1580	43	2225.5 2269	
Z4	Aller Halite		28.5	2297.5	
	Roter Fm		22.5	2320	
	Pegmattite-Anhydrite		10	2330	
			28	2358	
Z3	Leine Potash		66	2424	
	Leine Halite		105	2592	
	Haupt-Anhydrite		18	2611	
	Platten-dolomite		5.5	2616.5	
	Stassfurt Potash		33	2649	
Z2	Stassfurt Halite Formation		542	3191	
	Polyhalite		67	3258 3263	
			10	3274	
Z1	Carbonate	2059	28	3302	

Legend:
- Limestone
- Anhydrite
- Carnalite
- Halite
- Dolomite
- Mudstone
- Shale

b)

c)

Top Zechstein

Top Z3 Stringer

Base Zechstein

250 m
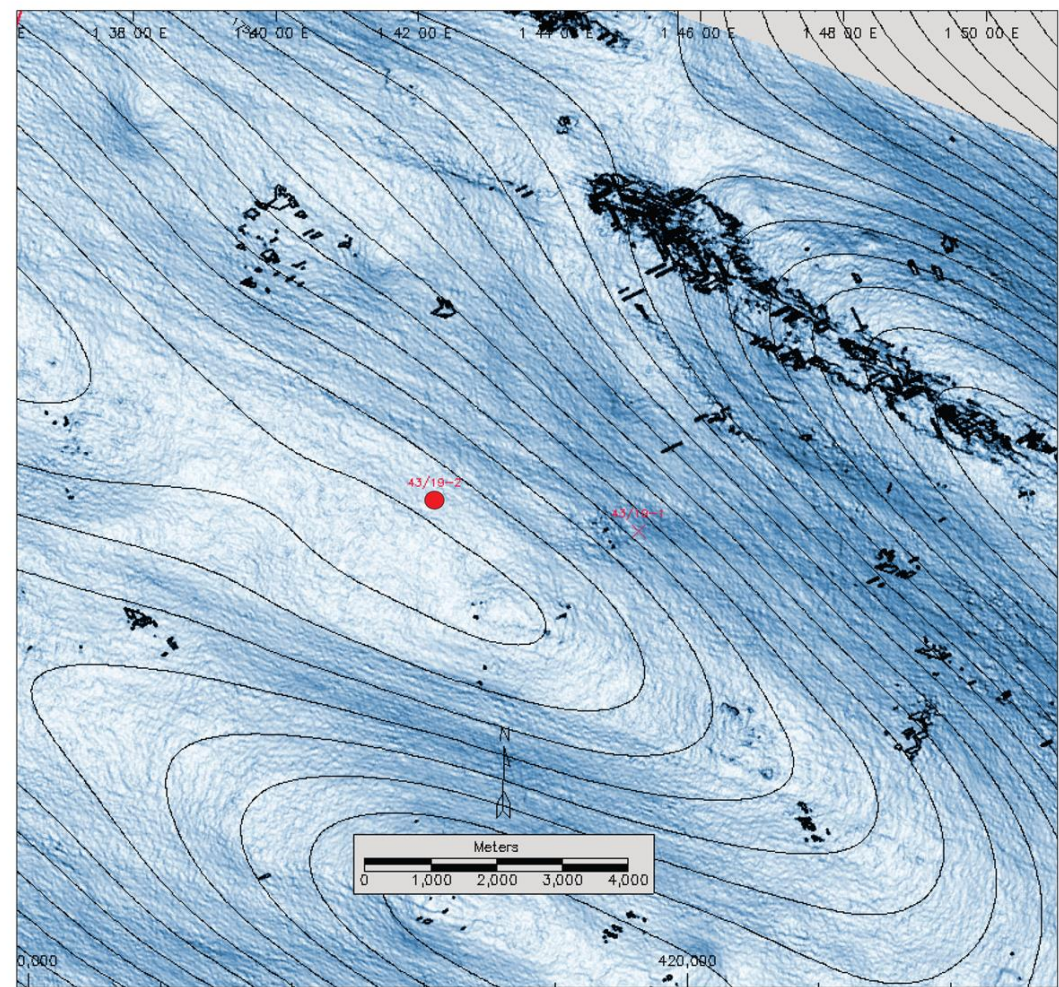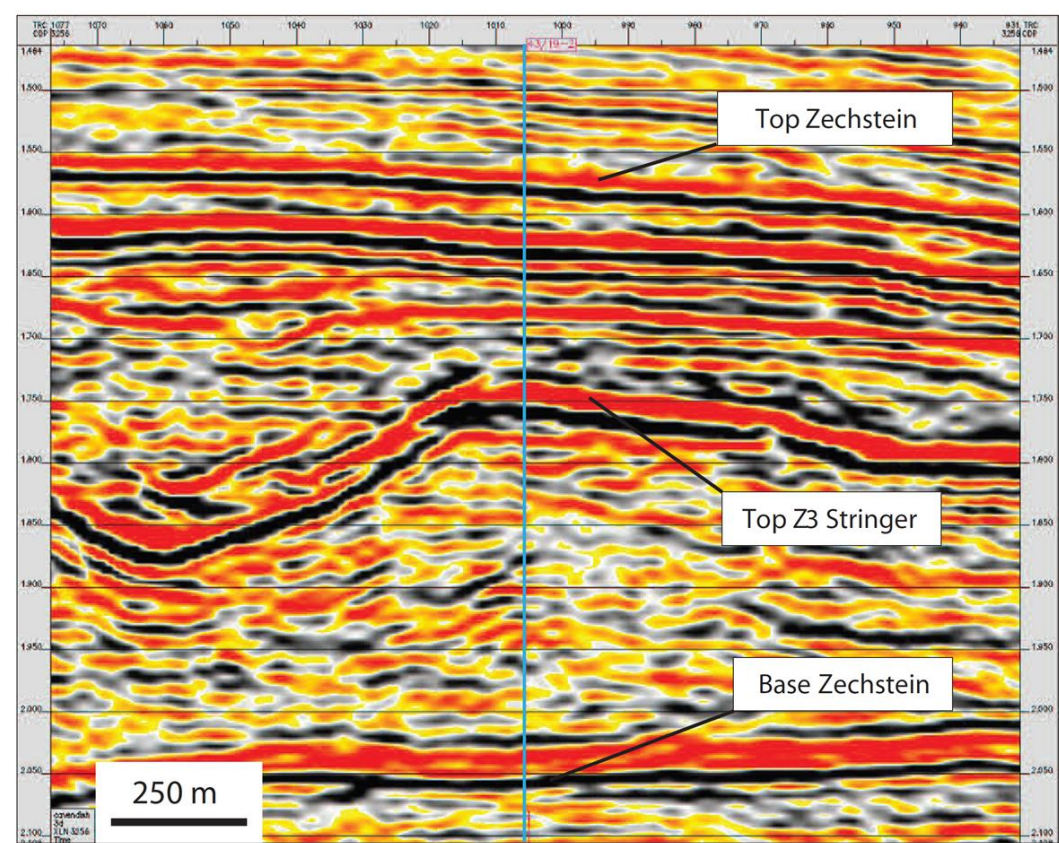
Fig. 3.10: Well 43/19-2 penetrated a considerable thickness of the Zechstein salt (1.1 km thick). The encountered Z3 Stringer has a thickness of 23.5 m (5.5 m Platten Dolomite plus 18 m Haupt Anhydrite) and is underlain by 33 m-thick layered potash salt. The overlying Z3 Leine Halite is only 100 m thick compared to the thick Z2 Stassfurt Halite (542 m).
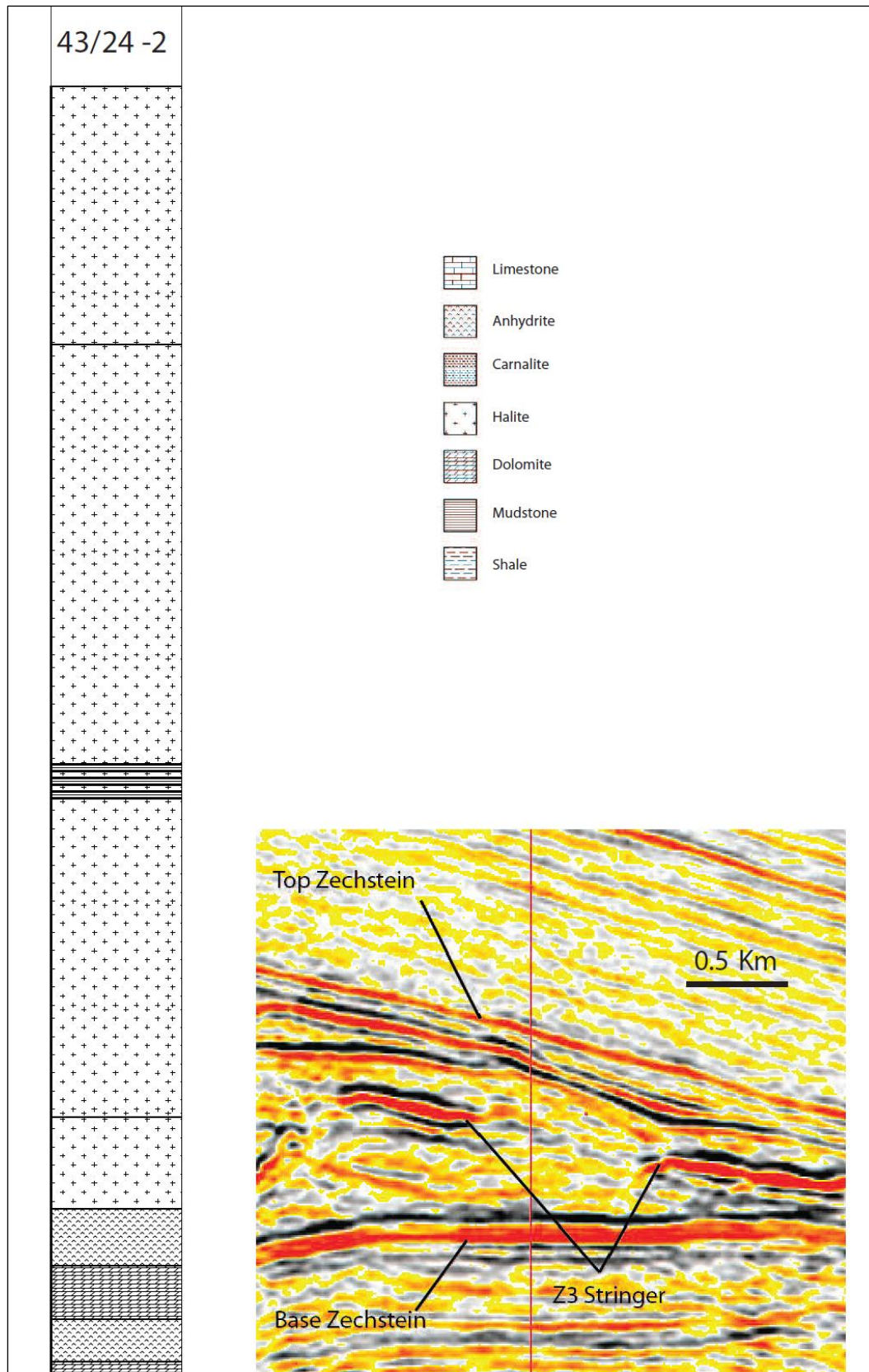
Fig. 3.11: (a) Stratigraphy of the Zechstein from well 43/24-2. Note the thin beds of mudstone and halite at the middle of the column, interpreted to be stringer remnants. (b) The position of well 43/24-2 through the Zechstein on the seismic section. Note the discontinuous stringer fragments.
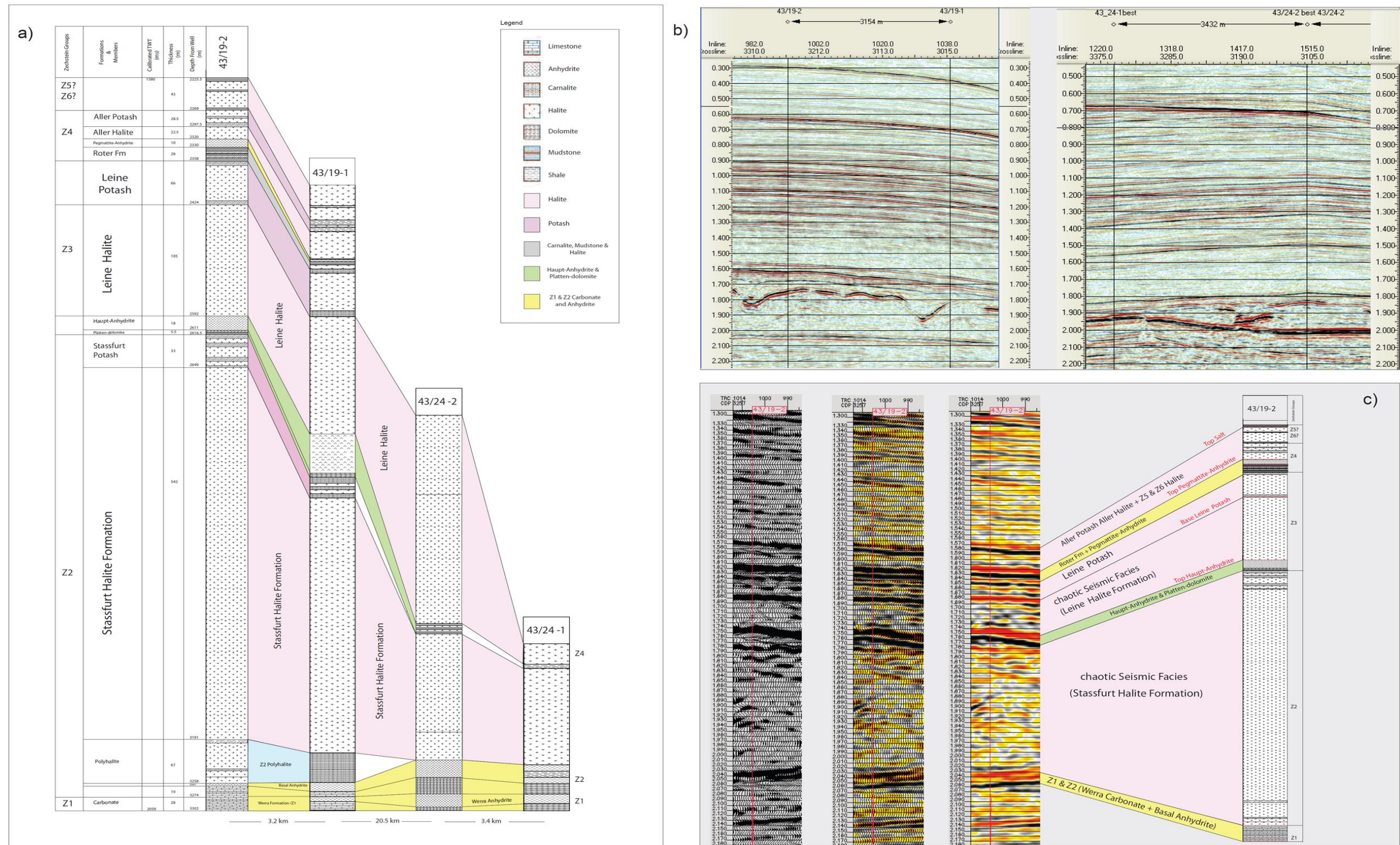
Fig. 3.12: Detailed stratigraphy of the Zechstein in the Silverpit area. (a) Well correlation panel. Well 43/19-2 and 43/19-1 in the Cavendish Field are about 3 km away from each other. Well 43/24-2 and 43/24-1 are from the Trent Gas Field about 20 km south of the Cavendish field. (b) The location of the wells on seismic profiles. Note the variation in thickness of the Zechstein from well 43/19-2 to well 43/24-1. (c) Well 43/19-2 to seismic tie.
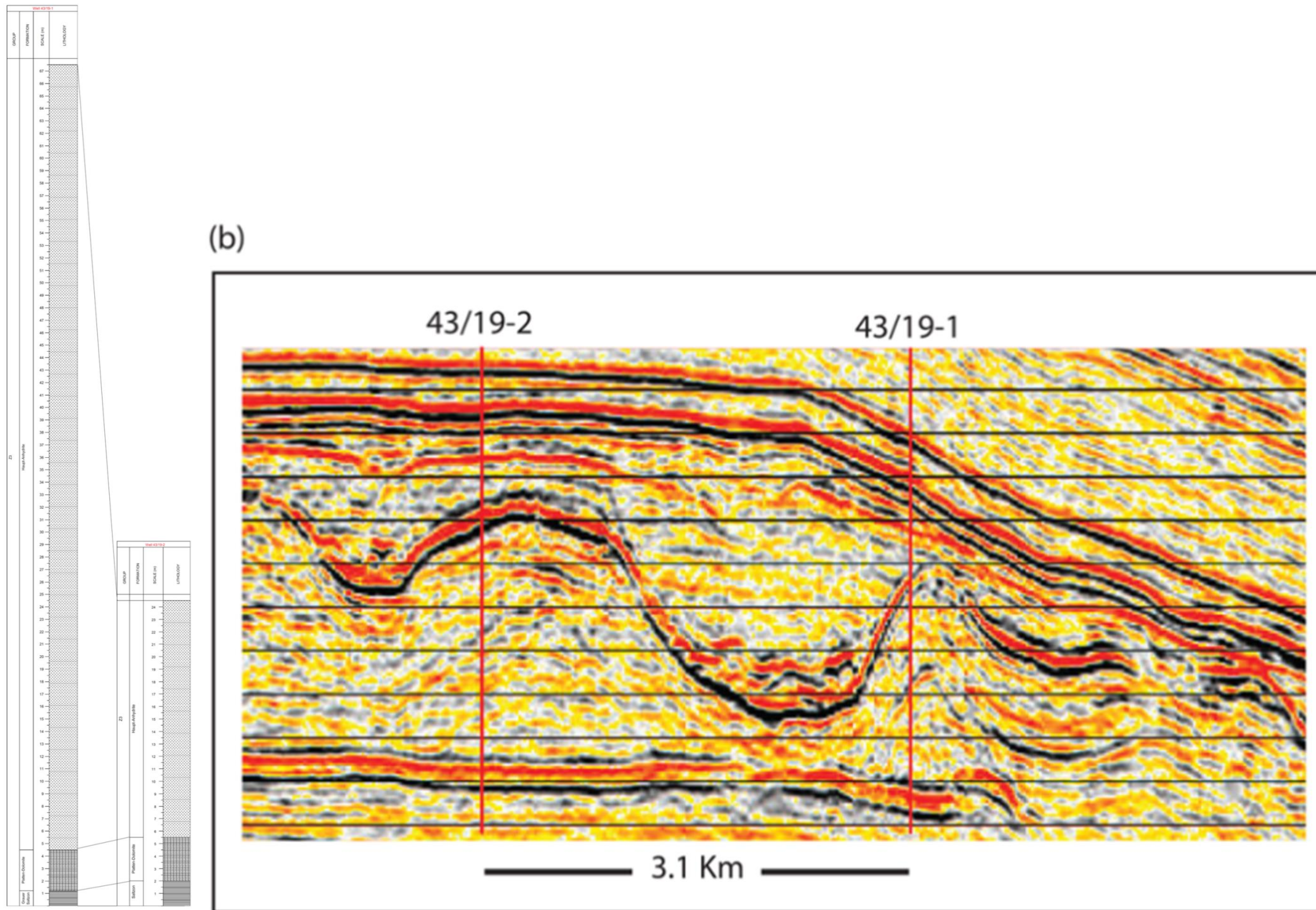
Fig. 3.13: Z3 Stringer correlation across the boreholes and on a seismic section. The thickness of the Z3 Stringer decreases from well 43/19-2 to well 43/19-1. Note the thin seismic reflector of the Z3 Stringer in well 43/19-1.

3.5.2 Seismic stratigraphy of the Zechstein Group

The Top Salt is a positive-amplitude reflector that represents the positive acoustic impedance contrast of the interface from the Bacton shale to the Z4/Z5 evaporite (downward increase in P-wave velocity). The Z4/Z5 layers are continuous, parallel reflectors with similar character as the overburden. These are multilayers of halite, mudstone, and anhydrite of the Z4-Z5 members. The base of these layers forms the upper roof of the ductile Z3 halite, which is characterised by chaotic seismic character (Fig. 3.12b,c).

The second reflection is the Z3 Stringer at the base of the Z3 cycle, which is also a positive, high-amplitude reflector generated by the transition of seismic waves from halite (4500 m/s) to denser dolomite and anhydrite (5500–6500 m/s) (van Gent et al. 2011). The high acoustic impedance contrast between the halite and the anhydrite makes the Z3 Stringer well-imaged on seismic data.

Below the Z3 Stringer, the seismic data is characterised by a chaotic thick layer belonging to the Z2 Stassfurt Halite member. The lower part of the Zechstein is a thick, positive reflection with constant thickness over the study area because of the carbonate and anhydrite layers at the base belonging to the Z2 basal anhydrite and Z1 Werra Formation, and has an average thickness of about 50 m (Fig. 3.11). Stratigraphically, the base Zechstein is the base of Z1 Werra Formation, which is a negative reflector. However, mechanically the top Z2 basal anhydrite is the brittle boundary for the ductile Z2 Stassfurt and Z3 Leine Halite members.

3.6   General description of the external and internal salt structures

The Top Salt surface displays elongated anticlines and synclines that strike dominantly in a NW–SE direction (Fig. 3.14b). The axes of the synclines and anticlines were annotated and classified using the contours of the Top Salt time elevation surface (Fig. 3.14a). The Zechstein salt has a similar topography as the Top Salt, indicating that Top Salt is the major controlling element of salt thickness (Fig. 3.14b). The thickness of the Zechstein salt is laterally variable due to salt movement (Fig. 3.14b). In addition to the Top Salt displacement, the sub-salt faulting creates a secondary thickness change at uplifted and subsided sub-salt blocks (Fig. 3.14b).

Four synclines (S1–S4) and five anticlines (A1–A5) were annotated (Fig. 3.14c). For detailed analysis of the intra-salt structures, the area was divided into domains of anticlines and synclines based on the regional Top Salt structure (Fig. 3.14c). Base Salt is characterised by ENE trending faults (Fig. 3.14d), playing a secondary role in reducing the thickness of the Zechstein (Fig. 3.14b). The Z3 Stringer surface shows intensive deformation of discontinuities and folding (Fig. 3.14e). The Z3 Stringer is characterised by large discontinuous areas below S1, while well-developed folds formed under Top Salt anticlinal regions.
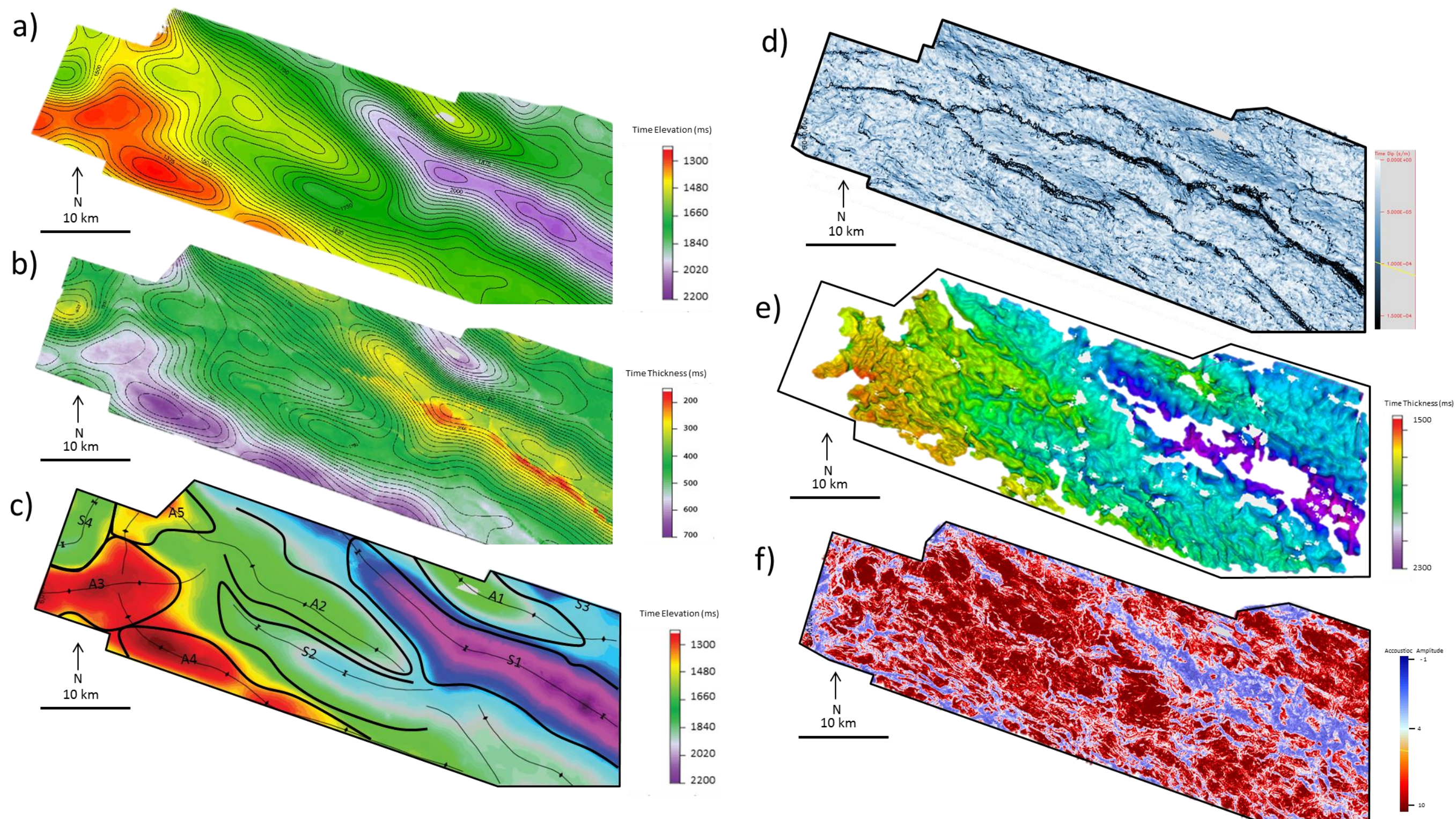
Fig. 3.14: (a) Two-way-travel-time (TWT) map of the Top Salt surface, classified into anticlines (A1-A5) and synclines (S1-S). (b) Time thickness map of the Zechstein salt. (c) The Zechstein structure divided into domains based on the regional Top Salt structures. These domains will help to analyse the intra-salt structures. (d) TWT structural map of the Base Salt with NW fault trends. (e) TWT map of the Z3 Stringer shows discontinuous zones and folding. (f) Z3 Stringer acoustic amplitude. Note the distribution of areas of low to zero seismic amplitude (blue, discontinuities) and high seismic amplitude (red).

3.7   Discussion

3.7.1 Stratigraphy of the Z3 Stringer

3.7.1.1   Well data

The detailed stratigraphic description of the Z3 Stringer from well data shows that the Z3 Stringer is characterised by a thin shale layer, 1–2 m thick, overlain by the Platten Dolomite Formation, which is approximately 4 m thick. The upper Haupt Anhydrite Formation is about 19 m thick in well 43/19-2 and reaches up to 63 m in thickness 3 km away in well 43/19-1 (Fig. 3.9 and 3.10). The other two wells, well 43/24-1 and well 43/24-2 in the Trent survey, penetrated the syncline of the Silverpit Crater and did not encounter the Z3 Stringer. Offshore Netherlands, the thickness of the Z3 Stringer generally ranges from 1 m to 40 m, but it is up to 150 m thick in areas where the Z3 Stringer forms synclines (van Gent et al. 2011). Where well 43/19-1 passes through the steeply plunging limb of the Z3 Stringer, it is unusually thick (Fig. 3.9). Flatter Z3 Stringer areas, which are less deformed, are assumed to represent the original stratigraphic thickness. Hence, the average thickness of the Z3 Stringer from well 43/19-2 is 25 m (19 m anhydrite plus 4 m dolomite plus 2 m shale).

3.7.1.2   Seismic data

The densities of the dolomite and anhydrite at greater depth are 2780 and 2980 kg/m^3, respectively; hence, the thick positive amplitude reflector of the stacked dolomite and anhydrite units is interpreted to be the competent Z3 Stringer within the ductile salt. On seismic profiles, the Z3 Stringer in well 43/19-2 is characterised by a high-amplitude reflection, whilst in well 43/19-1,

it is characterised by a weak seismic reflector (Fig. 3.12b and Fig. 3.13). However, in well 43/19-1, the Z3 Stringer is much thicker than in well 43/19-2. This has been interpreted to be related to the steep geometry of the Z3 Stringer in well 43/19-1, which impairs seismic imaging (see Strozyk et al. 2012; van Gent et al. 2012). Therefore, the weak contrast of the seismic reflector of the Z3 Stringer at highly dipping limbs might not be only related to thinning of the Z3 Stringer.

The Z3 Stringer has not been encountered in the southern wells below the syncline of the Silverpit Crater. This absence of the Z3 Stringer on well data coincides with its absence on seismic data, suggesting that the Z3 Stringer has been fragmented below the syncline structure during salt tectonics (Fig. 3.12).

3.7.2 Regional tectonics

3.7.2.1   Timing of salt movement

Syn-growth strata are observed to be initiated immediately above the high-amplitude unit and are followed by thickening of reflections at the middle of the synclines (Figs. 3.7). The high-amplitude unit belongs to the Balder Formation (Underhill 2009), suggesting that the syn-kinematic growth strata initiated from the lower part of the Early to Mid-Eocene Westray and Stronsay Groups (Fig. 3.4 and Fig. 3.7). The Base Nordland Group, or the so-called Oligocene-Miocene Unconformity, truncates the tilted strata on the flanks of the anticlines and represents the base of the upper post-kinematic units, signalling that halokinesis ceased in the Miocene.

3.7.2.2   Regional driver mechanism of salt tectonics

The Silverpit Basin is interpreted to have been formed by regional buckling during the Cenozoic for the following reasons:

1. The Upper Permian to Late Cretaceous post-salt megasequences display no evidence of growth or syn-kinematic deposits, suggesting that salt tectonics did not begin before the Cenozoic (Fig. 3.6).

2. The short period of salt movement which has been recorded from the syn-kinematic units, and the low relief of sediment thickening in the Cenozoic (Fig. 3.6) suggest that salt tectonics in the basin is unlikely to have been driven by differential loading. Salt structures that were created by sediment loading display thick sediment successions with clear syn-kinematic thickening, as in the South Oman Salt Basin (Al-Siyabi 2005; Schoenherr et al. 2007; Kukla et al. 2011).

3. The well-developed and elongated salt structures of anticlines and synclines, as well as the huge amount of truncation during the formation of fold structures in the Early Cenozoic, suggest that the basin is likely to have been driven by regional compressional buckling forces. In this case, the formation of regional-scale anticlines and synclines may have been simultaneous.

3.7.2.3   Regional driver mechanism versus intra-salt deformation

In the Cavendish area, the Permian Zechstein and post-salt sections of Mesozoic sediments form NW-SE trending fold structures of anticlines and synclines.

The Silverpit Basin in the Southern North Sea has been interpreted as part of a contractional zone because of the compressional event that happened

during the Cenozoic (i.e., the Mid-Tertiary inversion tectonics) (Stewart and Coward 1995; Stewart and Allen 2005). Other authors interpreted the fold structures to have been formed by salt withdrawal at depth by differential loading (e.g., Underhill 2004; Thomson et al. 2005; Underhill 2009). From these two models, how can the internal salt deformation be used as an indication for the regional-scale tectonics, as in both models synclines and anticline structures are formed?

A buckled basin will likely form synclines and anticlines simultaneously because the whole basin has been subjected to a simple shortening event. However, in the case of differential loading, assuming a vertical load is applied to a salt layer, regional synclines are likely to form at the beginning followed by salt evacuation and consequently the development of salt anticlines, domes, and diapirs in the adjacent areas. For the later model, the salt layer might move for kilometres before it starts to thicken to form pillow structures (Vendeville and Jackson 1992a; Rowan 1995; Hudec et al. 2009). This has been observed in many examples of salt tectonics (Hudec and Jackson 2007), and has been demonstrated by analogue and numerical modelling (McClay et al. 1998). Using this model, progressive phases of deformation along the Z3 Stringer are expected to form through time with variable structural styles. The intra-salt stringer is initially and dominantly exposed to the deformation that is related to the subsidence of Top Salt (deformations below salt synclines or minibasins) (Fig. 3.15).

However, by shortening the whole basin and the simultaneous development of regional synclines and anticlines, the intra-salt contraction within anticlines and domes forms simultaneously with the intra-salt extensional deformations

in the subsided regions (Fig. 3.15). This has also been demonstrated by analogue modelling of a basal ductile layer substrate that is overlain by overburden strata subjected to shortening (Harris et al. 2012). Similar regional fold structures to those in the Silverpit Basin are created. The intra-salt deformation (the green layer in Fig. 3.16) is characterised by fold structures under anticlines and stretching under synclines. The results show that ductile flow, shortening, and formation of isoclinal folds occur within anticlines. This analogue model suggests that shortening of a ductile layer will result in folding similar to that observed in the Z3 Stringer (discussed in more detail in chapter 4).
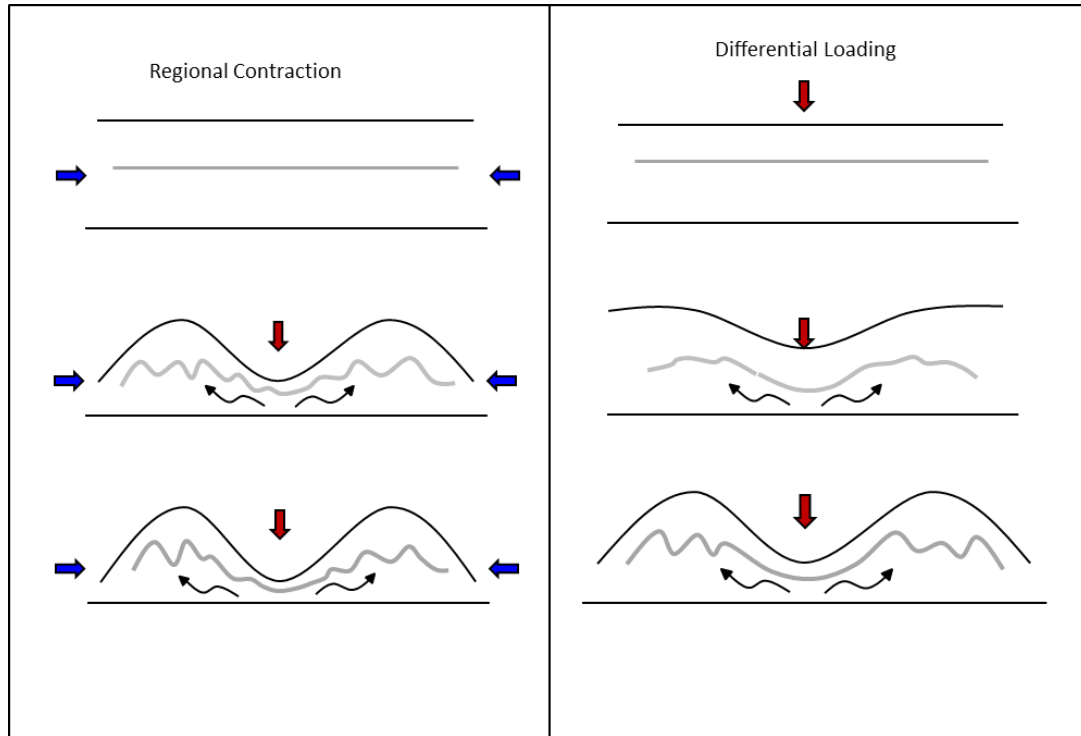
Fig. 3.15: Suggested models for the development of the folding of the regional Zechstein and the internal deformation styles. (1) Regional compression of the basin forms simultaneous Top Salt anticlines and synclines associated with simultaneous intra-salt deformation. Folds are also expected to form under synclines because of the initial shortening of the basin, which will result in an internal flow of the salt. (2) Differential loading by downward salt movement will start with downward displacement by Top Salt forming synclines followed by the development of anticlines at the flanks. The internal layer will expose extensional deformation first below regional synclines and will not fold significantly at this early stage below regional anticlines.
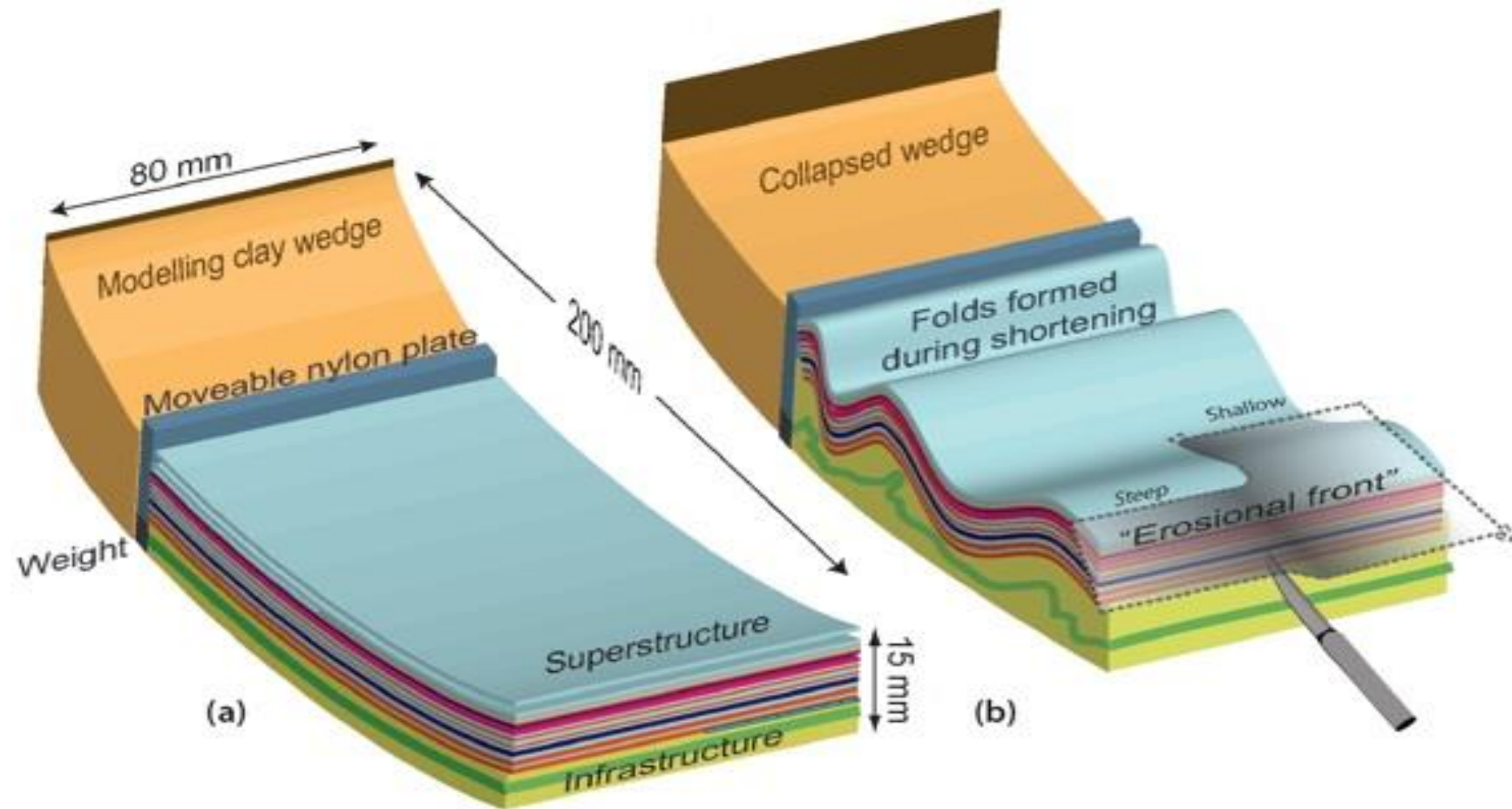
Fig. 3.16: Shortening a ductile layer in analogue modelling, similar to the Silverpit Basin. (a) Multi-layered infrastructure and superstructure overburden prior to deformation. The yellow and the green are the ductile layers. (b) Schematic diagram of previous layers after shortening is applied (after Harris et al. 2012).

3.8   Conclusions

- The detailed stratigraphic description of the Z3 Stringer shows that it is characterised by a thin shale layer, 1–2 m thick, overlain by the Platten Dolomite Formation, which is approximately 4 m thick. The upper Haupt Anhydrite Formation forms the dominant stratigraphy of the Z3 Stringer with thickness ranging from 19 m to 60 m.

- The syn-kinematic units in the Silverpit Basin recorded from Early Eocene to Late Oligocene indicate the period of salt activity in the basin and the development of the internal deformation.

- Shortening of the basin by regional compressional events is interpreted to be the main driver mechanism for salt tectonics. Bulk shortening of the Silverpit Basin resulted in the formation of detached regional anticlines with well-developed intra-salt folding and regional synclines of stretching and discontinuities.

- Analogue modelling of shortening a ductile layer overlain by thick overburden shows a similar regional structure within the superstructure and high shortening deformation within the ductile zone as it is observed for the Z3 Stringer.

- The regional driver mechanism influences the internal salt structural styles; however, the structural styles of the intra-salt may differ if a differential loading or buckling mechanism is applied to the basin. Thus the internal deformation can be used to predict the regional driving mechanism of salt tectonics.

Chapter 4: The kinematic evolution of the Z3 Stringer within areas of salt subsidence in the Silverpit Basin, Southern North Sea (SNS)

Abstract

This study investigates the kinematics and dynamics of the internal salt layers within areas of salt withdrawal, particularly in areas of salt subsidence. Salt withdrawal is defined as the movement of salt outwards from a subsiding region into an adjacent rising or uplifted region. The geometric details and the kinematic evolution of this mechanism inside the salt layer are not well documented in the literature. A 3D seismic case study from the Silverpit Basin in the Southern North Sea is used to present a summary of the kinematic evolution of an intra-salt structure within areas of salt subsidence from early salt tectonics to the subsequent welding stage. The study will contribute to a wider understanding of salt tectonics and the internal salt dynamics.

The internal salt structure was analysed by mapping a 23 to 63 m-thick intra-salt dominated anhydrite seismic marker known as the Z3 Stringer using the Top Salt surface as a reference for shortening and subsidence magnitudes. Stringer deformational styles were established from seismic profiles and 3D maps at variable Top Salt subsidence levels, and were used to generate 2D and 3D structural evolution models. An apparent relationship has been observed between the brittle deformation of the stringer and the amount of top salt subsidence. The structural propagation of the intra-salt stringer below areas of top salt subsidence begins with the formation of long-wavelength folds at the early stage of top salt subsidence. This is followed by lateral stretching and consequently thinning and re-flattening of the stringer when subsequent subsidence accumulates. The stringer then starts to break and fracture at zones of maximum thinning of the salt below the subsided region and is followed by fragmentation, isolation, and finally lateral separation of the stringer fragments for distances of up to 5 km. The result of this study strongly contrasts with

recently published studies on the structural evolution of the Z3 Stringer, which suggest that it has been frequently ruptured during salt depositional processes (e.g., Strozyk et al. 2014).

Understanding the evolution of the internal salt structure is very important for assessing hydrocarbon traps, for reservoir quality, sealing, maturity, charge, and migration. On seismic data, the complexities of the stringer deformation make it difficult to image, particularly in areas where the stringer is steeply dipping. A series of methodological steps were introduced here to overcome seismic imaging problems in steep stringer geometries. These steps could contribute to the seismic interpretation process of the poorly imaged, steeper parts of stringers. This is also important for other industrial applications such as geological storage and solution mining, where it is an imperative of operational procedures to avoid overpressured stringers whilst drilling, as they are potential drilling hazards.

4.1 Introduction

Regions of salt-induced subsidence have been called sinks and rim synclines (Trusheim 1960), withdrawal basins (Jackson and Talbot 1991), minibasins (Worrall and Snelson 1989), pods (Hodgson et al. 1992), or simply salt synclines (Fig. 4.1a). Salt withdrawal is the movement of salt from areas of subsidence into adjacent rising regions (anticlines, pillows, diapirs, salt domes) where the salt is accumulating (Fig. 4.1a,b). Salt withdrawal is caused by either stratigraphic differential sediment loading (Cohen and Hardy 1996; Koyi 1996; McClay et al. 1998; Gemmer et al. 2004; Gaullier and Vendeville 2005; Vendeville 2005; Warsitzka et al. 2013), tectonics by contraction (Humphris 1979; Rowan 2002; Rowan and Vendeville 2006; Ings and Beaumont 2010), or extension (Vendeville and Jackson 1992a,b; Jackson and Vendeville 1994). Because of these regional forces, salt can either thin or thicken to form salt welds, pillows, and diapirs.

Salt thinning and salt rising regions are two different structural domains (Hudec and Jackson 2007; Hudec et al. 2009). The first is where the salt is diverging away from the subsiding region, whilst the second is the contraction region where salt accumulates from adjacent synclines (Fig. 4.1b). The regional structures of these two domains are well documented in the literature (e.g., Jackson 1985; Talbot and Jackson 1987; Hudec and Jackson 2007; Hudec et al. 2009) (see also chapter 1). However, the detailed structural styles and the kinematic evolution of the internal salt structures are still poorly understood. In seismic data, salt structures are studied in two different ways. Most commonly, the evaporites are considered as structureless homogenous bodies (e.g., Jackson and Talbot 1989; Jackson and Vendeville 1994; Rowan 1995; Hudec and Jackson 2007; Hudec et al. 2009). Other studies focused on the details of the internal salt structures by mapping and analysing intra-salt

seismic markers known as stringers (Jackson et al. 1990; van Gent et al. 2011; Kukla et al. 2011; Cartwright et al. 2012; Fiduk and Rowan 2012; Strozyk et al. 2012; van Gent et al. 2012; Strozyk et al. 2014).

Complex intra-salt deformation including folding, thrusting, and lateral extensional related structures (e.g., boudinage) has been observed in seismic studies (Fiduk and Rowan 2012; van Gent et al. 2011; Strozyk et al. 2012). Similar types of deformation have also been observed in salt mines and borehole data (Jackson 1985; Talbot and Jackson 1987; Smith 1996) and in surface-piercing salt domes (Peters et al. 2003; Reuning et al. 2009). Recent studies of internal salt structures revealed layer-parallel extension of boudinage in areas of salt subsidence (Geluk 2000; Geluk 2007; van Gent et al. 2011; Strozyk et al. 2012; Strozyk et al. 2014).

Moreover, 2D geomechanical modelling of a viscous salt layer with a single competent, non-Newtonian carbonate inclusion exposed to progressive downward subsidence shows the formation of lateral diverging salt flow below the subsided region (Li et al. 2012a). This is followed by consequent fragmentation of the stringer in a manner similar to tensile failure, followed by separation of the fragments by salt flow. Such understanding of the geometrical evolution of the internal salt structure will contribute to the understanding of intra-salt reservoir quality and diagenesis (Al-Siyabi 2005; Schröder et al. 2005; Schoenherr et al. 2009; Reuning et al. 2009), seal potential (Daniilidis and Herber 2015), stringer overpressure and the associated drilling hazards (Williamson et al. 1997; van Gent et al. 2011), geological storage for waste disposal, and solution mining (Coelewij et al. 1978; Fokker et al. 1995; Evans and Chadwick 2009).

Continuous internal salt markers are rarely well-imaged in seismic either because of the difficulty of finding continuous sedimentary bodies within the salt (Cartwright et al. 2012) or because of poor seismic processing within the salt. In seismic processing, the salt bodies are commonly treated as homogenous bodies. Intra-salt inclusions (or stringers) and their velocity anomalies are generally ignored during seismic model-building stages (Ji et al. 2011; Rowan and Fiduk 2015). Intra-salt seismic imaging requires dedicated and targeted seismic processing and a robust velocity model, which will enable reliable depth prognosis for the stringers and the pre-salt stratigraphies (Hale et al. 1992; Bernitsas et al. 1997; Cavalca and Lailly 2005; Jones 2008; Jones and Davison 2014).

The limitation of seismic imaging within salt increases the challenges for seismic interpreters, thus increasing drilling risk. Drilling within the salt in some cases is obstructed by unexpected, seismically invisible stringer fragments associated with high-pressure kicks, which may cause major drilling hazards (Williamson et al. 1997; Kukla et al. 2011). Most of these non-imaged stringer fragments are related to steeply dipping portions of stringer (Sleep and Fujita 1997; van Gent et al. 2011; Strozyk et al. 2012; Jones and Davison 2014; Strozyk et al. 2014). Nonetheless, steeper stringer fragments can act as fluid migration pathways through the salt. If the stringer is highly brittle, fracture networks are expected to occur within the stringer, which could enhance fluid flow (Danilidis and Herber 2015). Thus, it is important to improve the interpretation of poorly imaged stringers within the salt.

4.1.1 Aims

This study aims to understand the kinematic evolution of intra-salt structures, specifically in areas of salt withdrawal (e.g., Top Salt subsidence) (Fig. 4.1b) from the early stage of salt tectonics to the subsequent welding stage. Detailed interpretation of the deformation of the intra-salt stringers at variable stages of salt tectonics will allow the understanding of the dynamics and kinematics of the salt and of the associated stringers.

In this chapter, this will be achieved by analysing a highly deformed intra-Zechstein seismic marker (known as the Z3 Stringer) within areas of salt-related subsidence using 3D migrated seismic data from the Silverpit Basin in the Southern North Sea. The results will contribute partially to the full picture of salt flow and to the understanding of intra-salt kinematics during subsidence.

The second aim of this study is to develop interpretation methods to tackle seismically non-imaged stringers within thick salt areas where the stringers are complexly deformed (below top salt anticlines). This will be achieved by introducing systematic steps based on seismic attribute applications to interpret non-imaged stringer fragments and to enhance the interpretation process, thus reducing interpretation uncertainties.
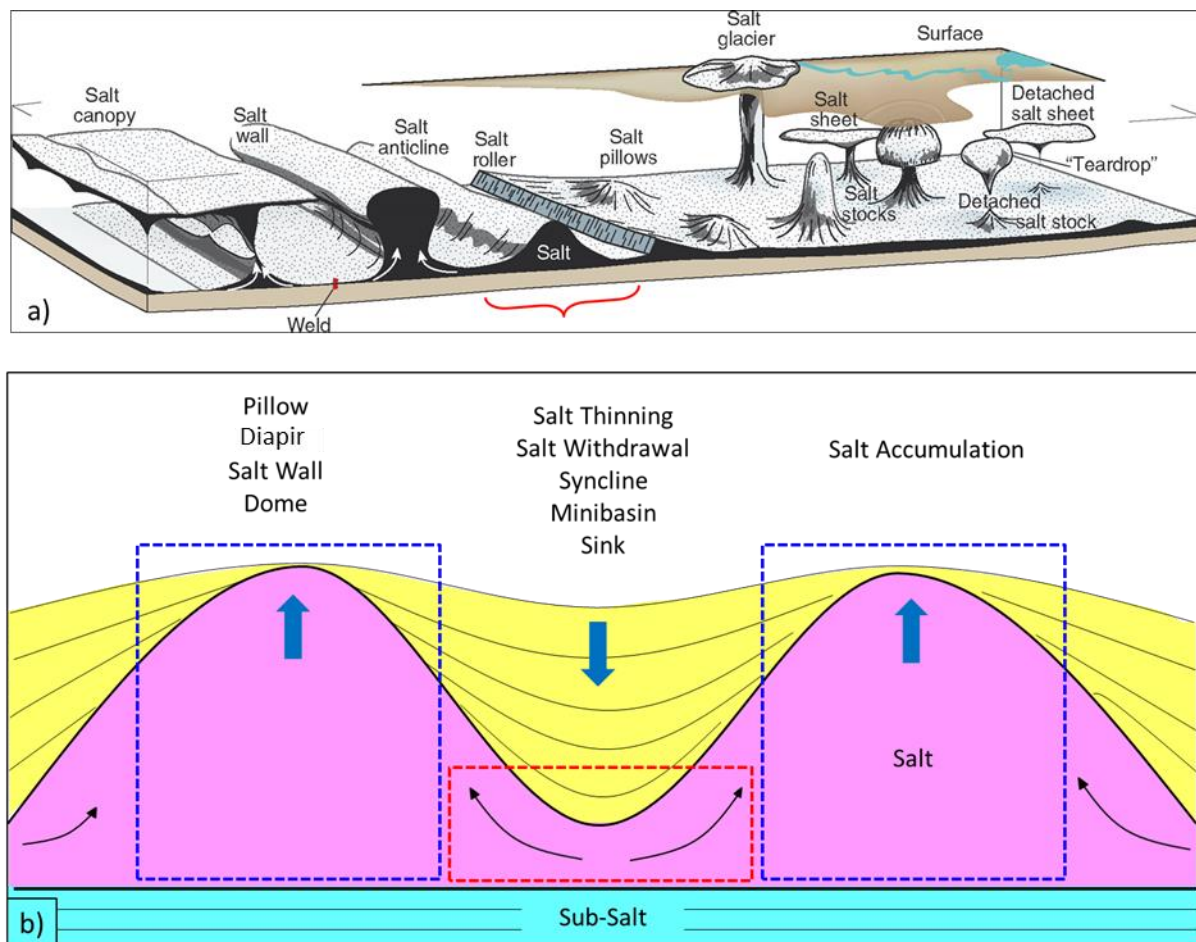
Fig. 4.1: (a) Various regional salt structures; linear structures to the left side and circular structures to the right. The degree of halokinesis increases away from the centre (after Fossen 2010). The red bracket highlights the shape and degree of halokinesis in the study area (Underhill 2009). (b) The salt structure, of anticlines and a syncline, shows two regional structural domains: a salt subsidence domain in the middle (also known as salt withdrawal basin, salt sink, syncline, minibasin) and regions of salt accumulation (anticline, pillow). The red box in the middle highlights the region that this chapter is focused on.

4.2   Data, methods, and workflow

4.2.1 Seismic data

This chapter is based on the structural interpretation of 3D post-stack time migrated seismic data from the Silverpit Basin, Southern North Sea. The interpretation was carried out using Petrel 2013 and Geoframe 2007. Overall, three seismic surveys were provided: Cavendish, Trent96, and Snsj07 (Fig. 4.2) with a lateral and vertical resolution of 25 m and 20 m, respectively. The Cavendish seismic cube is located in Block 43/19a around the Cavendish gas field, and has an area of 1293 km² (Fig. 4.2). The Trent96 survey is located around the Trent gas field, south of the Cavendish field. The Snsj07 survey trends NNE and is merged with the Cavendish and Trent surveys (Fig. 4.2). The Cavendish and Trent96 surveys were used in this study for 3D stringer interpretation. Because of poor seismic quality and high noise content within the salt section, the Snsj07 survey was only used for 2D cross-sectional analysis.

4.2.2 Seismic interpretation workflow

Three main horizons were interpreted in the Cavendish and Trent96 surveys: Top Salt, Base Salt, and Z3 Stringer. The Top Salt has been interpreted in all of the surveys to understand the regional structure of the study area. It was also used to determine the amount of subsidence and consequently the thinning of the Zechstein salt. Time thickness maps were generated for the Zechstein salt by combining Top Salt and Base Salt surfaces. The high density contrast between rock salt (2100 kg/m^3) and the anhydrite (2900 kg/m^3) (Koyi 2001), and consequently the high acoustic impedance contrast, makes the Z3 Stringer reasonably well-imaged on seismic data.

Unlike the Base and Top Salt, the seismic interpretation of the Z3 Stringer was challenging due to the presence of discontinuities and complex structures. The Z3 Stringer interpretation workflow commenced by mapping the reflector in areas where it is more continuous using the 3D seeded autotracking technique. This technique allows horizon mapping in all directions, and the interpretation follows the targeted reflector in areas where the amplitude is continuous. Where the Z3 Stringer is significantly deformed and highly discontinuous, a 2D manual interpretation technique was used instead.

After the completion of horizon interpretation, the new horizon was then transformed into a surface using a Petrel technique called "Structural Operation" to interpolate the gridding gaps between inlines and crosslines. The autotracked surface has high discontinuities of gentle and steep gaps (Fig. 4.3a,c). Because of the well-known seismic limitation of imaging steeply dipping stringers (e.g., Sleep and Fujita 1997; van Gent et al. 2011; Strozyk et al. 2012; Jones and Davison 2014; Strozyk et al. 2014), the autotracked surface was interpolated to fill all the gaps (Fig. 4.3b). In this case the Z3 Stringer is displayed as a continuous surface with no discontinuities, which will be later used for further analysis and seismic attribute analysis (Fig. 4.3b,d). Furthermore, seismic attribute surfaces were generated from the new interpolated Z3 Stringer surface. These include acoustic amplitude, RMS amplitude, and dip magnitude. RMS amplitude is the amplitude measured over a specified window around the interpolated surface (e.g., 5 ms, 10 ms).

Acoustic and RMS amplitudes were used to detect discontinuities within the Z3 Stringer. The non-interpolated Stringer surface is then superimposed with the dip-angle interpolated surface in order to identify the dip magnitude at discontinuities. The dip at which most of the stringer fragments are seismically not imaged was

determined to be 45°. Discontinuities were then classified into steeper (>45°) and non-steeper gaps (<45°) based on the dip surface. By filtering the discontinuities in the dip magnitude surface, shallow discontinuities can be illuminated on the seismic data and can be interpreted as real gaps (e.g., derived by tectonics). However, steeper discontinuities could either be continuous but seismically not imaged or have been fragmented vertically (e.g., boudinage). These have therefore been interpreted further on 3D maps and 2D profiles. A summary of the seismic interpretation and attribute generation to simplify the non-imaged stringers is presented in Fig. 4.4.
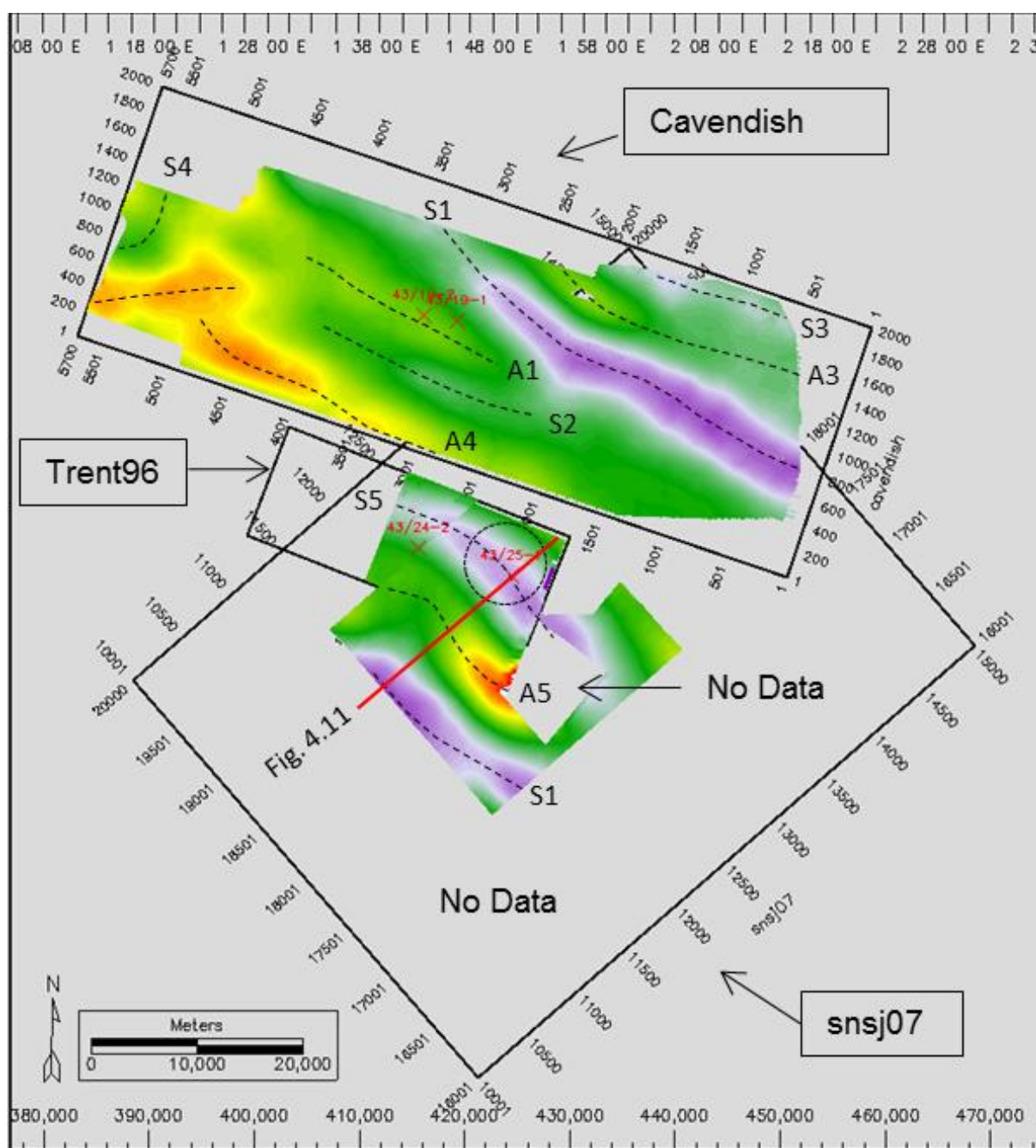
Fig. 4.2: The 3D seismic surveys used in this study: the Cavendish survey in the north and the Trent96 merged with snsj07, in the south. The dashed circle east of the Trent96 survey is the location of the Silverpit Crater. The three surveys are posted with the Top Salt two-way-travel-time surface. The dashed lines are fold axes of anticlines (A1–A5) and synclines (S1–S6) of Top Salt (after Coward and Stewart 1995).
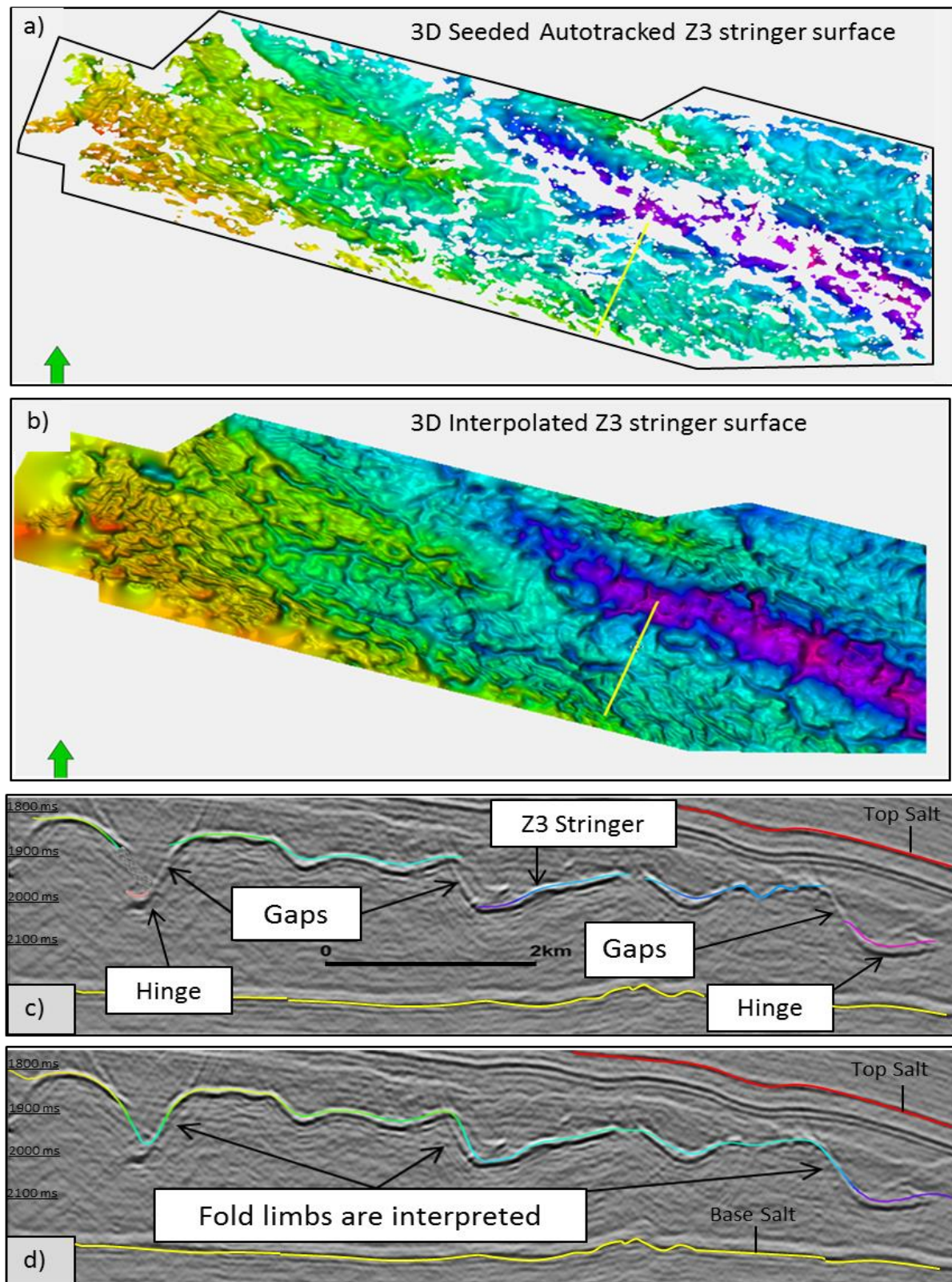
Fig. 4.3: Interpretation of the Z3 Stringer (a) TWT 3D seeded autotracked Z3 Stringer surface. (b) Interpolated Z3 Stringer surface. Note that gaps are filled. (c) The profile shows the 3D autotracked surface in Petrel. Note that the interpretation terminates in areas where the amplitude is missing (discontinuities). (d) The profile shows the interpolated interpretation. Note that discontinuities (e.g., fold limbs) are mapped.
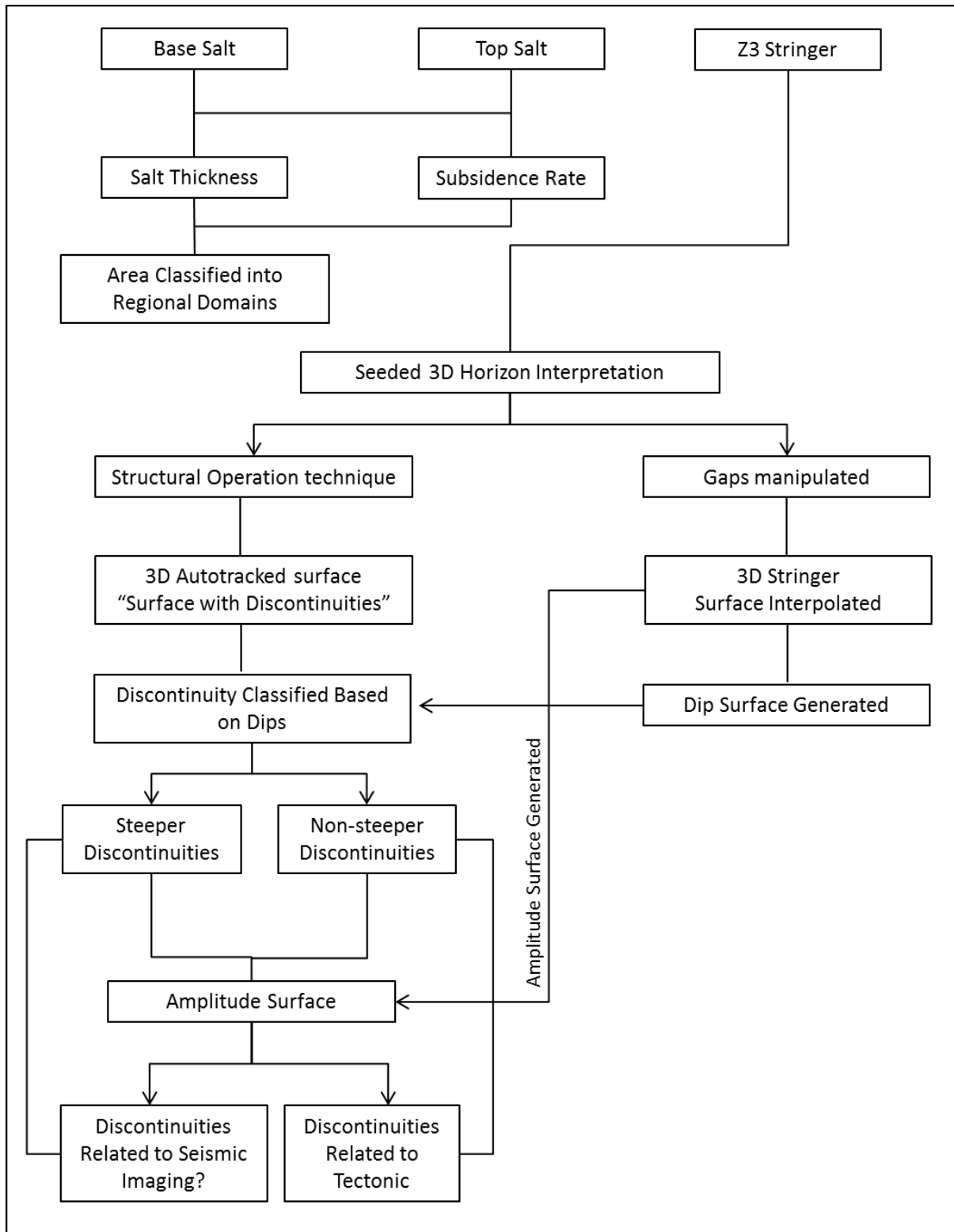
Fig. 4.4: Seismic interpretation workflow for the steep Z3 Stringer using Petrel 2013.

4.3   2D seismic interpretation of the Z3 Stringer under major synclines

4.3.1 Cavendish 3D survey

4.3.1.1 Base and Top Salt

In the Cavendish area, the sub-salt structure consists of SE–NW striking faults with major displacements only at the middle of the study area, and forms a NW–SE striking graben and horst blocks (Fig. 4.5a). The Top Salt forms low- to moderate-amplitude synclines and anticlines.

The Cavendish area was divided into eight domains based on the Top Salt regional structure. Four synclines (S1–S4) and four anticlines (A1–A4) form the large-scale structural elements in the Cavendish area (Fig. 4.2, see also Fig. 3.14c). Synclines (S1, S2, and S3) and anticlines (A1, A2, and A4) are elongated SE–NW structures (Fig. 4.2 and Fig. 4.5b). The folds on the western side, S4 and A3, are striking NE and ENE, respectively. In general, synclinal structures are associated with thin salt below them, whereas anticlines have thicker salt below. S1 is characterised by the highest downward displacement of Top Salt and thus the thinnest salt below (Fig. 4.5b). In contrast, A3 and A4 have the largest fold amplitudes and are therefore associated with the thickest salt sections. S2 and A2 are characterised by moderate fold amplitudes and limited thickness change (Fig. 4.5b). Base Salt is not significantly displaced by sub-faults in a wide area of the Cavendish survey; thus the Top Salt is considered the major indicator of gross salt thickness (Fig. 4.5b).

4.3.1.2 Internal Z3 Stringer

The Z3 Stringer is folded and highly discontinuous (Fig. 4.5c). Large areas of discontinuity occur along the strike of S1 with a scale of hundreds of metres to kilometres.
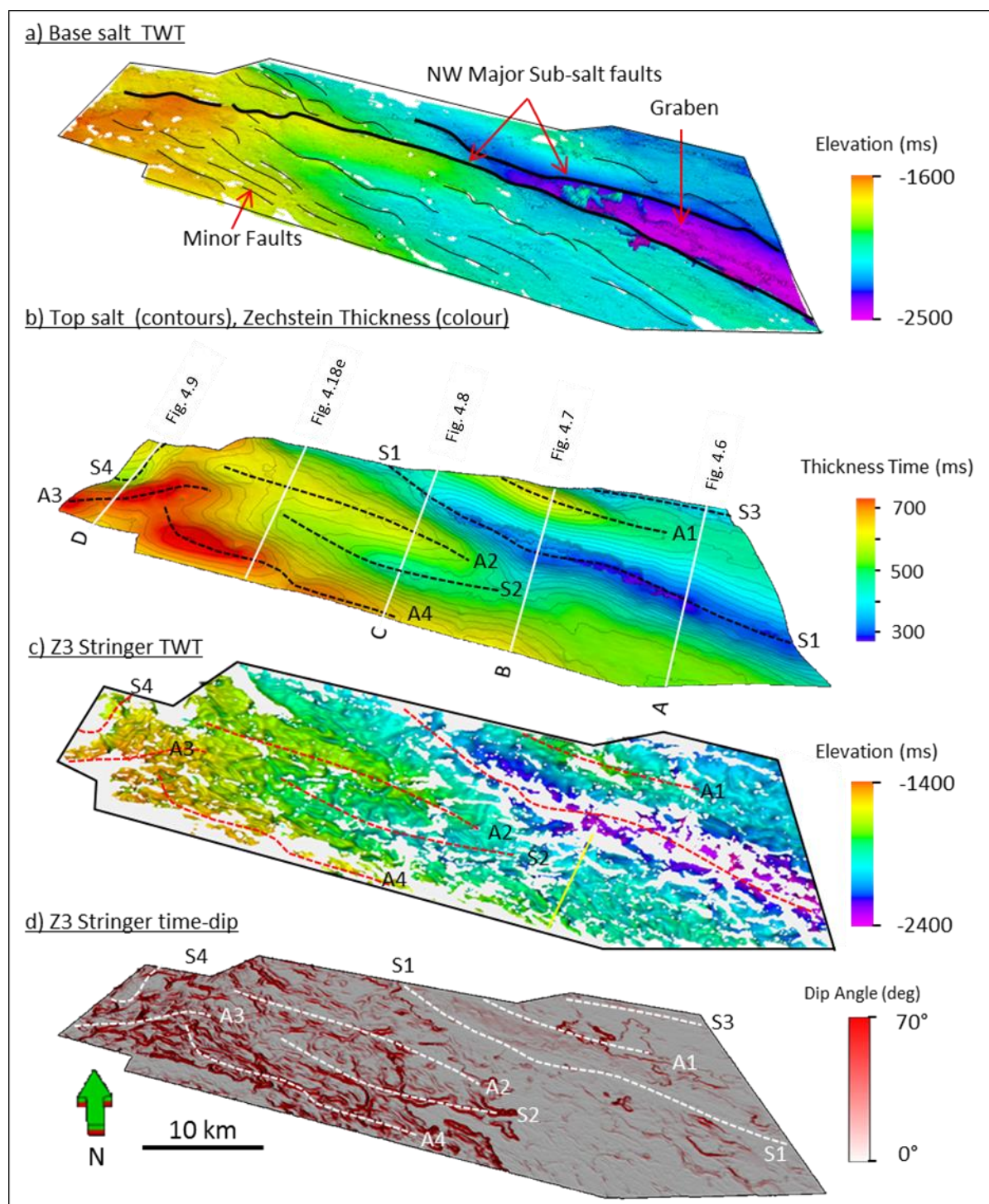
Fig. 4.5: Two-way-travel-time structure maps: (a) Base Salt. (b) Time thickness of the Zechstein salt (coloured surface) superimposed with the Top Salt surface (contours). (c) Two-way-travel-time autotracked Z3 Stringer surface. (d) Time-derived dip map of the Z3 Stringer. Darker shades of red indicate steeply dipping geometries.

The time dip surface of the Z3 Stringer displays shallow dip magnitudes in the east and steeper dips in the western areas (Fig. 4.5d). Minimum stringer dips found below S1 indicate that discontinuities occur within flat to gently dipping stringer fragments (Fig. 4.5c and Fig. 4.5d). However, gaps that occur below the area of A3 and A4, where the Zechstein salt is thick, are observed to form within steeper stringer parts (Fig. 4.5c and Fig. 4.5d).

Four NE–SW representative seismic profiles (Profiles A–D) are used to illustrate the internal structure style of the Zechstein below the Top Salt major synclines (Fig. 4.5b). Profile A and Profile B pass through S1, whereas Profile C and Profile D pass through S2 and S4, respectively.

Profile A

The profile passes through a large portion of S1 in the eastern side of the Cavendish survey and perpendicular to the sub-salt and post-salt structures (Fig. 4.5a,b). Significant reactivated extensional faults in the sub-salt section led to a series of horsts and grabens, none of which extends upwards to penetrate the post-Zechstein section, thereby showing the effective decoupling between the sub- and post-salt (Fig. 4.6). The salt section below S1 is reduced largely by Top Salt subsidence and secondarily by the sub-salt faults. Below the subsided region, the Z3 Stringer is broken into smaller single blocks with lateral displacements that range from 0.5 km to 2 km in a direction perpendicular to the regional strike of S1 (Fig. 4.6). A displacement of 2.1 km is recorded below the hinge of S1. The isolated stringer blocks illustrate flat to gently folded geometries and are surrounded by Z2 and Z3 halite intervals. In the northeast, the salt section is thicker and the Z3 Stringer is more continuous and folded. The presence of continuous reflectors crossing the stratigraphy in areas where the Z3 Stringer is not flat but highly folded or steeply

dipping might confuse the interpretation (marked with arrows in Fig. 4.6a). These are well known to be seismic-processing related artefacts (see more of intra-salt imaging problems in Hale et al. 1992; Bernitsas et al. 1997; Cavalca and Lailly 2005; Jones 2008; Jones and Davison 2014). In the southwest of the profile, some of the fold limbs are not present and instead seismic migration artefacts of curved styles occurred. Two initial assumptions were made to interpret the steeper limbs: (1) fold limbs are structurally broken (Fig. 4.6b) or (2) fold limbs are continuous but seismically not imaged (Fig. 4.6c).
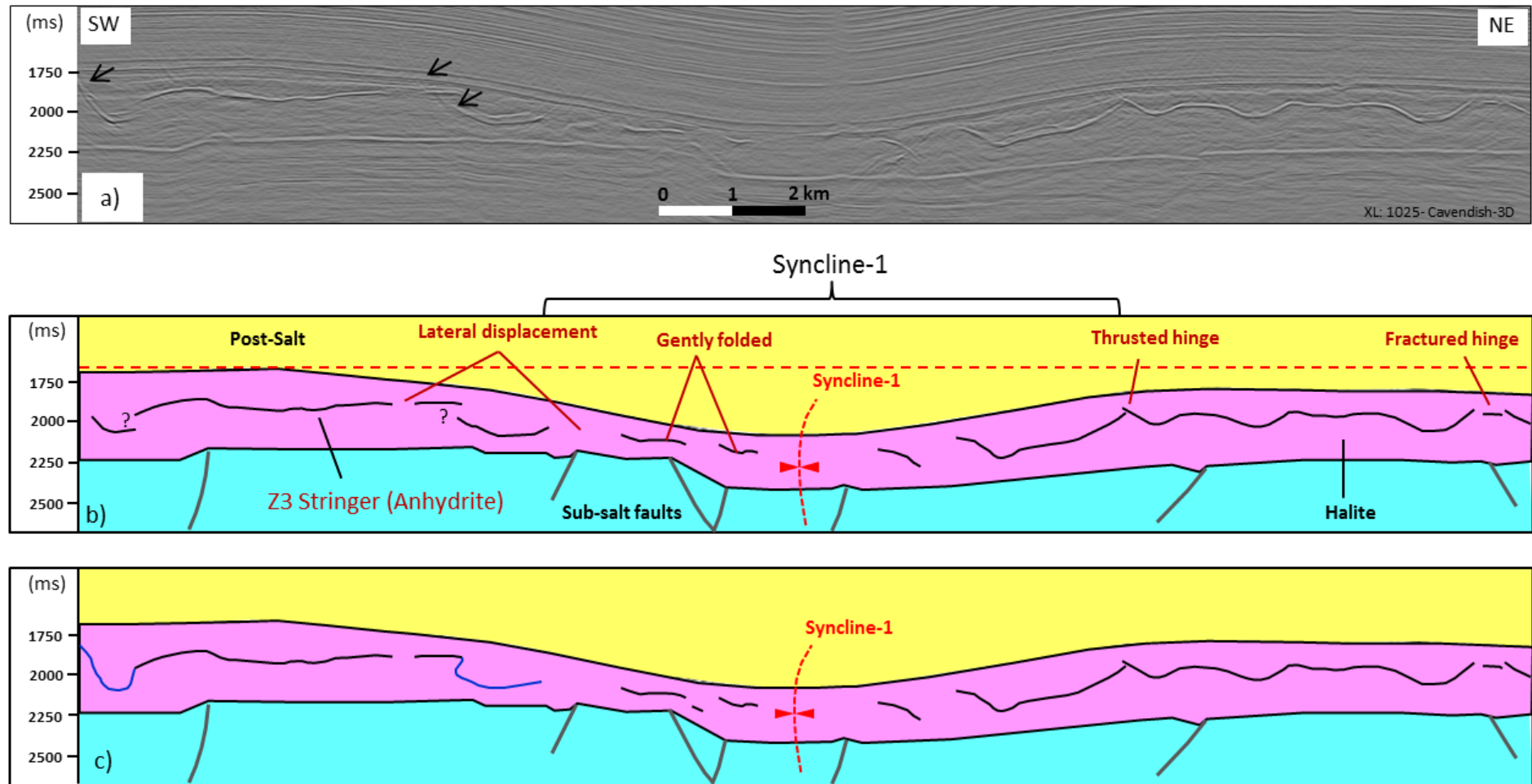
Fig. 4.6: Profile A (see Fig. 4.5b for location). (a) Uninterpreted seismic section intersected the hinge zone of S1. (b) Interpretation of the seismic profile. Note the gaps within folded structures to the left. (c) The continuous interpretation model for steeper discontinuities. Note the two folds to the left interpreted as continuous fold limbs (blue).

Profile B

The profile passes through the depocentre of S1, the centre of A1 in the northeast, and part of A4 in the southwest (Fig.4.7; for location see Fig.4.5b). Below the hinge zone of S1, the Z3 Stringer was broken into 300 m to 2 km of flat to gently dipping fragments with 1 to 2 km lateral gaps in between (Fig. 4.7). The maximum gaps occur at the middle of the hinge zone; however, the space between the broken blocks decreases while moving away from the hinge zone of S1 towards the southwest. Other discontinuities are found below A1 and A4 zones where the Zechstein salt is thick.

Within thicker salt zones, the Z3 Stringer formed well-developed folds (Fig. 4.7a). The dip magnitudes of the stringer below A1 and A4 are much greater than the stringer dips below S1. Stringer discontinuities below A1 and A4 occur at places where fold limbs are expected. These discontinuities can either be interpreted as fractured fold limbs (Fig. 4.7b) or part of seismic imaging limitations, and thus might be continuous or thin below the seismic resolution (Fig. 4.7c).

In a similar way to Profile A, two initial interpretation models have been proposed for interpreting vertical gaps. The first model is the *discontinuous model*, where gaps are interpreted as fractured fold limbs (Fig. 4.7b). The second model is the *continuous model,* where gaps that occur at steep geometries are interpreted as continuous fold limbs by connecting the end parts of the broken syncline hinge with the end parts of the upper fold limbs even though the intervening fold limbs are not imaged (Fig. 4.7c).
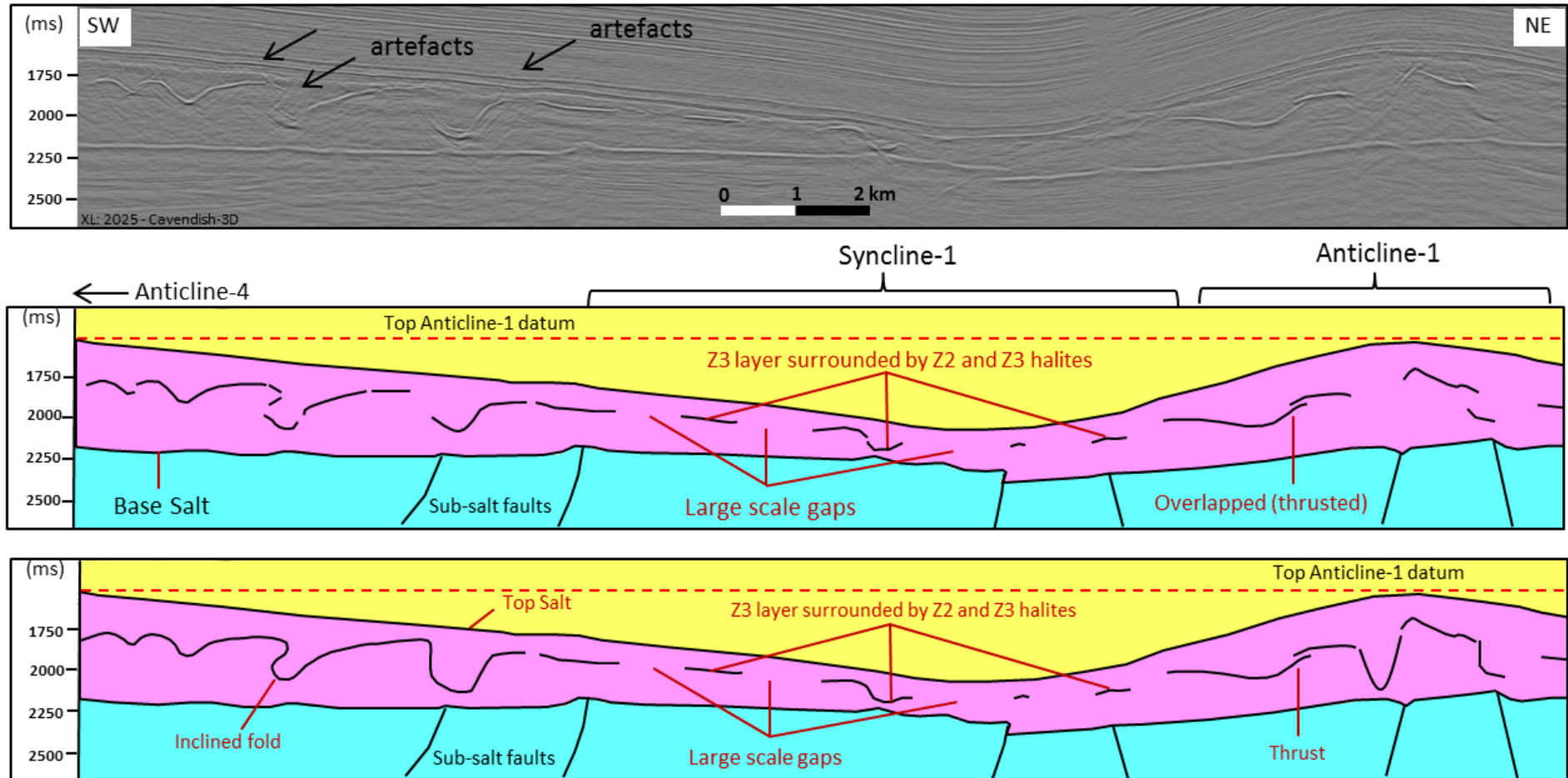
Fig. 4.7: Profile B (see Fig. 4.5b for location). (a) Uninterpreted and (b, c) interpreted seismic section across A4, S1, and A3. Note the long lateral displacement between the stringer fragments and the flat geometry of the broken stringer below the hinge and flanks of S1. (b) The discontinuous interpretation model. Note that stringer interpretation assumes no imaging limitation and that steeper gaps are real gaps. (c) The continuous interpretation model. Note that steeper gaps are interpolated to form syncline structures.

Profile C

The profile passes through the depocentre of S2 in the south, A2 in the middle, and S1 in the northeast (Fig. 4.8). Lateral displacement occurred below the hinge zone of S2. Below the southern flank of S2, the stringer is continuous and gently folded in spite of Top Salt subsidence. S1 is more subsided than S2 (red dashed line in Fig. 4.8b) and therefore extensional-related deformations appear more obvious (Fig. 4.8b). Discontinuities below S1 are more frequent, with extreme flatness of the stringer fragments, which may indicate the amount of stretching applied to the stringer during salt withdrawal phases.

Profile D

The profile passes through S4 and A3 in the western part of the Cavendish survey (Fig. 4.9). Below the hinge zone of S4 to the southwest, the Z3 Stringer is gently folded. However, along the northern flank of S4, the salt section is small and the Z3 Stringer is almost flat and has a similar geometry as the Top Salt. In the areas below A3, the Z3 Stringer is folded and complexly deformed with high seismic noise and migration artefacts where steep reflectors cross the stratigraphy.
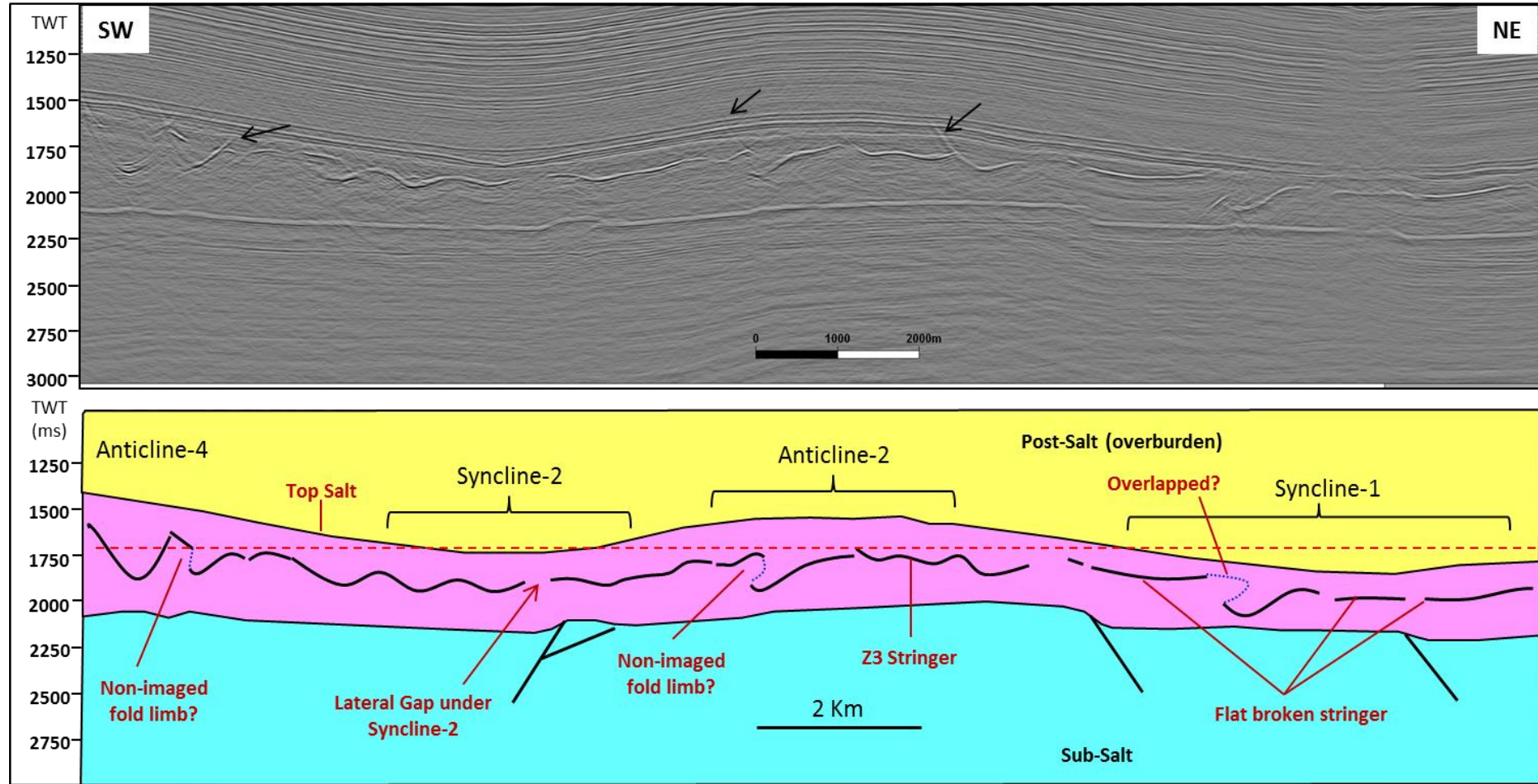
Fig. 4.8: Uninterpreted and interpreted Profile C (see Fig. 4.5b for location). The arrows highlight seismic artefacts. Note the stringer folding below S2 and the lateral gap close to the syncline hinge. Note the flat stringer blocks below S1. Steeper geometries are not picked by seismic data and thus may be continuous (dashed blue lines). The horizontal red dashed line is used to show the difference in subsidence between S1 and S2. Note that S1 is more subsided and thus a smaller salt section exists below; thereby, the S1 exhibits more stretching and lateral displacement than the S2.
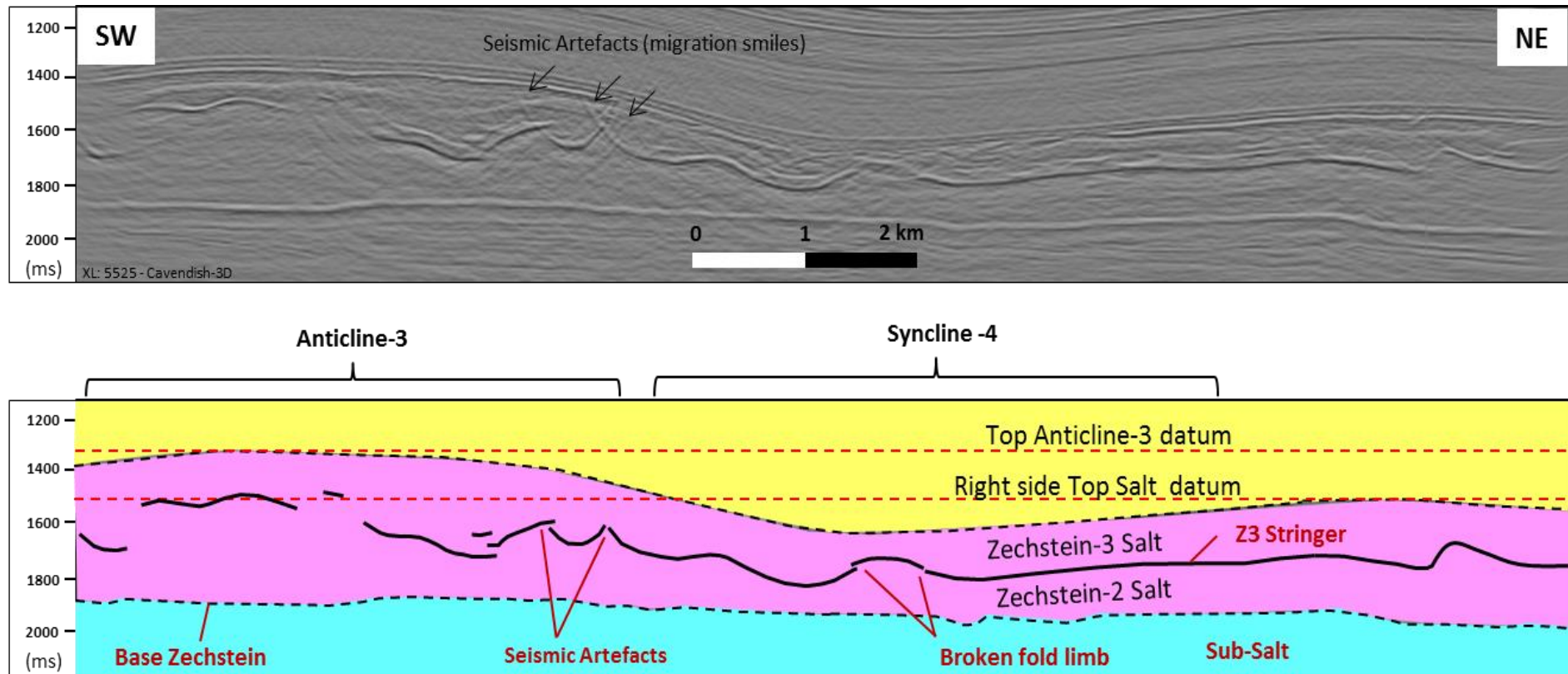
Fig. 4.9: Profile D (for location see Fig.4.5b). (a) Uninterpreted and (b) interpreted seismic profile. Note the behaviour of the Z3 Stringer with respect to the displacement of the Top Salt. From the middle to the right of the profile, the Z3 Stringer is almost parallel to Top Salt. Complex deformation in the form of folding and discontinuities occurred below the hinge of A3 towards the thick salt section in the southwest.

4.3.2 Trent 3D survey

The Trent 3D seismic survey is located a few hundred metres south of the Cavendish survey. The area is also affected by the NW trending sub-salt faults (Fig. 4.10a).

The Top Salt is characterised by a deep NW striking syncline structure (S5) in the middle of the survey and an anticline structure in the southern part (Fig. 4.10b). Along the strike of S5, the Zechstein salt is extremely thinned (Fig. 4.10c) by uplift of basement blocks (Fig. 4.10a) and Top Salt subsidence (Fig. 4.10b). An obvious relationship can be inferred between the salt thickness (Fig. 4.10c) and the displacement between stringers (Fig. 4.10d). Base Salt offsets with Top Salt subsidence strongly correlate with the structure of the Z3 Stringer, where it is observed to be highly fragmented into smaller blocks of 300 m to 5 km in length and widely displaced (Fig. 4.10f). The thick Zechstein salt in the southern part of the Trent survey is characterised by a thick salt section related to Base Salt low and by the formation of the Top Salt anticlines (Fig. 4.10c). Within these zones, the Z3 Stringer is complexly folded, with steeper fragmented geometries (Fig. 4.10e,f). This is discussed in further detail in chapter 5.
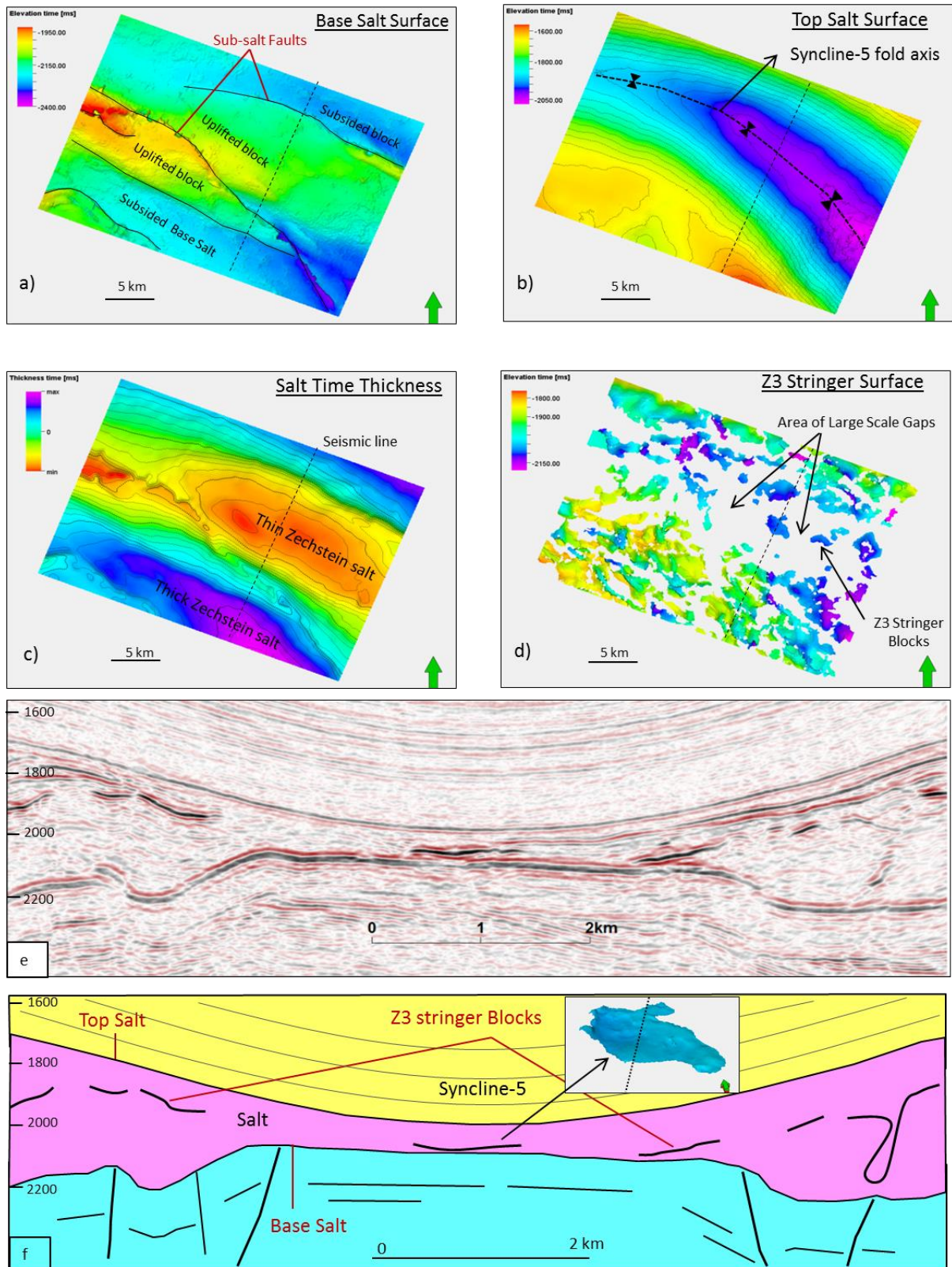
Fig. 4.10: TWT structure maps of the Trent96 survey. (a) Base Zechstein. (b) Top Zechstein. (c) Base Zechstein / Top Zechstein time isochron surface (salt thickness). (d) Z3 Stringer surface. (e–f) Uninterpreted and interpreted seismic profiles show sub-salt, intra-salt, and post-salt structural styles.

4.3.3 SNSJ07 survey

The SNSJ07 seismic survey is located south of the Cavendish area, and part of the survey is merged with the Trent96 survey. Inlines and crosslines strike NE–SW and NW–SE, respectively (Fig. 4.2).

A NE–SW seismic profile was selected to interpret the internal salt structure below S5, A5, and S6 (Fig. 4.2). The amplitude of these folds (S5, A5, and S6) is higher than the amplitude of folds in the Cavendish area. This reflects that the degree of halokinesis in the SNSJ07 area is higher than of that in the Cavendish area. Below the flank of S6, the Z3 Stringer is tilted and laterally displaced parallel to the Top Salt (Fig. 4.11a). Below S5 in the northeast, the salt section is thinned to its minimum thickness and only a single stringer fragment is found below the syncline. However, below A6, the stringer is significantly deformed within the Zechstein salt, which results in poor seismic imaging. Curved discontinuous stringer blocks occur at the upper part of the salt section and are interpreted as anticlinal hinges. Small reflectors are present in the lower part of the salt section, and some are curved upward (Fig. 4.11a). These fragments are interpreted as synclinal hinges. Therefore the whole structure can be interpreted as (1) complex fold structure with fractured limbs (Fig. 4.11b) and (2) folding with continuous limbs (e.g., isoclinal-tight upright folds) (Fig. 4.11c).

The first interpretation is based only on what is directly imaged on seismic data. The second scenario considers the limitations of seismic imaging and integrates structural examples from salt mines (e.g., Schléder et al. 2008) (Fig. 4.11a,b) or surface piercing salt domes (e.g., Seidle 1921) (Fig. 4.11d) where anhydrite stringers were folded within the salt section with isoclinal tight folds.
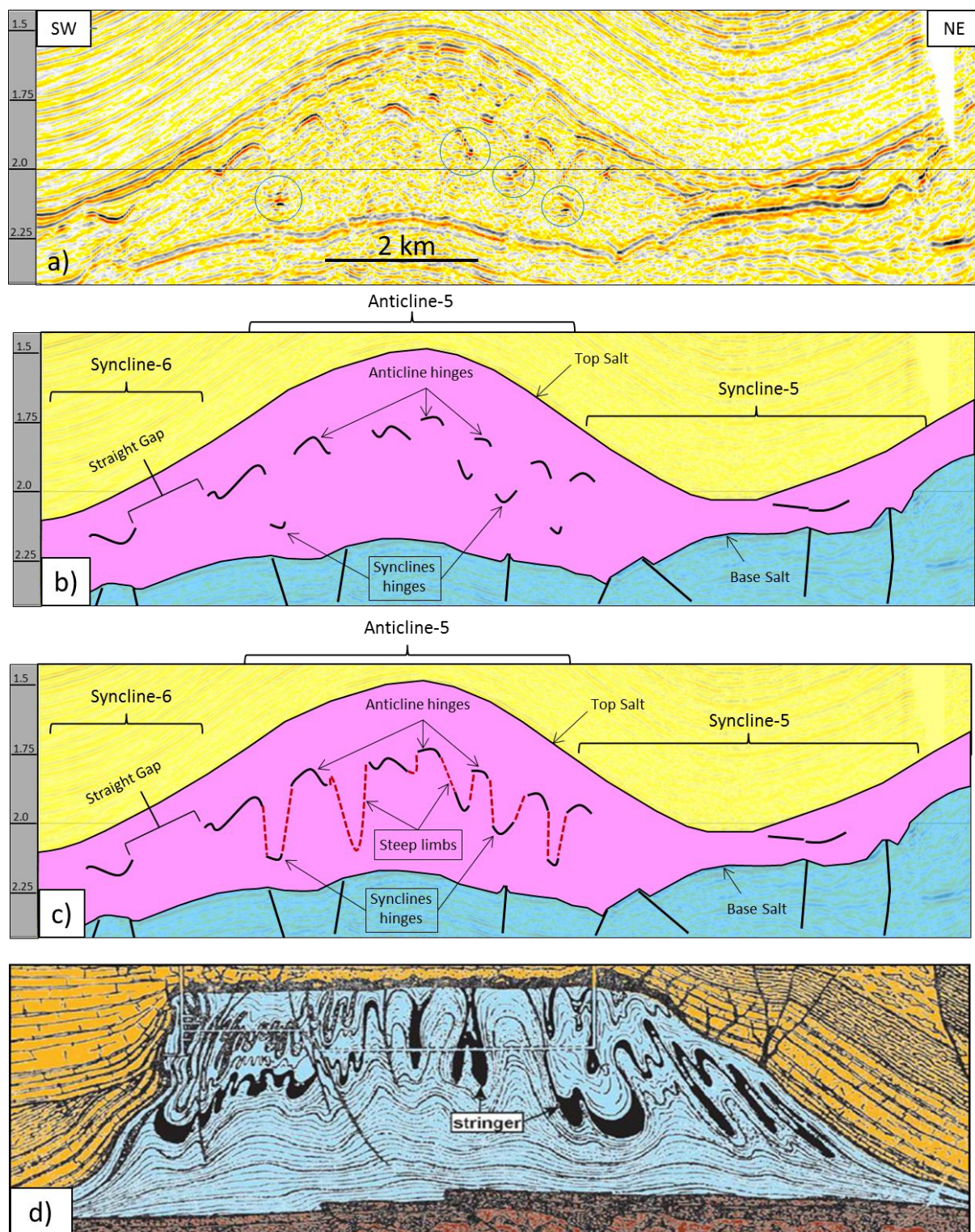
Fig. 4.11: (a) Seismic profile perpendicular to the overburden structure of the Snsj07 survey (see Fig. 4.2 for location). Z3 Stringer interpretation below A5. (b) The Z3 Stringer is highly fractured into fragments located at higher and lower depths. (c) The Z3 Stringer is mapped as a continuous folded layer. (d) Case study of internal Zechstein deformation through a salt dome (after Seidle 1921). Note the continuity of the stringer and the complexity of folding.

4.4 3D description of Z3 Stringer under major synclines

Regions that subsided below S1 and S5 were selected to study the three-dimensional strain of the Z3 Stringer. These areas are characterised by significant Top Salt subsidence and a highly thinned salt section, which consequently results in Stringer fragmentation and displacement with salt flow.

4.4.1 3D description of Z3 Stringer below S1

The region of extensional-related deformation of the Z3 Stringer below S1 is an area of about 10 km in width and more than 40 km in length along the strike and the flanks of S1 (Fig. 4.12). For a better description of the structural style of the stringer compared with post-salt geometry, the Z3 Stringer surface was superimposed with the Top Salt surface in order to understand the influence of the regional structure on the stringer deformation (Fig. 4.12a). The zone of maximum displacement occurs at the middle of S1 and strikes parallel to its fold axis (Fig. 4.12). The stringer has lateral large scale discontinuity (LLSD) along the hinge zone of S1 and lateral smaller scale displacements (LSSD) at a greater distance from the hinge zone, normally below the flanks of the regional syncline. The edges of the fractured Stringer are oriented NW, similar to the S1 fold axis. Stringer blocks surrounded by Z2 and Z3 salt are scattered along the zone of S1. The 3D stringer surface displays flat to shallow-dipping stringer blocks within the thin salt section. Folds are well-developed below the flanks of the regional syncline away from the hinge zone of S1. Two groups of folds occurred below the two flanks of S1, and they are opposite in both curvature and vergence (Fig. 4.12b). In map view, the fold axes are arcuate and convex outwards from the strike of S1. Fold vergence has been observed below the two flanks of the regional syncline where longer fold limbs (LFL) occur close to the regional structure and shorter fold limbs (SFL) form behind it (Fig. 4.12b).
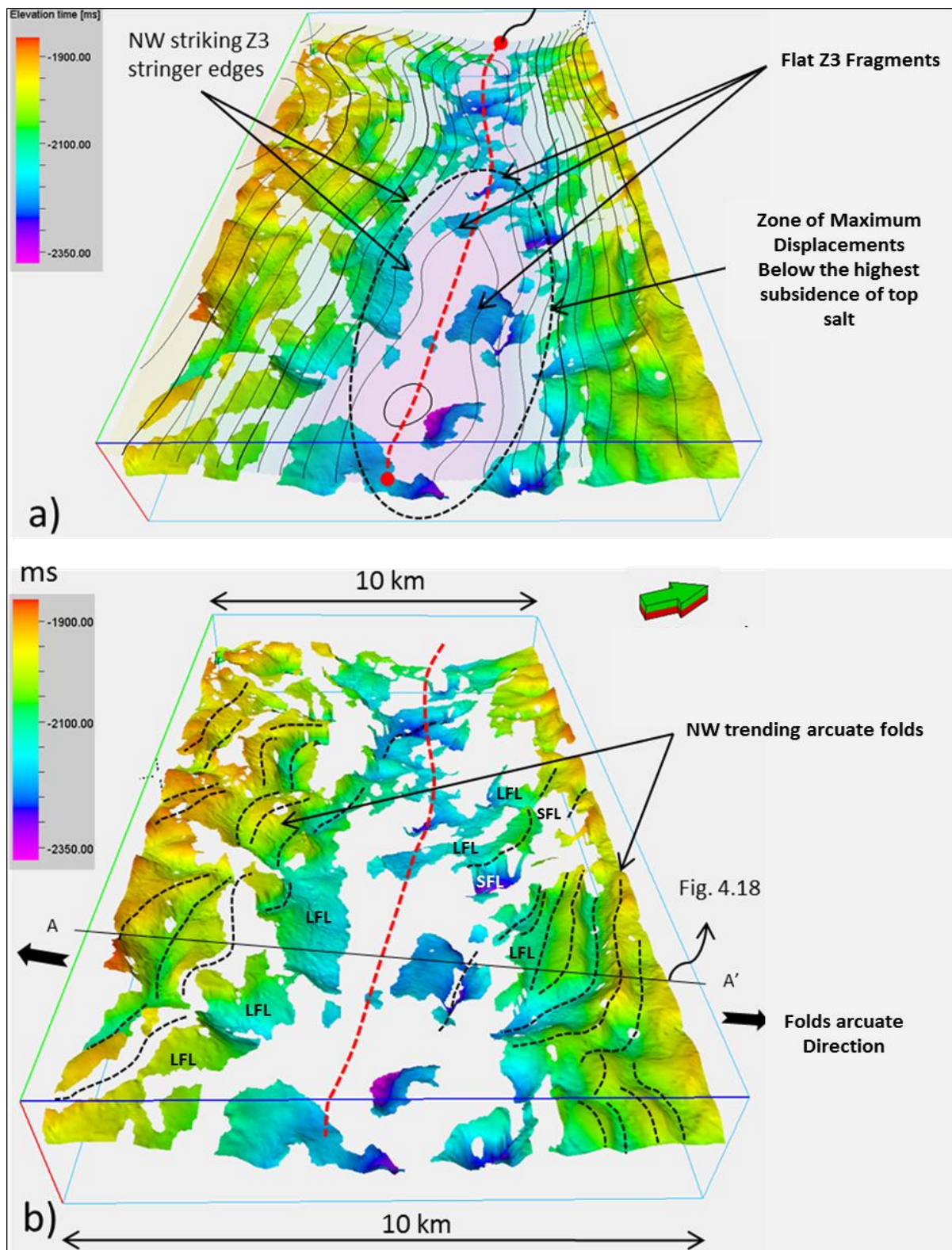
Fig. 4.12: Selected area below S1. (a) 3D autotracked (non-interpolated) Z3 Stringer surface superimposed with Top Salt topography displayed as contours. (b) Interpretations of (a). The strike of stringer fold axes below the flanks of S1 and the edges of the discontinuous blocks follow the same trend of the S1 fold axis. Note the opposite curvature direction of the two group of folds at the two sides. Note the vergence of the folds where the long fold limbs (LFL) are close to the regional syncline while the shorter fold limbs (SFL) are the ones behind.

4.4.2 3D description of Z3 Stringer below S5

Base Salt and Top Salt surfaces are superimposed with the Z3 Stringer surface in order to analyse the internal structure within the regional context (Fig. 4.13). Three regional structural elements can be identified based on the selected area. The thin salt section in the middle was the result of both S5 subsidence and uplift of the sub-salt horst structure (Fig. 4.13a). Two thick salt sections at the sides of the Trent survey form the other two structural elements in the region and are created by sub-salt graben structures and top salt thickening. The Z3 Stringer is largely fractured and laterally displaced within the thinned salt area. The stringer blocks have variable sizes and irregular boundaries. The 3D display shows flat blocks occur along the hinge zone of S5. However, complex folding with steep geometries occurs within the thick salt areas. A summary of the structure styles is shown in Fig. 4.13.

4.4.2.1 Geometrical measurements of the stringer fragments

Twenty stringer fragments were selected from the area below S5 (Fig. 4.14) for simple measurements of strike, length, width, and aspect ratio. The average length of the selected stringer blocks is 1408 m, and their average width is 463 m, with maximum and minimum lengths of 4046 m and 289 m and maximum and minimum widths of 1330 m and 200 m, respectively (Table 4.1). The maximum and average length/width of the fragments is 7.6 and 3.4, respectively, reflecting the predominantly elongated shapes of the fragments. The orientation of each block is the strike of the long axis drawn from the end parts of the fragment. The results show an average strike of 110° (Fig. 4.14 and Table 4.1). This strike is almost parallel to the regional S5 axis (~115°). By plotting strike readings of the fragments against their lengths, a direct relationship is found. Fragments which are more elongated (higher L/W, Table 4.1) tend to have a strike range between 90° and 120°, while less

elongated fragments have variable trends (Table 4.1). This suggests that elongated stringers have better orientation with the regional structure and almost sub-parallel to the S1 axis.

The stringer thickness in wells 43/19-2 (T1) and 43/19-1 (T2) is 23 m and 63 m, respectively. The average aspect ratios (W/T1 and W/T2) of these thicknesses are 21.1 and 7.3. Experiments on boudinage deformations show that thick layers have wider boudins than thin layers which tend to have smaller widths. Typical characteristic aspect ratios of boudins fall in the range of 2 to 4, and further layer-parallel extension will only increase the separation and displacement between the broken boudins (Fossen 2010). The reason for the bigger aspect ratios of the Z3 Stringer can be related to the uncertainties of its thickness (see chapter 3) or to the ductile behaviour of the anhydrite in the subsurface.
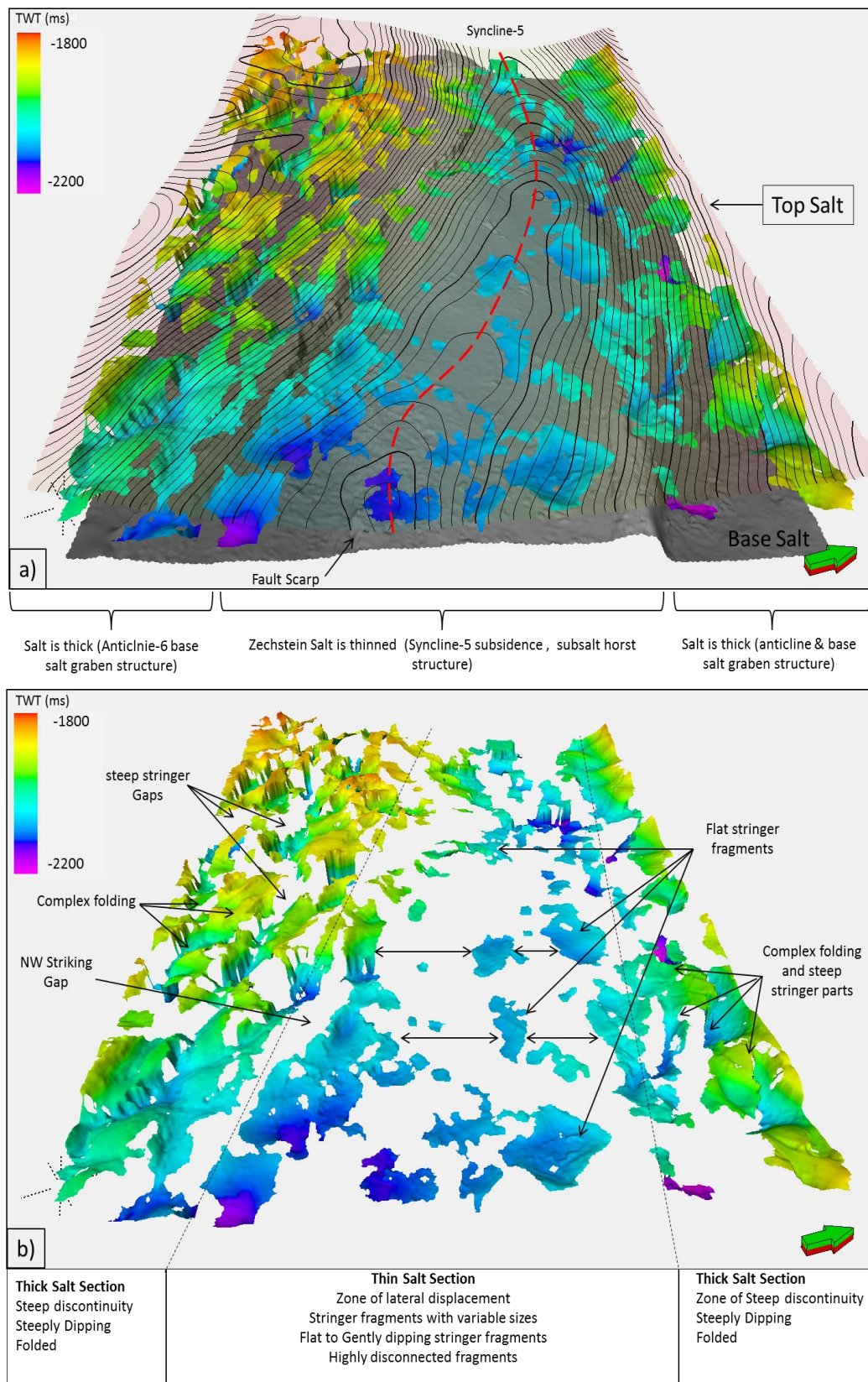
Fig. 4.13: Z3 Stringer time surface superimposed with top and base Zechstein. Note the alignments of S5 and sub-salt blocks. (b) Annotated Z3 Stringer surface. Note that the stringer blocks in the middle are almost flat. Complexity and shortening increase away from the centre to the sides of the study area where the Zechstein salt is thick. The horizontal extent of the surface is 10 km.
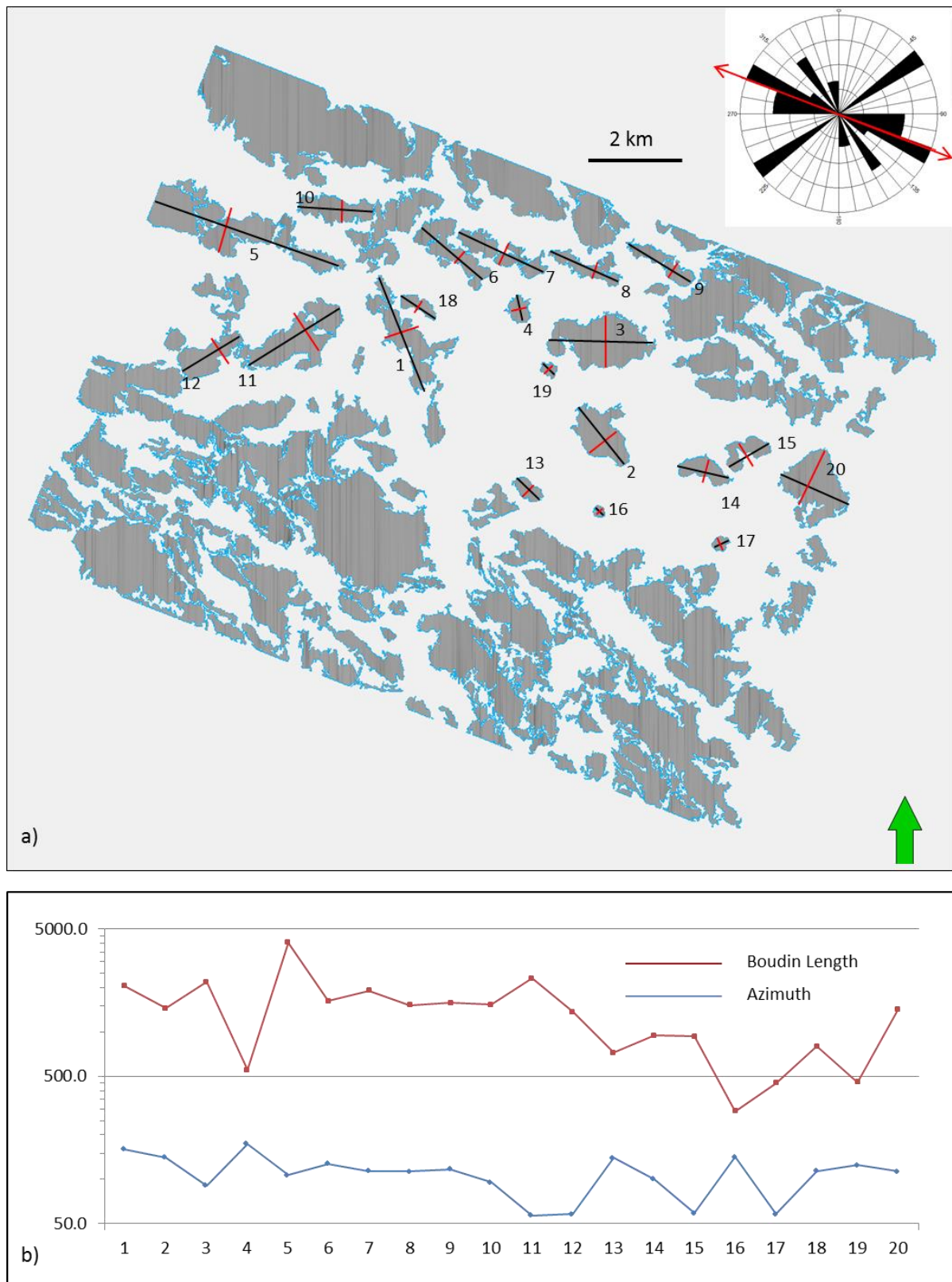
Fig. 4.14: (a) Trent96 map shows the Z3 Stringer blocks used for strike, length, and width measurements. The strikes are measured based on the longer diameter, which has been drawn by connecting the end parts. The width is calculated perpendicular to the length diameter. A mean strike of 110 is measured. (b) The strike vs. length of the fragments shows longer fragments tend to have strike close to the average.

Table 4.1: Geometrical measurements of 20 stringer fragments below the area of S5. (L) is the length of the fragments, (W) the width, (T1) the thickness of the Z3 Stringer from well 43/19-2, (T2) the thickness of the stringer from well 43/19-1, (L/T1) and (L/T2) are length divided by thickness, (W/T1) and (W/T2) are the aspect ratios based on the two thicknesses.

Blocks	Azimuth	L (m)	W (m)	T1 (m)	T2 (m)	L/T1	L/T2	W/T1	W/T2	L/W
B1	160.0	2050	558	23	63	89.1	32.5	24.3	8.9	3.7
B2	141	1447	673	23	63	62.9	23.0	29.3	10.7	2.2
B3	91	2189	1089	23	63	95.2	34.7	47.3	17.3	2.0
B4	174	553	353	23	63	24.0	8.8	15.3	5.6	1.6
B5	107	4046	565	23	63	175.9	64.2	24.6	9.0	7.2
B6	127	1627	250	23	63	70.7	25.8	10.9	4.0	6.5
B7	114	1907	400	23	63	82.9	30.3	17.4	6.3	4.8
B8	113	1524	200	23	63	66.3	24.2	8.7	3.2	7.6
B9	117	1575	250	23	63	68.5	25.0	10.9	4.0	6.3
B10	95	1535	441	23	63	66.7	24.4	19.2	7.0	3.5
B11	57	2308	522	23	63	100.3	36.6	22.7	8.3	4.4
B12	58	1372	424	23	63	59.7	21.8	18.4	6.7	3.2
B13	140	723	336	23	63	31.4	11.5	14.6	5.3	2.2
B14	100	950	450	23	63	41.3	15.1	19.6	7.1	2.1
B15	59	932	250	23	63	40.5	14.8	10.9	4.0	3.7
B16	142	289	260	23	63	12.6	4.6	11.3	4.1	1.1
B17	58	450	292	23	63	19.6	7.1	12.7	4.6	1.5
B18	114	801	311	23	63	34.8	12.7	13.5	4.9	2.6
B19	125	457	297	23	63	19.9	7.3	12.9	4.7	1.5
B20	113	1433	1330	23	63	62.3	22.7	57.8	21.1	1.1
Average	110	1408	463	23	63	61.2	22.4	20.1	7.3	3.4
Max		4046	1330	23	63	175.9	64.2	57.8	21.1	7.6
Min		289	200	23	63	12.6	4.6	8.7	3.2	1.1

4.5   3D description of the Z3 Stringer within thick salt sections

In areas where the salt section is thick and Top Salt forms well-developed anticline structures (e.g., below A3, A4, and A5), the stringer inside the salt section tends to be highly folded, with steeper fold limbs. In most cases, steep stringer parts are not well-imaged on seismic data due to seismic processing limitations (van Gent et al. 2011; Strozyk et al. 2012). This type of discontinuity is very common in the study area. It is characterised by seismically chaotic areas, including seismic artefacts such as smiles and crossing reflectors, between visible stringer fragments (e.g., Fig. 4.11a).

4.5.1 Interpretation workflow for steep discontinuities

The Stringer horizon probe (Fig. 4.15a) and the autotracked Stringer surface (Fig. 4.3a) are highly discontinuous stringer surfaces from both geological and seismic processing related discontinuities. The common style of steep related discontinuities is characterised by gaps located between visible syncline hinges at the bottom and part of the upper fold limbs at the top (Fig. 4.15a). Petrel was used to fill the gaps by connecting the end points of the structure using the interpolation technique to develop an interpolated surface of the Z3 Stringer (Fig. 4.15b). Dip magnitude and RMS amplitude surfaces were generated from the interpolated surface.

The dip at which steeper stringer segments were found to be absent was determined both on profiles and on the 3D surface (Fig. 4.15c). In a 1:1 scale, this dip was measured to be 45°± 2°. By merging the Stringer horizon probe-extracted surface over the 3D time dip surface, the gaps that occur in areas of high dip (>45°) are discriminated from those that form at shallower dips (<45°). If the dip of stringer discontinuities is found shallower than 45°, the gaps are interpreted as structural

discontinuities. However, if the gaps occur at more than the critical dip, then the stringer discontinuity is likely related to local seismic imaging and the interpretation is less confident.
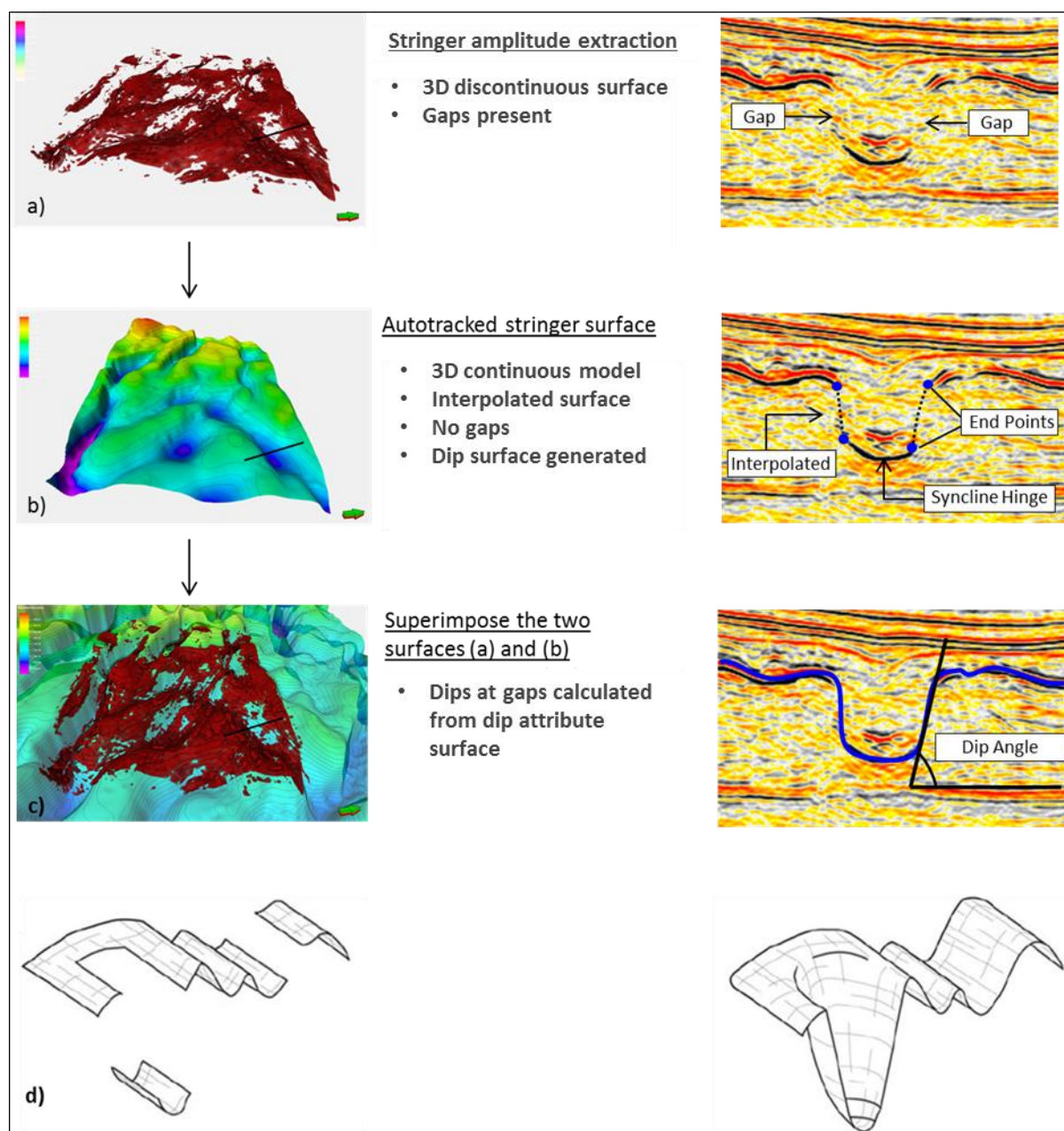
Fig. 4.15: Workflow to resolve the vertical gaps that form between visible stringer fragments. (a) Amplitude extraction of the Z3 Stringer. (b) Interpolated Z3 Stringer surface. (c) Amplitude extraction surface superimposed with the interpolated surface. (d) Sketches of possible end-member scenarios for the steep discontinuities. The first (left) shows fracturing of the stringer and a subsequent displacement of the fragment by vertical flows in the salt. The second (right) shows a continuous stringer with steeply inclined fold limbs which are seismically not resolved because of the thin and steep fold limbs.

4.5.2 Interpretation within selected areas

Two areas below A1 (Fig. 4.16a,b) and A5 (Fig. 4.16c,d) were selected to analyse and interpret discontinuities that occur at steep parts of the Z3 Stringer. RMS seismic amplitude, surface probe, and dip angle seismic attributes were generated from the interpolated surface of the Z3 Stringer to detect the locations of discontinuities and their dip magnitudes. By superimposing the 3D RMS seismic amplitude surface with the 3D surface probe, the areas of zero amplitude are located at steep parts of the stringer (Fig. 4.16a). However, gently dipping fold limbs, syncline hinges, and anticline hinges are continuous and well-imaged (Fig. 4.16a,b). Another area has been selected for RMS seismic amplitude (Fig. 4.16c) versus dip angle attribute (Fig. 4.16d). By comparing the dip angle surface with the seismic amplitude of the Z3 Stringer, the dip in areas of discontinuities can be determined.

The result shows a relationship between the distribution of the discontinuities and their dip magnitudes. The discontinuities are mainly located at steeper fold limbs (>45°), and most of high dip magnitudes are associated with minimum to zero seismic amplitudes (Fig. 4.16c,d). In contrast, the well-imaged areas of the Z3 Stringer fall within areas of shallower dips. The dip angle of the interpolated surface of the Z3 Stringer can then be used to differentiate between gaps that occur at steeper dips from those that occur at shallower dips.
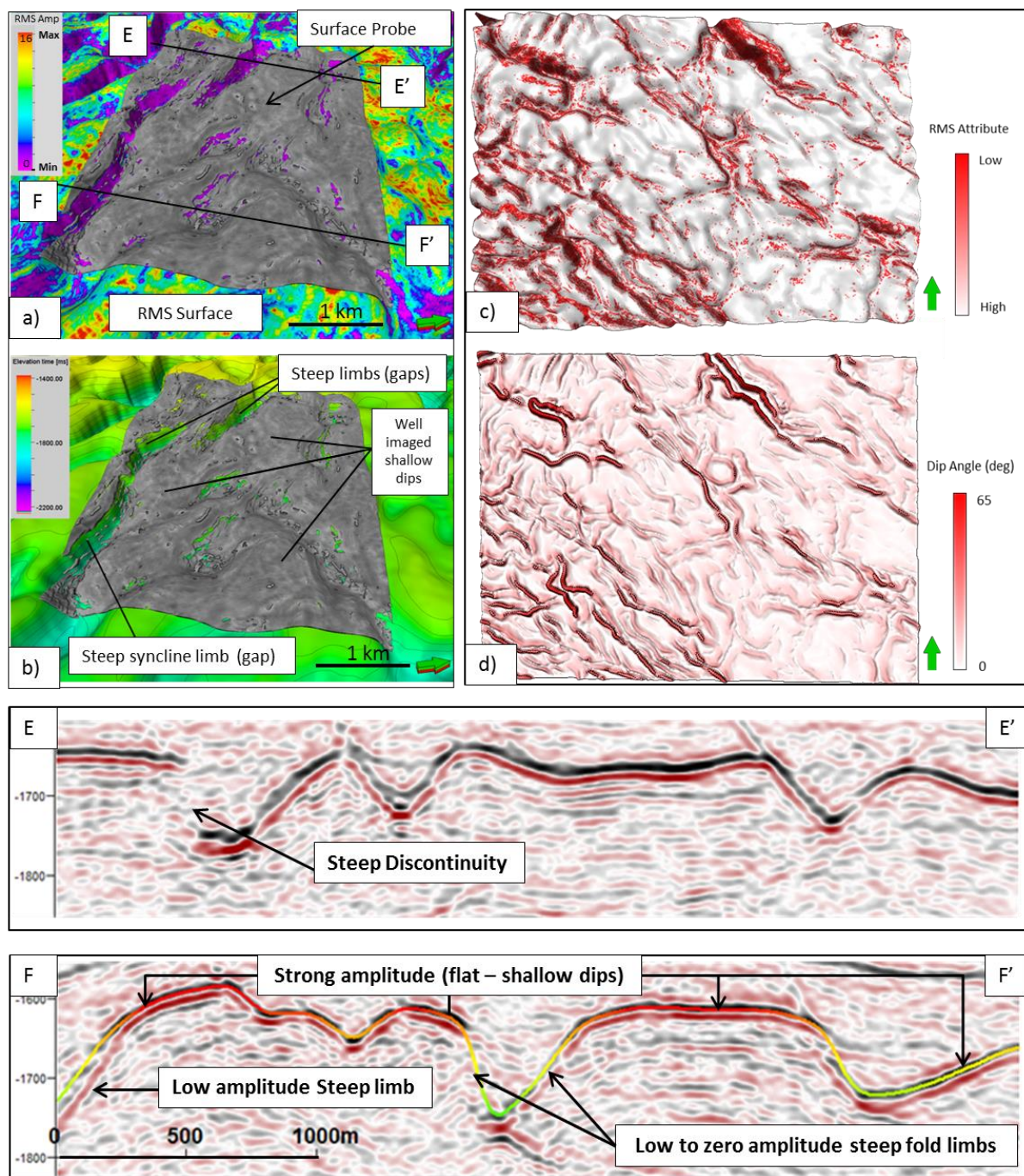
Fig. 4.16: The two areas selected for analysis of steep discontinuities of the Z3 Stringer (Area 1: a,b and Area 2: c,d). **Area 1**: (a) The 3D geobody surface probe (grey) represents the Z3 Stringer reflection amplitude and is superimposed with Stringer RMS amplitude surface (coloured surface) to detect amplitude strength and weakness. The purple colour represents zero seismic amplitude (gap), and red, maximum seismic amplitude. (b) The surface probe superimposed with the interpolated stringer surface. **Area 2**: (c) RMS amplitude surface displayed on the 3D stringer surface. (d) Stringer dip angle surface. (e,f) Profiles show that steeper dips are associated with low to zero seismic amplitudes (discontinuities), whilst shallow dips have higher amplitudes and thus good continuity.

4.6   Discussion

4.6.1 Interpretation of Z3 Stringer discontinuities

The discontinuities of the Z3 Stringer will be discussed in two contexts:

1. Within shallow stringer dips in areas below subsided Top Salt. These discontinuities include lateral large-scale and small-scale discontinuities. Their discussion will lead to the understanding of the salt dynamics and flow behaviour in areas of salt-induced subsidence, as well as the kinematic evolution of the stringer (including the timing of deformation and the geometrical evolution).

2. Within vertical stringer geometries in areas below Top Salt anticlines. The discussion of this part will contribute to the interpretation of Z3 Stringer discontinuities that have not been resolved on seismic data.

4.6.2 Lateral large-scale discontinuities below S1 and S5

The lateral large-scale discontinuity of the Z3 Stringer largely occurs in areas below S1 and S5 where Top Salt exhibits a large magnitude of subsidence (Fig. 4.12 and Fig. 4.13). Visible stringer fragments which are distributed within these areas are characterised by shallow dip magnitudes and displacements of 1–4 km. The shallow dip magnitudes are contradictory to the notion of seismic limitations that could be produced by steep reflections (Sleep and Fujita 1997; Shan and Biondi 2008; van Gent et al. 2011; Zhuo and Ting 2011; Strozyk et al. 2012; Jones and Davison 2014). Therefore, the fragments of the stringer below the regional extensional areas of S1 and S5 are interpreted as large-scale boudin structures formed by lateral extensional forces induced by the lateral flow of Z2 and Z3 halite away from the synclinal areas.

141

The occurrences of these large-scale displacements along the hinge zones of the major synclinal structures is an indication of large-scale diverging salt flow in a direction perpendicular to the strike of the elongated major synclines (Fig. 4.17b). Since the large displacements of the stringer were recorded along these regional synclines, the subsided Top Salt synclinal hinge, where the salt section appears thinned below, is the place where the salt starts flowing and diverging (Fig. 17c,d). The strike of the elongated fragments within the hinge zone of S1 supports this interpretation (Fig. 4.12 and 4.14a).

Additionally, the opposite curvature and vergence of the two fold groups below the flanks of S1 (Fig. 4.12b and Fig. 4.17b) provide evidence for two opposing flow directions with variable rates that may have largely relied on the subsidence magnitudes along the strike of S1 (see Fig. 4.12a). The curvature of the fold axis of an individual fold in plan view (Fig. 4.17b and Fig. 4.12b) has been interpreted to be related to the variable speed of salt flow. Highly subsided zones along the strike of the regional syncline would be expected to generate higher flow with higher speed, and consequently the stringer is folded with a curved axis and obvious vergence (Fig. 4.17c). However, such curvature and vergence are not found at the flanks of Syncline 2.

Top Salt-induced subsidence at S2 and S4 is considered to be low to moderate compared to S1 and S5 (Fig. 4.8 and Fig. 4.2). The stringer below S2 shows fold structures and small-scale lateral extensional displacements with no evidence of isolated individual fragments (Fig. 4.18c). Similarly, the stringer shows flat to gently folded geometry below S4 (Fig. 4.18d). This suggests a relationship between the amount of Top Salt subsidence and the degree of fragmentation of the stringer. A

similar result was found by geomechanical modelling of a non-Newtonian viscous salt with an embedded brittle elastic-plastic single stringer subjected to variable top salt displacement magnitudes (Li et al. 2012a) (Fig. 4.17e).

The elongated structure of the Top Salt synclines, which have been interpreted to be formed by regional buckling of the basin (see chapter 3), suggests that the extensional mechanism applied to internal salt structures below the regional synclinal hinge zone areas (S1, S5) is uniaxial extension (Fig. 4.17d). In this case, one strain component (e.g., ε_{xx}, perpendicular to the S1 axis) is more dominant than the other (e.g., ε_{yy}, parallel to the S1 axis). This is possibly supported by the close relationship between the mean strike of the long axes of the fragments and the strike of the regional structure (Fig. 4.14a and Table 4.1).

Similar approaches have been used in DEM numerical modelling (e.g., Abe et al. 2013) and analogue experiments (Kettermann 2009). However, isotropic layer parallel extension (pure flattening $\varepsilon_{xx} = \varepsilon_{yy}$) might be expected to occur below salt structures that resulted from differential loading, in particular where minibasins of spherical shape (e.g., Jackson et al. 2015) create multidirectional strain within the salt section, resulting in radial fracture propagation similar to chocolate tablets, as described experimentally by Ghosh (1988) and Zulauf et al. (2011). The deformation style of the Z3 Stringer below the elongated Syncline 1 and Syncline 5 could be compared with the stringer's deformation below circular minibasins in the South Oman Salt Basin (see chapter 7). This summarises the effect of regional salt tectonics on the intra-salt deformation, geometry, and style in areas of salt subsidence.
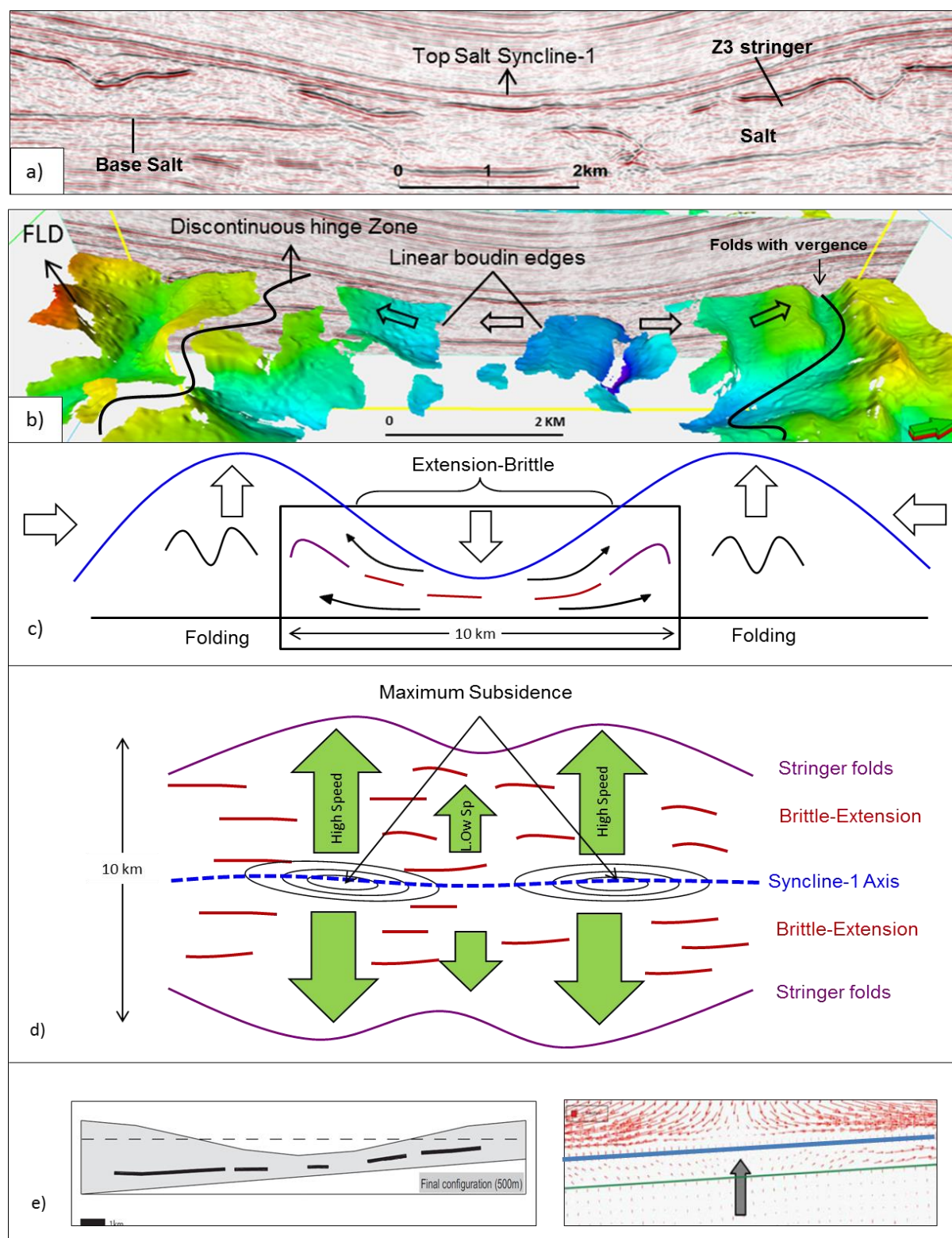
Fig. 4.17: (a) Representative seismic profile across S1 (see Fig. 4.12b for location, A-A') illustrating the large-scale displacement of the Z3 Stringer and the boudinage structure. (b) Superimposed with 3D stringer surface. (c) Simplified cross-sectional sketch of (a,b). (d) Simplified map view sketch of the flow direction and the formation of the opposite fold curvatures. (e) Numerical results after Li et al. 2012a. (Right) boudinage of competent stringer by downward Top Salt subsidence. (Left) Diverging flow below the subsided region.
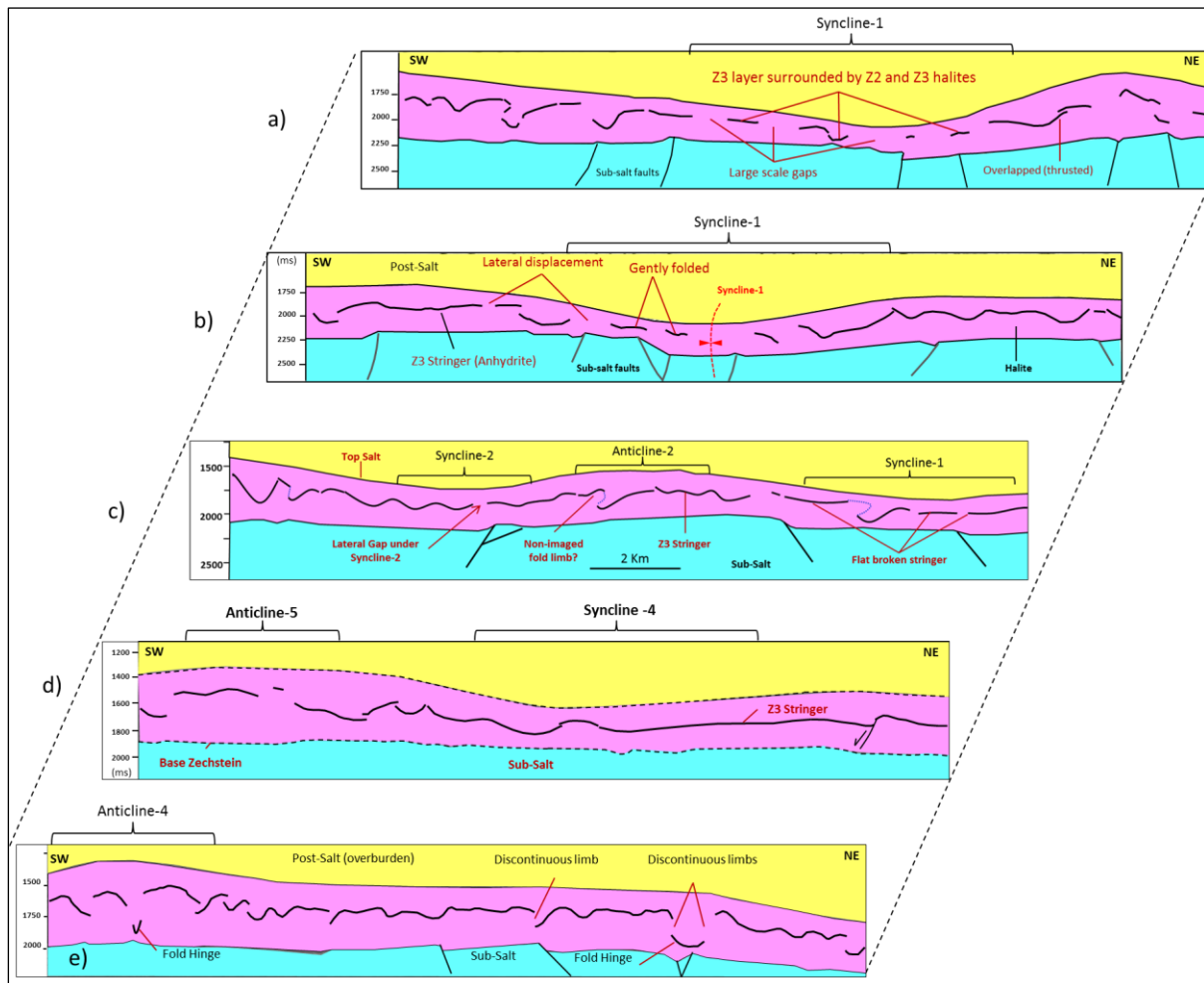
Fig. 4.18: Stringer structural style with progressive Top Salt subsidence and thickness change. Subsidence and salt thickness within major synclines increase from bottom (e) top to top (a). Note the change of the stringer structural style by the change in salt thickness and subsidence rate. Lateral displacement is associated with thinning of the Zechstein (e.g., a, b) whereas folds are formed in areas of non-subsided and thick (anticlines, pillows) salt sections (for locations see Fig. 4.5b).

4.6.3 Lateral small-scale discontinuities (LSSD)

The lateral displacement of the stringer was observed to decrease when moving away from areas of high subsidence. Profiles across S1 revealed lateral small-scale discontinuities (LSSD) with visible displacements of less than 500 m largely occur below the flanks of the regional synclines. These small discontinuities can occur within flat or gently folded stringer geometries (Fig. 4.19a). The morphology of the fracture patterns is either sharp linear boundaries (Fig. 4.19b), triple junctions with angular boundaries (Fig. 4.19c), or en echelon-like structures (Fig. 4.19d).

On 2D profiles (e.g., Fig. 4.19a), the stringer fragment seems to be isolated and could be interpreted as a boudinage structure that either formed simultaneously or was reworked during progressive deformational events. In map view, however, the majority of the LSSD gaps do not fragment the stringer into isolated parts. The gaps are either branched from the LLSD zone or form separately hundreds of metres away (Fig. 4.20a, b). The LSSD can either strike parallel, oblique, or perpendicular to the major syncline axis (Fig. 4.19b,c,d and Fig. 4.20c).

The shorter lengths and multidirectional strikes of the LSSD have been interpreted to be related to (1) the speed and rate of salt flow decreasing away from the source layer and the S1 axis, and thus resulted in smaller displacements away from the maximum subsidence zone with randomly oriented fractures that are not perpendicular to the main extension direction (Fig. 4.19d); and (2) the influence of an opposite flow generated from an adjacent regional structure, (e.g., Jackson 1985; Talbot and Jackson 1987; Hudec and Jackson 2007; Hudec et al. 2009; van Gent et al. 2011), which might reduce the withdrawal salt flow that comes from S1 and create multidirectional flow.
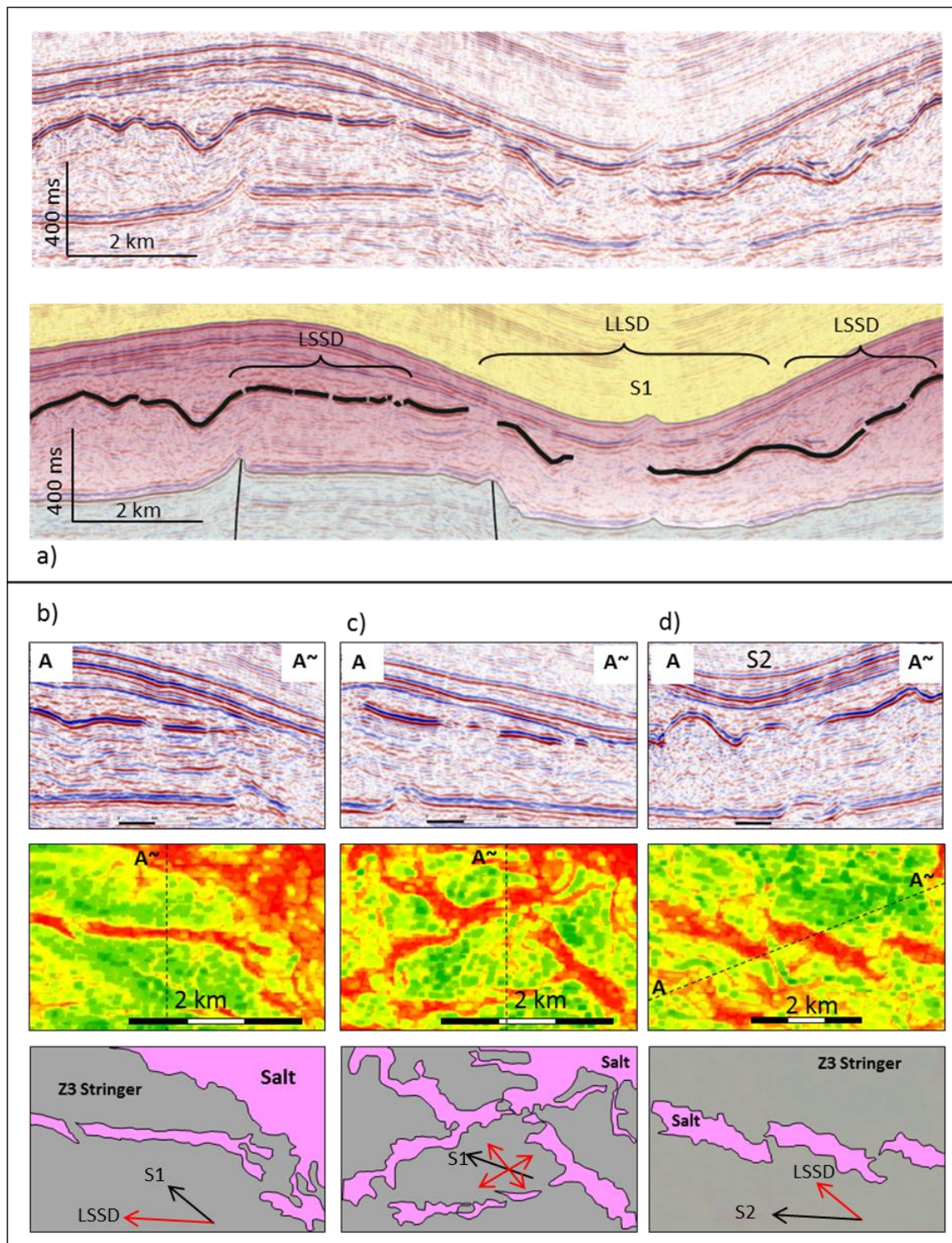
Fig. 4.19: (a) Uninterpreted and interpreted seismic profiles across S1 show the distribution of LSSD. Note that LSSD form below the flanks of the regional syncline, within a flat (left) or folded stringer geometry (right). (b,c,d) LSSD morphology (see Fig. 4.20a for regional location). (b) Linear LSSD of 400 m width and 3 km length oblique to the major syncline axis (S1). (c) Connected triple junction with major NE and NW strikes. (d) En echelon style oblique to the S2 axis.
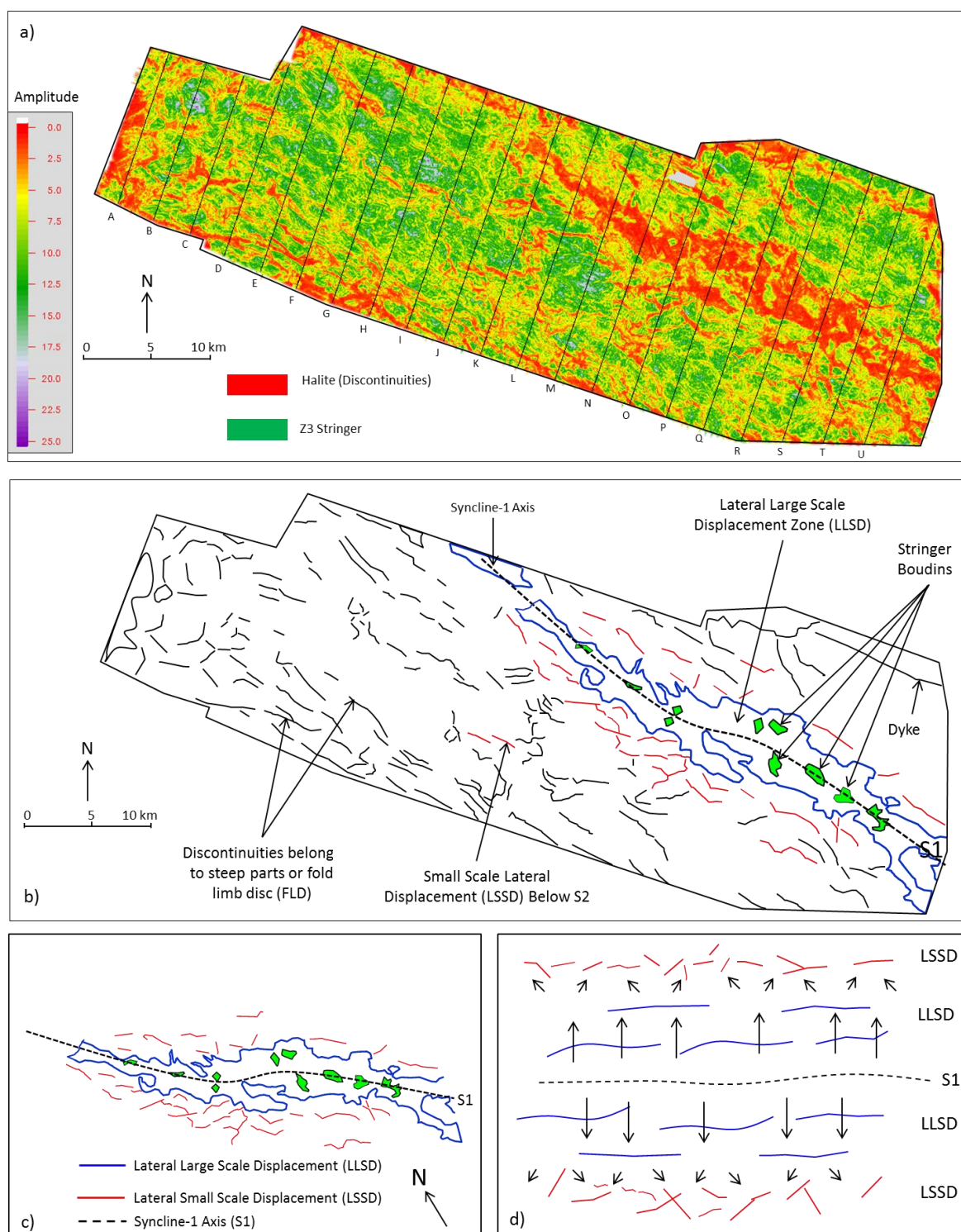
Fig. 4.20: Summary structural map of the Cavendish area showing discontinuities. (a) Acoustic amplitude surface of the Z3 Stringer shows discontinuities (in red). (b) Interpretation of discontinuities. Three main types of discontinuities were annotated: large-scale lateral displacements (LLSD), small-scale lateral displacements (LSSD), and steep stringer discontinuities or fold limb discontinuities (FLD). (c) LLSD and LSSD below the S1 area. (d) Conceptual sketch explaining strike variability of the LSSD related to the speed of the flow. Long arrows represent higher-speed salt movement, while short arrows, lower-speed salt movement.

4.6.4   Timing of Z3 Stringer brittle and boudinage deformation

Boudinage structures within salt deforming layers have been extensively discussed in the literature (Borchert and Muir 1964; Burliga 1996; Davison 1996; Smith 1996; Schléder et al. 2007; 2008; van Gent et al. 2011; Strozyk et al. 2012; Strozyk et al. 2014). Two models are suggested herein for the timing of the initial stringer brittle-boudinage structures for the dominated anhydrite Z3 Stringer:

Model 1: Early-stage boudinage before salt tectonics

This model suggests that the stringer has been frequently ruptured during early stages by one of the following mechanisms (Fig. 4.21a):

(a) The overburden above the stringer creates compaction at stresses that are sufficient to break the stringer before any salt tectonics.

(b) A high viscosity contrast between the stringer and the incompetent salt allows the stringer to collapse and boudinage with no lateral stretching (Bons et al. 2004) (Fig. 4.22f).

(c) There was an early syndepositional gravity gliding of the salt (Strozyk et al. 2014). Such structures then intensively deform during salt tectonics by folding within areas below synclines where salt is shortened and widely displaced by extensional deformation.

Model 2: Late-stage boudinage after salt tectonics

Alternatively, the stringer experiences brittle deformation during major salt movement and is largely localised in areas of high subsidence (Fig. 4.21b). Major salt tectonics in the basin has been recorded in the Early Cenozoic (Coward and Stewart 1995; Stewart and Allen 2005; Underhill 2009). In this model, the stringer does not reveal

significant structural deformation from the time of deposition in the Late Permian to Early Cenozoic.

The second model is more applicable for the brittle extensional-related deformations, since the Z3 Stringer has been observed to be continuous after halokinesis with either flat to gently folded structures, as in areas below S4 (Fig. 4.9), or folded with open-upright fold structure, as in areas below S2 (Fig. 4.8). This suggests the Z3 anhydrite stringer behaves in a ductile manner. As such, it could be concluded that it is extremely difficult to break the anhydrite stringer before salt tectonics and that any sub-salt fault reactivation is insufficient to induce salt flow and subsequent brittle deformation of the Z3 Stringer. It is argued here that the majority of the stringer brittle deformation occurred during salt tectonics and required a significant amount of stretching to produce frequent breaks and rupturing (e.g., S1 and S5).
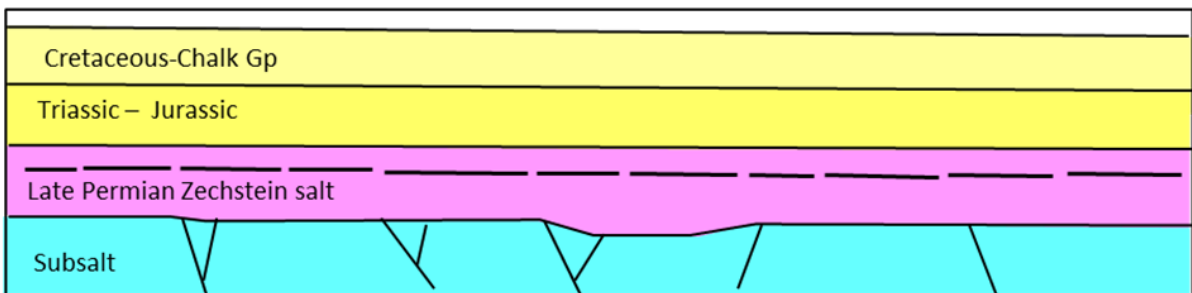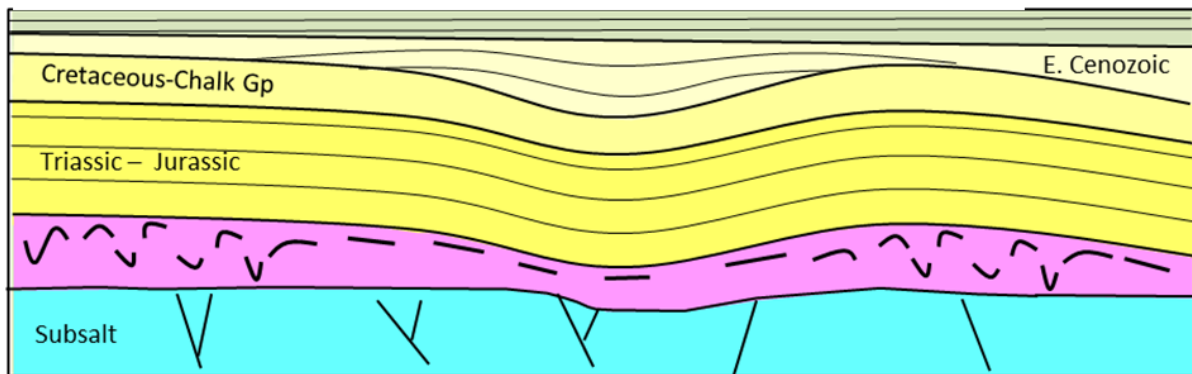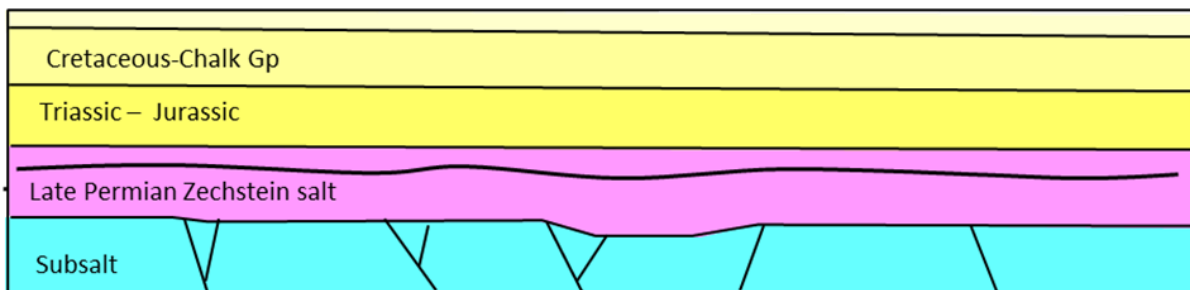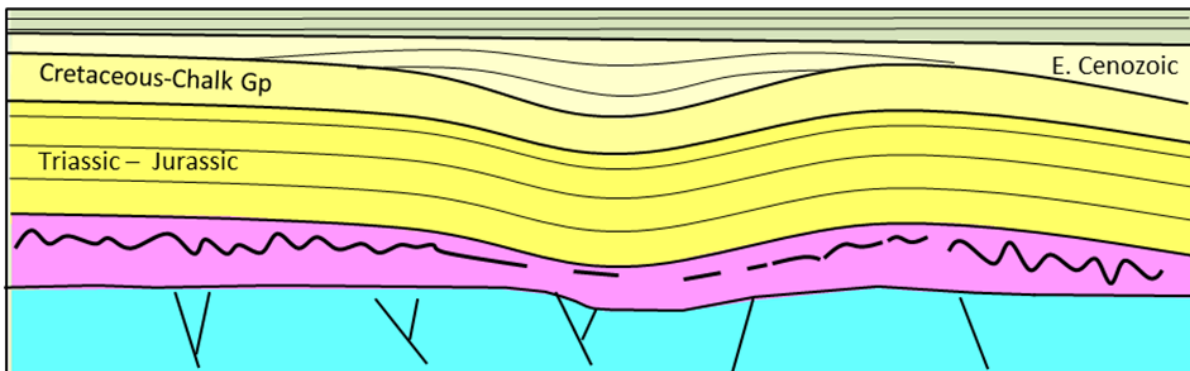
Fig. 4.21: 2D Conceptual sketches (not to scale). (a) Early stage of boudinage formation before major salt tectonics either during salt deposition or during the deposition of the Triassic-Cretaceous overburden. (b) Late-stage brittle-boudinage and folding in the Early Cenozoic time during salt tectonics in the basin. Refer to (Fig. 3.6) for scale and timing of megasequences.

4.6.5 Folding and boudinage below hinges and flanks of regional synclines

4.6.5.1   Boudinage within folded LSSD zone

The lateral small-scale brittle deformation structures formed within folded structures below the flanks of major synclines between the extensional subsided regions and the contraction zones (Fig. 4.22a,b). Such deformation can be interpreted as follows:

1. Simultaneous shortening and extension took place, shortening in one direction and extensional-brittle deformation in another direction (Fig. 4.22d). This type is common in highly rheological layered rocks (Grujic and Mancktelow 1995; Zulauf and Zulauf 2005).

2. The stringer was initially folded by salt flow during the early subsidence stage, and was subsequently stretched and fragmented during extreme thinning of the salt section.

3. Part of the stringer is subjected to zones of shortening, where part of the stringer fell into the shortening field and the remaining part is within the extensional brittle zone (e.g., transition zone).

4. The stringer progressively deformed and was dragged after being boudinaged during salt movement into folded-boudin trains during salt accumulation.

4.6.5.2   Folding below hinges of regional synclines

The majority of the stringer fragments in areas below extremely subsided synclines are flat (Fig. 4.10e, Fig. 4.13, and Fig 4.22a,b,c). In this case, the boudins are classified based on salt flow direction, where initial and large-scale gaps form below the hinge zone after the stringer was stretched by a diverging salt flow and resulted in almost flat boudin shapes (Fig 4.22c). However, gently folded individual fragments were also found (Fig. 4.6 and Fig.4.7). The mechanical properties of the stringer

within the salt and the presence of extreme lithological heterogeneities (e.g., weak potash layers below Z3 Stringer, see section 3.5.1.2) are considered factors contributing to folding within high lateral stretching areas. Moreover, the ductile behaviour of the anhydrite stringer itself causes the layer to fold even within zones of regional extension (van Gent el. 2011) and to fragment during extreme stretching. Highly brittle and competent stringers tend to be less folded and more boudinaged, such as the carbonate stringer in the South Oman Salt Basin (e.g., Li et al. 2012a).
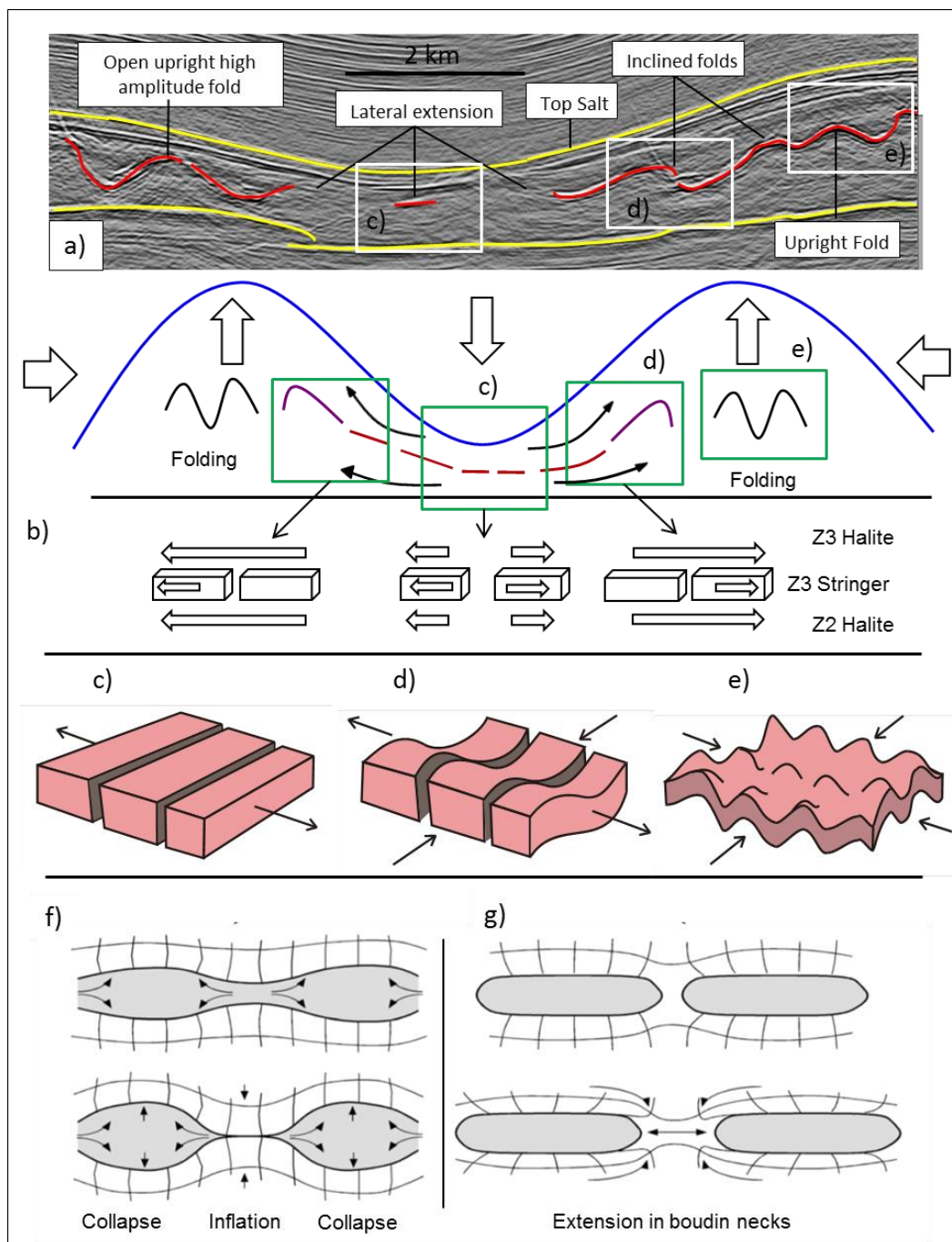
Fig. 4.22: Boudinage of the Z3 Stringer. (a) Profile across S1. (b) Simplified sketch of the common Z3 structural styles. (c) Boudinage classified based on salt flow direction where the initial and large-scale gap created below the hinge zone by stretching the stringer via opposite flow directions resulted in almost flat boudins. (d) Further away from the hinge, the stringer is stretched in one dominant direction, and the salt flows faster than the stringer, thus gaps occur. Folding may occur within this zone due to progressive deformation events, because of the transition from extension into contraction, or a combination of these two. (e) Folding of the stringer by salt accumulation from all directions, typical for a spherical pillow (e.g., A3). (f–g) Two boudinage processes (Bons et al. 2004) (f) Inflation and collapse upon emplacement, no lateral extension required. (g) Boudinage by layer-parallel stretching.

4.6.6 Interpretation of steep discontinuities below anticline structures

The seismic reflections of steep or thin stringers are strongly reduced or absent (Sleep and Fujita 1997; van Gent et al. 2011; Strozyk et al. 2012; Strozyk et al. 2014). Most steep stringer geometries are not imaged on seismic data (Fig. 4.11, Fig. 4.15, and Fig. 4.16). The most common stringer structure within areas of thick salt sections (i.e., below A1, A2, A3, A4 and A5) is a fold structure; as a result, most of the steep stringer parts are located within fold limbs.

Four possible end-member scenarios for such discontinuities are proposed. First, the stringer is continuous, with steeply inclined fold limbs that are seismically not resolved (Fig. 4.23a). Second, the stringer is too thin, below seismic resolution, and therefore could not be imaged (Fig. 4.23b). Third, the stringer is physically fractured and displaced vertically by salt flow as a boudin fragment (Fig. 4.23c). Fourth, the stringer is fractured parallel to the folded layer into smaller boudins that are either too steep or too small and thin to be imaged (Fig. 4.23d).

The Z3 Stringer was observed to experience brittle deformation only within areas of significant subsidence by Top Salt (e.g., S1, S5). The stringer is still continuous and folded below S2, with no significant brittle deformation (Fig. 4.8). Therefore, it can be inferred that the Z3 Stringer did not deform easily in a brittle manner during the early stages of subsidence, and a high rate of Top Salt subsidence was required for the anhydrite to reach the brittle phase and fail. However, the formation of a regional anticlinal structure is the opposite. Buckling of the basin with salt movement from areas where top salt has subsided into the generated anticline structure creates a contractional system inside the larger salt cored anticline (Hudec and Jackson 2007; van Gent et al. 2011). This contraction within the anticline structure is likely to fold

the ductile anhydrite stringer into high-amplitude folds (Fig. 4.11d). The anhydrite layer is sufficiently ductile to fold when shortening forces are applied parallel to the layering with no significant brittle deformation. Similar examples have been documented in salt mines (e.g., Wagner and Jackson 2011), salt outcrops (Fig. 4.11d) (Seidl 1921; Bornemann 1991), on seismic data in NW Europe (van Gent et al. 2011; Strozyk et al. 2012; Strozyk et al. 2014), and in model experiments (Zulauf et al. 2003; Zulauf et al. 2009). Therefore, the stringer is interpreted to rupture only if it has been highly stretched parallel to layering (e.g., below S1 and S5). A steeply inclined limb of folded stringer within compressional salt zones (e.g., regional anticlines, pillows) is unlikely to be the cause for generating brittle deformation, since stretching would be required to deform the stringer in a brittle fashion within the pillow structure.

The absence of any stringer fragments scattered between the upper and lower hinges, either in the limb area or displaced nearby, supports the continuity model of the anhydrite stringer within steeply folded structures. Therefore, vertically fragmented and displaced stringer limbs (Fig. 4.23c,d) might rarely be the case for non-imaged steeper parts within the core of regional anticlinal structures, except where the stringer has been reworked and dragged from the extensional regions (e.g., S1, S5) into areas of shortening (A1–A5).

The interpretation of the stringer in the Silverpit area cannot be applied as a case study for the late stage of halokinesis that requires vertical ascent of the stringer during the formation of salt domes or salt diapirs (e.g., Bornemann 1991; Koyi 2001; Peters et al. 2003; Reuning et al. 2009). Based on a cross-section of the Gorleben salt dome in Germany (Bornemann 1991), which is considered to be a late

halokinesis stage, the Z3 Stringer is still continuous up until the top of the dome. However, further examples are needed to confirm the continuity and folding of an anhydrite layer within salt accumulation zones at late stages of halokinesis (e.g., diapir build-up). Therefore, the continuity of the stringer within zones of salt contraction is at least applicable for areas of low to moderate halokinesis grade, similar to the salt pillows in the Cavendish area.
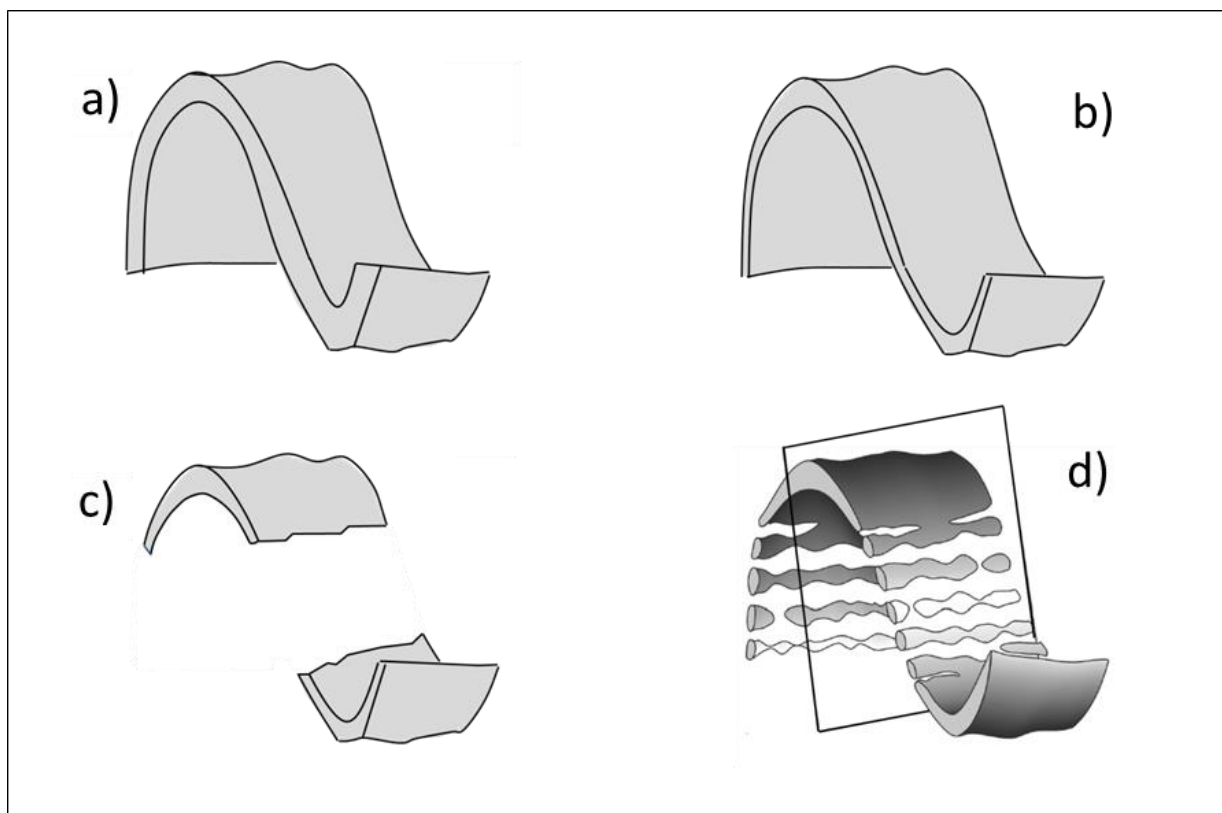
Fig. 4.23: Four possible scenarios to explain the vertical gaps between visible stringer fragments: (a) The stringer is continuous but too steep to be imaged. (b) The stringer is continuous but too thin to be imaged. (c) The stringer is fractured and disrupted vertically. (d) The steeper stringer part is fragmented into smaller boudins parallel to the folded layer; the fold hinges are thickened while the limbs are extended and boudinaged.

4.6.7 Kinematic evolution of the Z3 Stringer in areas of salt subsidence

4.6.7.1   Evolution modelling strategy

The stringer evolution model in this study is based on observations of seismic profiles and 3D maps focusing on the behaviour of the stringer at variable Top Salt subsidence magnitudes. The whole basin is regionally buckled, which resulted in the formation of NW–SE syncline and anticline structures (see chapter 3). This process also causes the Top Salt to move downwards to form elongated synclines and consequently reduce the salt thickness below. Since Top Salt is the major factor that controls the salt thickness, especially in the Cavendish area (Fig. 4.5b) (Underhill 2009), it has been chosen here as a reference for the subsidence rate and thus represents the stage of tectonics (i.e., early, middle, late; similarly: low, moderate, high). A similar application to test the stringer deformation was followed in numerical modelling (Li et al. 2009), where the stringer was subjected to progressive downward displacements by Top Salt. Therefore, a low grade of subsidence is considered in areas of less displacement by Top Salt (e.g., S2), whilst late-stage tectonics is from areas where Top Salt is highly subsided (e.g., S1 and S5).

4.6.7.2   2D structural evolution of the Z3 Stringer

Stage 1: Before any salt tectonics, the original configuration of the Z3 Stringer is interpreted to be flat. This interpretation is based on examples where the Z3 Stringer is almost horizontal and parallel to the Top Salt surface, with no evidence of folding or brittle deformation (e.g., Fig. 4.24a).

Stage 2: The second stage is the beginning of Top Salt subsidence. Stringer deformation developed during this phase was collated from areas where the Top Salt starts to sink. Areas below S2 were chosen to represent the structural style of the

stringer at the early stage of subsidence. The structural style of the stringer below the hinge zone of S2 shows an initial bending of the stringer (Fig. 4.24b). This is related to the initial flow of the upper halite Z3 member and possibly to an early withdrawal of the Z2 halite.

Stage 3: With progressive Top Salt subsidence, the Z3 Stringer forms large gentle-wavelength folds below the subsided areas (Fig. 4.24). Exceptional examples may occur where the stringer could also break below the thinnest zone of the subsided region simultaneously during the development of these regional folding (Fig. 4.24d). This could be interpreted to be related to local weaknesses within the stringer such as small faults or fractures that help to break apart the stringer at this stage. This suggests that stringer brittle deformation and development of folding can occur simultaneously during the same deformational event (e.g., Zulauf and Zulauf 2005).

Stage 4: During the next stage of the deformation, the Top Salt continues to subside and the cross-sectional area of the salt section is reduced. The Z3 Stringer is stretched and begins to have low structural relief (Fig. 4.24e). In a similar manner to the previous stage, during flattening and stretching, the stringer may exceed its tensile strength and break laterally. The shallow dips of the stringer below S1 and S5 suggest extreme stretching and flattening prior to the stage of lateral extension. The regional downward displacement by Top Salt and the overburden squeeze the salt section and induce high lateral salt flow, which ultimately reduces the chances of fold formation below the hinge zone.

Stage 5: Continuation of Top Salt subsidence reduces the thickness of the Zechstein salt by lateral salt flow, which causes the stringer to break significantly into single isolated fragments (Fig. 4.24f).

Stage 6: The stringer fragments are dragged and carried away from the subsided regions into the flanks of the synclinal structures. This lateral movement of the stringer fragments is estimated to reach up to 4–5 km in the present study area (Fig. 4.24f).
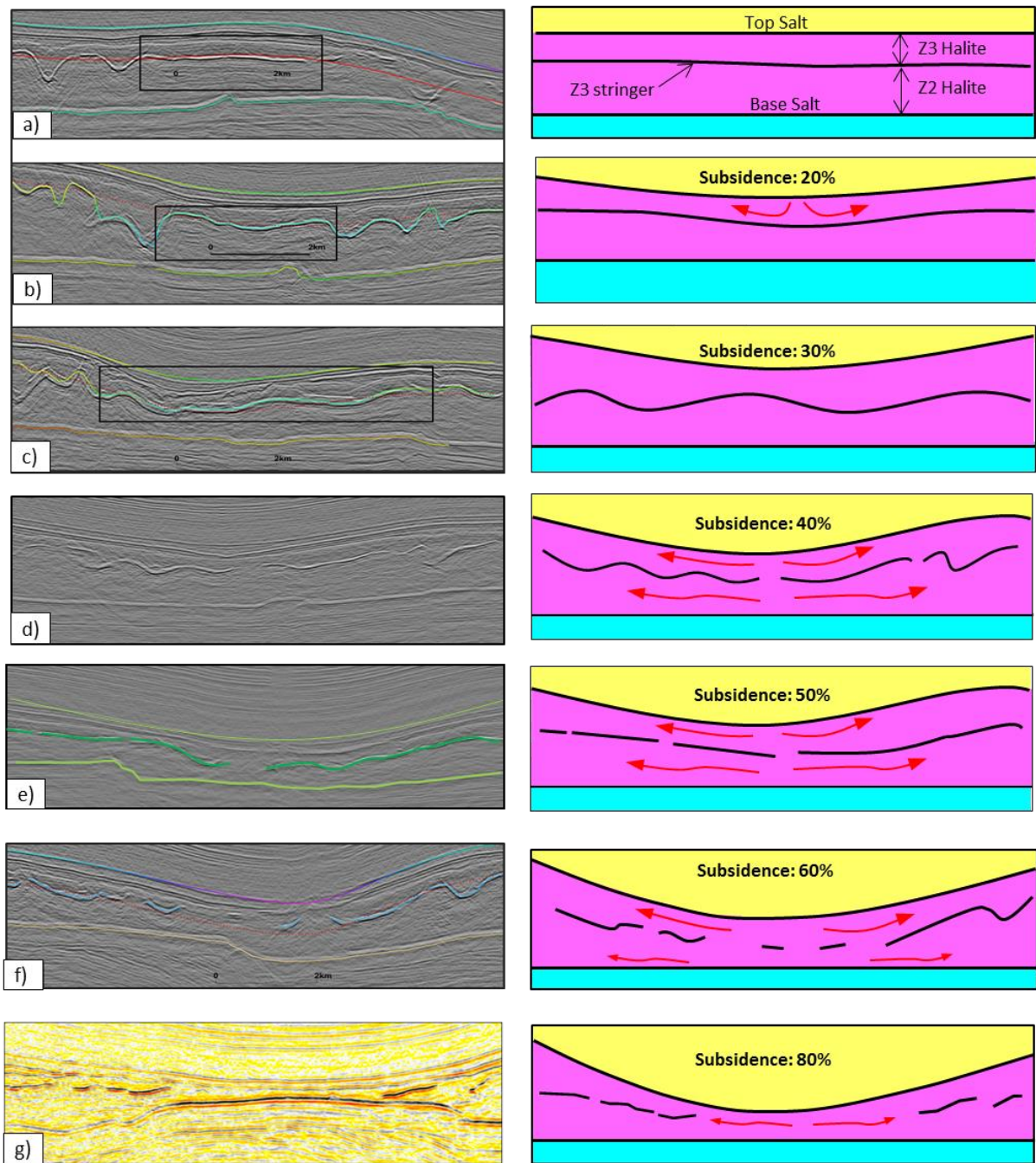
Fig. 4.24: Seismic profiles (a–g) at variable Top Salt subsidence magnitudes were selected to represent the stringer evolution from early salt tectonics to nearly the welding stage. The downward displacement magnitude of Top Salt (subsidence rate) increases from (a) to (g).

4.6.7.3   4D evolution of the Z3 Stringer

Areas of stringer deformation below S1 (Fig. 4.12) and S5 (Fig. 4.13) were selected to represent the final 3D configuration of the stringer structural styles at the late stage of Top Salt subsidence. The initial configuration of the Z3 Stringer before any Top Salt displacement is assumed to be flat (Fig. 4.25a).

Early salt tectonics created linear Top Salt synclines and anticlines. In the early stage of subsidence, the stringer formed elongated large-wavelength folds with axes parallel to the regional syncline (Fig. 4.25b). Examples of these folds can be observed below regional synclines of modest subsidence (Fig 4.24c and d). With progressive Top Salt subsidence, the thickness of the salt section is reduced by salt evacuation and therefore higher-velocity salt flow was generated, which consequently stretched and flattened the Z3 Stringer. This resulted in linear to irregular breaks almost parallel to the regional structure (Fig. 4.25c).

This alignment is similar to the formation of subparallel fracture alignments when uniaxial to sub-uniaxial extension is applied to the competent layer during the early stage of deformation, with the x to y strain ratio of 1:0 and 1:0.5 (Abe et al. 2013). The breaks within the stringer are then connected and linked up to form isolated stringer fragments, which were later carried laterally by salt flow for 4–5 km (Fig. 4.25d).

The final configuration is represented by a large zone of discontinuity where salt only yields smaller stringer fragments. The stringer is almost flat to gently folded in the middle of the subsided area and has a gentle, open inclined fold structure below the flanks of the regional syncline.
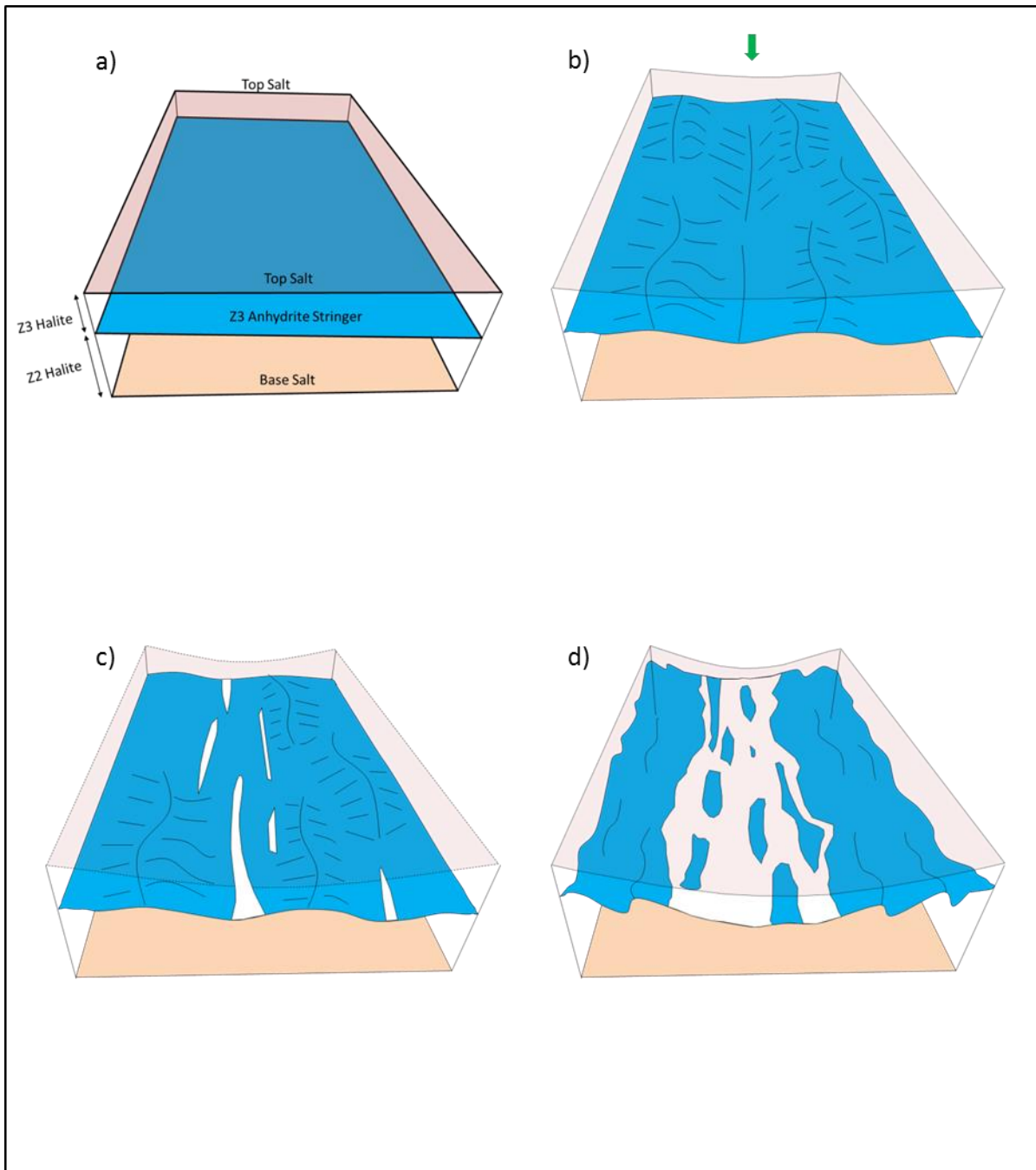
Fig. 4.25: 3D sketch of the structural evolution of the Z3 Stringer with progressive Top Salt subsidence from (a) to (d).

4.7   Conclusion

Internal salt structures were mapped using 3D seismic reflection data from the Silverpit Basin in the Southern North Sea with an aim of evaluating the kinematic evolution of the stringer in areas of salt subsidence related to regional basin buckling. The study concludes with the following:

- The presence of high-acoustic-impedance Z3 Stringer enables tracing the internal geometry of the salt structure and has significantly helped in improving our understanding of internal salt dynamics within areas of salt subsidence.

- The deformation of the intra-salt stringer is largely influenced by the regional deformational history.

- The structural propagation of the intra-salt Z3 Stringer below areas of Top Salt subsidence begins with the formation of gentle, long-wavelength folds, followed by lateral stretching, re-flattening, and finally fragmentation and lateral separation of the stringer fragments for distances close to 4–5 km.

- Top Salt structural and salt thickness surfaces are important tools to predict the internal structural style within the salt.

- In areas where the salt is subjected to high rates of subsidence, extensional related structures such as boudinage, lateral stretching, and fragmentation of the inclusions are generated. However, contraction-related structures (e.g., folds) are created in areas where Top Salt forms anticlines and the salt section is thick.

- The stringer is fractured and displaced laterally below regions of high subsidence (S1 and S5). However, modest Top Salt subsidence was still not

able to fracture the stringer (e.g., stringer below S2, S4), suggesting that the stringer brittle deformations were only initiated during the major salt tectonics in the Cenozoic.

- In areas where the salt section is thick, the stringer is easily folded and more resistant to brittle deformation; thus steeply inclined fold structures, which in most cases were not seismically imaged, are likely to be continuous or thinned during folding.

Chapter 5: 3D kinematic evolution of the intra-salt Z3 Stringer in areas of salt thickening in the Silverpit Basin, Southern North Sea Basin

Abstract

The kinematics of the intra-salt Z3 Stringer under local compressional domains have been summarised in three dimensions below five Top Salt anticlinal regions in the Southern North Sea.

The internal Z3 Stringer folds strongly correlate to the shape, trend, and tightness of the regional Top Salt anticlines. The Top Salt anticlines and synclines are classified as low-, moderate-, and high-amplitude folds. These magnitudes control the strain intensity of the stringer within the salt layer. Low regional Top Salt anticlines are associated with intra-salt gentle folds and broader hinges, while highly folded Top Salt anticlines are associated with tighter folds of open and close types. In addition, it has been noted that the shape of the Top Salt anticlines, whether linear or sub-circular, controls the alignment, orientation, and shape of the stringer folds.

For an elongated Top Salt anticline with high fold amplitude, four groups of stringer folds were formed: (1) non-cylindrical, curvilinear, tight upright folds, parallel to the regional structure formed at the crest of the regional anticline; (2) non-cylindrical curvilinear folds parallel to the regional structure but with inclined fold axes plunging towards the anticline crest, formed in the distal areas along the hinge zone of the regional anticline; (3) non-cylindrical tilted fold hinges perpendicular to the strike of the Top Salt anticline, formed at the middle flanks of the elongated anticline structure; and (4) non-cylindrical large-scale passive inclined folds formed at the basal part of the regional anticlinal domain close to the adjacent regional synclines.

For moderate-amplitude and elongated Top Salt anticlines, the stringer folds are dominantly curvilinear upright with horizontal hinge lines parallel to the regional anticlinal strike. Low-amplitude linear Top Salt anticlines generate upright gentle

folds but with broader hinges. Sub-circular and domal Top Salt anticlinal shapes generate multidirectional constrictional folds of domes and basins.

Such results led to the conclusion that these folds were largely formed by buckling mechanisms during the major tectonic phase of the basin in the Early Cenozoic.

5.1   Introduction

5.1.1 Background studies

Seismic and experimental observations on external salt layers have shown the presence of regional salt structures such as salt domes, salt diapirs, salt walls, salt pillows, salt anticlines, salt synclines, and salt minibasins (Hudec and Jackson 2007) (Fig. 5.1). The internal salt deformation of these regional structures can be divided into two main domains: (1) The first is an intra-salt extensional domain, created in areas below regional synclines and minibasins, where the whole salt layer is thinned. The internal competent stiff layers at such domains experience lateral fragmentation, boudinaging, and lateral displacement (van Gent et al 2011; Cartwright et al. 2012; Strozyk et al. 2012; Strozyk et al. 2014) (Fig. 5.2a,b,c). The structural evolution of the stringer below areas of Top Salt synclines has been discussed in chapter 4. (2) The second is a compressional domain below salt thickening regions such as salt domes and salt anticlines. This is characterised by shortening-related deformation such as open to isoclinal, upright to recumbent folds (van Gent et al 2011; Cartwright et al. 2012; Fiduk and Rowan 2012; Strozyk et al. 2012; Strozyk et al. 2014; Jackson et al. 2015) (Fig. 5.2a,b,c,e).

Such internal structural domains of extension and contraction have been observed seismically, experimentally, and geologically. For example, analogue modelling simulating gravity spreading of a tilted basin shows the formation of complex shortening-related deformations, which include isoclinal and recumbent folds in the contracted, down-dip thickened zone (Dooley et al. 2008; Cartwright et al. 2012) (Fig. 5.2b). Internal salt studies in the contractional part of the Santos Basin revealed the formation of large-scale simple upright open folds, inclined thrusted folds, and

isoclinal recumbent folds (Fig. 5.2c and 5.2d), all formed during bulk shortening of the basin (Davison et al. 2012; Fiduk and Rowan 2012; Jackson et al. 2015). Similarly, studies of intra-salt layers in the contraction part of the Levant basin revealed upright detachment buckle folds and thrust-ramp folds formed during an early gravity-spreading of the basin (Cartwright et al. 2012). The Z3 anhydrite-carbonate stringer present onshore and offshore Netherlands revealed complex deformations in areas below salt domes (van Gent et al 2011; Strozyk et al. 2012; Strozyk et al. 2014). Outcrop and mining observations of the Z3 Stringer deformations within salt domes revealed high-amplitude isoclinal, upright folds formed at the middle of the structure, while inclined folds formed below, on the flanks of the salt dome (Seidl 1921) (Fig. 5.2e). Similar high-amplitude folds below salt domes have been observed on seismic data from the north of the Netherlands and the Southern North Sea (Strozyk et al. 2014). Scaled physical experiments also provide insights into salt domes' kinematics and internal structures (Jackson and Talbot 1989; Koyi 2001).

In simple cases, internal salt structures within thickened salt diapirs have simple, upright, and symmetrical internal anticlines (Fig. 5.2f). The internal layers were entrained with the upward salt flow without being fractured. Similar continuity of intra-salt layering was found in the Gorleben salt dome, where the Z3 Stringer is steeply dipping within the dome and was carried upwards by salt movement for more than 3 km without significant fragmentation in the stringer (*cf.* Bornemann 1991; Bauerle et al. 2000) (Fig. 5.2g). However, using numerical modelling, Koyi (2001) found that the vertical uplift of the internal competent layers may eventually result in significant brittle extensional deformation during the development of the salt dome. Recent seismic studies of the Z3 anhydrite stringer within the Zechstein salt onshore and

offshore Netherlands suggest the combination of boudinage and folding within the salt dome (van Gent et al. 2011). The flow into the dome creates vertical extension of the steeply inclined stringer, which leads to tensile failure, while coeval horizontal compression creates constrictional folds with steeply inclined axes. Talbot and Jackson (1987) suggested more extreme folding within the salt diapir. The stem of the diapir is characterised by vertical fold axes known as curtain folds (Fig. 5.2h).

Although there are many examples of diapirs exposed at the Earth's surface, such as the Great Kavir in Iran and the salt domes in Oman, such exposures are largely two-dimensional (Jackson et al. 1990). In addition, salt domes are mostly exposed to dissolution near and at the surface, which leads to rotation and a chaotic juxtaposition of the internal stringers, hence strongly masking the original internal structural configuration (Jackson et al. 1990; Reuning et al. 2009). Furthermore, the internal structure of exposed diapirs can be strongly deformed by gravity spreading of salt extruding at the Earth's surface, such as the external salt diapirs in Iran (Talbot and Jackson 1987; Talbot 1998; Talbot and Aftabi 2004). Mining data yield only a quasi-3D appreciation of intra-salt structure due to the relatively limited distribution of mine galleries and boreholes. Thus most of the intra-salt structure is inferred from limited three-dimensional coverage provided by cross-sectional sketches, boreholes, and galleries. Seismic data, on the other hand, is the best source of information to analyse the 3D internal salt structure (van Gent et al. 2011; Strozyk et al. 2012). However, this is still poorly documented in the literature and only a few studies have been recently published (van Gent et al. 2011; Cartwright et al. 2102; Strozoyk et al. 2012; Strozoyk et al. 2014). Thick salt is typically acoustically transparent on seismic reflection data, and internal salt stratigraphic markers that record strain are typically poorly imaged (van Gent et al. 2011). Even in

the presence of a high-amplitude reflection within the salt layer, seismic imaging limitations are likely to occur within the salt due to the complexity of the internal structure and the occurrence of steeply dipping intra-salt geometries (Strozyk et al. 2012). Such limitations may challenge the interpretation and the data may need further corrections in order to generate realistic intra-salt geometries (van Gent et al. 2011). Therefore, the 3D description of intra-salt structures, especially in thicker salt regions, is not fully understood and is still poorly presented in the literature.

5.1.2 Aims of this chapter

The Silverpit area in the Southern North Sea is an important area for understanding the early internal deformation of the Zechstein salt under a compressional regime because of the following reasons:

1. A well-imaged anhydrite stringer known as the Z3 Stringer (Underhill 2009) present in the study area can be used to analyse the internal structure of the salt in three dimensions (see chapters 3 and 4).

2. The regional external salt structures form anticlines of low-moderate and high fold amplitudes (Underhill 2009), which posits the basin as a suitable case study for understanding the early to late kinematic evolution of intra-salt deformation below anticlinal regions.

3. The Z3 Stringer in the basin is situated between two purely thick halite intervals, known as Z2 Halite and Z3 Halite, so the Z3 Stringer is a good marker to test models for the internal salt kinematics without underestimating sub- and post-salt structures such as faulting (van Gent et al. 2012) and shearing (Cartwright et al. 2012).

This aim of this chapter is to understand the kinematics of the intra-salt Z3 Stringer in areas of salt thickening in the Southern North Sea Basin. Five Top Salt anticlinal structures with variable shortening magnitudes were selected from the Cavendish 3D seismic survey in the Southern North Sea for the analysis of their internal deformation. The main focus is to present a high-resolution 3D study of intra-salt deformation by providing new insights into their detailed structural styles below each of the regional compressional anticlinal structures. An additional aim is to test the

relationships between shortening, shapes, and orientation of the regional Top Salt structure with the internal deformation of the stringer using quantitative analysis of strike, interlimb angle, and wavelength measurements, as well as qualitative descriptions based on 3D curvature attributes and 2D seismic profiles.
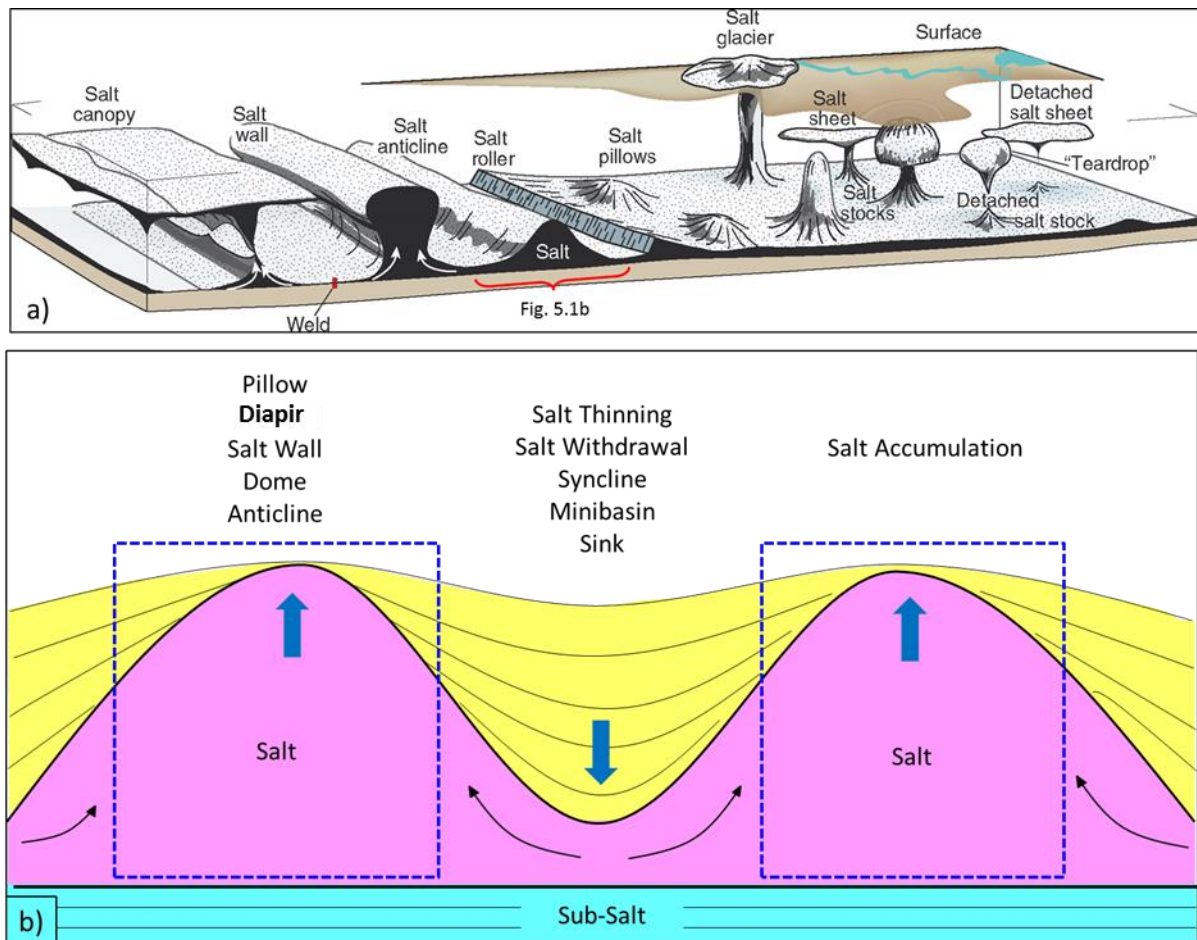
Fig. 5.1: (a) Large-scale salt structures (after Fossen 2010); linear structures to the left side and circular structures to the right. Degree of halokinesis increases away from the centre. The red brace highlights the shape and degree of halokinesis in this study. (b) Salt structure of anticlines and a syncline shows two regional structural domains: a salt syncline domain in the middle and regions of salt accumulation (anticline, pillow). The two blue boxes highlight the regions that this chapter is focused on.
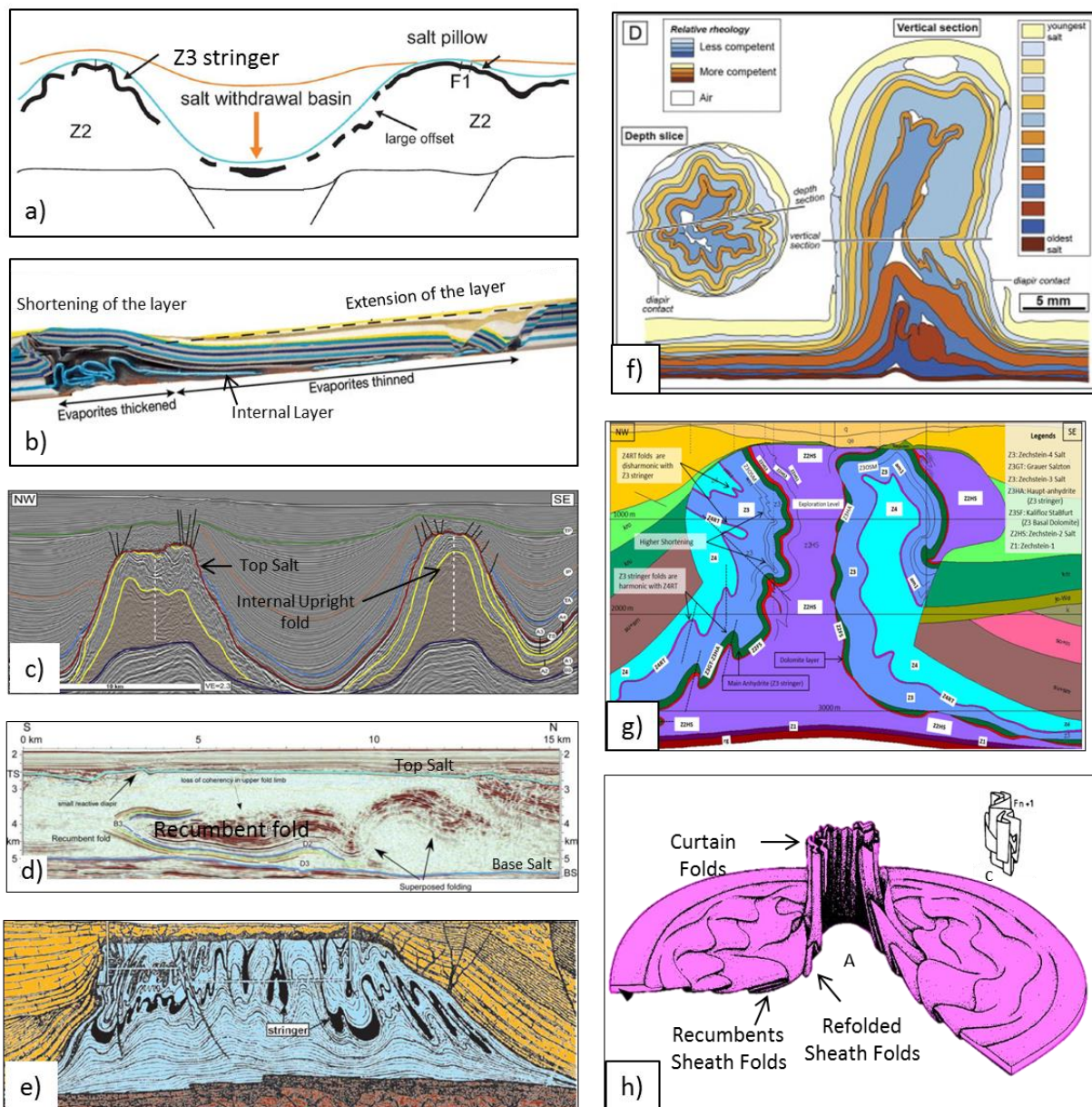
Fig. 5.2: Examples of intra-salt structures. (a) Strozyk et al. (2014). (b) Cartwright et al. (2012). (c) Jackson et al. (2015). (d) Fiduk and Rowan (2012). (e) Seidle (1921). (f) Escher and Kuenen (1929). (g) Bornemann (1991). (h) Talbot and Jackson (1987).

5.2   Methods and workflow

A 3D post-stack time migrated seismic survey from the Cavendish Field in the Silverpit Basin, Southern North Sea, was used for structural interpretation of the Z3 Stringer within the Zechstein salt (see chapters 2 and 4 for geophysical details). The study is based on qualitative and quantitative descriptions of the highly deformed Z3 Stringer. In order to separate the deformation of the stringer that formed within regional synclines from that formed within regional anticlines, five major anticlinal domains were highlighted. The Top Salt structure was divided into domains of anticlines based on Top Salt topography, the thickness of the salt layer, and the shape of the regional anticlines (Fig. 5.3a). These domains are Anticline 1 Domain (A1D), Anticline 2 Domain (A2D), Anticline 3 Domain (A3D), Anticline 4 Domain (A4D), and Anticline 5 Domain (A5D). This allows the description of the stringer deformation only within areas of salt thickening. By applying the mean curvature seismic attribute to the Top Salt surface, the boundaries between Top Salt anticlines and Top Salt synclines can be distinguished (Fig. 5.3e). Mean curvature allows the recognition of the dominant orientation of the fold whether it is a synform or antiform (Lisle and Toimil 2007). Areas of zero mean curvatures are planes; therefore, mean curvature allows the discrimination between antiform and synform similar to an inflection line (Fig. 5.3e).

The qualitative analyses of the intra-salt Z3 Stringer are based on seismic profiles, 3D structural maps, and 3D seismic attributes. Fold curvature attributes were applied to the stringer folds for a better description of their curvatures, strike measurements, and for testing and describing their cylindricity (Lisle and Toimil 2007).

The qualitative description was supported by quantitative structural analyses. These include wavelength, interlimb angle, and strike measurements of the folded Z3 Stringer in each regional anticlinal domain. A 1:1 scale was used for the measurements by scaling the horizontal seismic scale to be equal with the vertical thickness of the well 43/19-2 (Fig. 5.3c). The wavelength and interlimb angle were measured individually in each domain on profiles perpendicular to their strike. Interlimb angle measurements were used in order to understand the tightness of the stringer folds. The strikes of the anticlines and synclines of the Z3 Stringer were traced using the maximum and minimum curvature attributes. The traced segments were then imported into ArcGIS to generate rose diagrams.

Curvature attributes

The basic descriptions of folds rely on the assumption that folds are cylindrical (i.e., the surface can be described as consisting of antiforms and synforms in two dimensions). Geological surfaces, however, are non-cylindrical in nature and much of the geometrical information is lost if simplistic descriptions are used (Lisle and Toimil 2007). Curvature computations have been employed by structural geologists to describe the geometry of folded surfaces (e.g., Roberts 2001; Lisle and Toimil 2007), to quantify the degree of deformation or strain in deformed strata (e.g., Lisle 1994), and to predict fracture orientations and densities in bent strata (e.g., Bergbauer 2002). Four important curvatures were used in this study to analyse the fold structures of the Z3 Stringer: minimum, maximum, mean, and Gaussian curvatures. In this study, curvature attributes were used for four major purposes:

1. For the regional Top Salt structures, mean curvature was applied to the Top Salt surface to determine the borders between anticlines and synclines, where

zero curvature (Fig. 5.3e, yellow lines) reflects the inflection surface of the folds and thus distinguishes anticlines from synclines (Lisle and Toimil 2007).

2. For the Z3 Stringer folds, mean curvature was used to classify the stringer folds into synclines and anticlines, with inflection surfaces in between.

3. Minimum curvature was generated for better detection of synclines and their hinge lines in the Z3 Stringer (Fig. 5.3f).

4. Maximum curvature was generated to detect positive curvatures of antiforms and their hinge lines in the Z3 Stringer (Fig. 5.3g).

5. Maximum and minimum curvatures help to describe the folds in three dimensions, as well as simplifying the tracing workflow of synclines and anticlines for strike calculations. In addition, minimum curvature can help detecting minor synclines within the major anticlines. Similarly, maximum curvature can help detecting minor anticlines within the major synclines. Gaussian curvature is an important method for describing the cylindricity of the folds by classifying them into zero curvature (plane), dome, basin, and saddle (Fig. 5.3d, see also chapter 2 for more details).
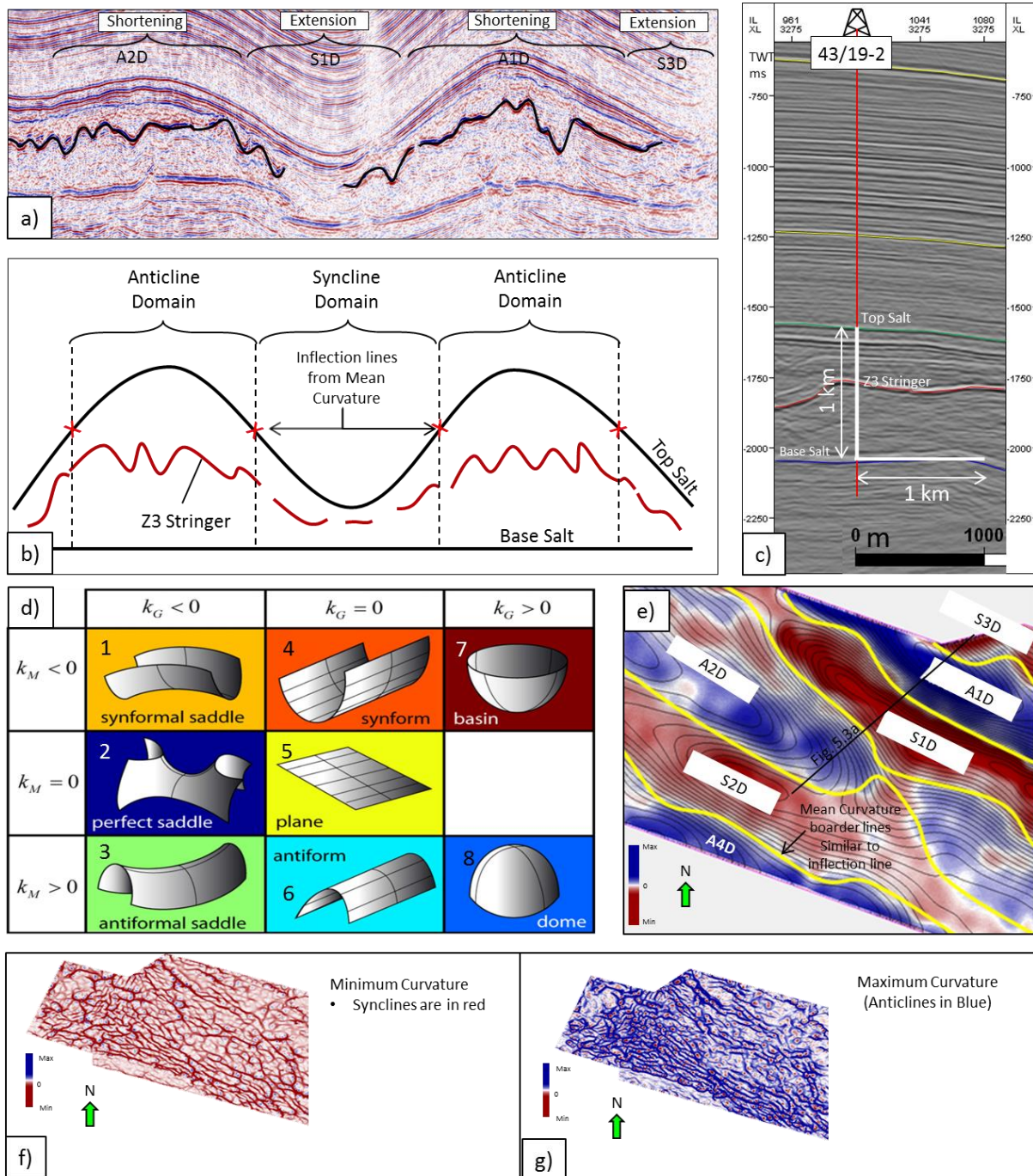
Fig. 5.3: (a) Seismic profile across the eastern part of the Cavendish Survey shows the difference in the Z3 Stringer structural styles below Top Salt anticlines and synclines. (b) Simplified 2D sketch based on the mean curvature attribute of Top Salt in (e). (c) Approximately 1:1 scale (measured from well 43/19-2). (d) Fold classification based on mean curvature (KM) and Gaussian curvature (KG). Cylindrical folds are where KG is equal to zero (4, 6). Non-cylindrical folds (includes 1, 2, 3) are where the KG is not equal to zero (after Roberts 2001). (e) The mean curvature attributes of the Top Salt surface determining the extent and the borders between Top Salt anticlines and synclines. (g) Maximum curvature attribute of the Z3 Stringer folds. Note that synclines (red) and anticlines (blue) are well represented in both curvatures.

5.3   External salt structure

The Top Salt in the Cavendish area forms low- to moderate-amplitude anticlines and synclines, which significantly control the thickness of the underlying salt (Fig. 5.4a,b). The eastern Top Salt folds (A1, S1, A2, S2, S3, and A4) are oriented NW–SE with elongated planforms. However, the western folds (A3, S4 and A5) are oriented NE– SW to N–S with sub-circular planforms (Fig. 5.4a). Superimposing Top Salt topographic contours over the salt thickness surface indicates that the salt thickness is correlated with the Top Salt geometry (Fig. 5.4b).

The Cavendish area was divided into five anticlinal domains based on the Top Salt surface (Fig. 5.4b).

- A1D is an elongated anticline structure with maximum length and width of 11 km and 7 km, respectively. The maximum thickness of the Zechstein at the anticline hinge of this domain is 660 ms (1400 m). The topographic change observed within the anticline is bounded by the presence of S1 and S3 to the south and the north, respectively (Fig. 5.4c).

- A2D is located in the middle of the study area, and has an average thickness of 478 ms (approximately 1 km) across a large area of the basin. The thickness change between A2 and its adjacent S2 is negligible because of folding of the sub-salt layers in a similar way as the Top Salt.

- A3D is a sub-circular anticlinal structure in the southwestern part of the Cavendish survey. The domain is bounded by S4 to the west, A4 to the southeast, A2 and S2 to the east, and A5 to the north (Fig. 5.4).

- The A4D is an elongated NW–SE domain located in the south of the study area. The southern part of the domain is not fully covered in the Cavendish data (Fig. 5.4a, b, and c).

- The A5D is a part of an anticlinal structure located in the northern part of the study area. The full extent and shape of the A5D are unknown (Fig. 5.4c).
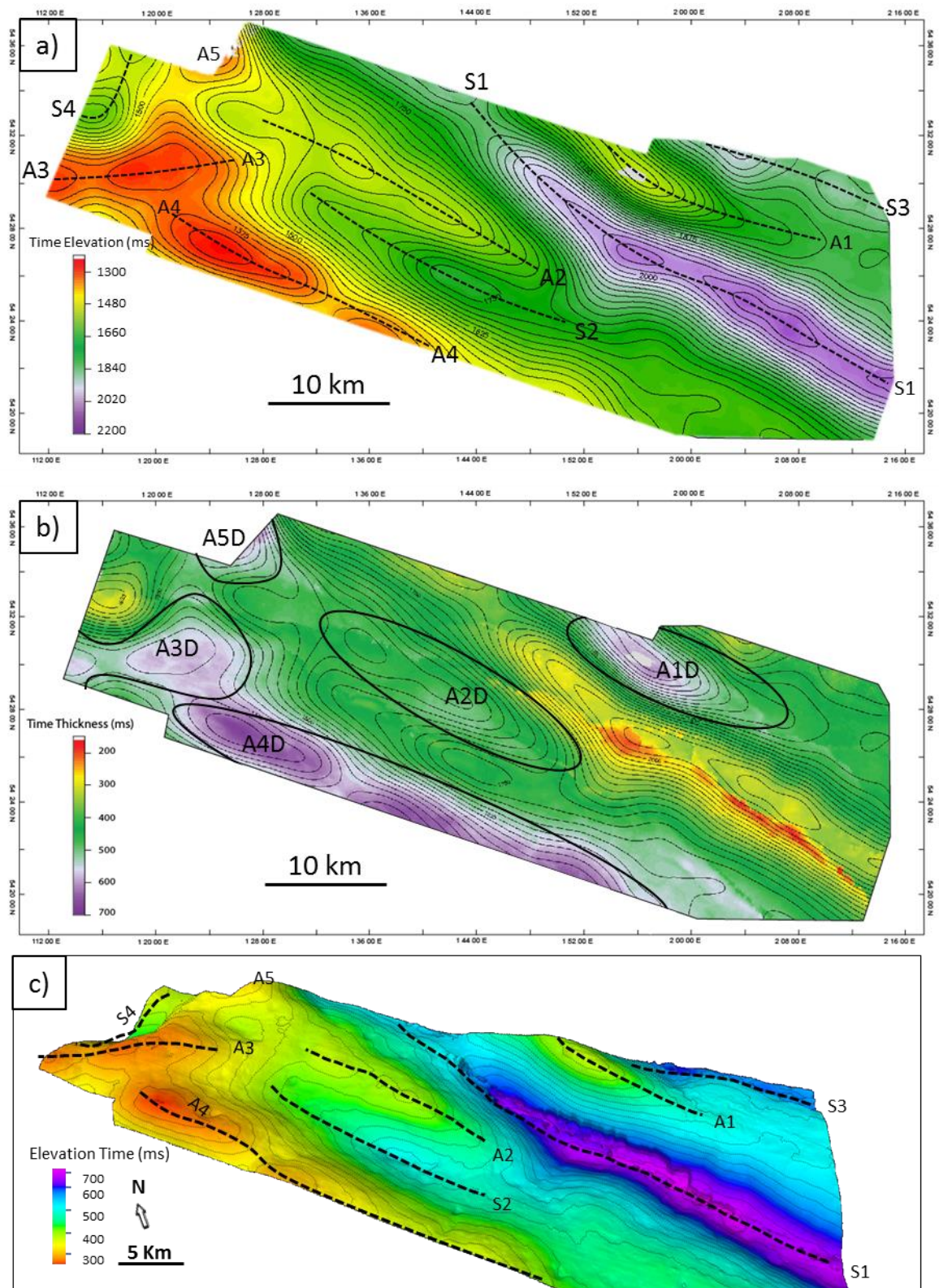
Fig. 5.4: Regional Zechstein structure. (a) Two-way-travel-time of Top Salt. (b) Time thickness of the Zechstein salt (coloured surface) superimposed with Top Salt (contours). Note that the thickness of the Zechstein has an almost similar structure to the Top Salt. The five anticlinal regions are highlighted. (c) 3D view of the Top Salt surface.

5.4   Generic 2D description

The regional structure of the Zechstein is characterised by salt-related anticlines and synclines with variable wavelengths and amplitudes. These synclines and anticlines have variable intra-salt deformational styles. Major Top Salt synclines generate internal stretching, resulting in extension and boudinage deformations inside the salt layer.

The amplitude map of the Z3 Stringer (Fig. 5.5a) is useful to indicate discontinuities in the seismic reflector, and has been structurally interpreted in chapter 4. The stringer discontinuities below S1, S3, and part of S4 have been interpreted to represent large-scale extensional deformation (Fig. 5.5a). The profile across the Cavendish survey shows a large-scale extensional gap of the stringer layer below S1 (Fig. 5.5c). Similarly, extensional-related discontinuities formed below S3 (Fig. 5.5c). However, few discontinuities are present below Top Salt anticlines (A1, A2, A3, and A4; Fig. 5.5a). These discontinuities are related to steeply dipping geometries and thus are seismically not resolved, because of the limitations of the reflection method (van Gent et al. 2011; Strozyk et al. 2012) (see also chapter 4).

The interpreted Z3 Stringer surface has consequently been interpolated across any gaps formed within steeply dipping stringer parts (e.g., within steep fold limbs) (Fig. 5.5b). The interpolated surface of the stringer indicates that the dominant deformations below Top Salt anticlines are fold structures (Fig. 5.5b). The stringer folds below A3D are complexly folded (Fig. 5.5b); however, folds below A4D have a more linear shape (Fig. 5.5b). The upper enveloping surface of the stringer anticlines below A1D is harmonic with the Top Salt, which means that the stringer was regionally elevated during the development of A1 (Fig. 5.5c). Regions of flat and

undeformed Z3 Stringer with diameters from 5 to 10 km were observed in areas of less deformed Top Salt structure, such as the eastern part of S2 and A2 and the northern flank of A2 (Fig. 5.6a). Long-wavelength folds with broader anticlines were formed below S2 (Fig. 5.6e). The stringer folds below the low-amplitude A2 are more gently folded than those below S2 (Fig. 5.6f). The tightness of the folds increases below the well-developed A4D and A3D (Fig. 5.6g,h). The stringer folds below the hinge zone of A1 are upright and more shortened, while being inclined below the flanks of A1 (Fig. 5.6h). Such inclination can also be seen below the flanks of S1 (Fig. 5.6d). The interlimb angle of the folds below each domain is shown in Fig. 5.7. Anticlinal domains tend to have tighter stringer folds than synclinal domains. Open to close folds form below the core of A1D, A3D, and A4D, while gentle folds form below S4D and S1D (Fig. 5.7a). The wavelengths of the folds below two selected regional synclines (S1D and S4D) and three selected regional anticlines (A1D, A2D and A4D) are shown in Table 5.1.
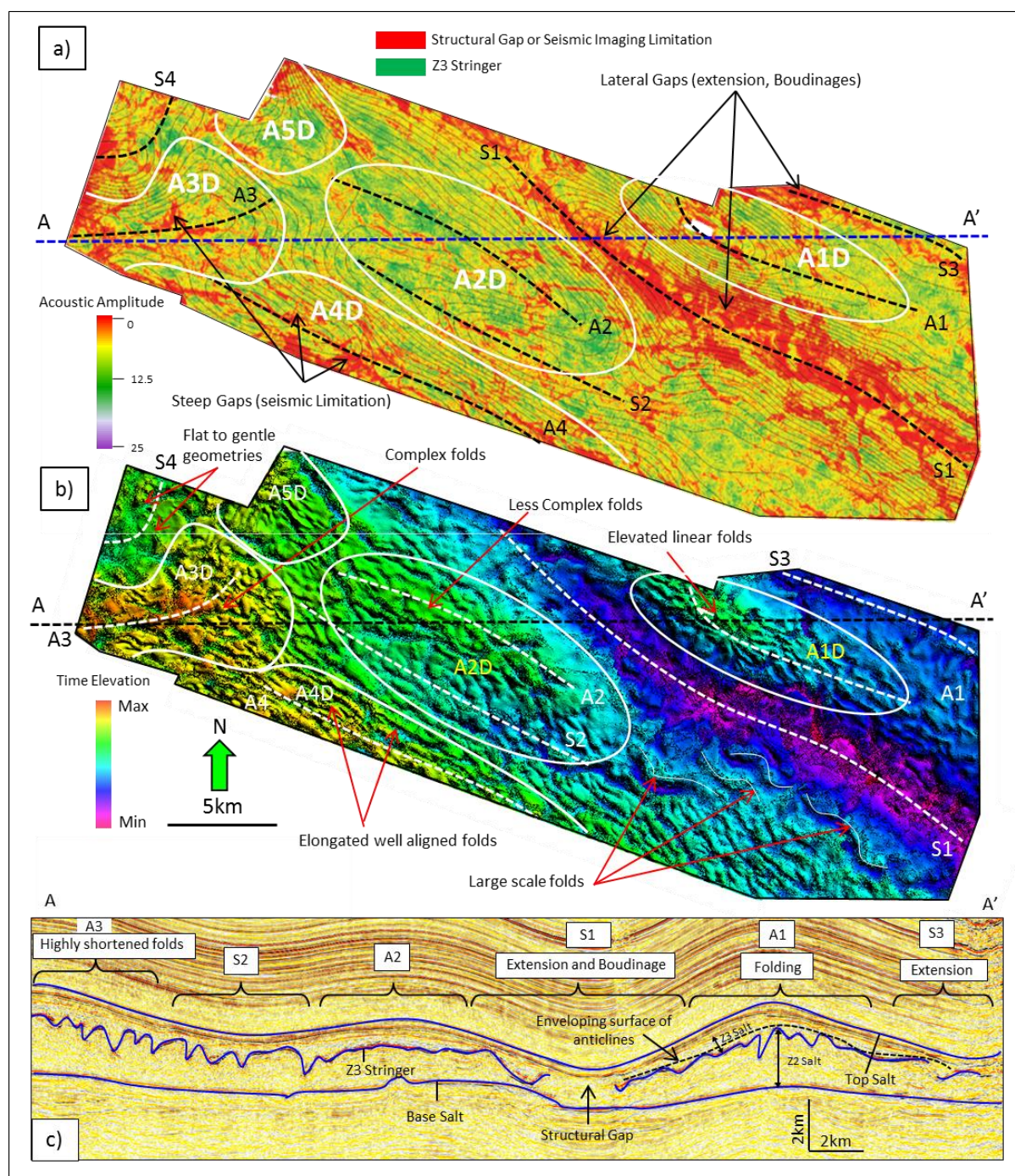
Fig. 5.5: Seismic interpretation of the Z3 Stringer in the Cavendish survey. (a) Z3 Stringer amplitude map (coloured surface) superimposed with Top Salt topography (contours) shows zero seismic amplitudes or gaps (in red), and strong seismic amplitudes represent continuous stringer (in green). The gaps are either structurally derived (e.g., below S1 and S4) or part of seismic limitations (areas below A1D, A3D, and A4D). (b) 3D TWT interpolated Z3 Stringer surface shows more complex folding below regional anticlines. (c) Regional profile across the main regional structures. Note the complexity of folding in each domain.
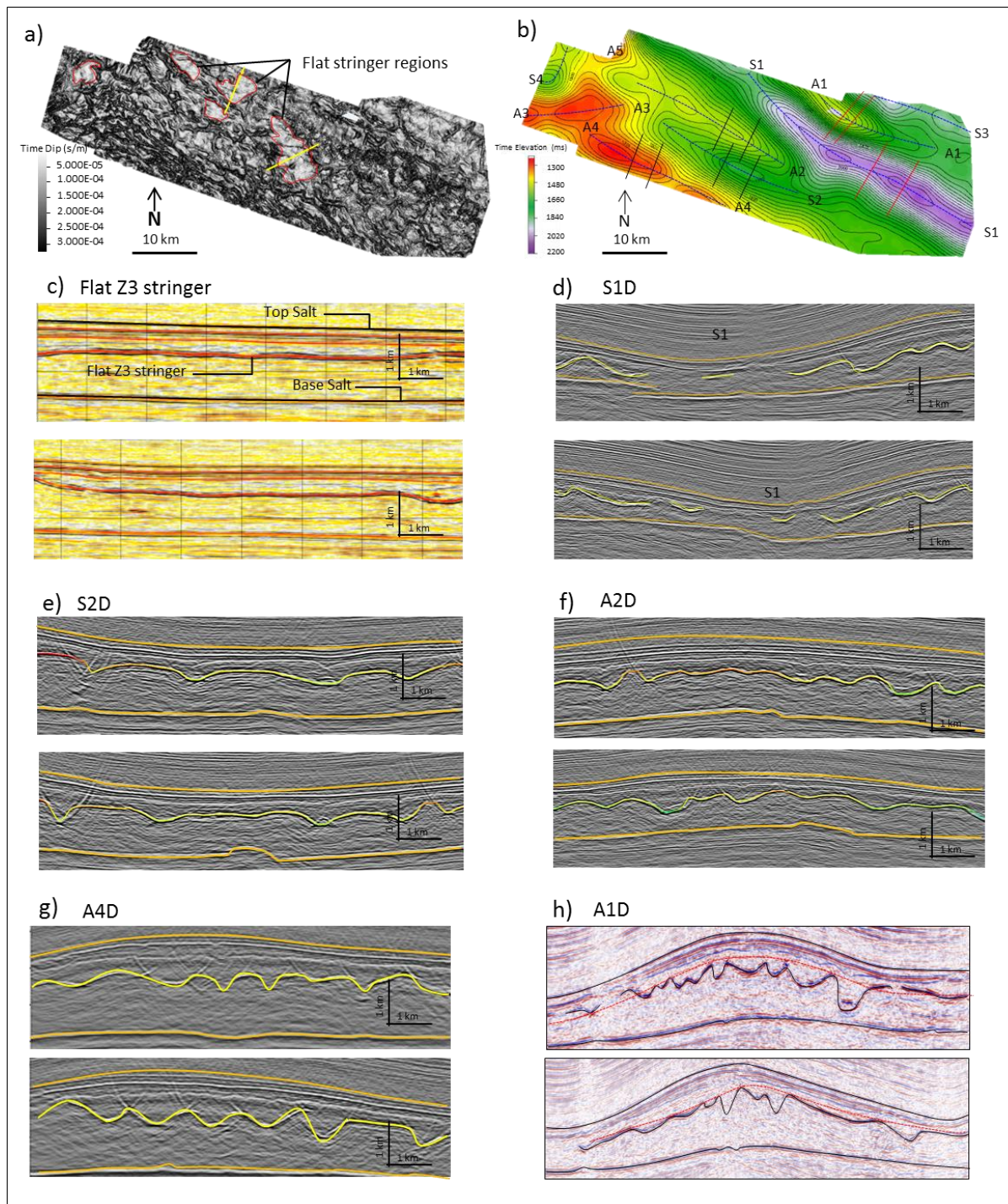
Fig. 5.6: (a) Time dip surface of the Z3 Stringer. (b) Top Salt TWT structure map. Black lines represent seismic profiles c to d. (c) Seismic profiles across flat stringer zones. (d) Seismic profile across S1D. (e) Profiles across S2D show large-scale gentle folds to flat geometries. (f) Seismic profiles across A2D display upright gentle folds. (g) Profiles across A4D show open upright folds with high amplitudes. (h) Profiles across A1D.
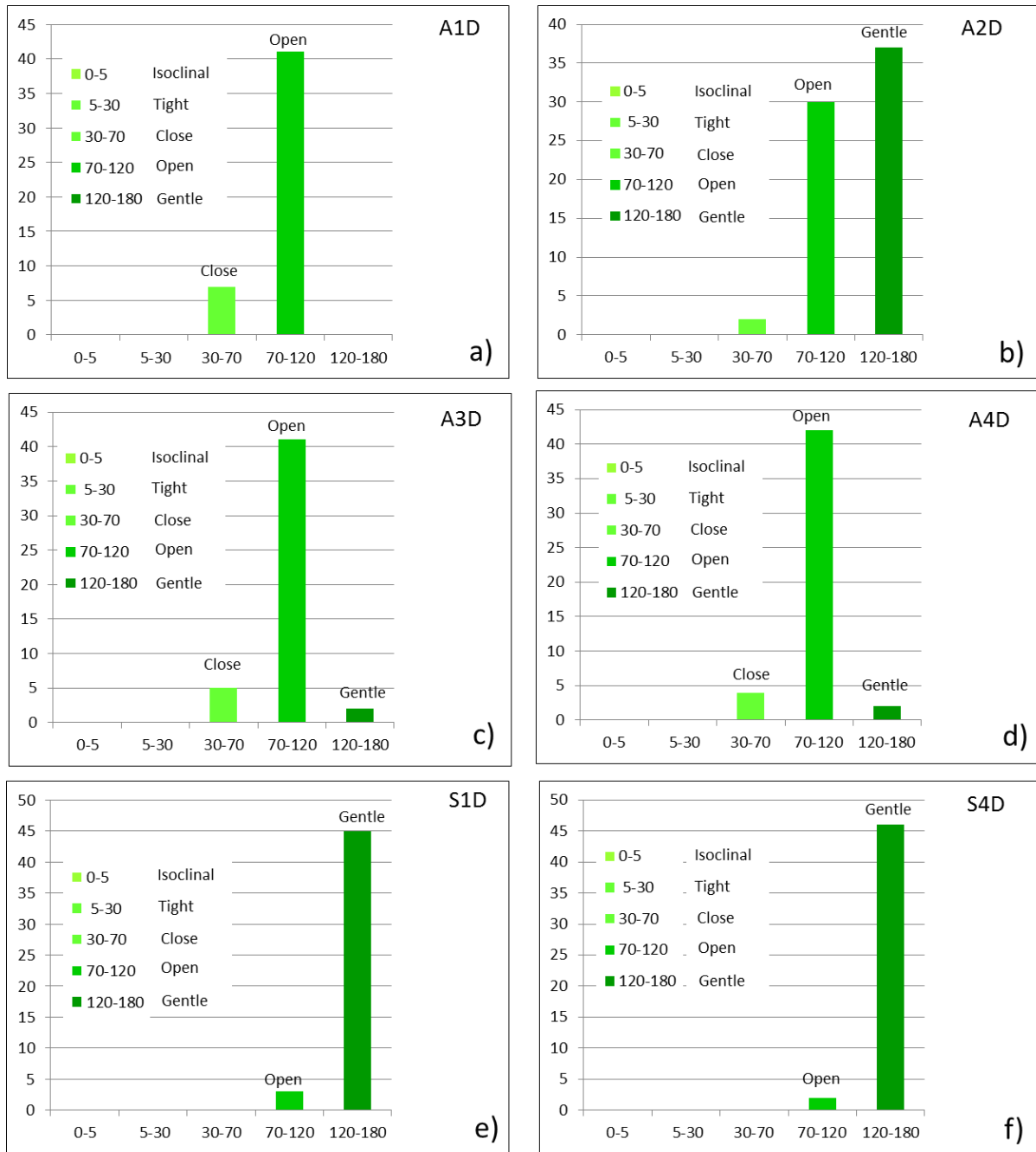
Fig. 5.7: The interlimb angles of the Z3 Stringer folds below each domain, displayed as histograms. The X-axis and Y-axis represents the interlimb angles and the number of the folds used, respectively. Angles are grouped into fold classes (i.e., isoclinal, tight, close, open, and gentle) based on the fold tightness classification of Fleuty (1964). See Appendix 5.1 for the measurements. See chapter 2 for the classification of the folds based on the interlimb angle.

Table 5.1: Wavelengths of the Z3 Stringer folds below two synclinal domains (S1D and S4D) and three anticlinal domains (A1D, A2D, and A4D). Note the long wavelengths of the folds below synclines (S1D and S4D) and the shorter wavelengths of the folds below anticlines (A1D and A4D). A2D is characterised by moderate fold wavelengths. All readings are in metres.

	S1D	S4D	A1D	A2D	A4D
Number of folds	42	27	34	36	42
Mean	1797	1451	592	1287	589
Median	1607	1455	525	1335	563
Mode	865	1337	500	1350	617
Std. Deviation	641	94	185	152	154
Range	2123	234	698	563	582

5.5 Detailed 3D description of the Z3 Stringer

The three-dimensional description of the Z3 Stringer below the anticlinal domains is based on 3D time surfaces and curvature attributes. Each domain is introduced individually.

5.5.1 Anticline 1 Domain (A1D)

The A1D is located in the northern part of the study area (Fig. 5.4), and is bordered to the south by Syncline 1 and to the north by Syncline 3. The 3D display of the stringer folds within this domain reveals regional elevation of the fold structures (Fig. 5.8). The folds are structurally deeper around the flank of the domain and become shallower and tightly folded below the domain crest (Fig. 5.8a). The stringer folds within the domain can be divided into two groups: an inner area, representing the group of folds below the crest of the anticlinal domain, and an outer area, representing the flanks of the domain (Fig. 5.8a). Four groups of folds have been observed (Fig. 5.8a,b): (1) NW–SE upright curvilinear folds parallel to the strike of the A1 at the centre of the domain; (2) NW–SE curvilinear folds parallel to the regional structure with tilted and doubly-plunging hinges towards the core of the anticline, at the western and eastern flanks of the elongated A1D; (3) NE–SW and N-

S striking curvilinear folds with hinges perpendicular and oblique to the regional strike of the A1, in the middle of the outer flanks area; and (4) regional long strike folds with large wavelengths, in the distal area of the domain.

The amplitude and frequency of the stringer folds are higher along the hinge zone of the A1 and decrease gradually away from the crest of the domain (Fig. 5.8b). The folds within the inner area in the middle of the domain are upright with tighter wavelengths. However, folds at the flanks of the domain are wider and inclined in cross-sectional view (Fig. 5.8b,c). The mean wavelength of the stringer folds below the A1D is 592 m (Table. 5.1). The majority of the folds within the inner area of the domain have interlimb angles between 70° and 120° (Fig. 5.8a); based on fold tightness, these folds are classified as "*open folds*" (Fleuty 1964). Few folds have tighter angles, and they are classified as "*close folds*" (interlimb angles ranging from 30°to 70°).
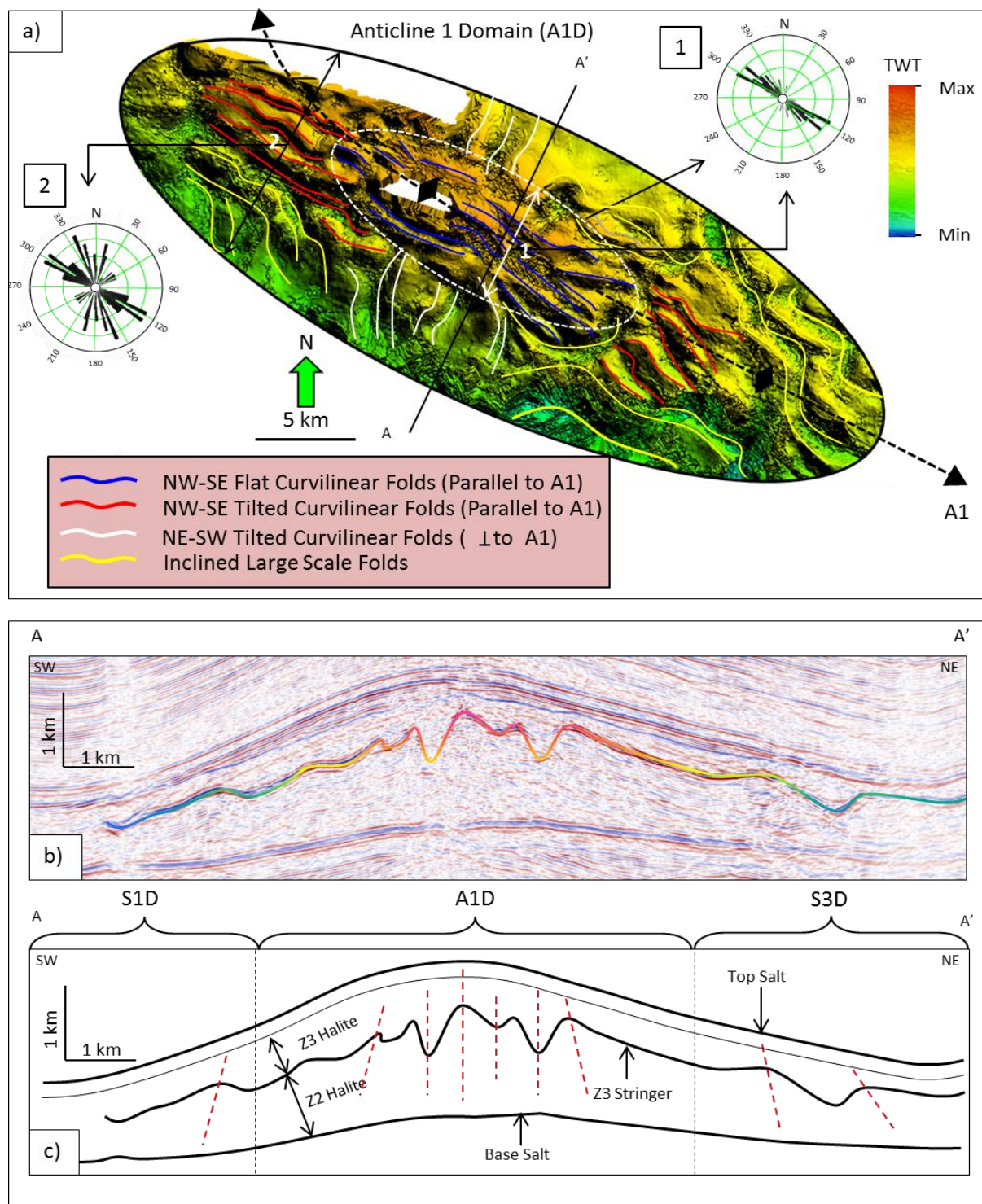
Fig. 5.8: (a) 3D TWT surface of the Z3 Stringer within Anticline 1 domain (A1D). The stringer within the core of the domain is intensively folded with tight folds and consistent NW–SE strikes. Four types of folds are annotated. (b and c) Uninterpreted profile across the A1D displays tight upright folds within the core of the anticline and inclined long-wavelength folds below the flanks of the regional Top Salt structure.

5.5.2 Anticline 2 Domain (A2D)

The Top Salt A2 anticline is less folded relative to the anticlines A1, A3, and A4 (Fig. 5.4). The salt thickness is almost constant in the areas below A2 and S2 (Fig. 5.4b). The interlimb angles of the Z3 Stringer folds below A2D show that more than 50% of the folds are "*gentle*" and 40% are "*open folds*" (Fig. 5.7). The mean wavelength of the folds is 1,287 m, which is twice that of the folds below the A1D (Table. 5.1). The Z3 Stringer time map displays an elevated group of folds below the A2D characterised by broader anticlinal hinges and narrower synclinal hinges (Fig. 5.9a,b). Profiles across A2 and S2 display the internal fold style of each domain (Fig. 5.9g,h). The folds below A2 are gently folded and elevated within the regional structure, while folds below S2 are broad with flat hinges (Fig. 5.9g).

Minimum curvature attributes of the Z3 Stringer display the negative curvatures (synclines) of major- and minor-scale folds (Fig. 5.9c), whereas maximum curvature attributes display positive curvatures (anticlines) of major and minor scales (Fig. 5.9d). The major synclines are well detected by minimum curvatures, indicating that minimum curvatures are aligned with the hinge zones of the folds (Fig. 5.9c). Maximum curvatures, on the other hand, show that some anticlinal hinges are broader and sometimes hinges formed at the sides of the antiform shape (Fig. 5.9d,g). The minimum curvature attributes also indicate minor-scale synclines within the major anticlines, suggesting that the hinge lines are not straight, and instead they are folded and thus non-cylindrical (Fig. 5.9c). These minor folds are perpendicular to the major ones. Tracing the major anticline and syncline fold axes of the Z3 Stringer (Fig. 5.9e) revealed that the overall trend of the folds is NW–SE, parallel to the regional structure (Fig. 5.9f).
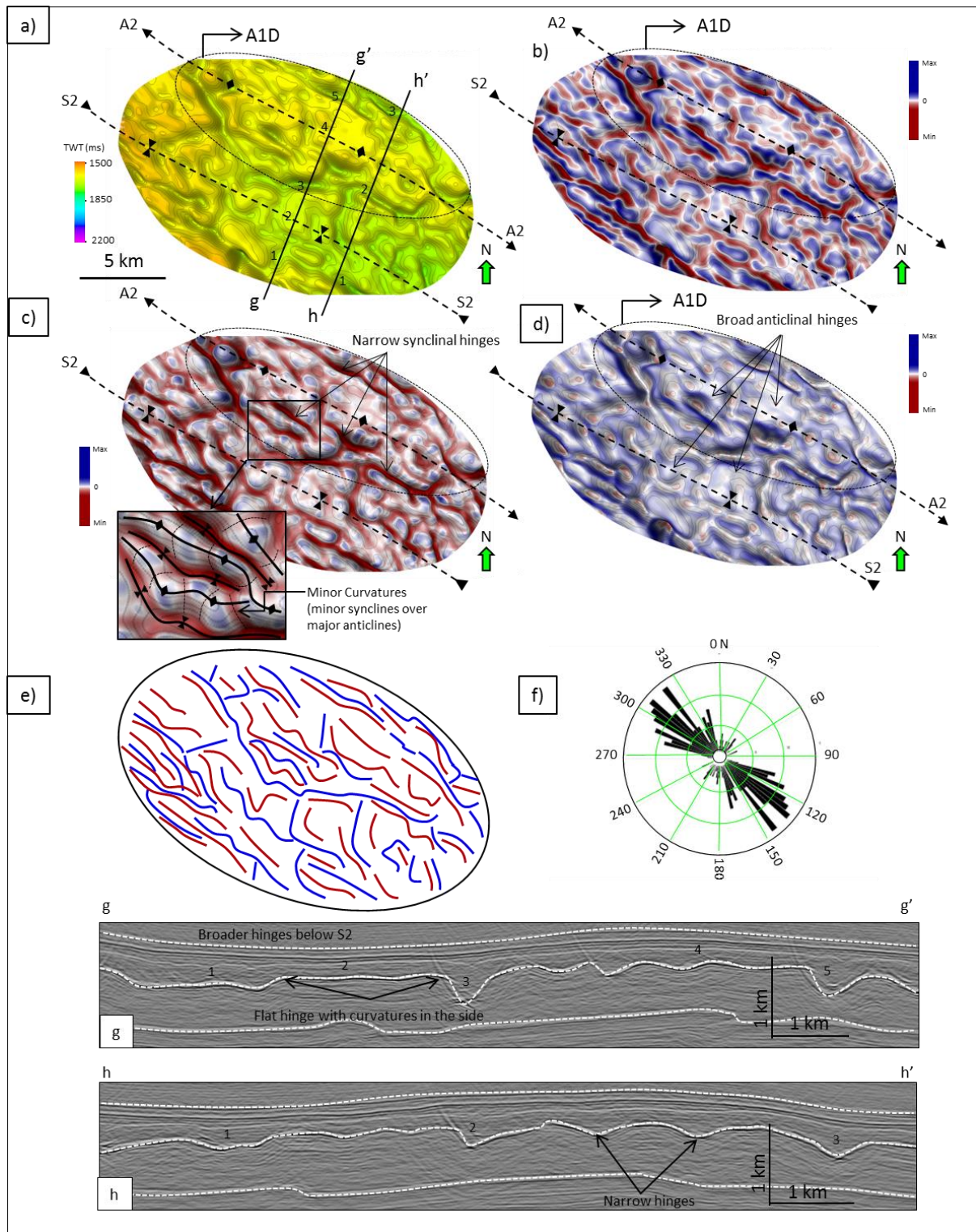
Fig. 5.9: Z3 Stringer deformation below A2D. (a) Z3 Stringer TWT. (b) Mean curvature. (c) Minimum curvature. (d) Maximum curvature. (e) Stringer synclines and anticlines annotated from the minimum and maximum curvatures, respectively. (f) Rose diagram of the fold axes shows NW dominant direction. (g) and (h) 2D seismic profiles across A2D; see (a) for location. Note the wide anticlinal hinges and narrow synclinal hinges. Numbers (1–5) show the locations of the structures on the map and profiles.

5.5.3 Anticline 3 Domain (A3D)

The A3D is located in the western side of the Cavendish survey (Fig. 5.4), within a thick salt section, and is sub-circular in shape. The thickness of the salt can reach up to 1410 m in the middle of the domain. The Z3 Stringer was complexly folded into synclines and anticlines of dome and basin shapes (Fig. 5.10a). The folds are rarely linear in shape. The interlimb angles for these folds are between 70° to 110°.

The Z3 Stringer mean curvature attribute, which displays the major synclines and anticlines of the Z3 Stringer surface, shows lateral upright anticlines and synclines of dome and basin shapes as well as plunging fold axes (Fig. 5.10b). Similar steeply plunging folds but with smaller degree of curvatures can be seen using the minimum curvature attributes (Fig. 5.10c).

The detailed description of the non-cylindricity of the stringer folds below this domain was done by applying Gaussian curvature attributes (Fig. 5.11). The folds are characterised by dome and basin shapes (similar to folds number 7 and 8 in Fig. 5.3d), and they are connected by anticlinal and synclinal saddle shapes (similar to fold # 1 and # 3 in Fig. 5.3d). Cylindrical anticlines and synclines (i.e., fold number 4 and number 5 Fig. 5.3d) do not exist. Saddle shapes are folds that combine two opposite curvatures, either anticlinal saddle or synclinal saddle (folds # 1and # 3 in Fig. 5.3d). This structural style reflects the non-cylindricity of these folds.
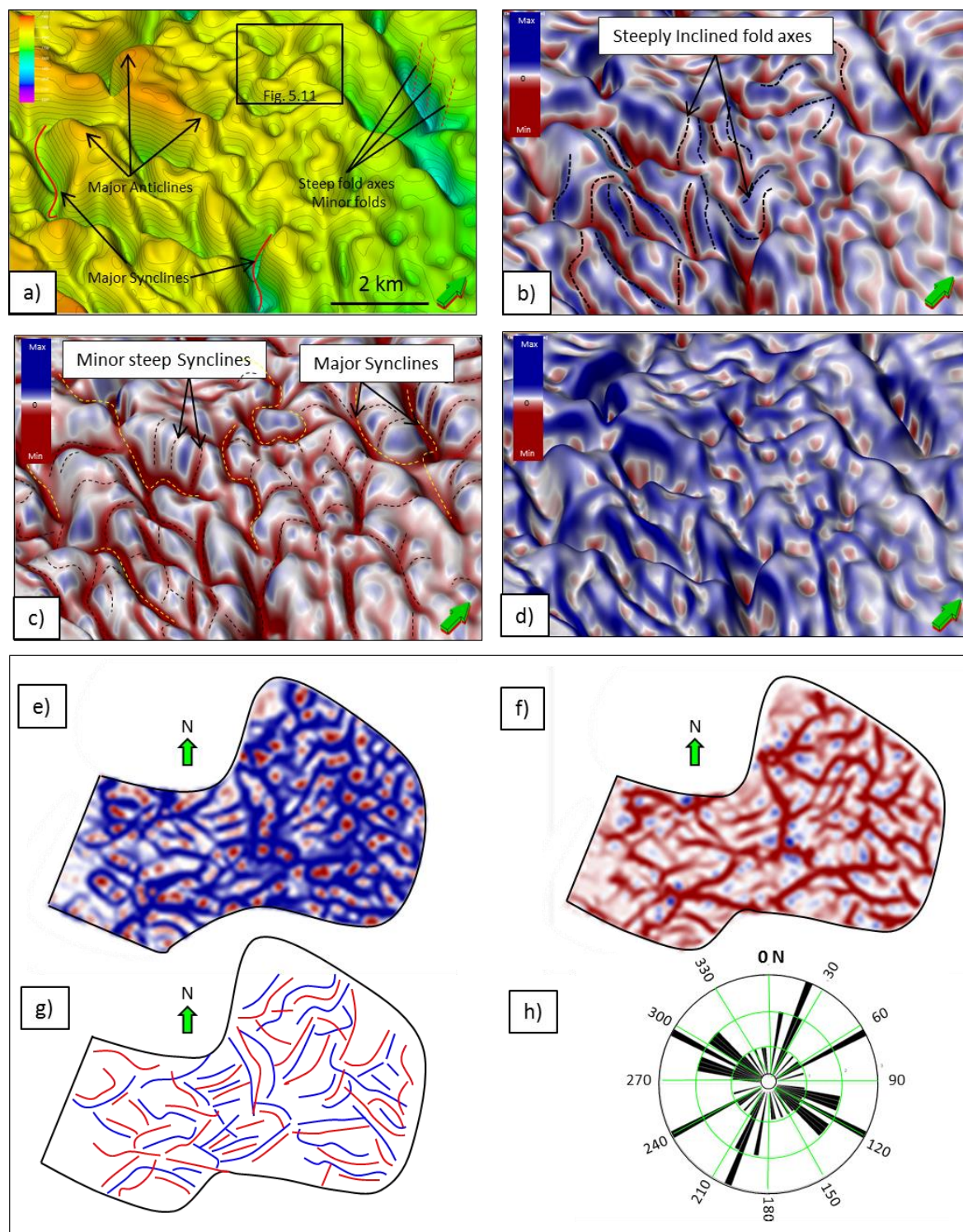
Fig. 5.10: Z3 Stringer deformation below Anticline 3 Domain (A3D) (a) Z3 Stringer TWT. (b) Mean curvature attributes show the major synclines and anticlines on the Z3 Stringer surface. Note the steeply dipping folds. (c) Minimum curvature attributes highlight negative curvatures (red) of major and minor synclines of the stringer. (d) Maximum curvature displays positive curvatures and thus highlights anticlines of the stringer (in blue). Both the major and minor anticlines are shown, including the minor anticlines within the major synclines. (e) 2D maximum curvature and (f) 2D minimum curvatures used to annotate anticlines and synclines, respectively in (g). (h) Rose diagram of the fold axes shows multidirectional strikes.
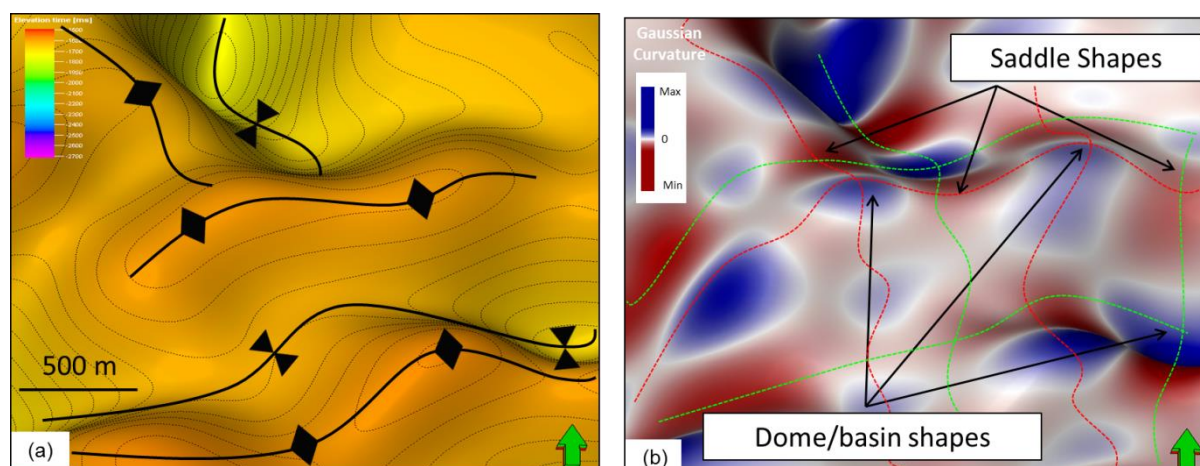
Fig. 5.11: Detailed 3D description of the Z3 Stringer folds (see Fig. 5.10a for location). (a) Contoured 3D time surface shows the major anticlines. (b) 3D Gaussian curvature attribute surface. Blue colours indicate positive Gaussian curvature, either basins or domes (similar to folds number 7 and 8 in Fig. 5.3d). Red colours indicate negative Gaussian curvatures, or saddle folds (similar to folds number 1 and 3 in Fig. 5.3d).

5.5.4 Anticline 4 Domain (A4D)

Unlike the A3D, the A4D is an elongated NW–SE striking anticline structure (Fig. 5.4). The Z3 Stringer displays NW–SE elongated curvilinear doubly plunging upright anticlines and synclines (Fig. 5.12b,g). The major synclines and anticlines strike NW–SE, parallel to the regional structure (Fig. 5.12a,d). However, along the strike of each major fold, the hinge line forms minor synclines and anticlines which are perpendicular to the major curvatures. Consequently, the hinge lines are not zero curvature (straight hinge lines), and instead they curve, forming synforms and antiforms, which reflects the non-cylindricity of the folds (Fig. 5.12b,e).

The folds of the Z3 Stringer are tighter, with smaller hinge zones where the salt reaches it maximum thickness (Fig. 5.4). However, the stringer folds in the eastern part of the domain are less tight and with longer strikes (Fig. 5.12b,c). Most of the anticlines and synclines have profiles penetrating the folds below A2D, S2D, and A4D, showing the increase in tightness and frequency of the folds and the decrease in fold wavelengths below A4D (Fig. 5.12g,h).
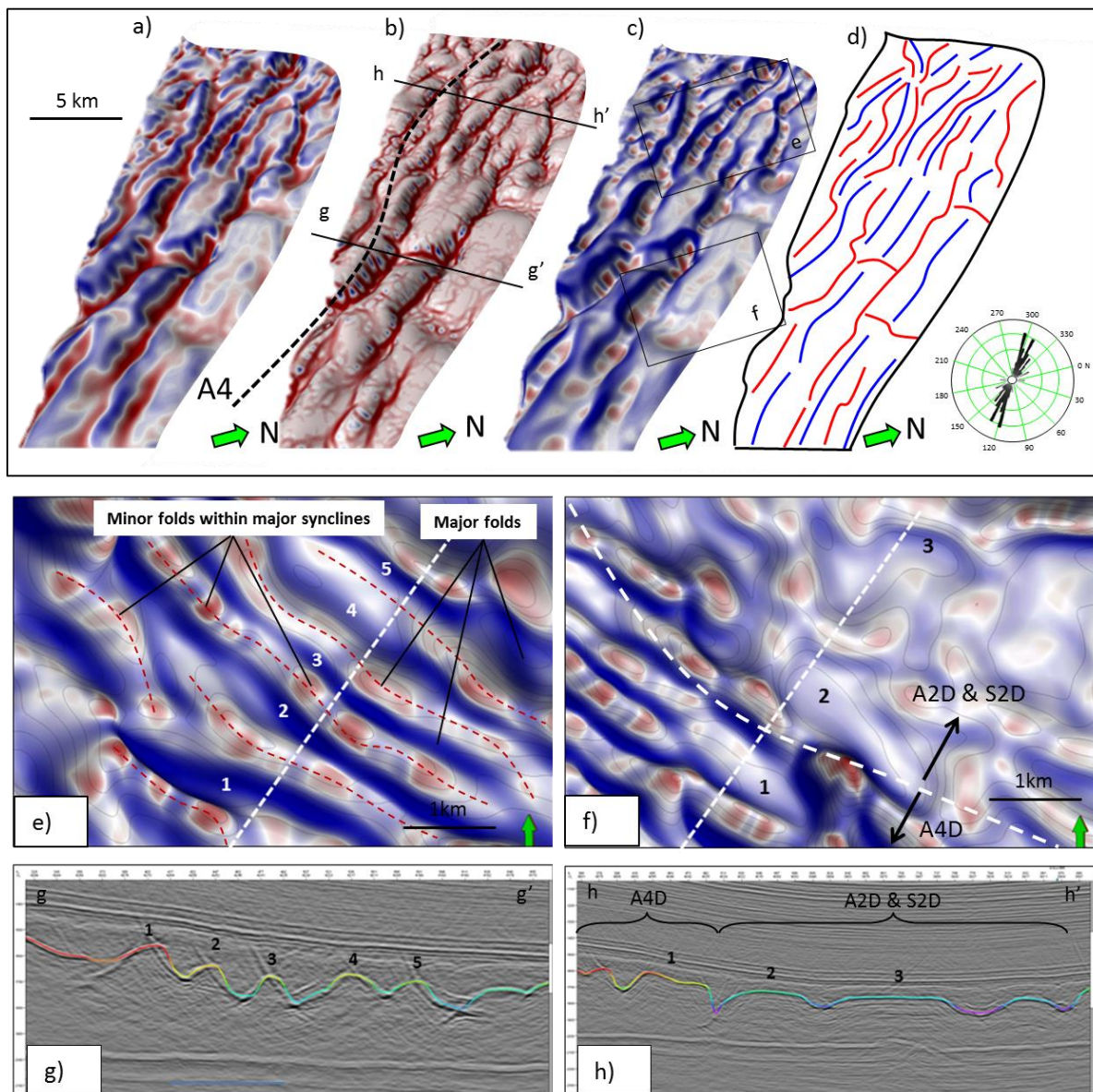
Fig. 5.12: The Z3 Stringer below Anticline 4 Domain (A4D). (a) Mean curvature attribute displays the major anticlines and synclines of the Z3 Stringer. (b) Minimum curvature highlights major synclines and the detailed minor synclines. (c) Maximum curvature attribute displays the antiforms of the Z3 Stringer. (d) Annotation of the synclines (red lines) and anticlines (blue lines) shows well-aligned NW direction. (e) and (f) Zoom-in on the folds in (c). Note the details of minor folds within the major synclines. (g) Seismic profile across A4D shows that both anticlines and synclines are well-folded. (h) Seismic profile across S2D and A4D.

5.5.5 Anticline 5 Domain (A5D)

A5D is part of a small domal structure in the northwestern area of the Cavendish survey (Fig. 5.4). The full extent of the anticlinal structure is not covered by the Cavendish survey. The internal Z3 Stringer around the flanks of the domain is characterised by folds with inclined hinges and radial patterns, striking towards the centre of the domain (Fig. 5.13a, b). However, upright folds (e.g., Fig. 5.13a,b,c,d) are formed at the crest of the regional anticline. Regional syncline stringer folds form around the flank of the domain.

A seismic profile across the eastern folds displays frequent refolding of previously wider anticlinal hinges into smaller folds (Fig. 5.13e). The folds on the southern flank of the domain are characterised by narrow synclinal hinges and elevated wider anticlinal hinges (Fig. 5.13f). The anticlinal hinges are welded to the upper roof of the Zechstein-3 brittle layers by thinning of the Z3 salt and thickening of the Z2 salt (Fig. 5.13f).
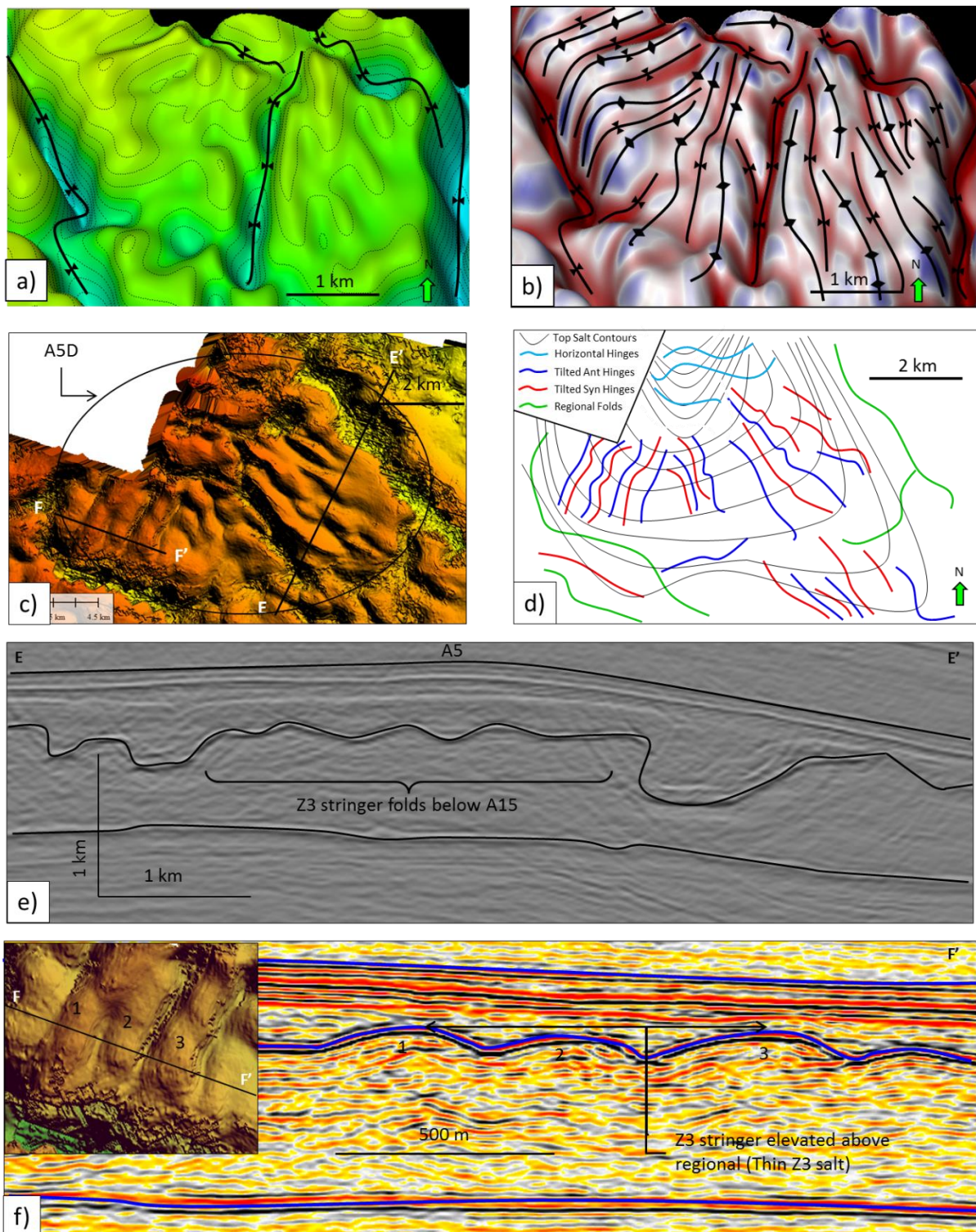
Fig. 5.13: The Z3 Stringer folds structural style below A5D. (a) TWT of the Z3 surface. (b) 3D Minimum curvature attribute shows radial and non-cylindrical folds with inclined and steeply dipping fold hinges. (c) Plan view of 3D time elevation surface of the Z3 Stringer folds below A5D. (d) Interpretation of the folds in (c) shows four styles of folds. (e) A 2D seismic profile passing through the NW–SE folds into the eastern flank of the domain. (f) Profile across the southern flank of the A5D through the NNE striking folds.

5.6   Discussion and summary

5.6.1 External salt structure

A1D, A3D, and A4D are considered to be well-developed anticlines with large fold amplitudes. A2D has smaller fold amplitude compared to A1D, A3D, and A4D. A1, A2, and A4 are interpreted as linear Top Salt structures, whereas A3D and A5D have sub-circular to polygonal structures (Fig. 5.4c). Based on the structure of Top Salt and thickness of the Zechstein salt, A1, A3, and A4 have been significantly folded, while A2 is the least folded anticline (Fig. 5.4a and b).

5.6.2 Tightness and wavelengths of the Z3 Stringer folds

The dominant fold types of the intra-salt stringer below A1D, A3D, and A4D are open folds with mean interlimb angles of 88°, 98°, and 94°, respectively (Fig. 5.7). Gentle folds are rarely found below these domains. However, the Z3 Stringer below S1D and S4D is gently folded, with average interlimb angles of 147° and 150°, respectively. Close and open folds are rarely observed below these domains. The stringer folds from the A2D domain display both open and gentle fold types with a mean interlimb angle of 122° (Fig. 5.7). Fold wavelength measurements of the stringer folds revealed smaller wavelengths below A1D and A4D than A2D, and much bigger wavelengths below synclinal domains S1D and S4D (Table 5.1).

In summary, the lowest fold interlimb angles and smaller fold wavelengths are found below mature anticlines (i.e., A1D and A4D), whereas wider interlimb angles and bigger wavelengths are observed below regional synclines (e.g., S1D and S4D). The A2D has anticlines with intermediate interlimb angles and wavelengths.

5.6.3 Two-dimensional evolution model

Using the profiles in Figure 5.6, the stringer kinematic evolution can be staged based on the magnitude of the deformation of the Top Salt surface. Each Top Salt anticline represents a certain amount of shortening, thus early stringer deformational styles are from areas below A2D, whereas late stages were noted from areas below A1D, A3D, and A4D.

The presence of flat stringer regions at the current structural configuration supports the quiescence of the stringer prior to salt tectonics (Fig 5.6a, c). It also underestimates the occurrence of syndepositional deformations or intra-salt stratigraphic and diagenetic processes that might change the geometry of the stringer (e.g., van Gent et al. 2011; Strozyk et al. 2014). Therefore, the stringer has been interpreted to be flat at early stages before the occurrence of any tectonic events in the basin (Fig 5.14a). Below less folded regions of the A2D, the stringer folds form regional low-amplitude upright gentle folds with broader hinges (Fig 5.6d and Fig 5.14b). However, below more folded regions of the A2D across the depocentre of the A2D, the stringer folds are folded by open and gentle folds (Fig 5.14c and 5.9h). In some cases, the synclinal hinges of these folds are narrow, while the anticlines have broader hinges (Fig 5.9h and 5.14d). This can be interpreted in two ways: (1) The original stratigraphic position of the stringer within the salt section where the salt above the stringer (Z3 Halite) is less than the salt below (Z2 Halite), and therefore it probably had enough space to generate synclines. However, opportunity for salt flow is limited by the small thickness and space available above the stringer and therefore resulted in wide anticlinal hinges. (2) The stringer is underlain by 35 m of potash salt, which is a weak K-Mg salt rock much less dense

than halite (ranges between 1.5 kg/m^3 and 1.8 kg/m^3 according to Urai et al. 2008). This might induce extreme rheological heterogeneities and high viscosity contrast with the stringer layer (Urai et al. 2008; Raith et al. 2015). However, such geometries of narrow synclinal hinges and broader anticlinal hinges are less developed in areas below highly shortened regional anticlines such as the stringer folds below the A4D and the A1D. The stringer below the A4D is well-folded and forms upright open anticlines and synclines with almost similar hinge widths (Fig 5.14d). The high shortening of the regional structure in the A4D area might overcome the influence of the rheological heterogeneities and allow the formation of well-developed anticline and syncline open-fold structures.

The final structural configuration of the Top Salt in the study area has been interpreted where the Top Salt anticline structure is bounded by two synclinal structures (Fig 5.14e). An example of such structure is the A1D (Fig. 5.4a, c). Unlike the A4D, the A1D is bounded by the major S1 to the south and the S3 to the north.

The occurrence of A1 between well-developed synclines (i.e., S1 and S3) creates steeper Top Salt flanks, which have an influence on the internal structural style of the stringer (Fig 5.15a). The Z3 Stringer below the flanks of the A1D tends to form inclined large-wavelength folds, with an obvious vergence away from the regional synclines (Figs. 5.14e, 5.15a, and 5.6d). The longer limbs of these folds are tilted parallel to the Top Salt surface. Although the A4 is well developed and has the maximum salt thickness below (Fig. 5.4a,b), such inclination and vergence of the stringer folds is not created below the southern flank of the A4D (Fig 5.15b). This is because the southern flank of the A4D is gentle, since the S2 has a smaller synclinal magnitude compared to S1 and S3 (Fig 5.15b). In some cases, the final phase of

shortening of the regional A1 might result in the formation of long-wavelength inclined folds at the flanks of the well-developed Top Salt anticline, while extreme shortening of the stringer folds is concentrated only at the crest of the anticline (Fig 5.15a,b). Although the stringer below A1 has been exposed to intensive deformation, the final structural configuration might give lower shortening results compared to those below anticlines of low to moderate amplitude.
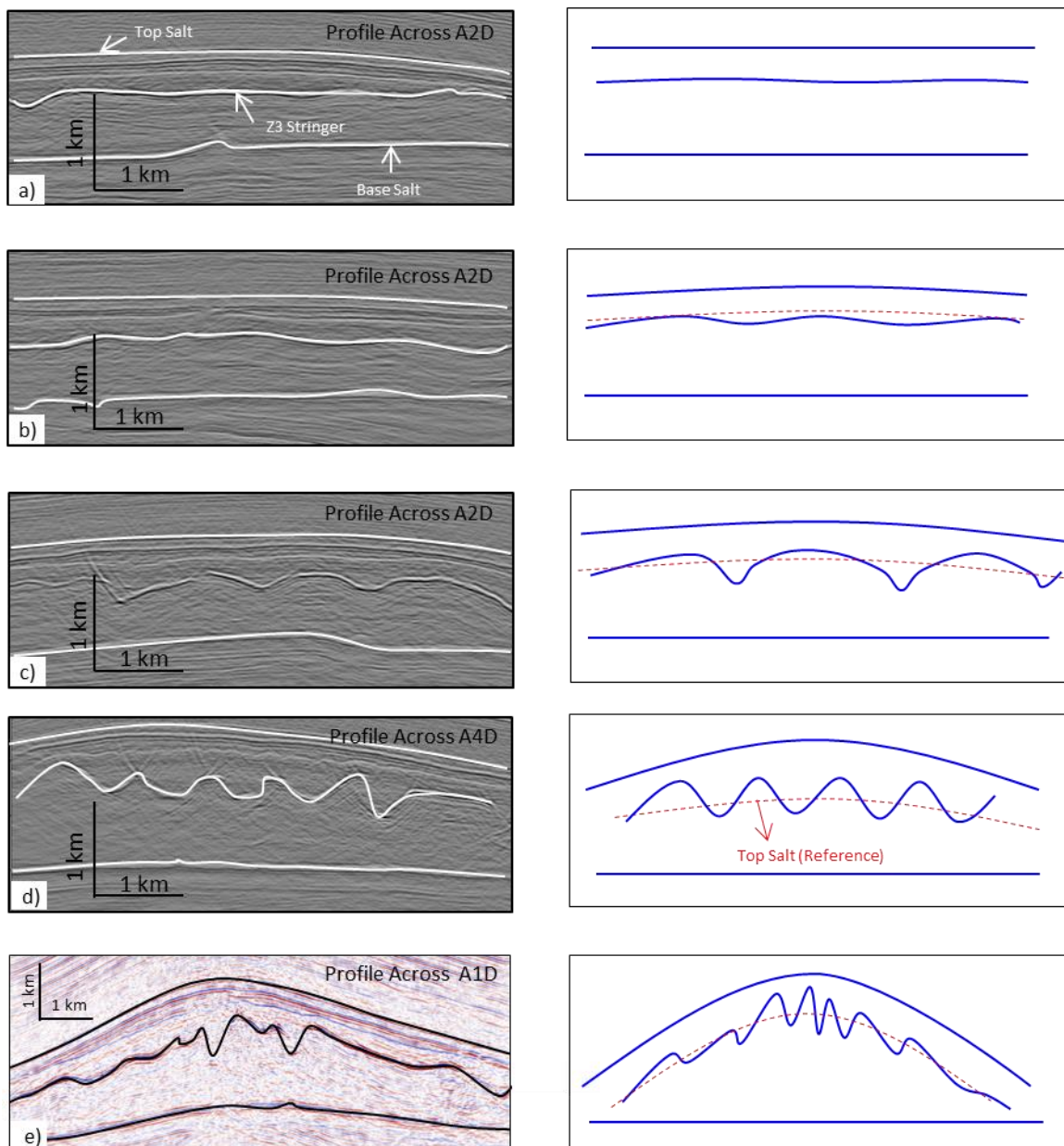
Fig. 5.14: Schematic showing Z3 Stringer fold evolution with increasing Top Salt shortening (left). The Top Salt is shifted downwards as a reference for the stringer anticline/syncline amplitudes (red lines).
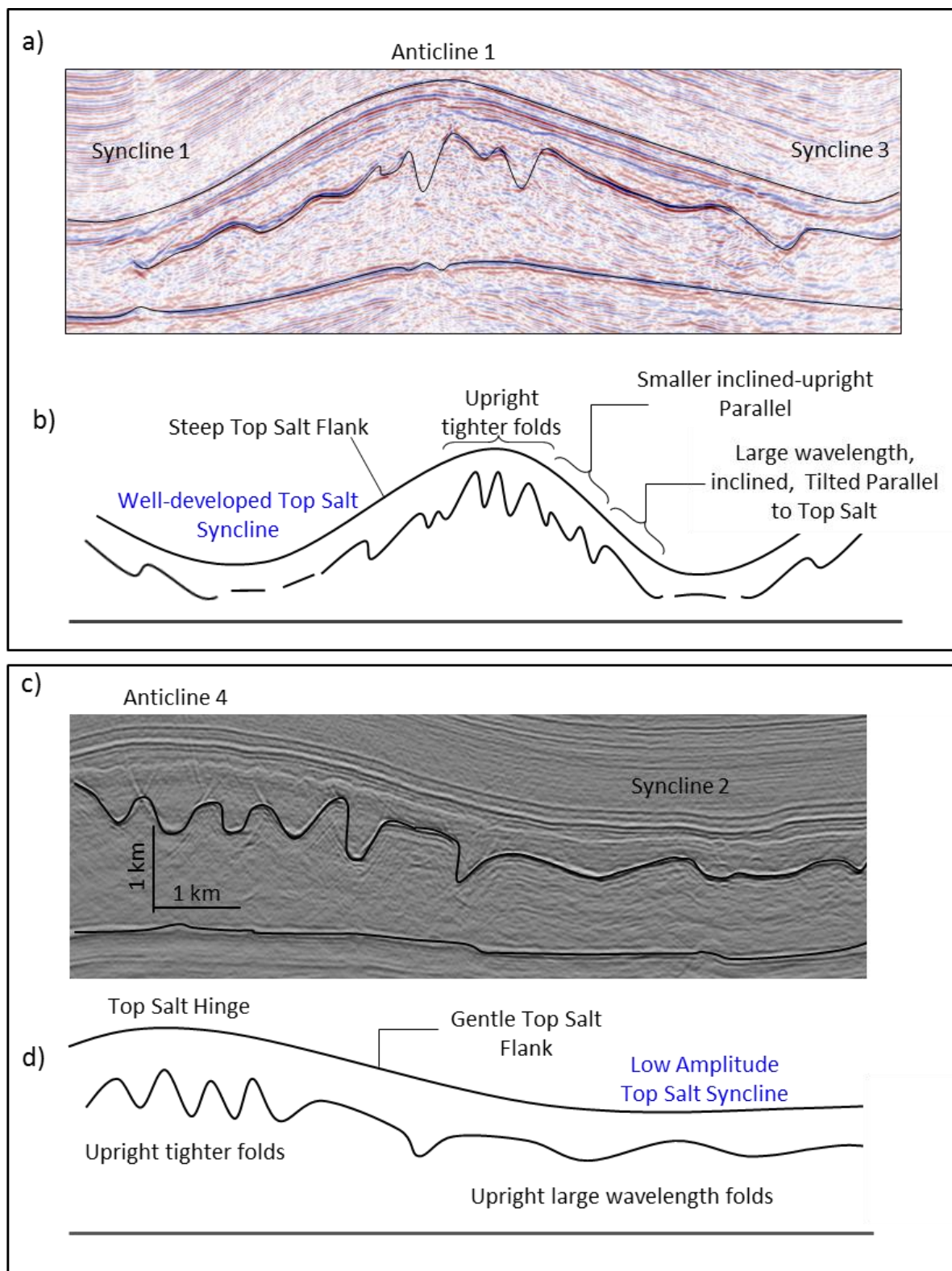
Fig. 5.15: The influence of Top Salt geometry on the internal structural style of the Z3 Stringer. (a) Steeper flanks at the sides of A1 form between well-developed synclines (S1 and S3). (b) Simplified 2D sketch shows the common structural style of the Z3 Stringer at such Top Salt geometries. (c) Z3 Stringer style below gentle flank of A4 because of the small amplitude of S2. (d) Simplified 2D sketch.

5.6.4 Three-dimensional evolution of the Z3 Stringer

5.6.4.1   Folds below Top Salt linear anticlines

The Top Salt and the Zechstein thickness maps show that A2 is less folded compared to A4 (Fig. 5.4b). The 3D view shows a clear change in the style of the folds below the A2D/S2D from those of the folds below the A4D (Fig. 5.16a). Although the A2 is linear in shape, the stringer folds below the A2D have sinusoidal and wide anticlinal hinges with long wavelengths (Fig. 5.16a). The NW–SE elongated A4D in the southern part of the basin experienced upright curvilinear NW–SE internal stringer folds. The tightness and the alignment of these folds increase towards the core of A4 (Fig. 5.16a). The hinge lines of the major maximum and minimum curvatures (major stringer synclines and anticlines) of these folds are parallel to the regional structure (Fig. 5.16b). However, along the hinge lines of these anticlines and synclines, minor curvatures of depressions and culminations occur (Fig. 5.16c). This means that the folds are non-cylindrical in shape, and there are anticlinal and synclinal saddles or elongated domes and basins (Fig. 5.16c).

The southern and northern flanks of the A1D are largely influenced by the adjacent S1 and S3. These synclines have an impact on shaping the folding style at the flanks of the A1D (Fig. 5.15a). The basal part of the flanks of the A1D is characterised by large-wavelength verging folds (Fig. 5.17b). These folds are driven by salt evacuation from synclines and are similar to passive flow folds (Figs. 5.17b,e). Plunging folds that are perpendicular to the regional structure (Fig. 5.17b,e) characterise the middle steeper flank in the centre of the domain. Similarly, hinge folds formed at the edges of the domain with strikes parallel to the regional structure (Fig. 5.17b,e). The hinges of the stringer folds are gradually elevated from lower

depths in the lower part of the domain flanks to shallower depths in the upper part of the flanks, and finally fatten at the crestal zone of the regional anticline (Fig. 5.17c,d). Tighter, higher-amplitude upright folds with consistent NW–SE striking folds that are parallel to the regional structure (Figs. 5.17b,e) characterise the stringer folds below the core of the anticline.
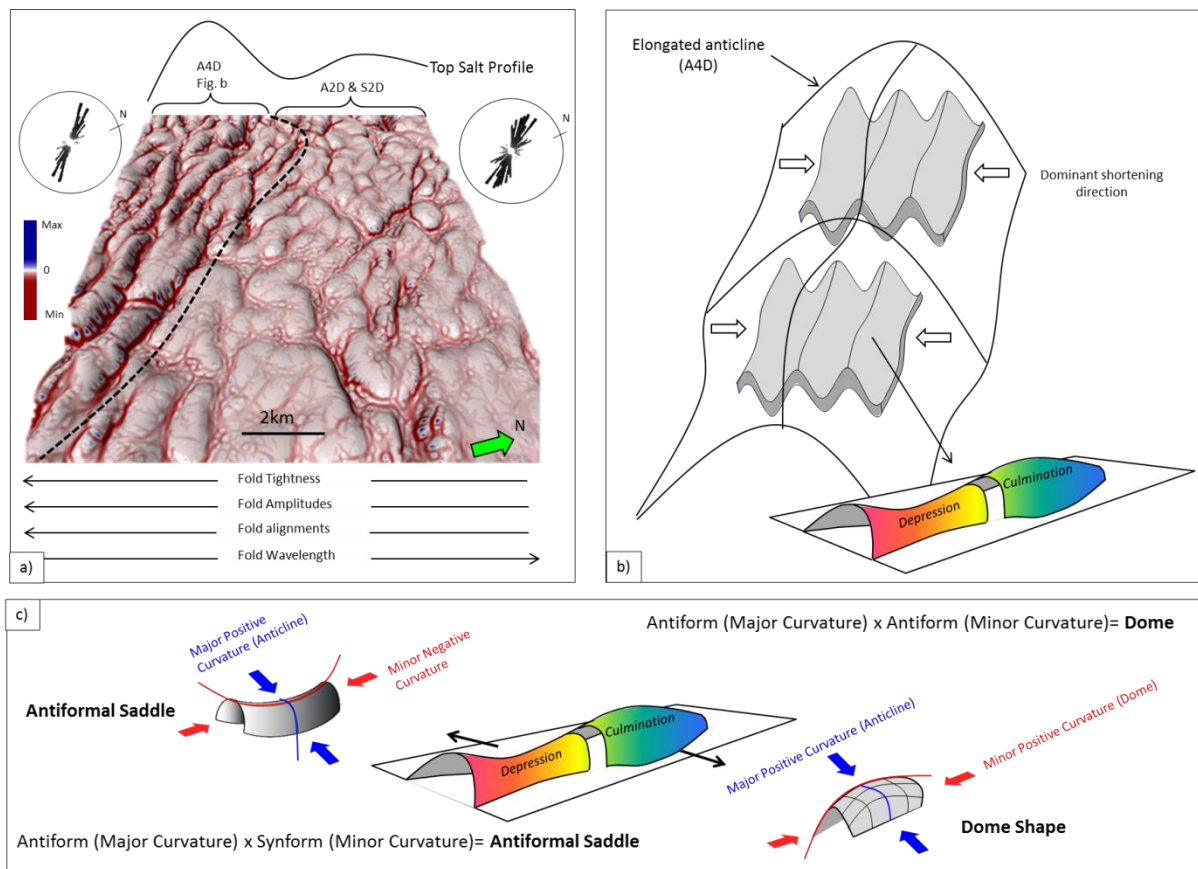
Fig. 5.16: The Z3 Stringer structural styles below the elongated A2D and A4D.
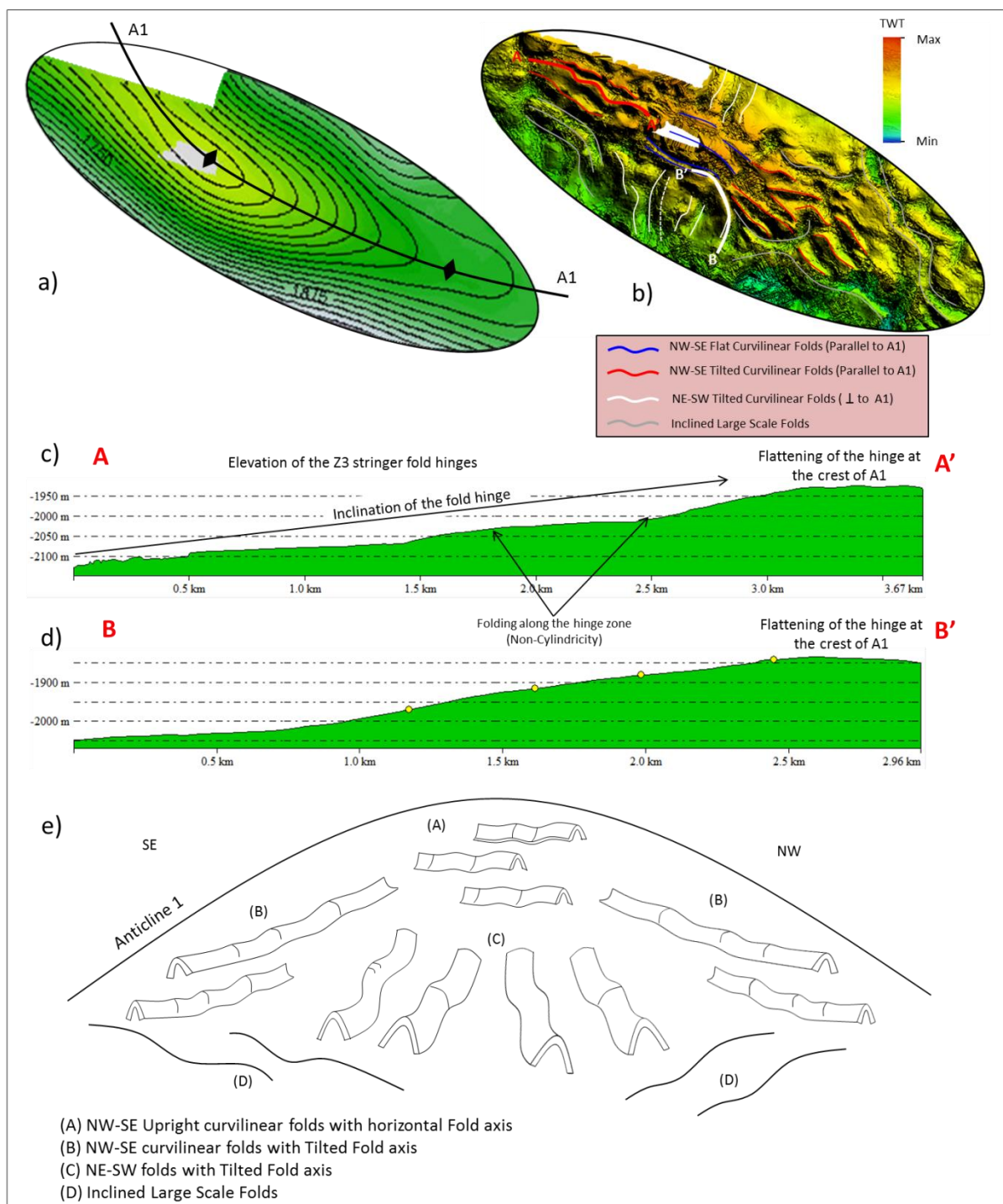
Fig. 5.17: The Z3 stringer structural styles below the elongated A1D. (a and b) 3D time surface of the Z3 Stringer below A1D. Four groups of folds at different part of the domain. (c and d) 2D cross-section along the hinge zone of the stringer folds (see (b) for locations). Note the inclination of the hinges at the flanks and the horizontal hinge shapes at the anticline crest. (e) 3D sketch summarizing the fold styles at each part of the domain.

5.6.4.2   Folds below non-elongated Top Salt anticlines

Non-elongated anticlines such as the A3D and A5D form more complex stringer folds than those below linear anticlines (e.g., A4D). The folds below the A3D are multidirectional and highly non-cylindrical in shape (Fig. 5.18a). The folds characterised by basins and domes are connected by saddle synclines and anticlines (Fig. 5.11). The majority of these folds are non-cylindrical upright folds; however, their limbs are also folded to form steeply plunging fold axes (Fig. 5.10b and Fig. 5.18b). Such complex multidirectional structural styles of the stringer folds are compatible with the external shape of the A3D. Unlike A4, the dome and non-elongated shape of the A3 might create constrictional contraction inside the domal A3D area.

The folds below the flanks of the A5D are curvilinear non-cylindrical folds (Fig. 5.18c), with hinges and minor curvatures along the hinge axes (Fig. 5.13b). The folds form a radial pattern around the regional flanks of the domain. The inclination of the axes of the folds that form around the domain flanks decreases away from the crest of the anticline to very shallow degrees at the lower part of the flanks (Figure 5.17). However, the folds that occur close to the crest of the A5 have sub-horizontal fold axes but with multidirectional strikes (Fig. 5.18c, d). Such geometrical shapes of the stringer fold structures can be interpreted as resulting from a constrictional mechanism as the stringer moved along with the salt flow into the salt structure (Fig. 5.18d).
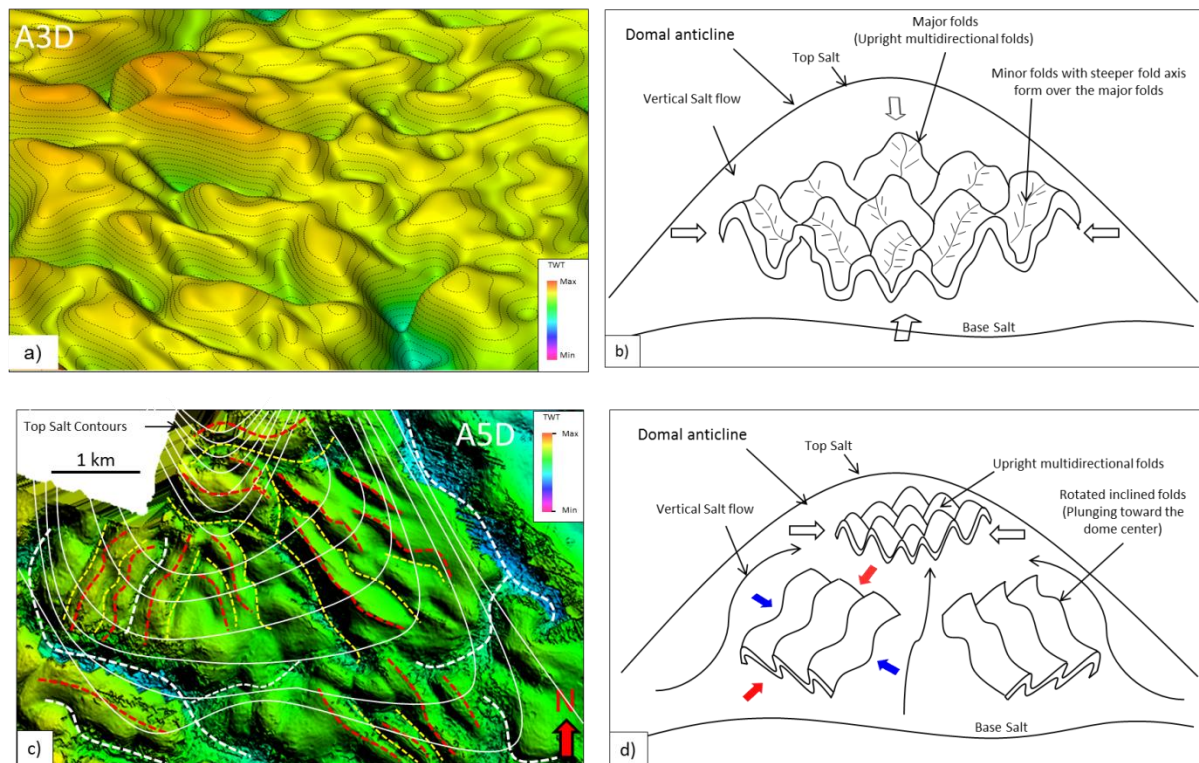
Fig. 5.18: Stringer folds below non-elongated Top Salt anticlines. (a) 3D time surface of the stringer folds below A3D. (b) 3D sketch of the Z3 Stringer folds characterised by major non-cylindrical upright domes and basins with minor folds with steeper fold axis. (c) Intra-salt folds below part of the circular A5D. The white lines represent the contours of the Top Salt anticline. (d) 3D sketch of the domal top salt structure in (c) shows radial linear tilted folds axes at the flanks of the regional structure, while non-cylindrical folds with multidirectional strikes form at the core of the regional anticline.

5.7   Conclusions

The internal Z3 Stringer in the Cavendish area in the Southern North Sea was used to investigate the internal kinematic evolution of the intra-salt structures within areas of salt thickening (i.e., Top Salt anticlinal structures). Stringer structural styles have been gathered from five Top Salt anticlinal structures for qualitative and quantitative descriptions, which helped to understand their kinematic evolution. The magnitude of Top Salt anticlinal deformation is used as a reference to analyse the stages of deformation of the intra-salt.

- The internal deformation of the Z3 Stringer within areas of Top Salt anticlines is largely contractional-related deformation of fold structures with variable scales and strain magnitudes.

- Unlike observations of the intra-salt multi-layered evaporites in the Eastern Mediterranean (e.g., Cartwright et al. 2012), this study revealed highly non-cylindrical buckled folds. The degree of non-cylindricity increases when the external shape of the Top Salt is spherical, allowing the development of multidirectional, steeply plunging intra-salt folds.

- Top Salt elongated and well-developed anticlinal structures generate non-cylindrical curvilinear folds (e.g., A4D). These folds formed along the hinge zone of the regional anticline, with tilted fold axes below the flanks of the regional anticline and horizontal to sub-horizontal fold axes in areas within the crest of the regional anticline. Top Salt non-elongated and well-developed anticlinal structures generate highly non-cylindrical multidirectional upright folds associated with steeply dipping fold axes (e.g., A3D). Such folds might

be elevated during the rise of the domal shape to form radial patterns of steeply dipping fold axes (e.g., A5D).

- The kinematic evolution of the initially flat Z3 Stringer started with the development of large-wavelength gentle folds during early stages of shortening of the anticlinal structures (e.g., folds within A2D), followed by folds with higher amplitude and tightness, (close to open folds) with more progressive shortening of the Top Salt anticline (e.g., folds within the A4D). The final phase of shortening of the regional anticlines produced long-wavelength, inclined and highly plunging stringer folds at the flanks of the regional structure, and extreme shortening of tight folds at the crest of the regional anticline (e.g., folds within the A5D).

Chapter 6: Salt tectonics and stratigraphy of the Ara Group Evaporites in the Birba Area, South Oman Salt Basin

Abstract

This study describes the stratigraphy and regional structural evolution of the Ara Group evaporites and the associated intra-salt carbonate stringers in the Birba area in the South Oman Salt Basin. A combination of 3D seismic reflection data, three regional 2D seismic lines, and well data was used for this purpose. The chapter discusses the regional salt tectonics in the basin and describes the structure and stratigraphy of the stringers on a regional scale. From the interpretation of wireline logs, the lithology of the Ara Group includes halite, limestone, dolomite, and anhydrite. Seismic-well calibration revealed the presence of at least five intra-salt carbonate stringers in the Birba Area. The lower four stringers are observed both on seismic and well data. The upper A5C stringer is locally deposited and significantly discontinuous, and thus is rarely found. The carbonate stringers in the Birba area have limited original stratigraphic extent and isolated distributions, and were further fragmented during subsequent salt tectonics. Seismic interpretation of the Top Salt shows the presence of five minibasins, MB-1 to MB-5, and large structural walls of thick salt, formed by down-building during sediment loading. The sediments that deposited within the minibasins are characterised by distinctive syn-kinematic packages which were filled into the depocentre through a complex interaction of sediment loading, faulting, and halokinesis. The dynamic evolution of the basin fill is indicated by striking shifts in the location of the depocentre.

6.1   Introduction

6.1.1   Importance of the Ara Group

The South Oman Salt Basin is composed of six evaporite-carbonate cycles of infra-Cambrian age known as the Ara Group evaporites. These evaporites form the primary petroleum system for the South Oman Salt Basin (SOSB) and represent a unique self-charging petroleum play (Al-Siyabi 2005; Amthor et al. 2005; Schoenherr 2007). The Ara Group consists of salt walls and diapirs, which contain four to five carbonate stringers 20–200 m thick termed "A1C–A5C", which formed at depths of 3 to 5 km (Al-Siyabi 2005). The carbonate stringers are significantly deformed by halokinesis (Peters et al. 2003; Al-Siyabi 2005; Reuning et al. 2009).

The most important explored and producing fields from the stringers in the South Oman Salt Basin are the Birba and Harweel oil fields (Al-Siyabi 2005). These fields contain well-developed intra-salt carbonate stringers containing carbonate source rocks, which are in close proximity or even within layered reservoirs that are sealed by the surrounding salt (Amthor et al. 2005). The reservoirs are commonly overpressured, and consist of porous dolomitic carbonates encased in salt at depths of 3–5 km (Al-Siyabi 2005).

However, some drilled reservoirs have failed to produce at significant rates due to poor reservoir quality related to diagenetic processes such as porosity plugging by bitumen and evaporite minerals (Al-Siyabi 2005; Schoenherr 2007). The Ara carbonate stringers also represent significant drilling hazards due to their fluid overpressure (Kukla et al. 2011). Hence, it is imperative to understand their complex deformation, reservoir quality and distribution, fault system and sealing capacity, and the depositional environments.

6.1.2 Aims of this chapter

The aims of this chapter are the following:

- To provide a detailed lithological description of the Ara Group and understand the petrophysical properties of rock salt and the associated A1C–A4C stringers.

- To understand the influence of the stratigraphy of the evaporites on the structural styles of stringers.

- To establish a stratigraphic framework of the Ara carbonate stringers before halokinesis in order to be able to differentiate the stratigraphic features of stringers from those deriving from salt tectonics. Understanding the original depositional geometry of the stringers will help to interpret the structural features and improve reservoir quality and prediction.

The following steps were taken to achieve the above-stated aims:

- Well-to-seismic calibration, to accurately identify and interpret the four seismically visible stringers and understand their seismic character.

- Well-to-well correlation using wireline logs, to understand the petrophysical properties of the evaporite facies.

- Vertical and lateral stratigraphic description of the stringers, to understand the extent of the stringers, the lateral lithological changes, and the depositional environment of the stringers.

- Tectono-stratigraphic evolutional models of the basin using 2D seismic profiles.

6.2   Data and methods

The data used in this chapter include the following:

1. An onshore 3D time migrated seismic survey from the Birba area in the South
    Oman Salt Basin (Fig 6.1) is a wide azimuth acquisition survey that covers a
    surface of about 2,100 km^2. The acquisition and processing seismic
    parameters of the survey are shown in Table 6.1.

2. Three regional 2D seismic lines crossing the 3D data were used to
    understand the regional setting of the salt basin (Fig 6.1).

3. The data also include 28 wells that penetrated the Ara Group and the
    associated stringers (Fig 6.1). These wells were used to map and identify the
    stringers and other key horizons, as well as to examine the stratigraphy of the
    evaporites.

Eight key horizons have been mapped through all the 3D Birba survey (Fig. 6.2).
These include Base Salt (A0C), Top A1C, Top A2C, Top A3C, Top A4C, Top Salt,
Base Natih Formation, and Top Natih Formation. Top and Base Salt were interpreted
to understand the thickness and geometry of the salt layer. Top Salt is a very
important surface that displays salt structures in the area such as salt walls, salt
minibasins, and minibasin flanks. The overburden horizons, Top and Base Natih,
were used to analyse the overburden megasequences. Other overburden horizons
were only used for local analsyis such as understanding the development of
minibasins (e.g., MB2 in section 6.5).
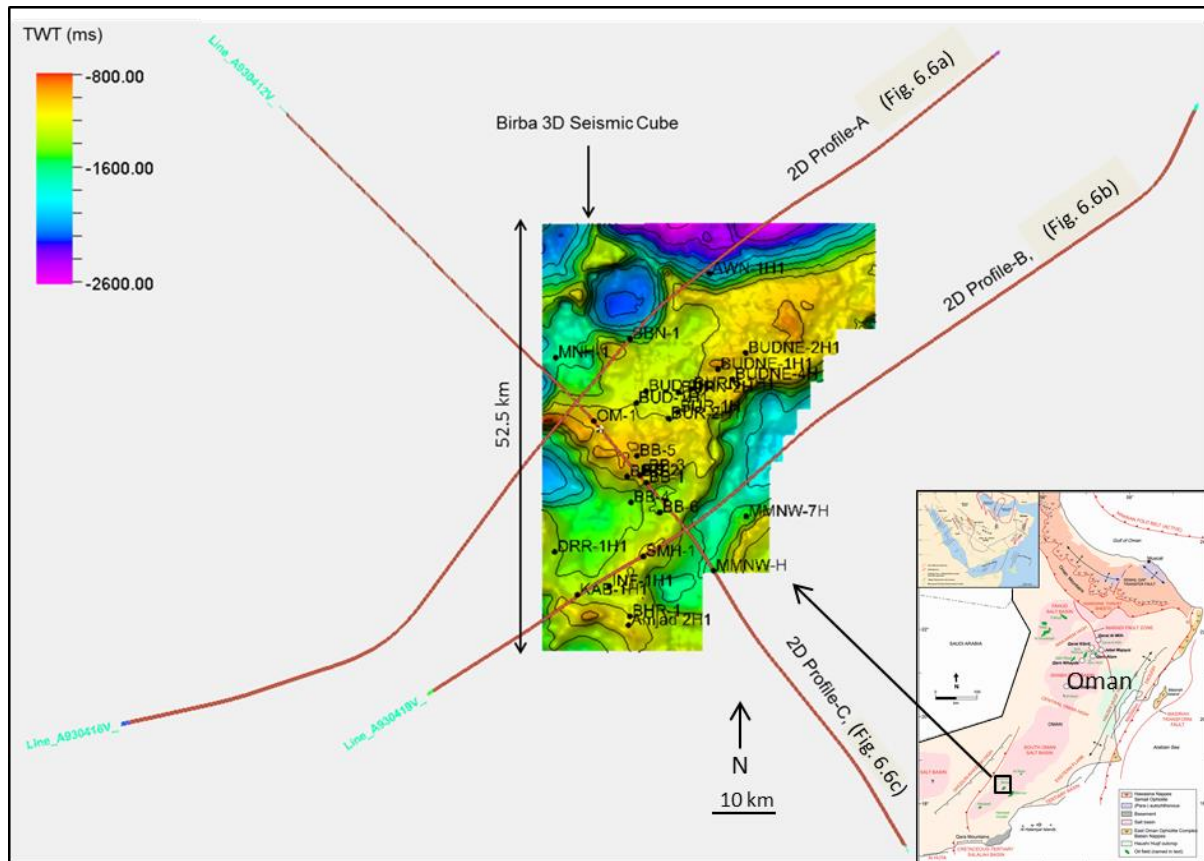
Fig. 6.1: The data used in this chapter include a 3D seismic cube shown here with the Top Salt surface, three regional 2D lines with NW and NE strikes, and 28 wells that penetrated the carbonate stringers. For better display of the wells see (Fig. 6.7). For coordinates and location of the study area see (Fig. 6.3).

Table 6.1: Acquisition and processing geophysical parameters of the Birba 3D WAS survey.

Receivers	25 × 200 m
Sources	50 × 50 m
Frequencies	6 to 86 Hz
Acquisition CMP	12.5 × 25 m
Processing CMP	25 × 25 m
Processing Fold	2000
In-line Offsets	±4.9875 km
X-line Offsets	±3.975 km
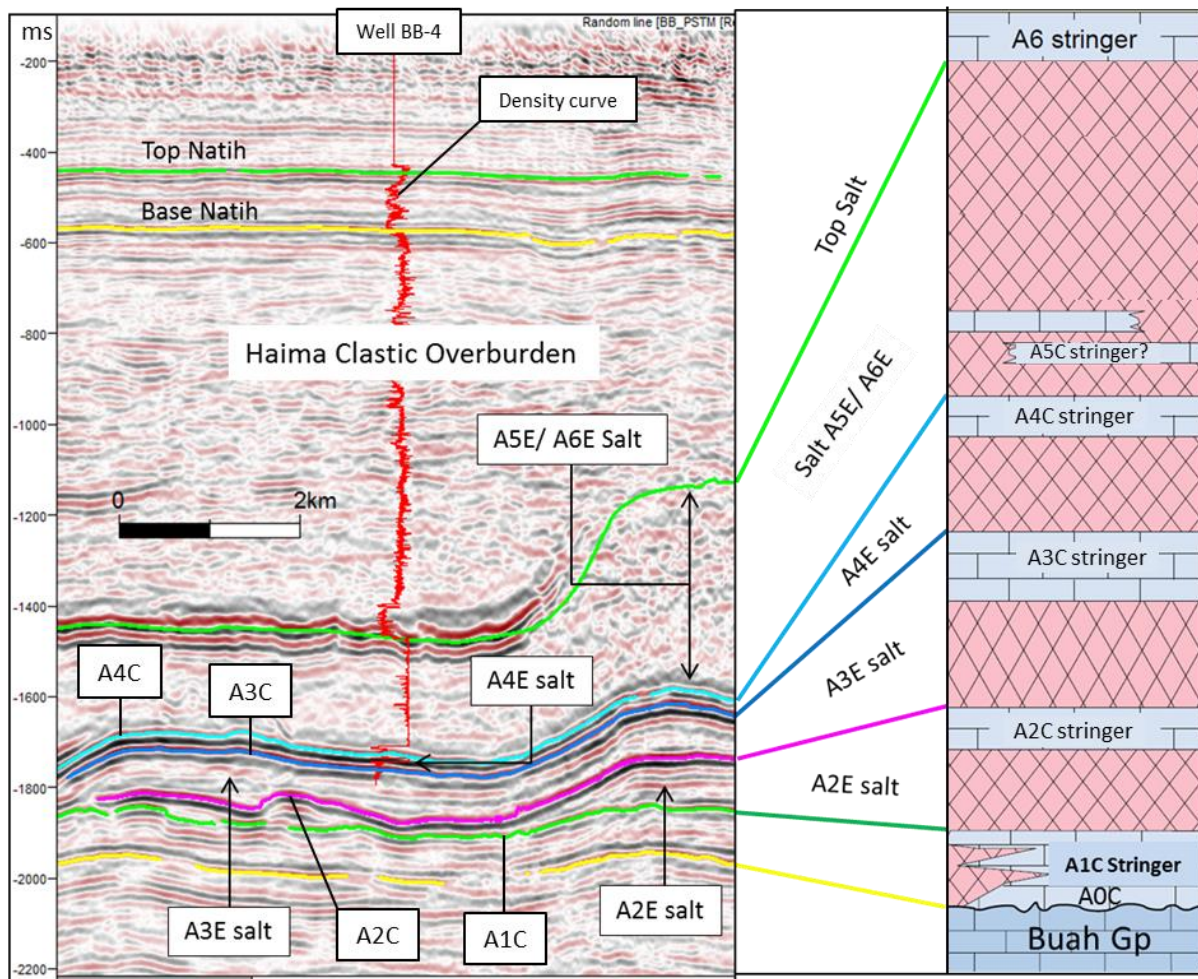
Fig. 6.2: (Left) Seismic section displays the key horizons interpreted in this chapter. The intra-salt carbonate stringers include A1C, A2C, A3C, and A4C, with A2E, A3E, and A4E salt intervals in between. The upper A5E and A6E halites form the most thickness of the evaporites. Note that the Top Salt surface is seismically not imaged to the right. The A4C and A3C stringers are close to each other and separated by a thin halite unit (A4E), as represented by the right shift in the density curve. Above the salt is the Haima Supergroup, mainly composed of clastic units of sandstone and shale.

6.3   Geological setting

Oman is located in the eastern part of the Arabian Plate (Fig. 6.3). This tectonic plate is bounded by a collision margin to the north and northeast (Taurus/Zagros Zone), rifted margins to the southeast (Arabian Sea, Gulf of Aden), the Red Sea to the southwest, and a strike-slip margin to the west (Dead Sea transform fault), (Al-Barwani and McClay 2008) (Fig. 6.3). The South Oman Salt Basin (SOSB) is one of three restricted salt basins that include the Ghaba Salt and the Fahud Salt Basins (Fig. 6.3).

The SOSB is an asymmetric NE–SW striking salt basin with a lateral extent of 400 km and a width of 150 km. The basin is characterised by a series of salt ridges and minibasins that formed above a NW-striking Proterozoic basement (Al-Barwani and McClay 2008). The SOSB is bounded by the Ghudun High and Western Margin to the west, the Tertiary Basin to the east, and the Central Oman High to the north (Fig. 6.3).

The case study area is in the Birba Oil Field, which is located in the southern part of the SOSB, northeast of the Harweel Field and west of the Marmul Field (Fig. 6.3). Six surface-piercing salt domes crop out in the desert of interior North Oman in the Ghaba Salt Basin (Fig. 6.3). The outcrops provide significant information on the dynamics of the Ghaba Salt Basin, and an analoge for the deep buried carbonate stringers in the SOSB (Peters et al. 2003; Al-Siyabi 2005; Reuning et al. 2009). However, until now, very little data have been published on these prominent topographic and geological features (Peters et al. 2003; Reuning et al. 2009).
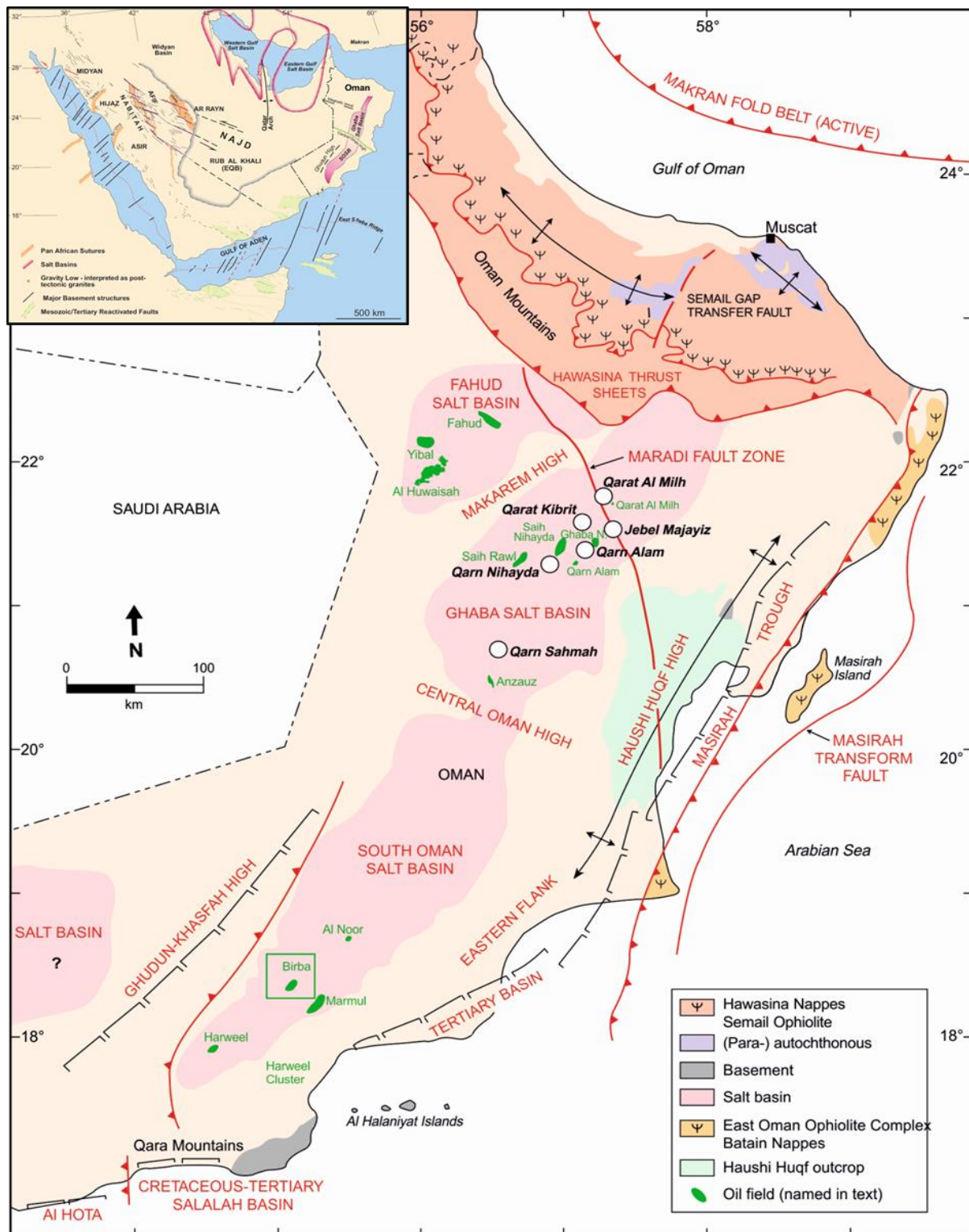
Fig. 6.3: Tectonic map of Oman with oil fields displaying the distribution of the three Oman Salt Basins i.e., South Oman Salt Basin (SOSB) in the south, Ghaba Salt Basin in the north, and Fahud Salt Basin in the northwest. Note the SW–NE trend of the SOSB. The six Ara salt domes that outcrop in the Ghaba Salt Basin are shown as white circles. The study area (green square) is located in the southwestern part of the South Oman Salt Basin (after Peters et al. 2003).

6.4 Chronostratigraphy of the South Oman Salt Basin

6.4.1 Overview and background

The sub-salt deposits in the South Oman Salt Basin belong to the Neoproterozoic Huqf Supergroup, which contains both continental siliciclastic and marine carbonate of the Abu Mahara and Nafun Formations (Fig. 6.4). These have been deposited in a strike-slip setting followed by tectonic quiescence and subsidence (Al-Siyabi 2005; Amthor et al. 2005). Later uplift created topographic changes, segmentation of the basin, and fault-bounded sub-basins, which were filled by the Ara Group in the Late Neoproterozoic (Al-Siyabi 2005). Regional differential subsidence of the basin in the Late Neoproterozoic and during the deposition of the Ara Group led to the formation of a transgressive to highstand environment and the deposition of carbonate/evaporite cycles (A0–A6). The cycles allowed the deposition of at least six isolated carbonate layers known as the Ara carbonate stringers, with thickness ranging from 20 to 200 m (A1C–A5C), at the lower part of the group, and A6C at the top of the salt (Mattes 1990; Loosveld et al. 1996; Al-Siyabi 2005) (Fig. 6.4).

In the Early Cambrian, massive continental clastic sediments were derived from basement highs in the west and deposited into the Ara Group, resulting in regional differential loading of the basin, which led to intense deformation and fragmentation of the intra-salt carbonate stringers (Al-Siyabi 2005) (Fig. 6.5b). This event is obvious on seismic data, and is related to the Nimr and Amin Groups of the lower Haima Supergroup (Al-Barwani and McClay 2008) (Fig. 6.4 and Fig. 6.5b). The Haima Supergroup is significantly variable in thickness, largely controlled by halokinesis, and reaches up to 2500 m in thickness of clastic deposits within minibasins and thinner deposits over elevated salt walls and salt domes (Fig. 6.5b). In the Middle to

Late Cambrian, growth faults over the salt ridges and the reactivation of basement faults created a second phase of salt tectonics (Loosveld et al. 1996) (Fig. 6.5b). The end of halokinesis is indicated by the presence of the conformable and horizontal layers of the Natih and overlying formations (Al-Barwani and McClay 2008) (Fig. 6.5b).
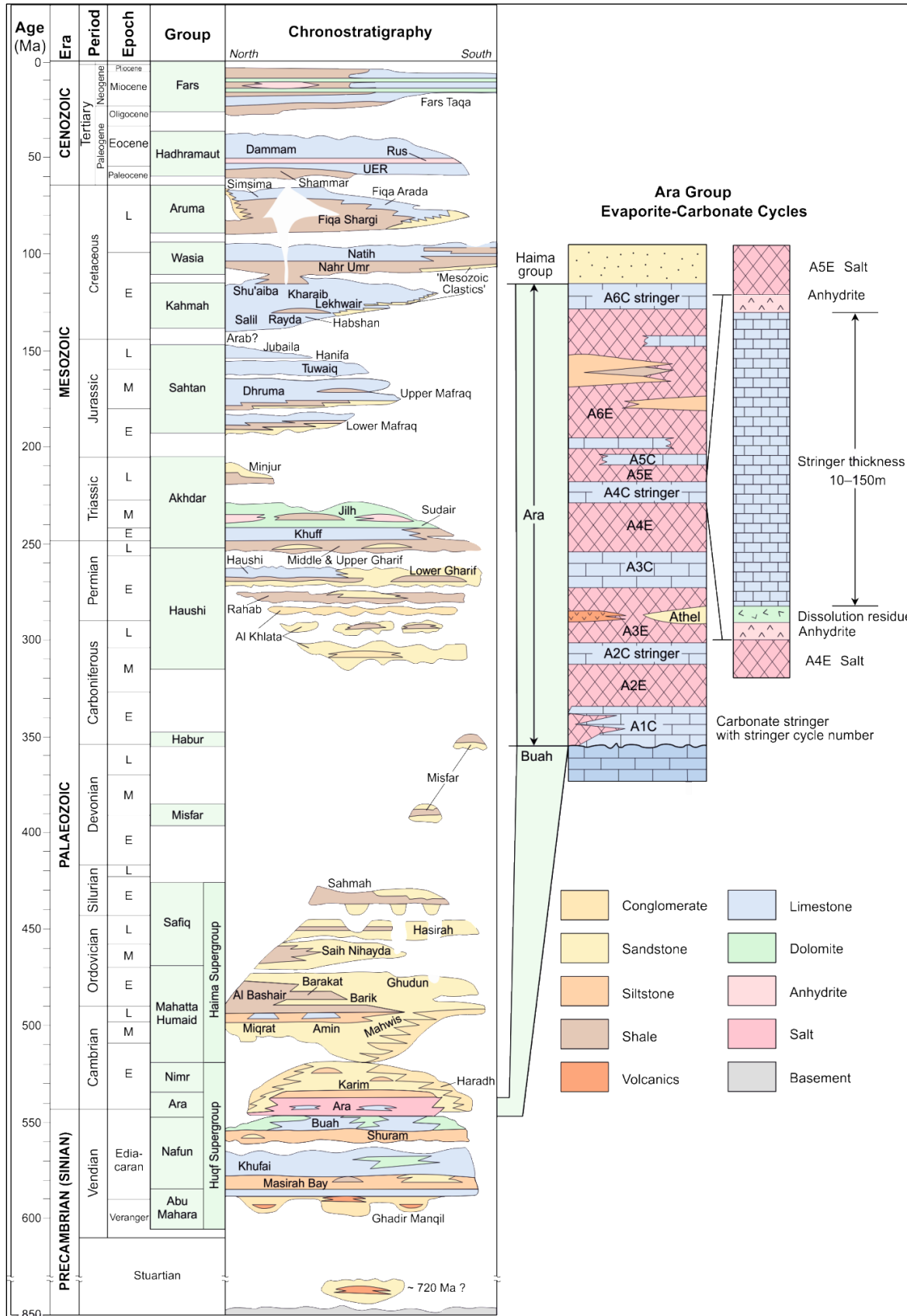
Fig. 6.4: Stratigraphy of the South and North Oman with a detailed stratigraphic column of the typical Ara Group. The brittle carbonate stringers are the A1C to A6C, and the halite salt intervals in between are the A1E to A6E (modified after Peters et al. 2003).
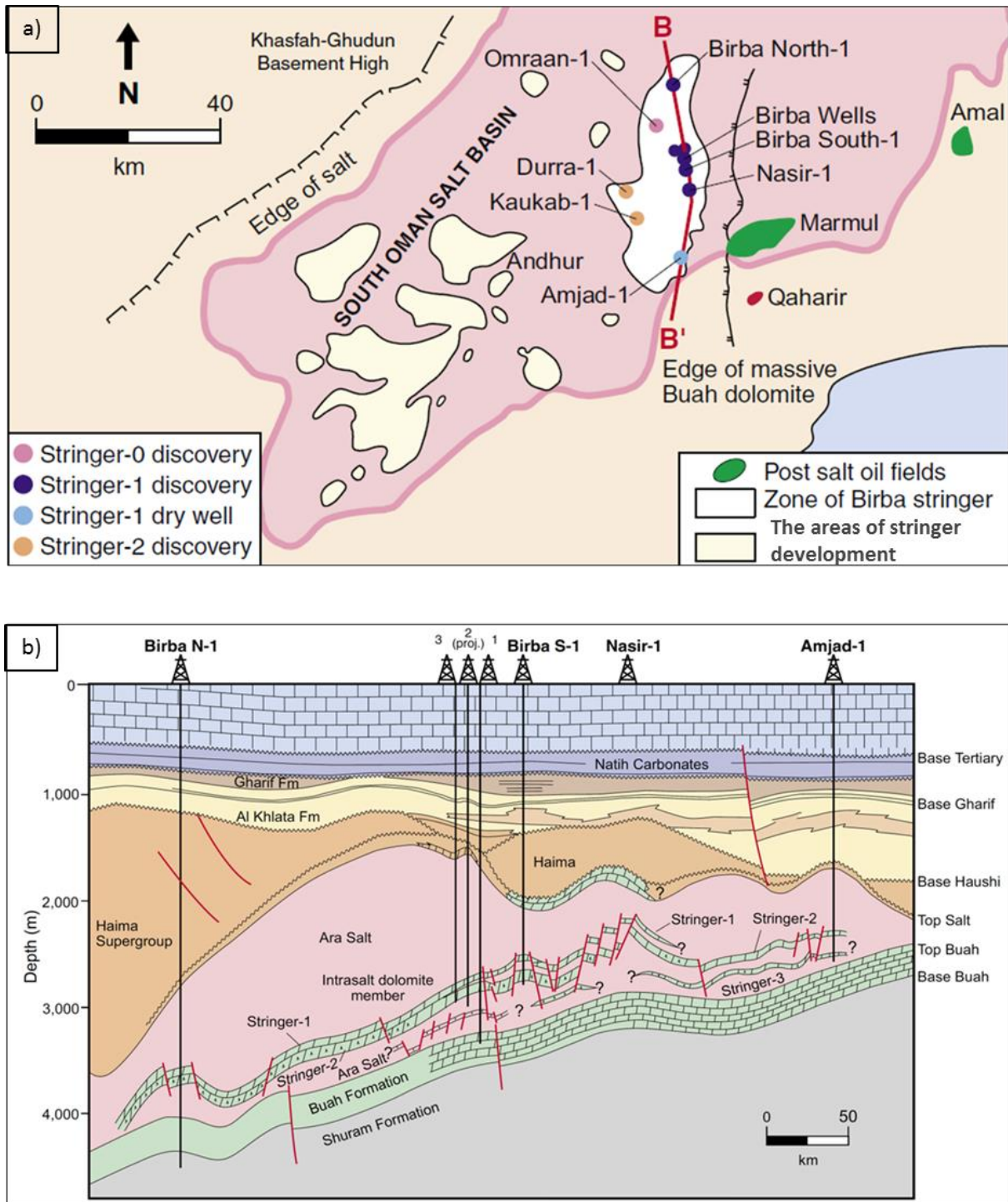
Fig. 6.5: (a) South Oman intra-salt play map created after Birba-1 (BB-1) hydrocarbon discovery. (b) Interpreted N–S seismic profile across the Greater Birba area showing the basin geometry, stratigraphic extent, and structural configuration of carbonate stringers (after Al-Siyabi 2005). Note that the carbonate stringers are classified as Stringer-1, 2, 3, and 4 from the top to the base, which is the old terminology of the stringers. Note the discontinuity of the A6C stringer at Top Salt in the middle (green coloured).

6.4.2   Regional seismic profiles across the Birba field

Three regional 2D seismic lines were used to describe the structure of the SOSB on a regional scale (Fig. 6.6). The basin is regionally tilted and deepening towards the northwest, associated with major thickness of the overburden, while shallowing towards the southeast with thinning of the salt layer and the overburden (Fig. 6.6c). It is clear that Top Salt-subsided regions are associated with a thick succession of the Haima Supergroup; thus, the variable salt thickness is largely controlled by halokinesis during post-salt deposits. However, there is no significant topographic change of the base Ara, and therefore it has a limited effect on the thickness of the Ara Group compared to Top Salt.

The stringers are not regionally continuous and display local distributions especially above sub-salt structural highs where marine carbonates are expected to be deposited (Fig. 6.6b,c). In some areas, the stringers are obvious with at least four visible layers. However, in other areas, for example, the southwest of KAB-1H1, only the lower stringer (A1C) is observed (Fig. 6.6b). In general, the intra-carbonate layers are largely prevailing in the Birba area. The interpretation of regional seismic lines indicates that the stringers are not laterally extended along the SOSB and can be isolated for tens of kilometres, which suggests that the distribution of the stringers is significantly influenced by their depositional environments.
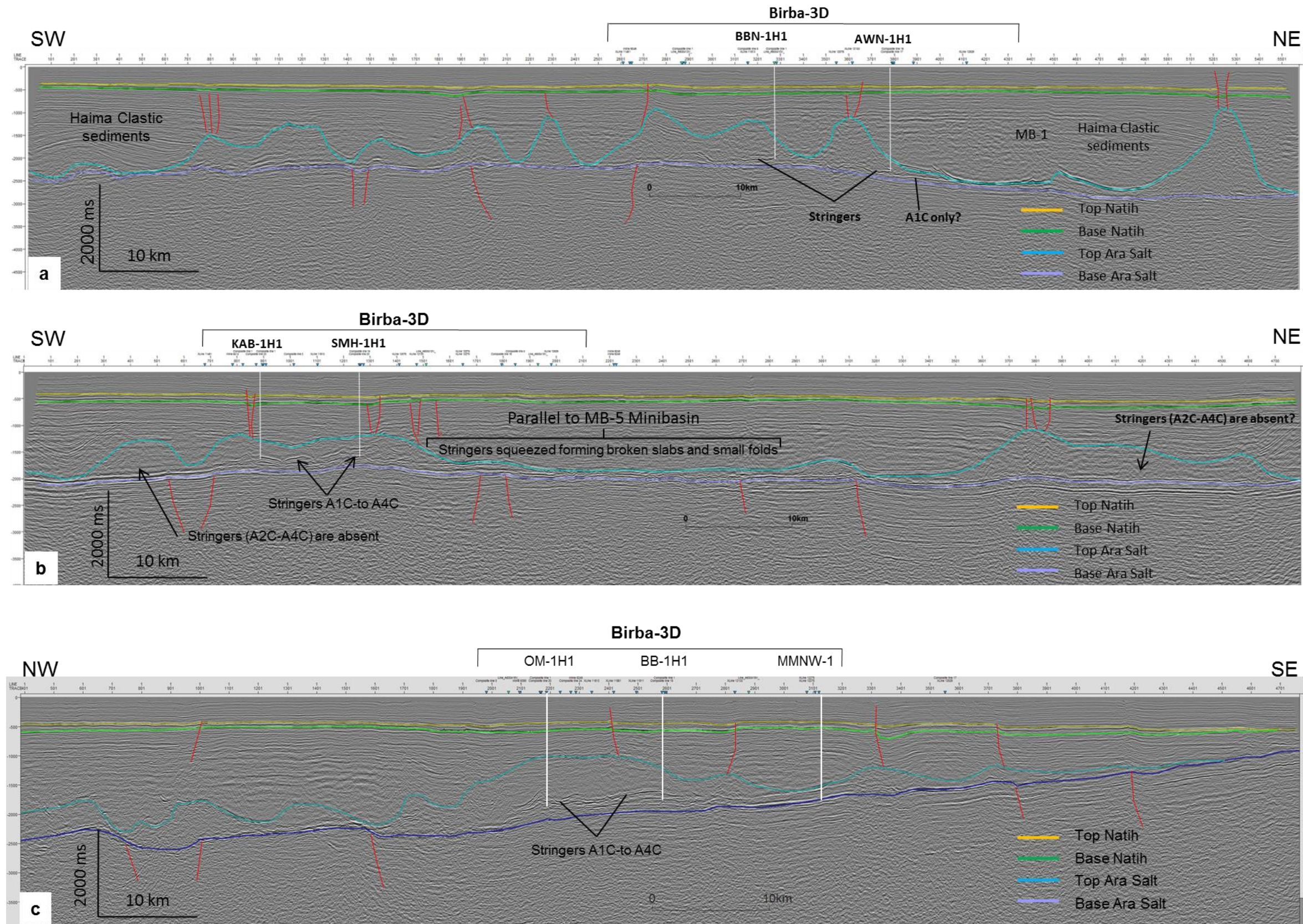
Fig. 6.6: Interpreted 2D regional profiles from the SOSB crossing the 3D Birba area and some wells (see Fig. 6.1 for location and Fig. 6.7 for wells and minibasins). Note the stringers are widely distributed in the Birba area. The Ara salt and the associated Ara carbonate stringers are thinning and terminating to the southeast. Profile B indicates that MB-5's long axis is oriented northeast, with a scale reach to 50 km.

6.4.3 Tectono-stratigraphy of the Birba Area

6.4.3.1   Top Salt structure

The seismic interpretation of the Top *S*alt in the Birba 3D survey revealed five minibasins (MB-1, MB-2, MB-3, MB-4, and MB-5) and irregular salt walls (Fig. 6.7). Minibasins are areas where salt evacuation creates synclines, which were later filled by additional sediments (Hudec 2009; Andresen et al. 2011; Li et al. 2012a; Peel 2014). The minibasins in the Birba area are randomly oriented with variable shapes. The shape of the minibasins is either rounded (e.g., MB-2) or elliptical with irregular flanks (e.g., MB-1, MB-3, MB-5; Fig. 6.7). MB-1 and MB-4 have an E–W trend, whilst MB-5 is striking NE (Fig. 6.7). A well-to-seismic correlation profile is used to identify the tops and the extent of the stringers in the basin (Fig. 6.8). The A1C–A4C stringers occur in the lower Ara Group and are vertically separated by halite intervals of variable thickness, ranging from 10 m to 200 m.

6.4.3.2   Large-scale megasequences

Four seismic profiles oriented N–S (Profile A–D) and an E–W profile (Profile E) were used to investigate the regional salt structures and the tectono-stratigraphy of the basin (Fig. 6.7).

Profile A

Profile A passes through the MB-1, MB-3, and MB-4, in the western part of the study area (Fig. 6.9). Clear indications of syn-kinematic deposits and variable thickness above the Ara Group were observed on seismic data. Specifically, the tilt and growth of the post-salt units indicate deposition during salt movement (Fig. 6.9).
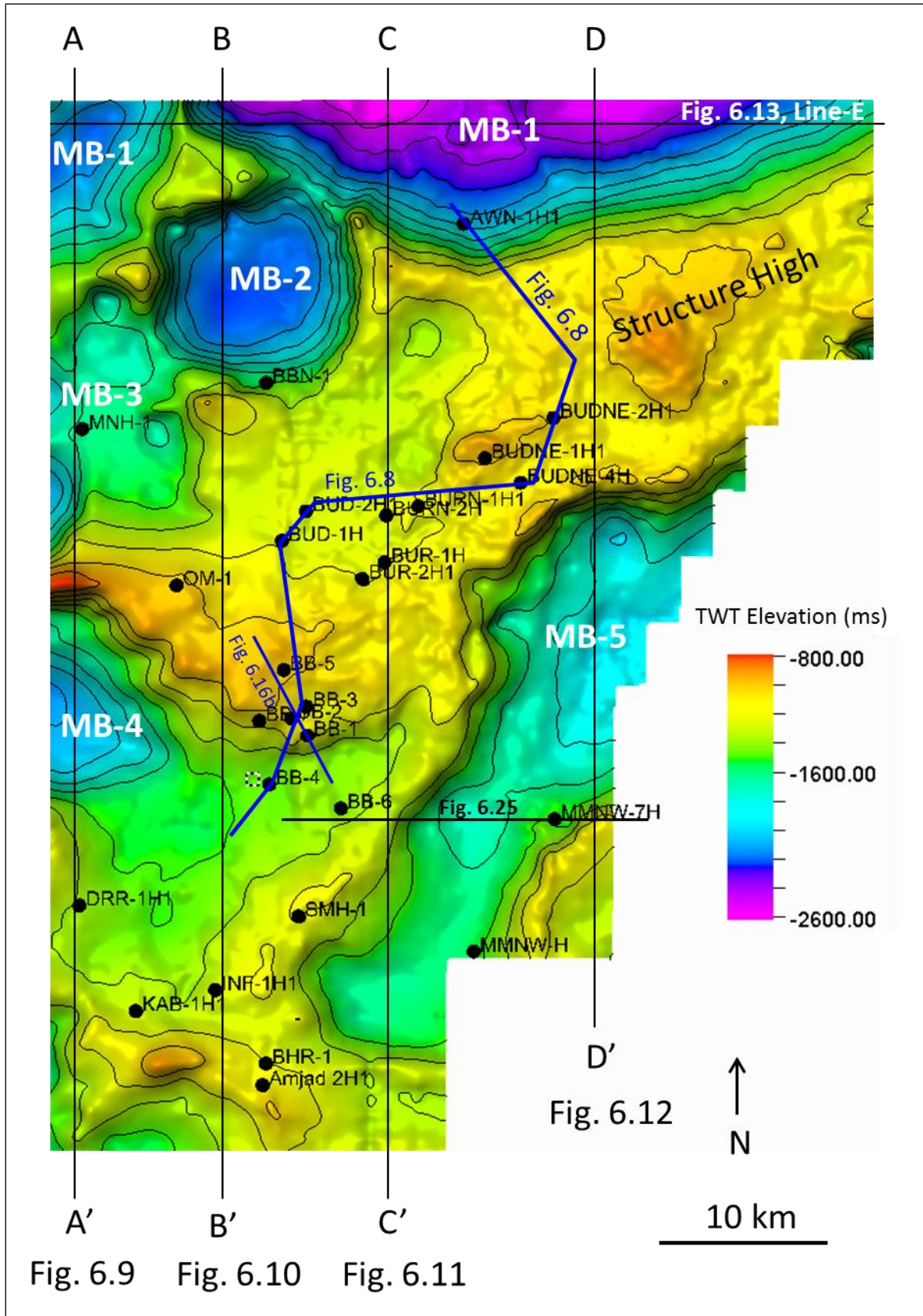
Fig. 6.7: Top Salt time structure map highlights the main minibasins with the location of the wells. Note the irregular shape of Top Salt structures. The N–S lines are the profiles selected for interpretation.
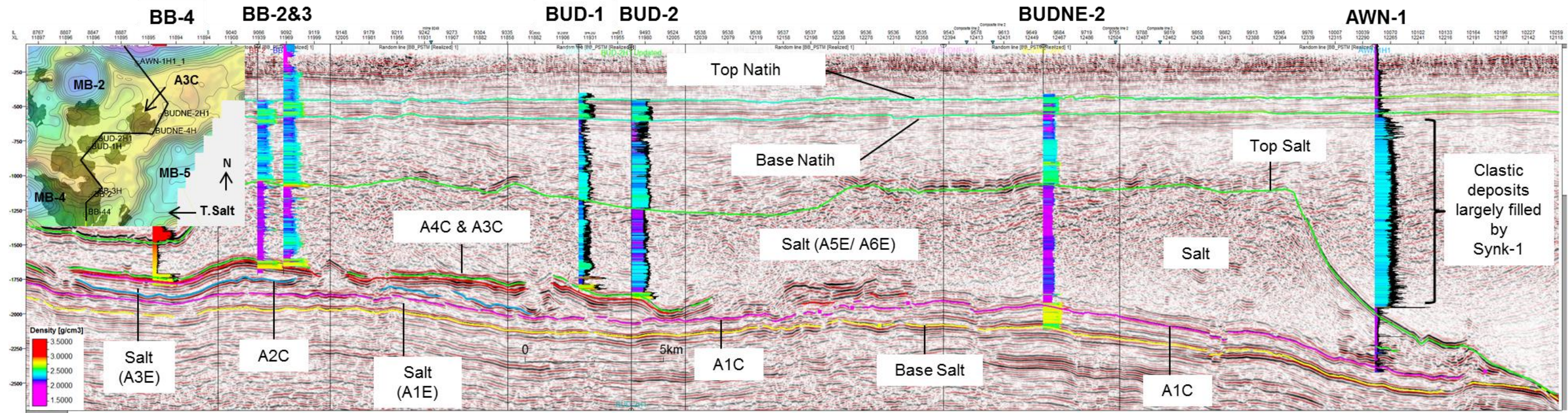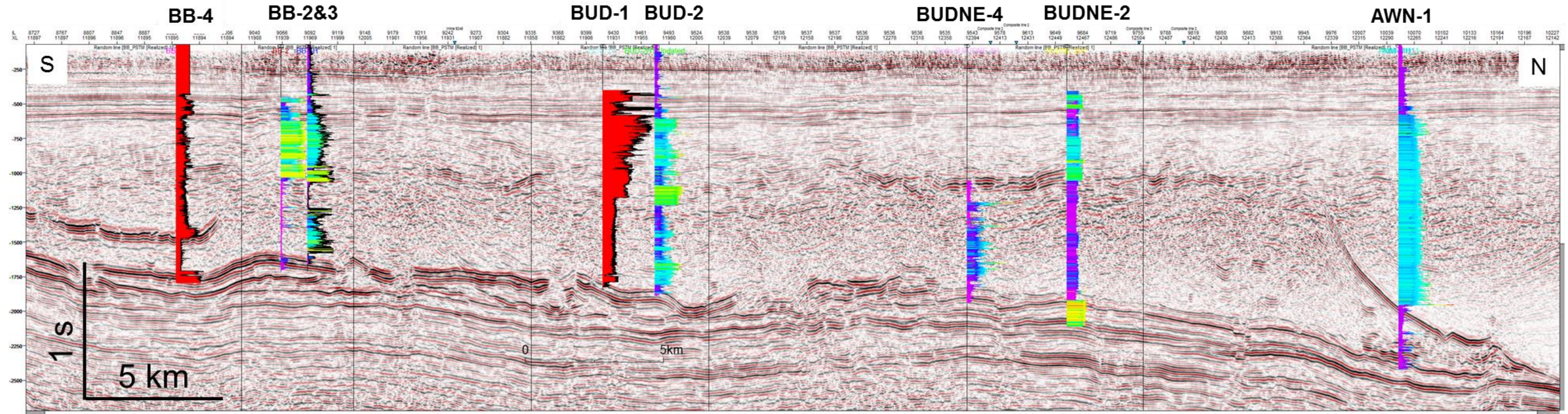
Fig. 6.8: Well-to-seismic calibrated profile with key horizons (see Fig 6.7 for location). Logs are posted as density, sonic, and gamma ray. Note that Top Salt is not imaged in some areas (e.g., middle of the profile). Note the change in the density logs at Top Salt and at the carbonate stringers. An increase in the gamma ray curve above the salt in AWN-1 indicates syn-kinematic clastic deposits. The horizon interpretations displayed on the profile are base Ara (yellow), A1C (pink), A2C (blue), A3C (red), and A4C (green). Wells BB-2, BB-3, BB-4, BUD-1, and BUD-2 all penetrated the A4C and A3C stringers. BUDNE-2 in the north penetrated the sub-salt section and only found the A1C stringer.
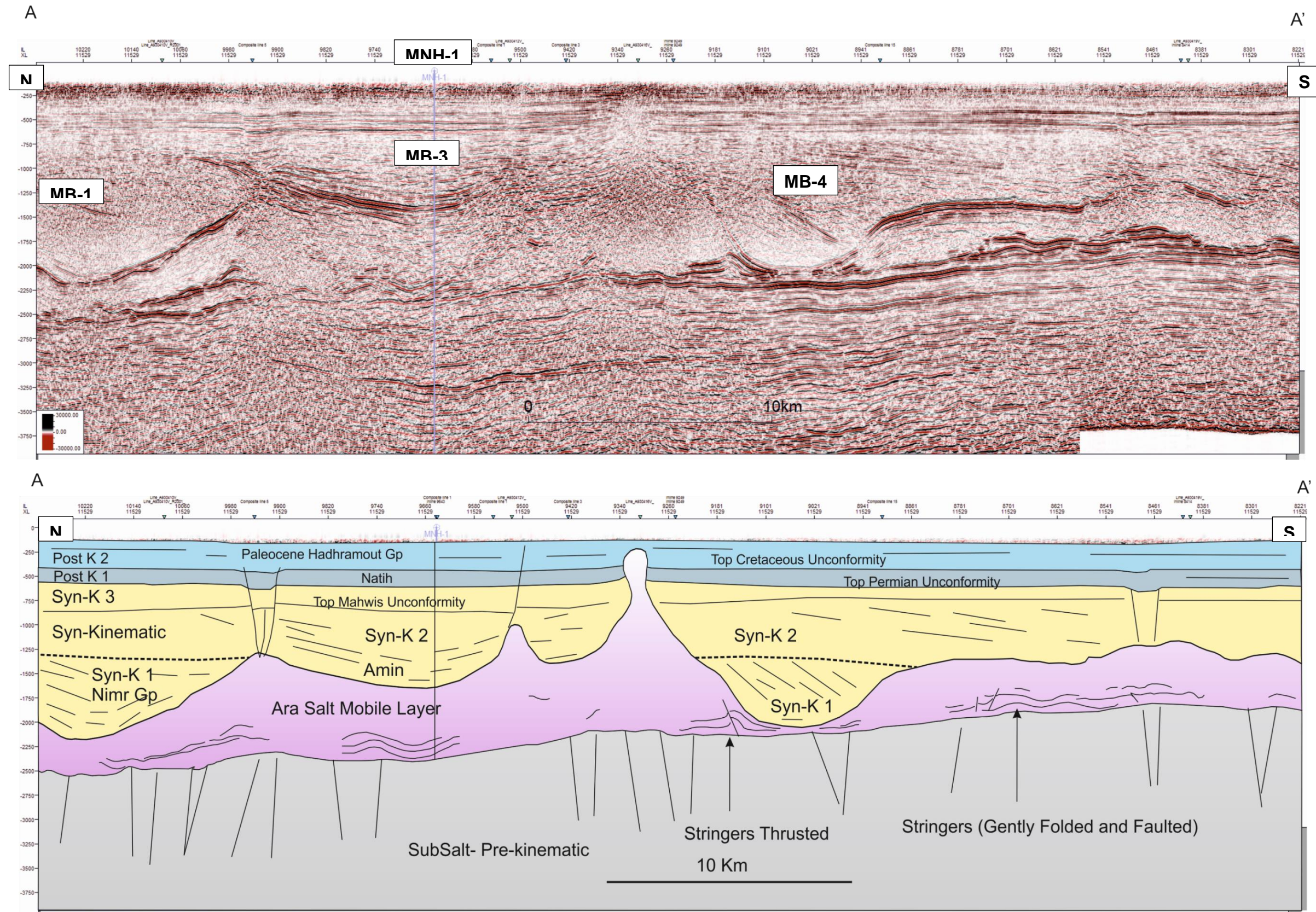
Fig. 6.9: Uninterpreted and interpreted Profile A (see Fig 6.7 for location). Note that the deeper minibasins are filled by Syn-kinematic-1 (Nimr Group), which is not observed in shallower minibasins.

The massive deposits above the Ara Group at the cores of the MB-4 and MB-1 belong to the lower part of the Haima Supergroup, the Nimr Group (Fig. 6.4), which was deposited during salt tectonics (Al-Siyabi 2005; Al-Barwani and McClay 2008). The shallower MB-3 formed at structurally lower depth and has less overburden accumulation. Well MNH-1H1, drilled through the centre of the MB-3, shows that the base of the minibasin was filled by the clastic Amin Group (Fig. 6.9). The deeper Nimr Group was not encountered by this well. Well AWN-1H1, drilled at the limb of the MB-1 (Fig. 6.7), penetrated the deeper Nimr Group (Fig. 6.8). The well reports of the AWN-1H1 show that the basal unit is part of the Nimr Group of the lower Haima Supergroup (Fig. 6.7). This suggests that deeper minibasins (e.g., MB-1 and MB-4) were filled initially by older deposits (i.e., termed here as Syn-kinematic Unit-1) and therefore formed earlier than the shallower MB-3, which has been filled by younger sediments (i.e., Syn-kinematic Unit-2; Fig. 6.9b). Post-salt extensional faults created more accommodation spaces during the deposition of the Syn-kinematic Unit-3 (Fig. 6.9). Post-kinematic units begin at the base Natih and extend up to the earth's surface (Fig. 6.9b). The stringers are highly deformed below the MB-1 and MB-4 and folded below the northern flank of the MB-4 (Fig. 6.9b).

Profile B

This profile passes through the MB-1 and MB-2 in the north, and part of the MB-4 in the south (Fig. 6.10). The Ara Group is thinner in the south, where the profile crosses part of the MB-4. The MB-2 displays thick sediment accumulation and is characterised by gentle to steeply dipping thickening wedges. These sediments are syn-kinematic units that deposited during the creation of the minibasin by salt evacuation. Extensional faults with growth units formed above the salt structures and created further accommodation where the stringers are more continuous.
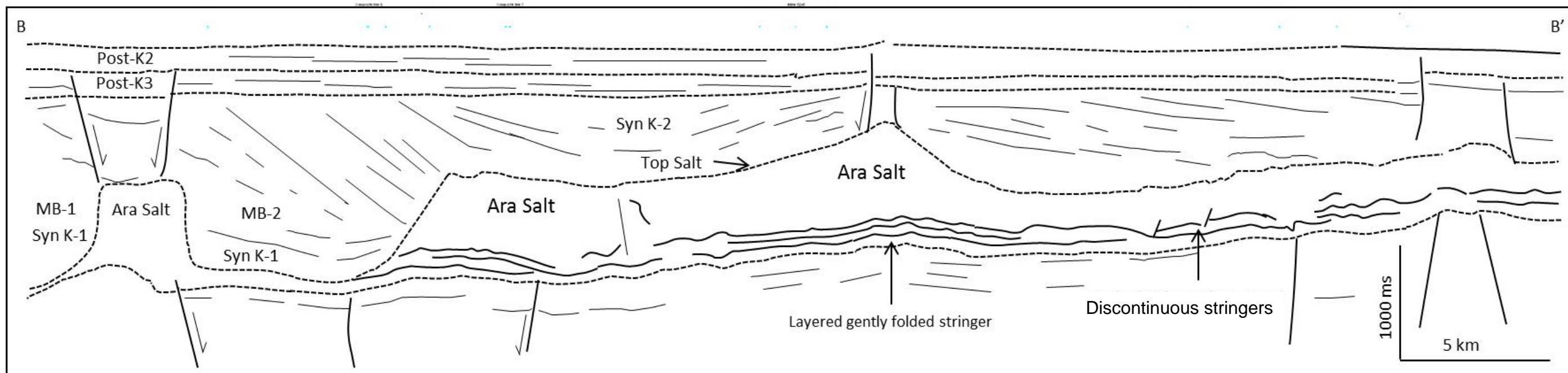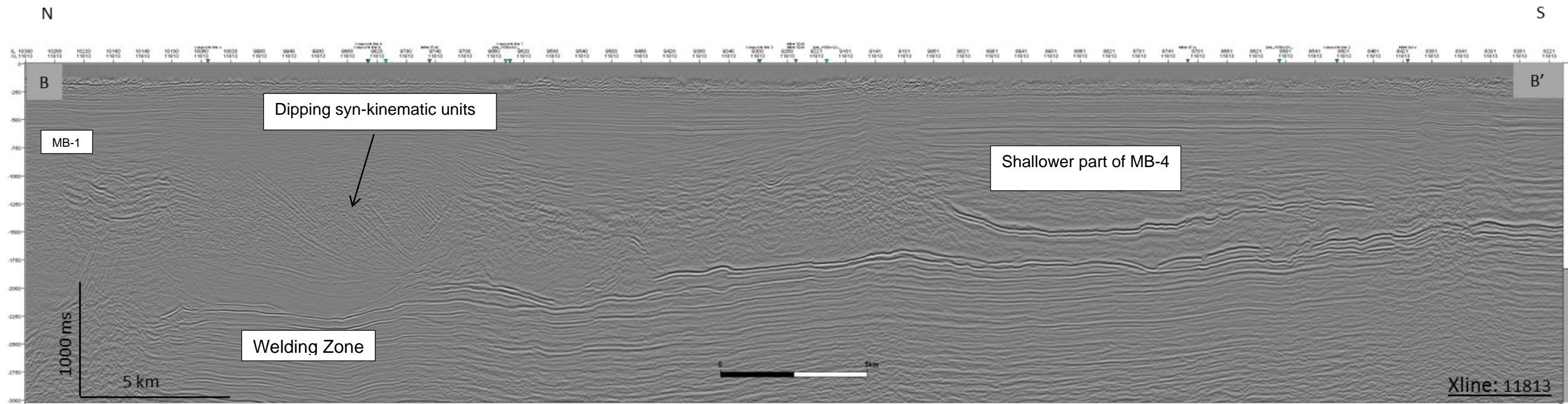
Fig. 6.10: Uninterpreted and Interpreted Profile B (see Fig. 6.7 for location). Note the dipping and thickening of the geometry of the syn-kinematic sediment fill over MB-2.

Whilst the stringers were found south of MB-2, no stringer remnants could be seen at the depocentre of the minibasin where Top Salt is welded over the basal Ara (Fig. 6.10).

Profile C

The profile passes through the MB-1 in the north, the salt wall in the middle, and the southern part of the MB-5 in the south (Fig. 6.7). The post-salt sediments above the MB-1 are characterised by a chaotic zone of featureless reflections, indicating high seismic noise and poor seismic signal (Fig. 6.11). The stringers are significantly deformed into single fragments just below the salt wall of the MB-1. The welded areas underneath the MB-1 and MB-5 show no traces of stringers.

Profile D

The profile passes through the MB-1 in the north, the thick salt wall in the middle, and the MB-5 in the south (Fig. 6.7 and Fig. 6.12). The structural high salt wall is bounded by the E–W striking MB-1 to the north and the NE-SW striking MB-5 to the south. Well data (AWN-1H1 and MMNW-7) show that the depocentres of the two minibasins were filled by the early growth units that belong to Syn-kinematic Unit-1 (Nimr Group) followed by Syn-kinematic Unit-2 (Fig. 6.12). The stringers in the southern limb of the MB-1 are broken into smaller fragments and dipping parallel to the Top Salt surface. Below the southern limb of the MB-5, the stringers are intensively deformed into smaller fragments with dips similar to Top Salt. Below the southern part of the salt wall, only the A1C stringer is observed. Sub-salt faults extended upwards and largely faulted the A1C stringer (Fig. 6.12).
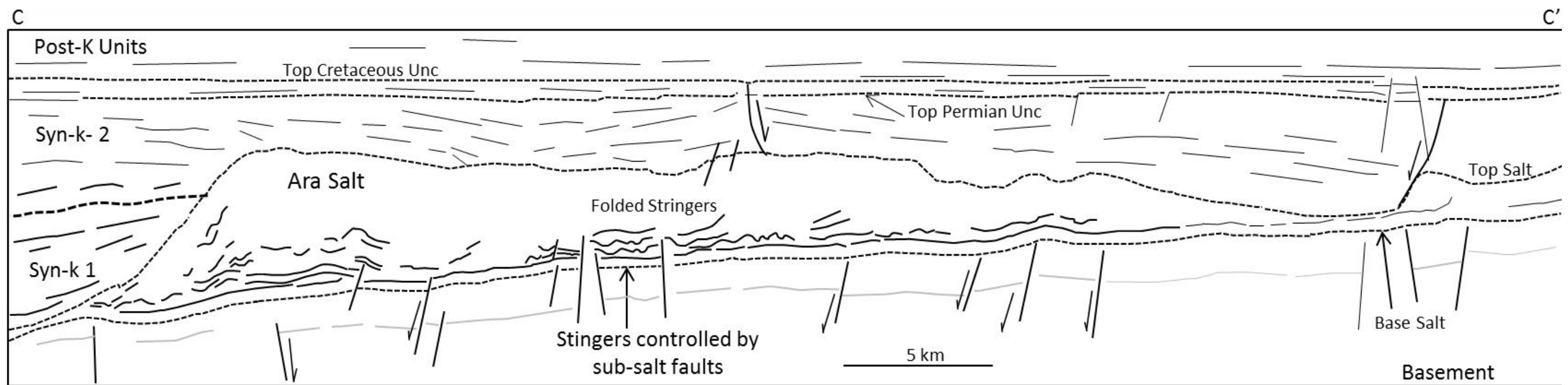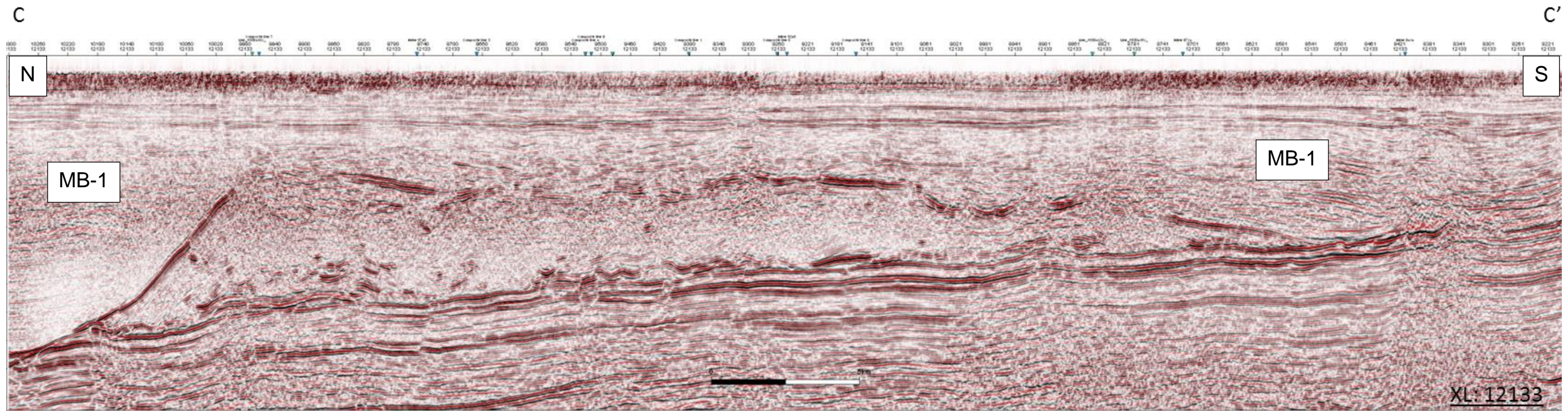
Fig. 6.11: Profile C passing through the MB-1 in the north to the southern edge of the MB-5. Note the stringer distribution and structural styles at the regional deformation scale.
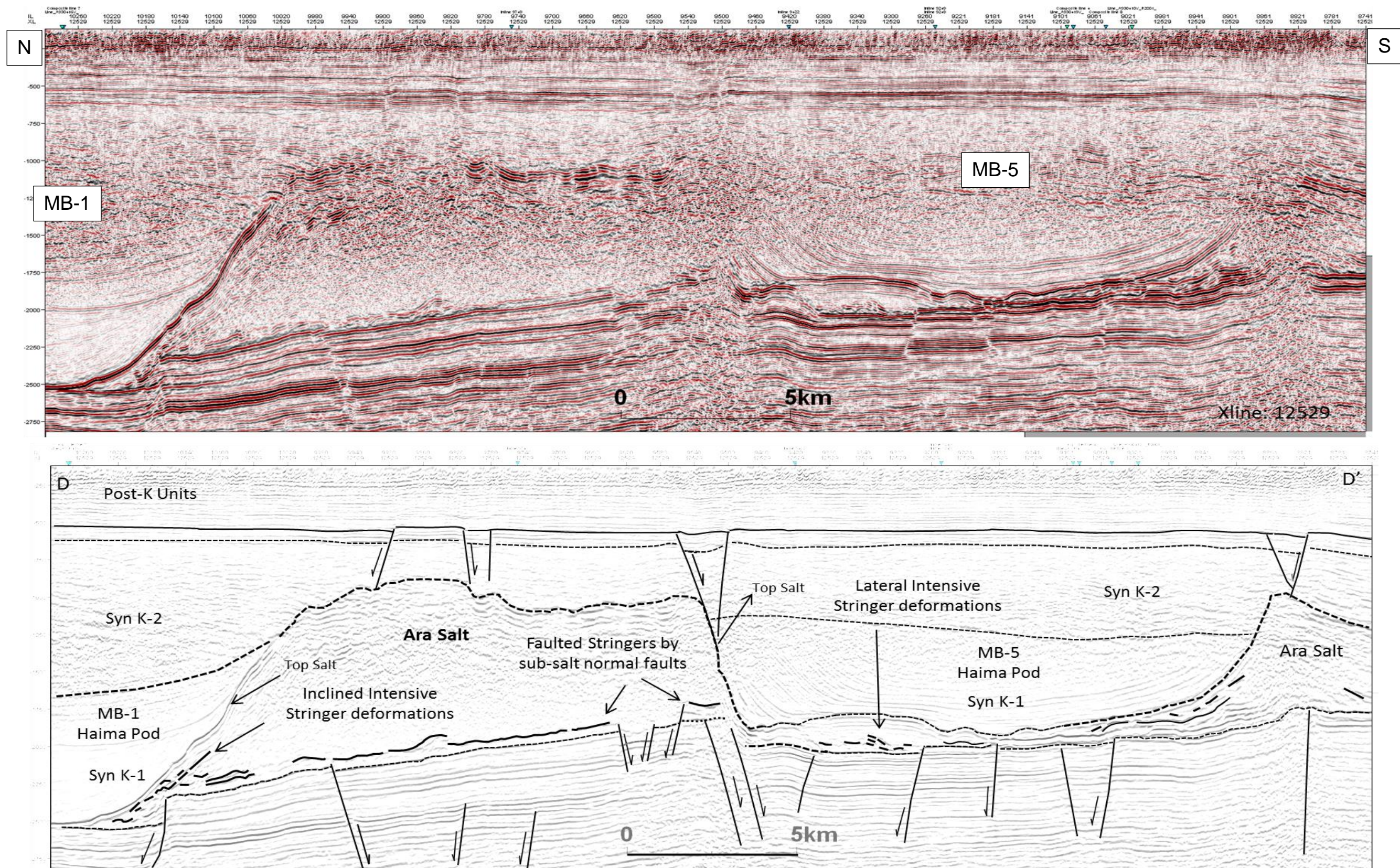
Fig. 6.12: Uninterpreted and interpreted Profile D (see Fig 6.7 for location). Note the welded salt in the MB-5 over the Ara carbonate stringers. Salt rise creates faulting and secondary load.
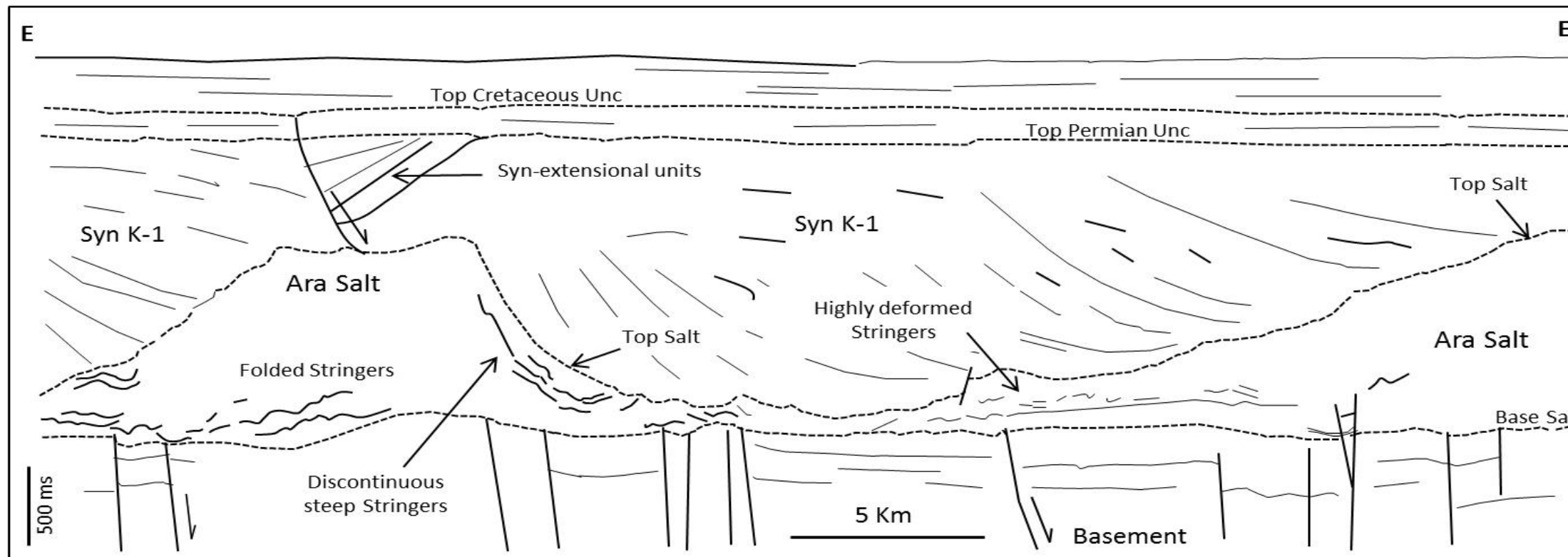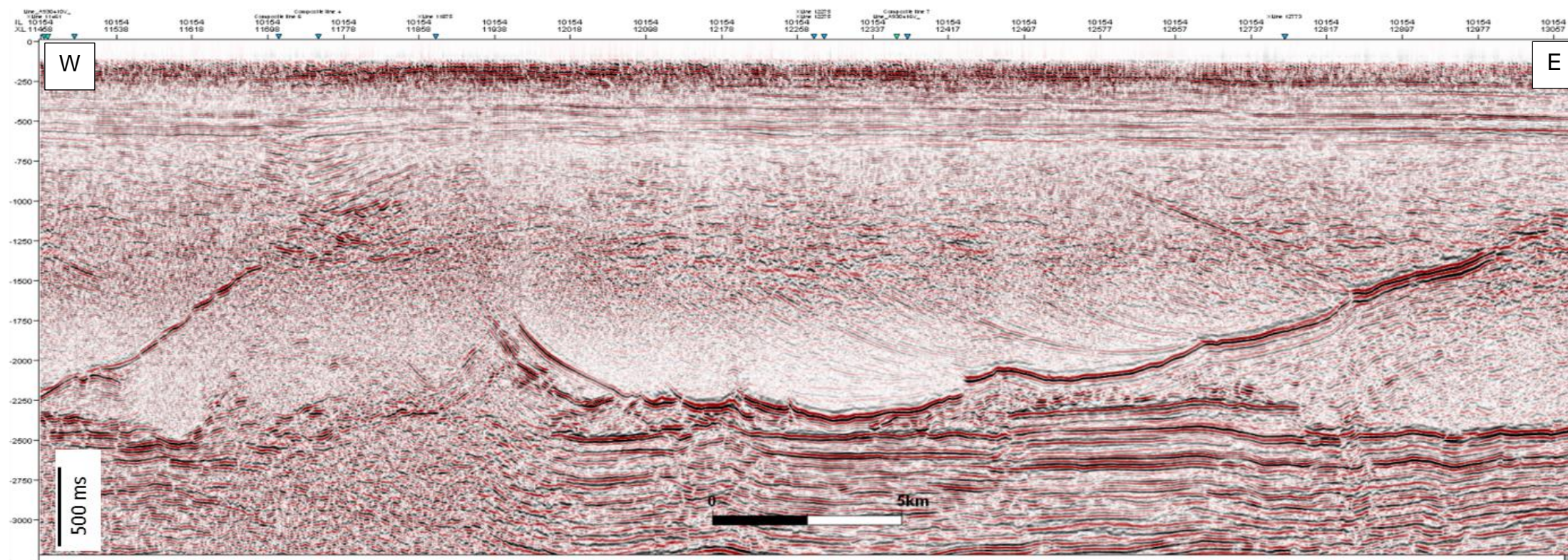
Fig. 6.13: Profile E is an east–west profile passing parallel to the MB-1. The massive sediments cause the salt to withdraw laterally until salt is welded with the stringers.

Profile E

Seismic line-E is oriented E–W and passes through the MB-1 in the north of the study area (Fig. 6.13). Syn-kinematic sequences are shown as long tilted reflectors downlapping the Top Salt surface. Syn-extensional growth strata are observed above the salt wall in the western side of the line formed. Above the salt wall, a clear syn-extensional growth unit deposited against the fault and extended up to the Top Cretaceous Unconformity. The stringers are intensively deformed below the minibasin into small-scale fragments. In the western limb of the minibasin, the stringers are discontinuous, tilted, and elevated by salt movement (Fig. 6.13).

6.5   Geometry of minibasins: Development of the MB-2

The geometrical details of the post-salt sediments that filled the minibasins (Haima pods) and their source and direction are more complex than observed on a large scale. For the three different geometries observed within the MB-2, refer to Unit-1, Unit-2, and Unit-3 shown in Fig. 6.14h. Unit-1 at the base displays less rotated geometry, while Unit-2 and Unit-3 are highly dipping with opposite thickening wedges (Fig. 6.14h). Note that the thickening wedge of Unit-2 is rotated upwards due to the uplift of the eastern flank of the minibasin (Fig. 6.14h).

In order to unravel the minibasin development, time thickness maps were generated from Top Salt to the top of each unit (Fig. 6.17a–d). In addition, in profiles, the tops of these units were backstripped using the flattening technique (Fig. 6.14e,f,g). The time thickness map of Unit-1 displays maximum thickness positioned in the middle to the NE part of the minibasin (Fig. 6.14b). Similarly, the time thickness map of Unit-2 displays more eastward thickening shift, which might suggest that the sediments were transported from the SW towards the NE (Fig. 6.14c). Backstripping the top of Unit-2 (Fig. 6.14b) reveals a downward prograding wedge thickening towards east

and thinned towards west. The thickness map of Unit-3 shows maximum thickness is located at the north of the minibasin (Fig. 6.14d). Such shift of minibasin depocentres might reflect the change in sediment source, which consequently changes the depression areas of Top Salt. The complex geometries of the minibasin filling packages are possibly due to the progressive displacement during basin fill.
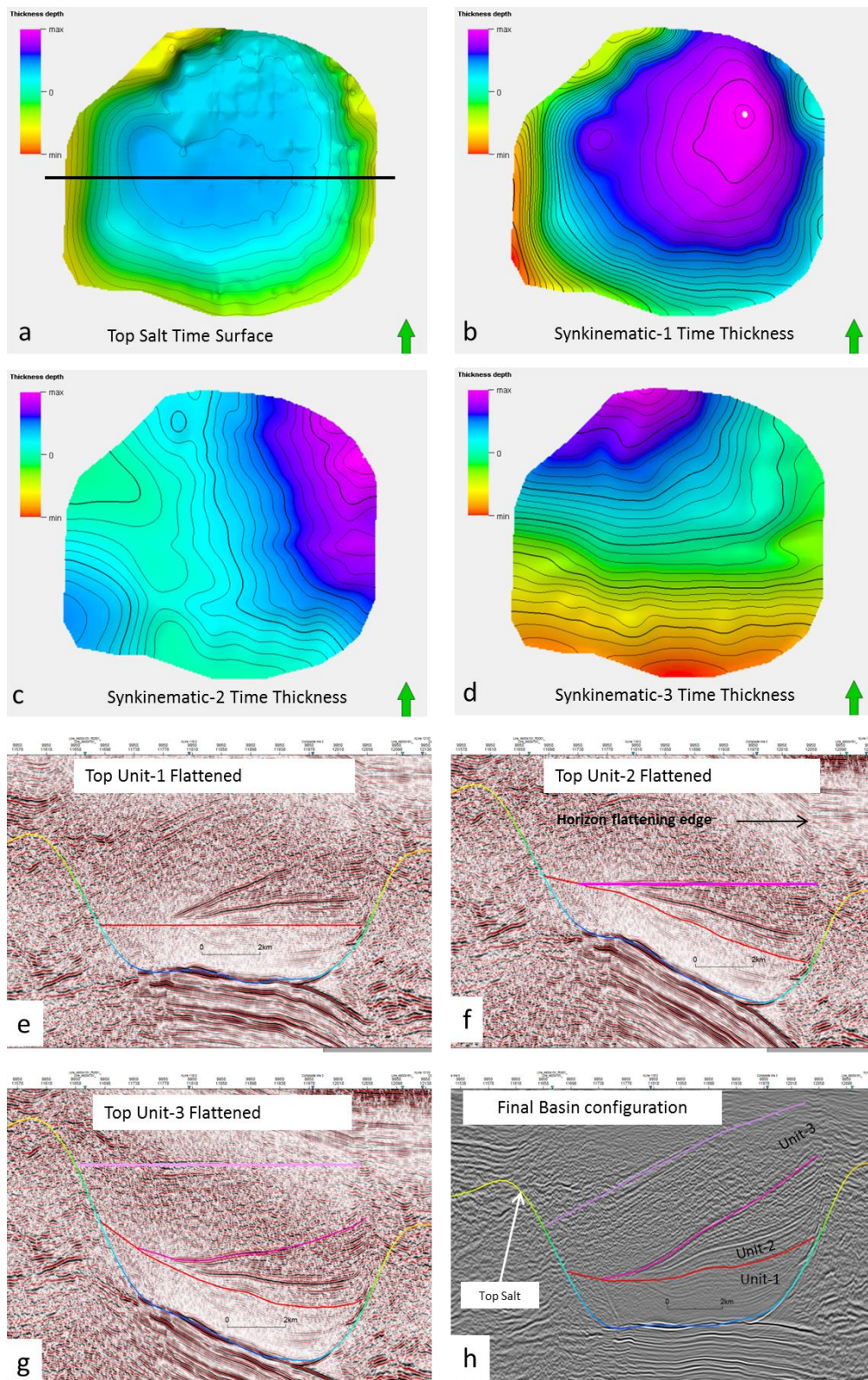
Fig. 6.14: Seismic interpretation of the syn-kinematic units over the MB-2. (a) Top Salt time surface map of the MB-2. (b–d) Time thickness maps of the Syn-kinematic Unit-1, 2, and 3 (minimum thickness in red and maximum thickness in purple). Note the shift in the position of the depocentre within each unit. (e–g) Flattening the tops of the interpreted units. (f) Eastward downward thickening of Unit-2. (h) The final shape of the basin geometry as observed on the seismic section.

6.6   Stratigraphic and petrophysical description of the Ara Group evaporites

6.6.1 Ara Salt and carbonate stringers

The interpretation of the Ara Group using petrophysical wireline logs is based on the case studies of Schreiber (1988) and previous interpretation of penetrated stringers in the South Oman Salt Basin (e.g., Al-Siyabi 2005) (Fig. 6.15). Several wells were used to interpret the evaporite layers using wireline logs, such as interval delta time or sonic wave (DT), gamma ray (GR), density (RHOB), resistivity (MSFL), and neutron logs. By superimposing these logs, the evaporite rocks can be easily identified.

The Ara Group is mostly composed of halite salt (density of 2000 kg/m^3), limestone, (2700 kg/m^3), dolomite (2800 kg/m^3), and anhydrite (2900 kg/m^3). The large density variation between the halite and the other brittle rock makes the density log a valuable tool to define the evaporite facies. In general, pure halite has low gamma ray, low density, and high resistivity values (Fig. 6.15 and Fig. 6.16).

The Top Salt is characterised by a sharp shift on the DT curve (sonic) to lower values where it changes from the upper clastic shale or sandstone (Lower Haima Supergroup) into the salt section (Fig. 6.16a). The average DT value calculated in the salt section from well BUD-2H1 is 218.5 µs/ft (~0.00072 s/m in SI unit) (Fig. 6.16). The density curve is sharply decreasing due to the low density of salt (~2040 kg/m^3). Halite rock has high resistivity and low neutron readings. The GR curve in general shows low values (~10 API) almost constant through the halite section, indicating the absence of shale or clastic feldspar sediments within the salt. Because of the lack of radioactive related deposits (e.g., shale) within the upper section of the

Ara salt in well BUD-2H1, the upper halite layers below Top Salt are characterised by low gamma ray values of approximately 10 gAPI (Fig. 6.16a).

Compared with the surrounding halite salt, the stringers are characterised by an increase in density and decrease in sonic velocity, which is typical for carbonate rock (Fig. 6.15; Fig. 6.16b, and Fig. 6.17). Stringers are dominated by carbonate bodies of limestone and dolomite. Thin anhydrite layers are also present within the stringers. Anhydrite is denser than limestone, and therefore it is easily identified on the density curve (Fig. 6.15).

On seismic profiles, the A4C and A3C stringers are indicated by a positive reflector due to the increase in velocity and density (i.e., acoustic impedance) (Fig. 6.17). The negative reflector in between represents the salt layer, which belongs to the A4E salt (Fig. 6.17). The A2C stringer is separated from the overlying and underlying strata by a zone of chaotic reflections belong to A2E and A3E salt. The salt intervals between stringers are significantly variable due to either grounding or folding of the stringers.
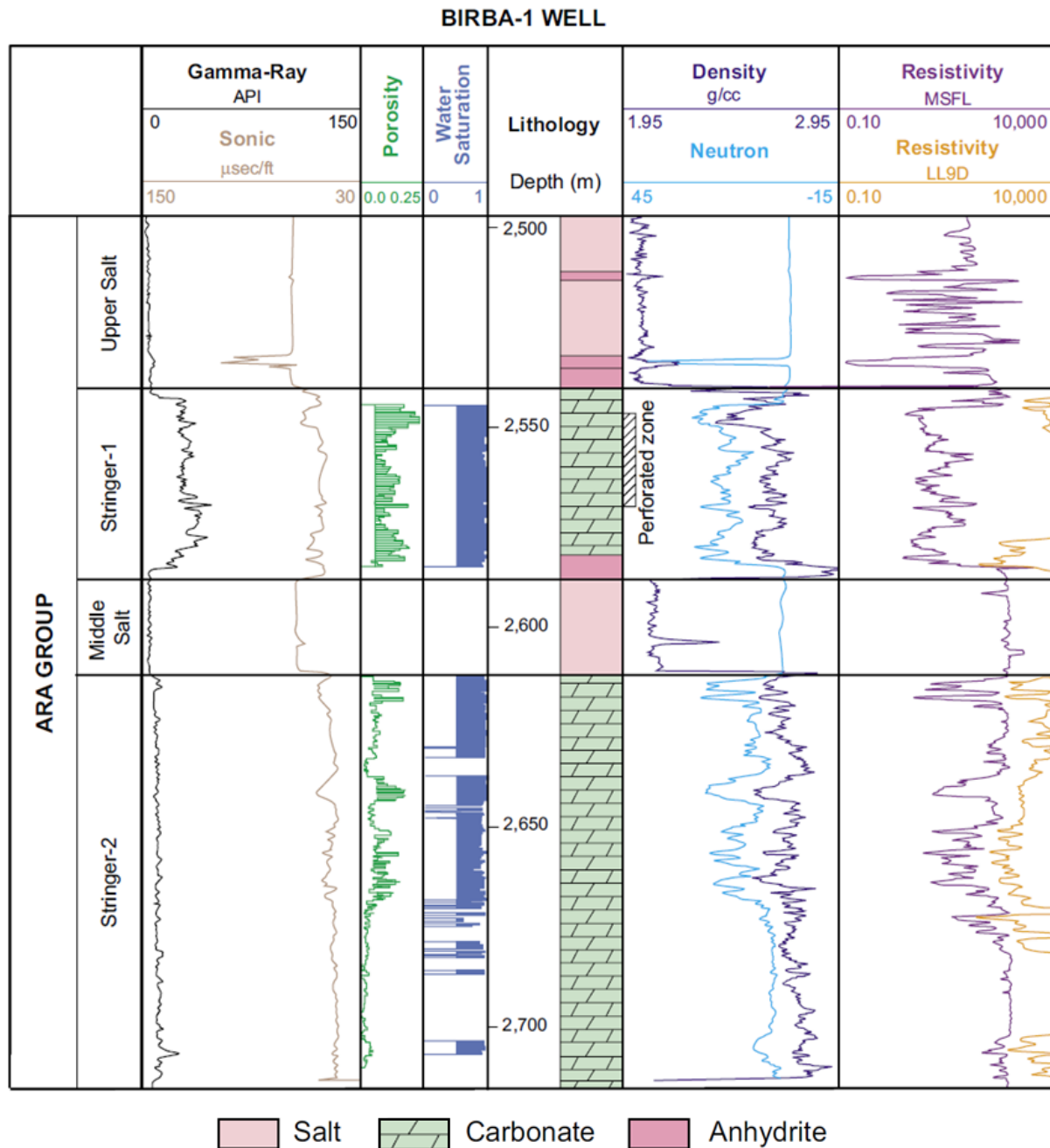
Fig. 6.15: Typical wireline log response for the evaporite facies of the Ara Group. Note the density variation from halite (~2000 kg/m^3), anhydrite (base Stringer-1 of ~3000 kg/m^3), and carbonate (dolomite and limestone ~2800 kg/m^3 and ~2900 kg/m^3, respectively). Also note the low gamma ray for salt and the constant sonic log reading, both indicating a clean halite section with no shale or mudstone intervals. Logs are from well Birba-1 from the South Oman Salt Basin. Stringer-1 (A4C) is an oil-bearing dolomite interval (after Al-Siyabi 2005).
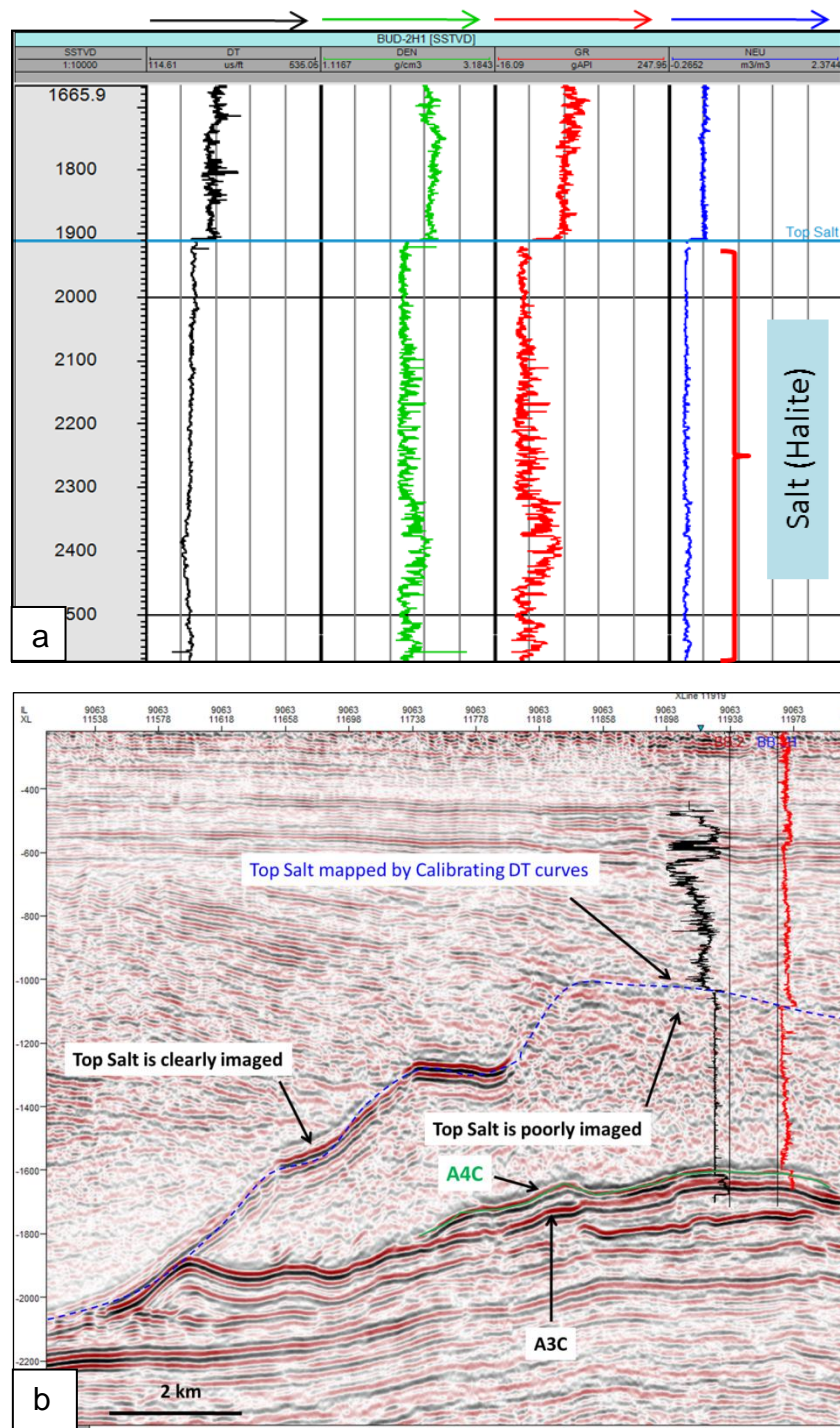
Fig. 6.16: (a) Petrophysical characterization of the Top Salt from BUD-2H1. Arrows at the top indicate the increasing direction of the wireline log readings. The horizontal blue line is the Top Salt surface. Note the decrease in sonic (DT, black), density (green), gamma ray (red), and neutron (blue) curves. (b) Well-to-seismic calibration of the Top Salt, A4C, and A3C stringers using wells BB-1 and BB-2 (see Fig. 6.7 for location). Note that Top Salt is not imaged on seismic data to the right side of the profile. Using DT and density curves, the interpretation of Top Salt can be guided. Note also the change in the DT and sonic log readings at the level of A4C and A3C stringers.
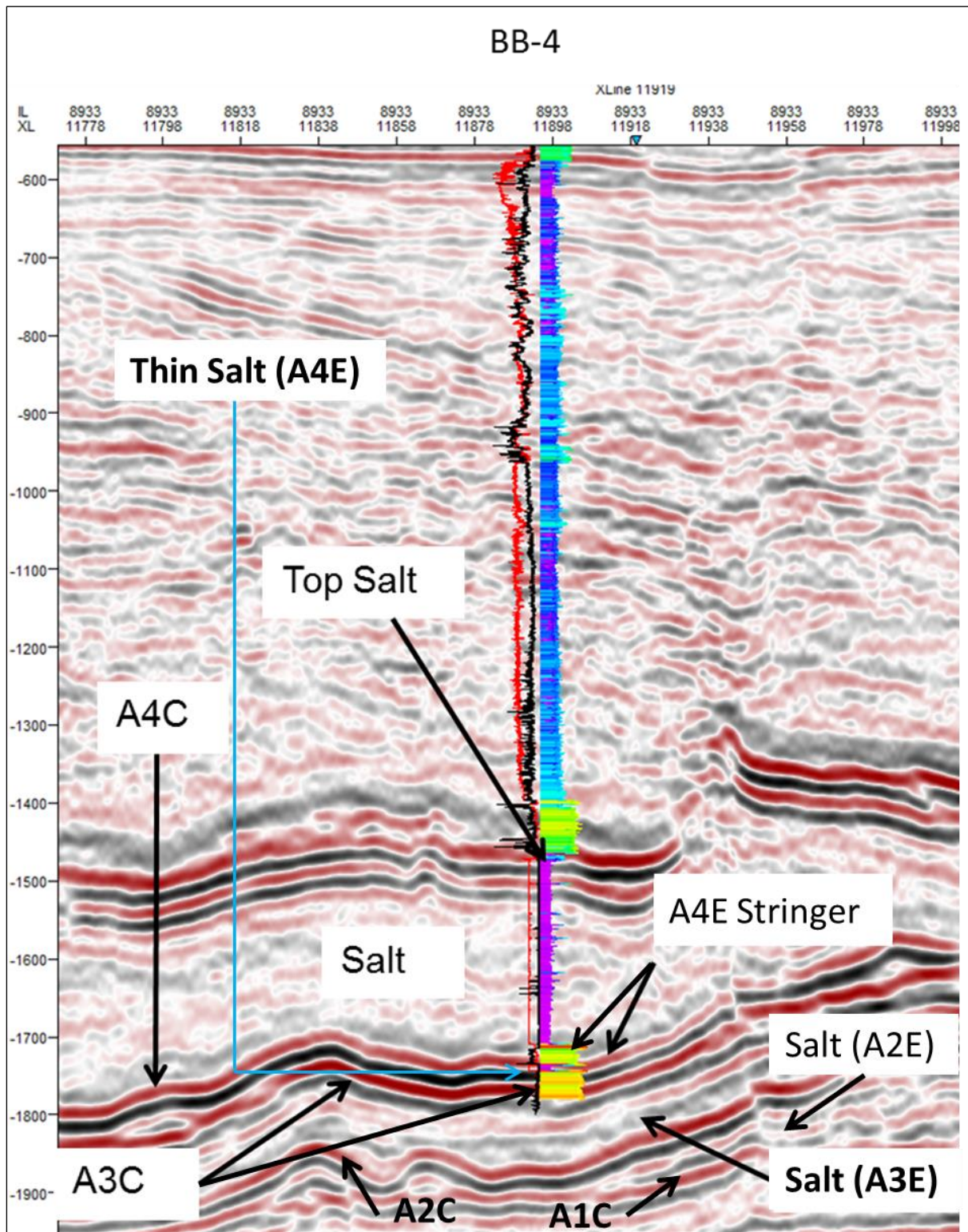
Fig. 6.17: Well-to-seismic tie of the Ara stringers using the density curve of well BB-4. The well reaches a depth below the A3C stringer. Note the two high-density carbonate layers belong to A4C and A3C stringers, and the thin halite salt in between belongs to the A4E salt.

6.6.2 Vertical stratigraphic description of the Ara Group Evaporites

6.6.2.1   Typical stratigraphic section

Well AWN-1H1 is located in the north of the study area at the limb of the MB-1 (see Fig. 6.7 for location). The well penetrated three thick carbonate stringers in the lower part of the Ara section (Fig. 6.18). The upper part of the Ara Group is 634 m thick and is composed of clean halite that belongs to the A5E/A6E halites. This unit has low gamma ray (10 gAPI), low density (2040 kg/m^3), and low DT values (228 µs/ft ~ 0.00075 s/m in SI unit), which are typical values for halite rock.

The upper stringer is the A4C stringer, which is composed of two dolomite layers with one anhydrite unit in between them. The anhydrite is identified from the sharp shift of density and gamma ray curves. The A4C stringer is underlain by 100 m-thick halite that is part of the A4E salt. The A4E salt in turn is underlain by the A3C stringer and characterised by 44 m of dolomite. Another salt interval, 146 m thick, just below the A3C, belongs to the A3E salt. The continuous lower stringer A1C is seismically well known by its regional extent over the whole basin (Al-Siyabi 2005). Under AWN-1H1, the A1C is characterised by a 10 m-thick layer of anhydrite at the top followed by a thick carbonate layer of dolomite (Fig. 6.18).

6.6.2.2   Complex stratigraphic section

In some cases, more stringers than expected were found, and these are interlayered by halite intervals with variable thicknesses. The MNH-1H1 in the eastern side of the study area encountered at least 12 carbonate layers separated by halite (Fig. 6.19). In this case, it is difficult to correlate these layers to their stringer cycles by using only wireline logs. Therefore, core or cutting data are required to identify the stringer facies.
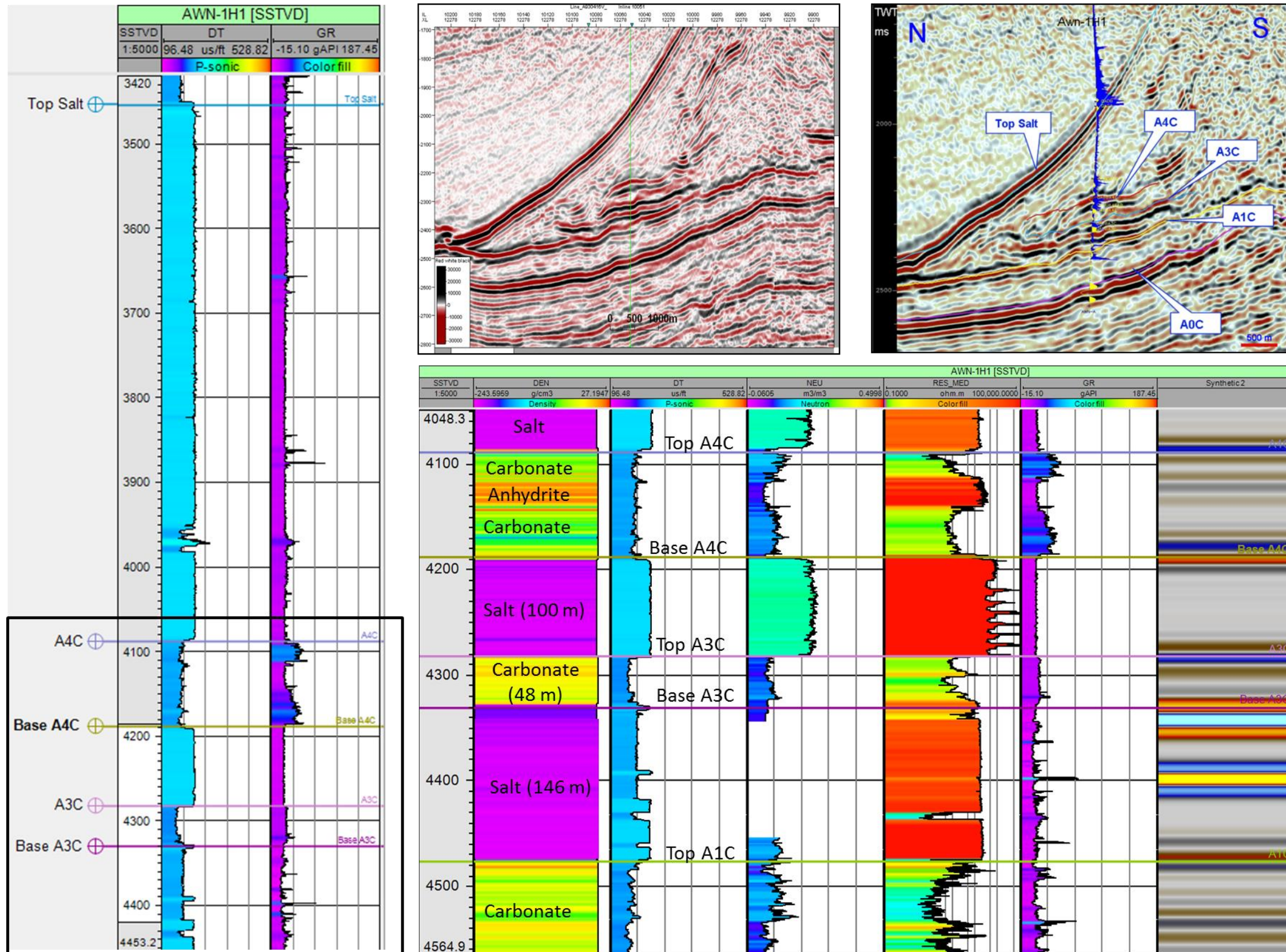
Fig. 6.18: Well-to-seismic calibration of well AWN-1H1 (see Fig. 6.7 for location). Note the three carbonate stringers belong to the A1C, A3C, and A4C stringers. The A2C stringer is not observed in this well.
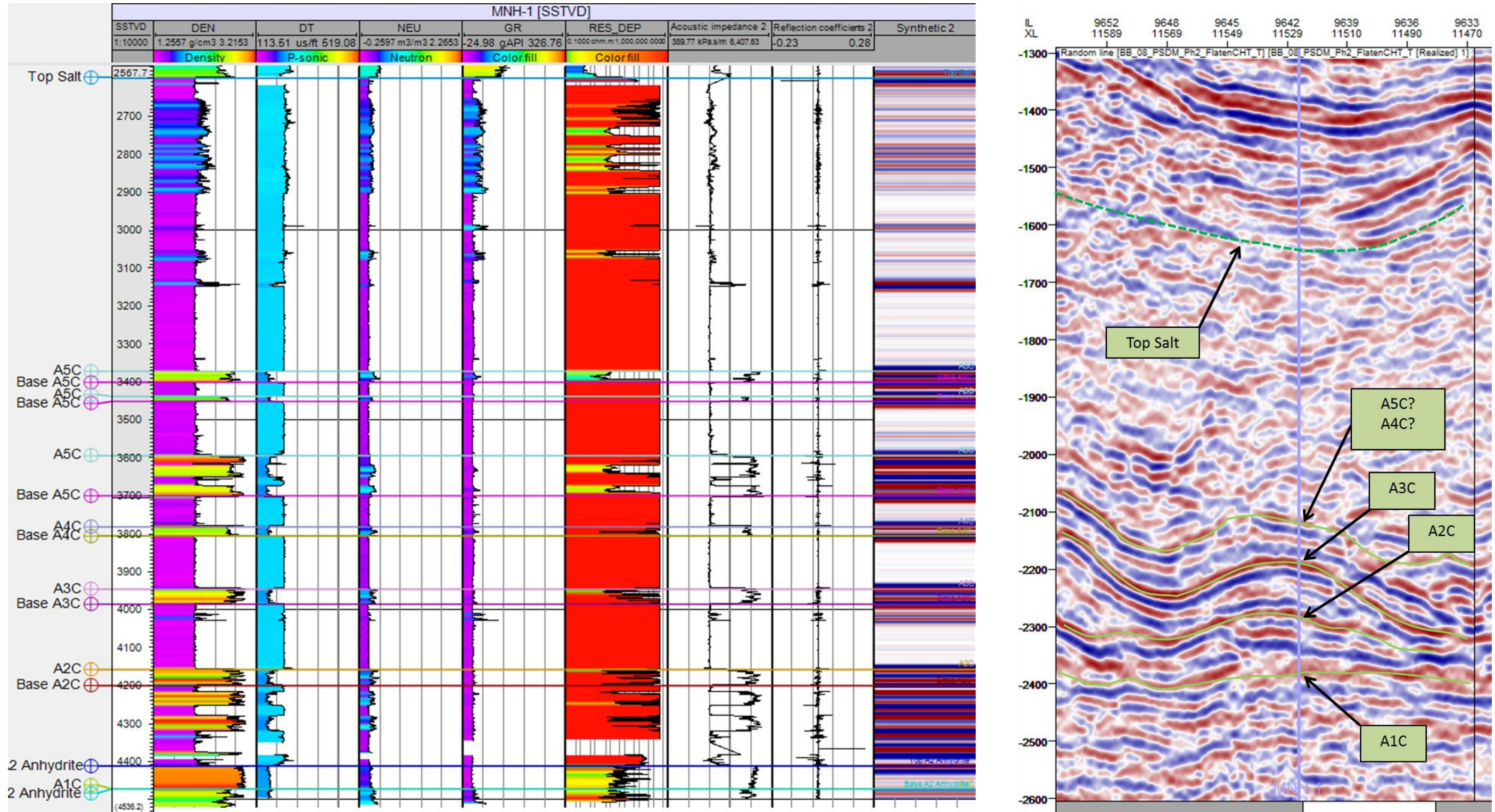
Fig. 6.19: Well MNH-1H1 in the western side of the study area (see Fig. 6.7 for location). Note the presence of 11 to 12 carbonate/anhydrite layers separated by halite intervals in between.

6.6.3 Lateral stratigraphic description and seismic character of the stringers

6.6.3.1   Correlation of BUR-1H1 and BUR-2H1

BUR-1H1 and BUR-2H1, located 1369 m from each other, were selected to observe the lateral stratigraphic changes of the carbonate stringers and the halite members in between (Fig. 6.20). No significant thickness change is observed in the A4C and A3C in the two wells, with only a 5 m-thick halite member separating them. This conformable continuity between A4C and A3C in the two wells coincides with the lateral continuity observed on seismic data (Fig. 6.20). In the BUR-2H1, the strong seismic reflection appearing above the A4C is 90 m thick and is interpreted to be the A5C stringer.

6.6.3.2   Correlation of BUD-1H1 and BUD-2H1

Well BUD-1H1 is 1884 m apart from BUD-2H1 (Fig. 6. 21). The seismic sections across the two wells display continuous and correlatable A4C and A3C stringers. The petrophysical interpretation shows two carbonate units (A4C and A3C) separated by an anhydrite unit in the middle. The thickness of the A4C in BUD-1H1 and BUD-2H1 is 65 m and 56 m, respectively. The increase in thickness of the A4C in BUD-1H1 is interpreted to be related to the oblique drilling of the stringer.

The A2C anhydrite stringer is not encountered in the wells or seismic data. However, by taking an arbitrary line (line B in Fig. 6.21c) to the west, a strong seismic reflection appears between the A1C and A3C stringers (Fig. 6. 21b). The seismic amplitude of this reflection decreases sharply to the west and instead very low amplitude presents below the well. This facies is similar to the facies between A4C and A3C, which has been encountered by the two wells. Therefore, this layer is interpreted to be the A2C anhydrite.
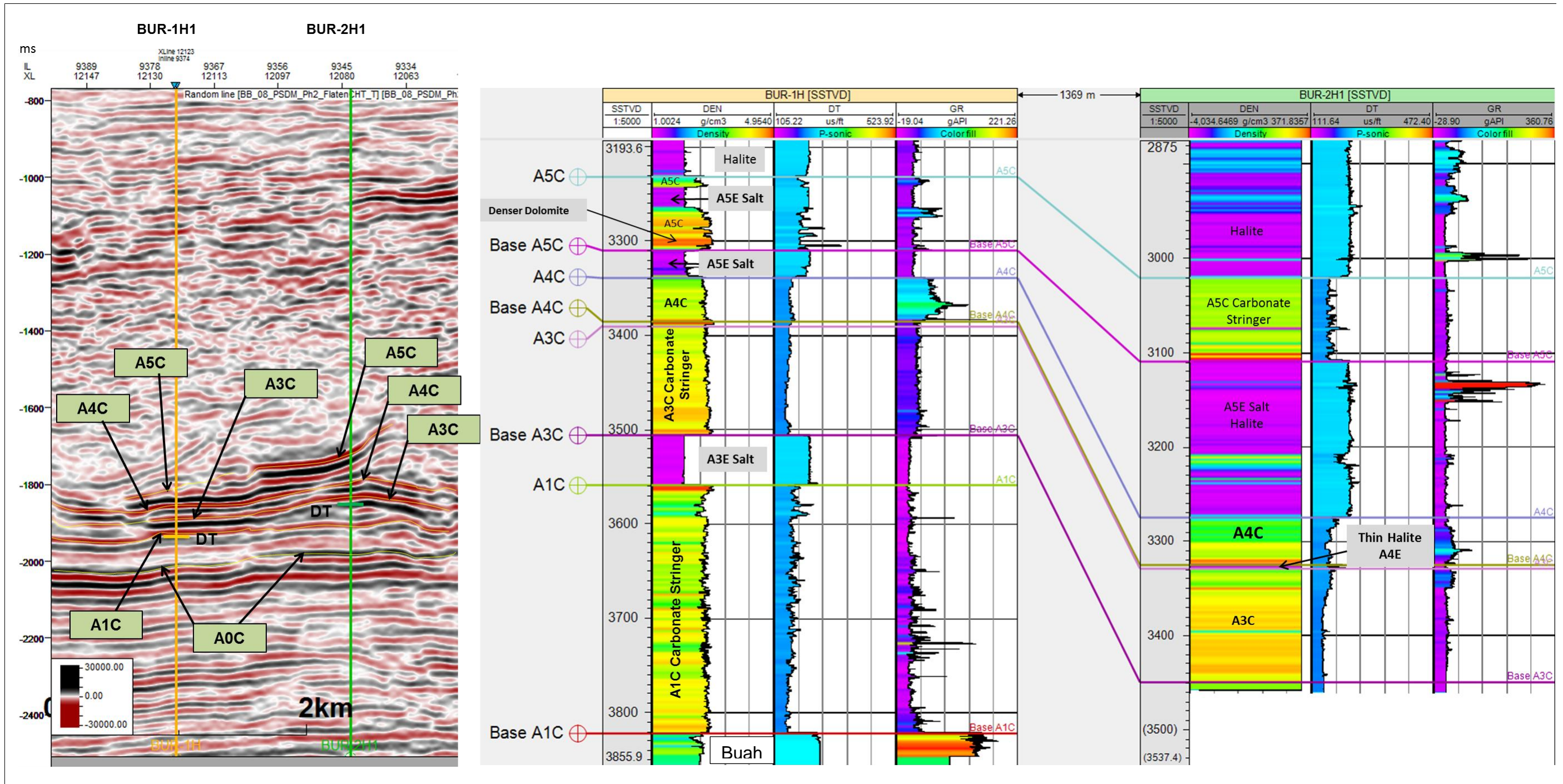
Fig. 6.20: Well BUR-1H1 and BUR-2H1 seismic-to-well correlation. Note the presence of the A5C stringer with high seismic amplitude under BUR-2H1 and a weak reflector at BUR-1H1. Note that A2C stringer is not observed in BUR-1H1.
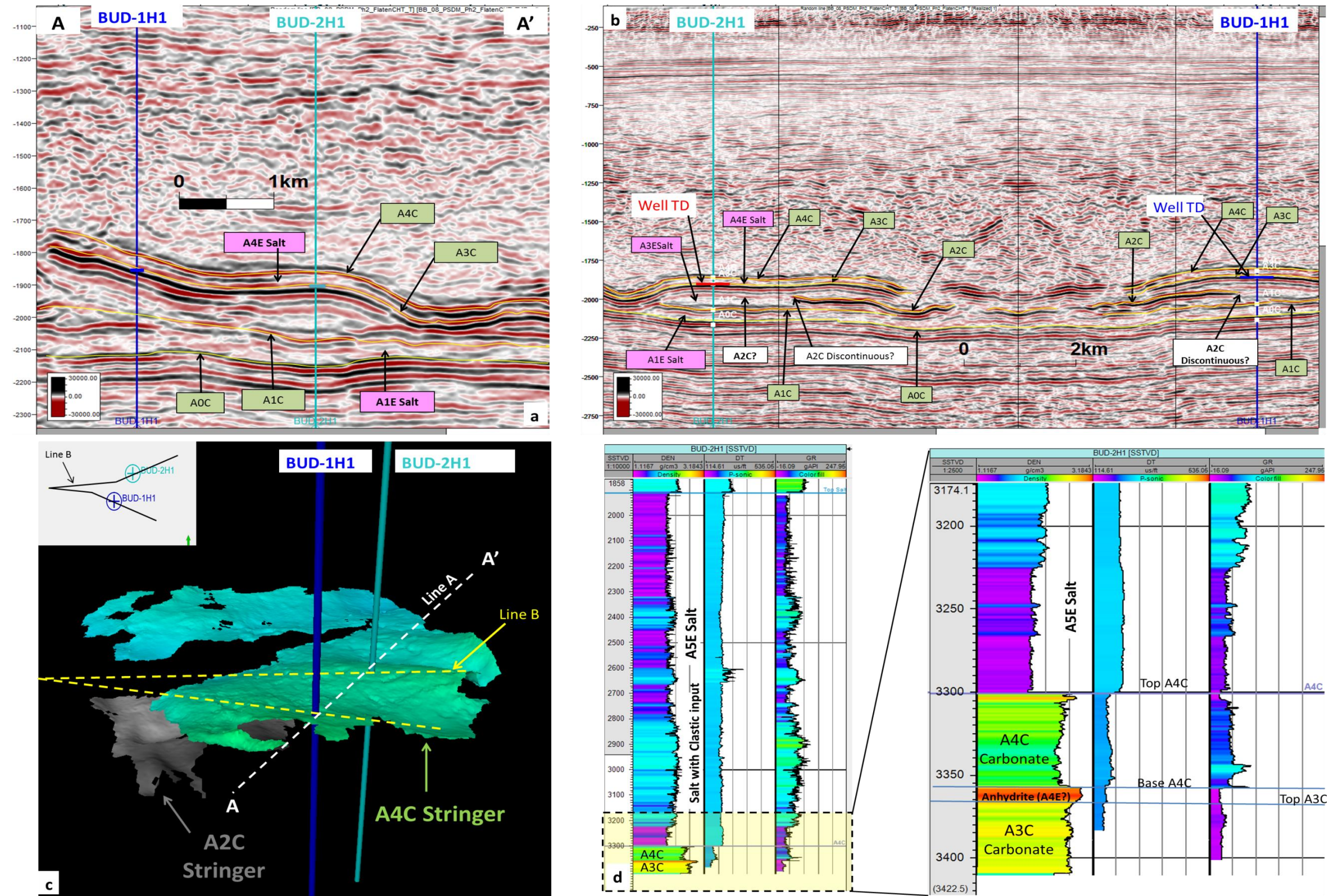
Fig. 6.21: Well BUD-1H and BUD-2H correlation. (a) Straight seismic line connecting the two wells shows conformable A4C, A3C, and A0C stringers. Note that A2C is not present in the two wells. (b) Composite (arbitrary) line passing through the A2C in the western side of the two wells (see Fig. 6.21c for location). (c) 3D time structure map of the A4C and A2C stringers. (d) Petrophysical logs used to interpret BUD-2H1. The high gamma ray reading in the salt section above the A4C stringer is interpreted to be related to the presence of siliciclastic materials such as siltstone and shale within the salt.

6.6.3.3 Correlation panel for Birba wells (BB-1–BB-6)

Six Birba wells (BB-1- BB-6) east of the MB-4 (Fig. 6.7) were drilled to target the A4C and A3C stringers, and were selected here to examine the stratigraphy of the penetrated stringers (Fig. 6.22). The two A4C and A3C stringers are observed in well data as two carbonate units separated by either anhydrite (BB-2, BB-3, BB-5) or halite (BB-1, BB-4, B-6) (Fig. 6.22). The average thickness of the A4C and A3C carbonate units is 50 m and 100 m, respectively. No significant lateral facies change is observed in the first five wells except the lateral change of A4E from halite into anhydrite. On seismic data, the A4C and A3C are strong-amplitude reflectors (Fig. 6.23). In the northeast of the study area, well BUDNE-4H1 does not show any stringers at the A4C and A3C level, even though the seismic loop is consistent with the A4C and A3C (Fig. 6.24). The seismic amplitude of the A4C and A3C stringers is weak in BUDNE-4H1 and BUDNE-2H1 compared with the normal seismic character of the stringers in BB-3 and BB-4 (Fig. 6.24). Well BUDNE-2H1, about 4 km northeast of BUDNE-4H1, found a thin (~5 m) carbonate layer above the A1C stringer (Fig. 6.24). Therefore, the stringers with such seismic character are interpreted to be very thin or absent. This lateral discontinuity in the A4C and A3C could be related either to the original stratigraphic extent of the stringers or to halokinesis. MMNW-7 is drilled in the deeper part of the A1C level (see Fig 6.7 for location). The stratigraphy of the Ara Group is completely different than that observed in the middle and western sides of the study area. The lower part of the Ara Group shows a 60 m-thick layer of salt followed by a thick silicilyte unit with high GR, interpreted as shale, and a unit with low GR, interpreted as siltstone (Fig. 6.25). This silicilyte unit is interbedded by three 10 m-thick denser units of dolomite. The A1C is possibly correlated with the lower 10 m-thick dolomite (Fig. 6.28).
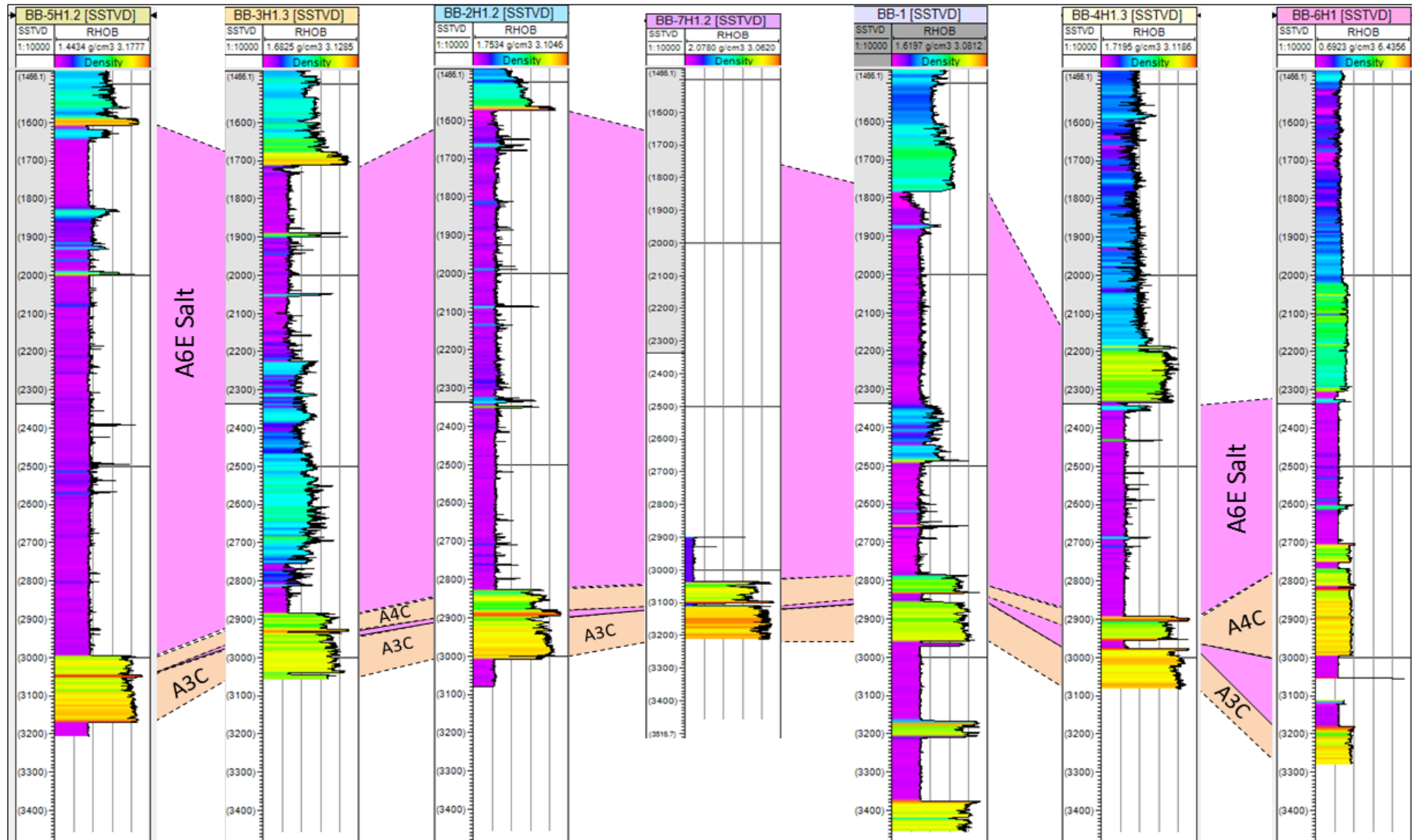
Fig. 6.22: Correlation panel for Birba wells (BB-1 to BB-7). Note the A4C and A3C stringers separated by anhydrite (left wells) and halite (right wells).
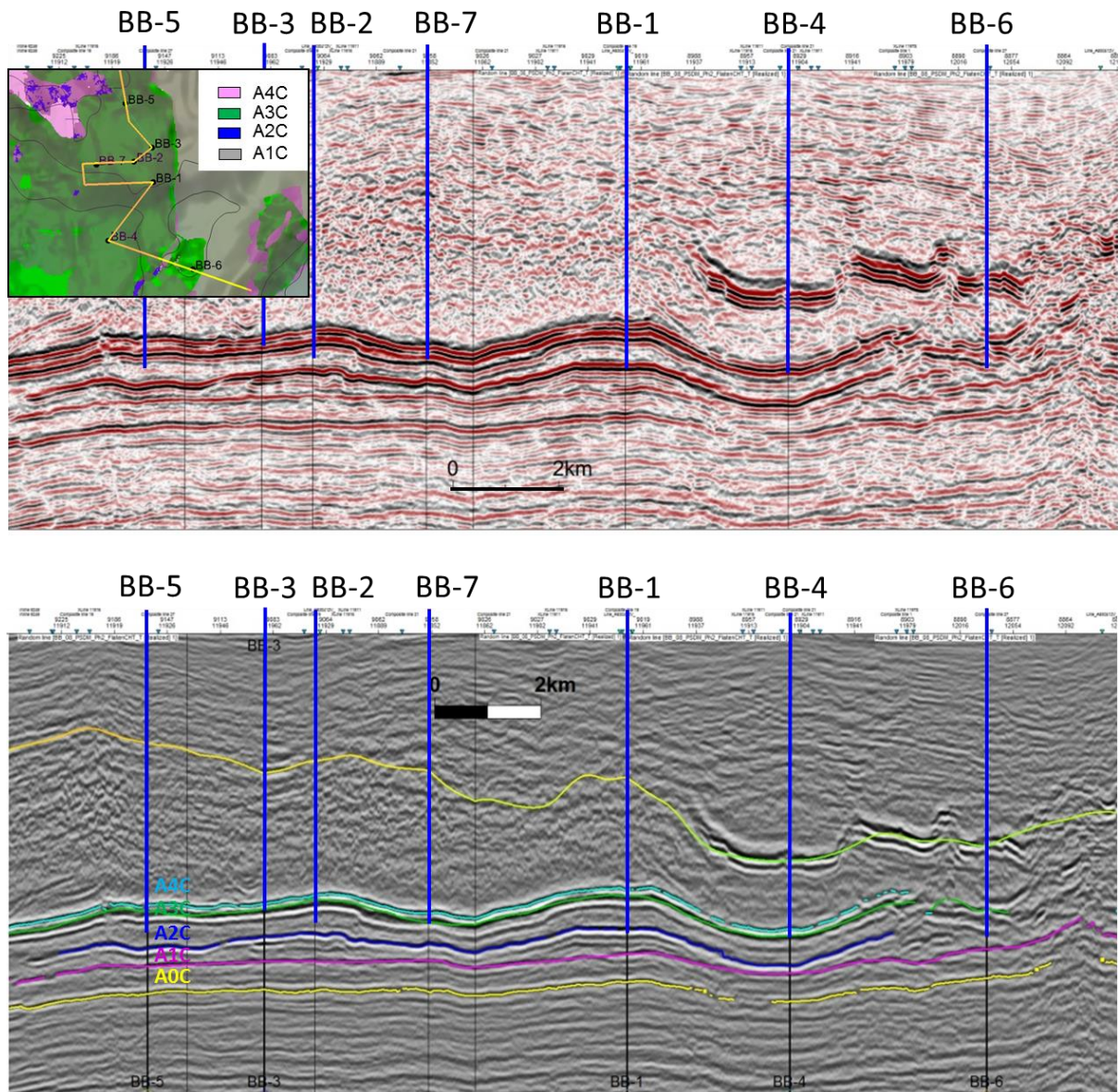
Fig. 6.23: Composite seismic profile passing through Birba wells (BB-1 to BB-6). All the wells terminate at the A3C (BB-3, BB-4, BB-7) and at A3E (BB-2, BB-5). Note the constant thickness of the A3C and A4C stringers.
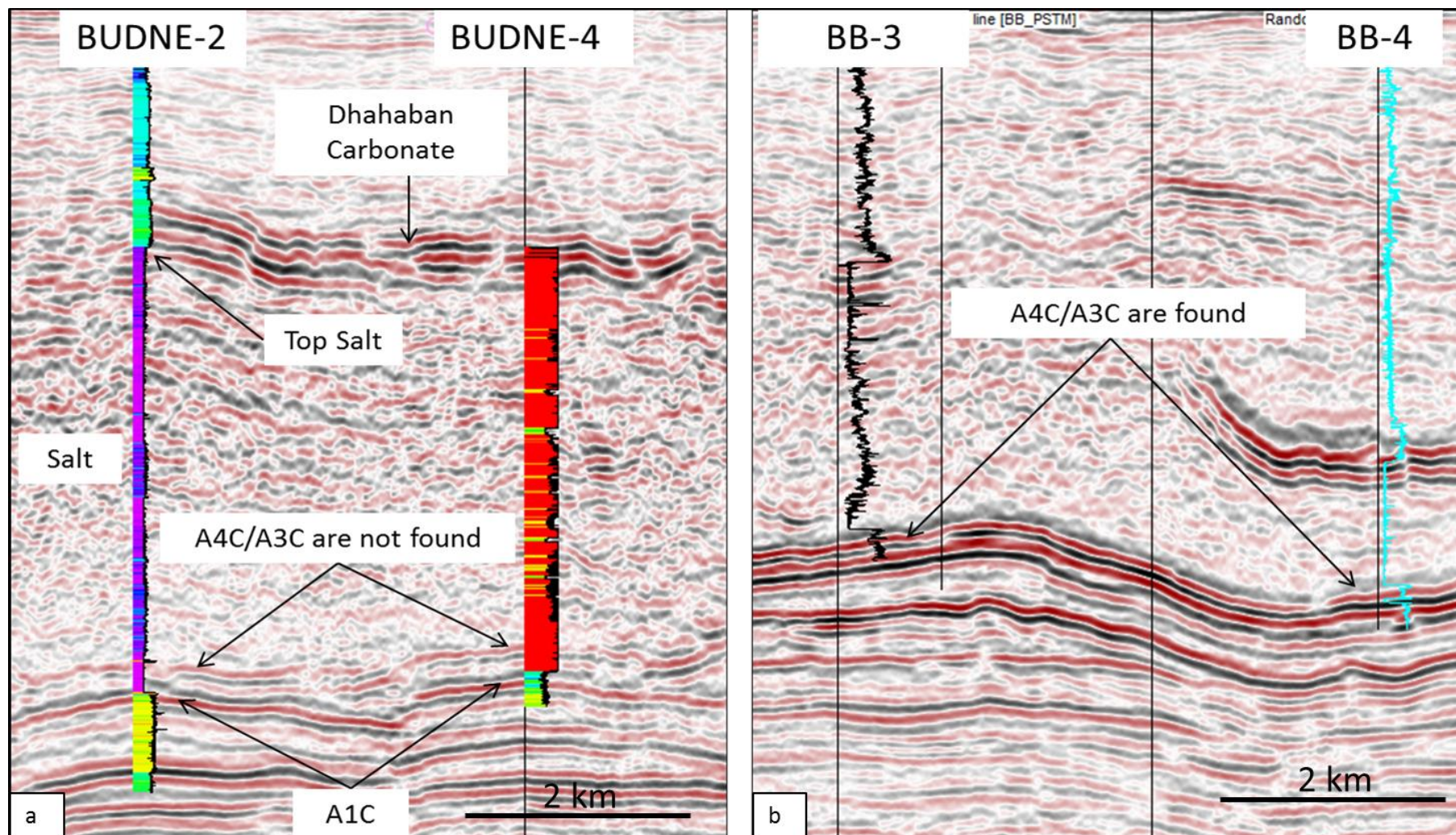
Fig. 6.24: (a) Seismic-to-well calibration of the density curve in BUDNE-2H1 and resistivity curve in BUDNE-4H1. Note that only the A1C has been found in logs (yellow intervals), while the upper A3C and A4C stringers were not found, despite the presence of a weak seismic loop. Note also that the A1C is not underlain by any salt interval in well BUDNE-2H1. (b) The A4C and A3C within BB-3 and BB-4. Note the strong seismic character of the A4C and A3C stringers. The two stringers are found in the two wells.
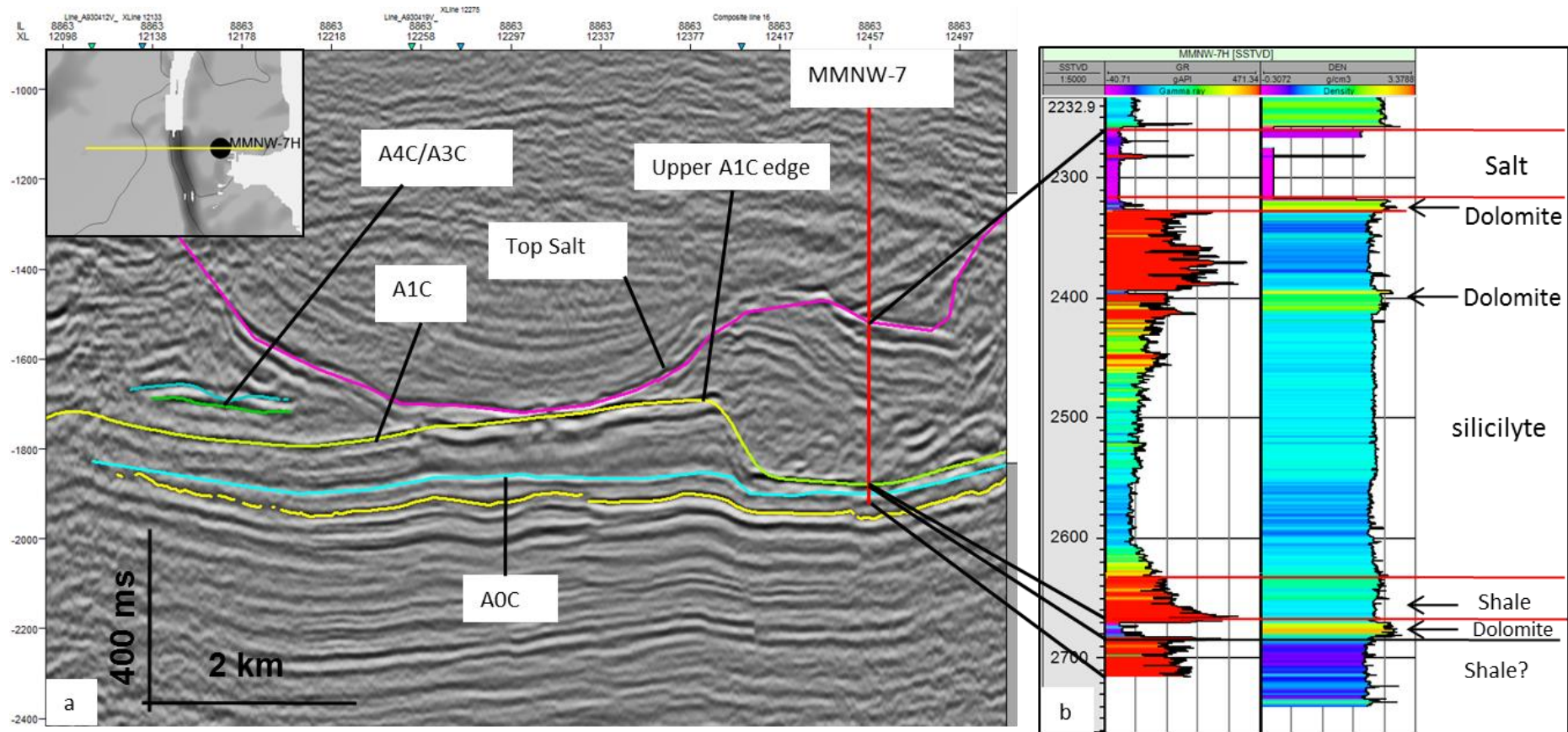
Fig. 6.25: Well MMNW-7 (see Fig. 6.7 for location). (a) E–W profile (inline-8863) passing through the MMNW-7 displays the geometry of the Ara Group and stringers. (b) Gamma ray (left) and density curve (right) of well MMNW-7. Note that the Ara Group contains a thin salt section (60 m thick); the rest of the chaotic zone is a silicilyte unit of shale (high GR) and other clastic sediments (low GR) with thin dolomite layers characterised by higher density (2700–2800 kg/m³) and low GR readings (yellow sheets on the density curve).

6.7   Results of seismic interpretation

6.7.1 A1C stringer

The A1C stringer is continuous in most of the study area and has similar topography to the base and pre-salt (Fig. 6.26a). The data in the northwestern side of the study area is poor and therefore the stringer was not mapped at that location (Fig. 6.26a). In the eastern part of the study area, the A1C stringer forms a platform margin trending almost NNE–SSW with a steep slope dipping to the east (Fig. 6.26). The A1C is not deformed significantly as the upper stringers (A2C–A5C), and it has been largely affected by sub-salt faults. An initial interpretation is that the A1C stringer in the Birba area is not underlain by salt (Fig. 6.24a).

6.7.2 A2C stringer

The A2C stringer is locally distributed in the western part of the study area (Fig. 6.26b). Profiles perpendicular to the stringer show that the A2C and the overlain A3C and A4C stringers are discontinuous from the east and west with downlapping geometries (Fig. 6.27a,b). The A4C stringer is observed to pinch out earlier than the A2C and A3C slabs, which are extended a few hundred metres further (Fig. 6.27a,b). The local extent and the separated blocks of the A2C stringer in the Birba area can either be interpreted stratigraphically or tectonically (see chapter 7 for more details).

6.7.3 A3C and A4C stringers

The stringer is largely distributed in the middle and south of the study area (Fig. 6.26c). Smaller fragments of 4–6 km of the A3C stringer are distributed in the northern part of the study area, south of the MB-1 and MB-2 (Fig. 6.26a).

The A4C stringer has almost similar extent to the A3C stringer in the northern part of the study area (Fig. 6.26d). The A4C and A3C stringers are seismically mappable in the Birba area. The two stringers share almost similar extent, trend, and discontinuities (Fig. 6.26c,d). This is because of the absence of a thick salt layer between the two stringers, which reduces the effect of diapirism, folding, and discontinuities (Fig. 6.24b and Fig. 6.22).

If the A4C and A3C surfaces are superimposed with the Top Salt surface, the stringers are not found under the depocentres of minibasins (Fig. 6.29 and Fig. 6.30). Therefore, the disappearance of the stringers is strongly related to salt tectonics. However, in the northeastern part of the structural high area, and especially east of BUDNE-2 and BUDNE-4, the stingers are not observed although the salt section is thick and has almost constant thickness (Fig. 6.30b,c).
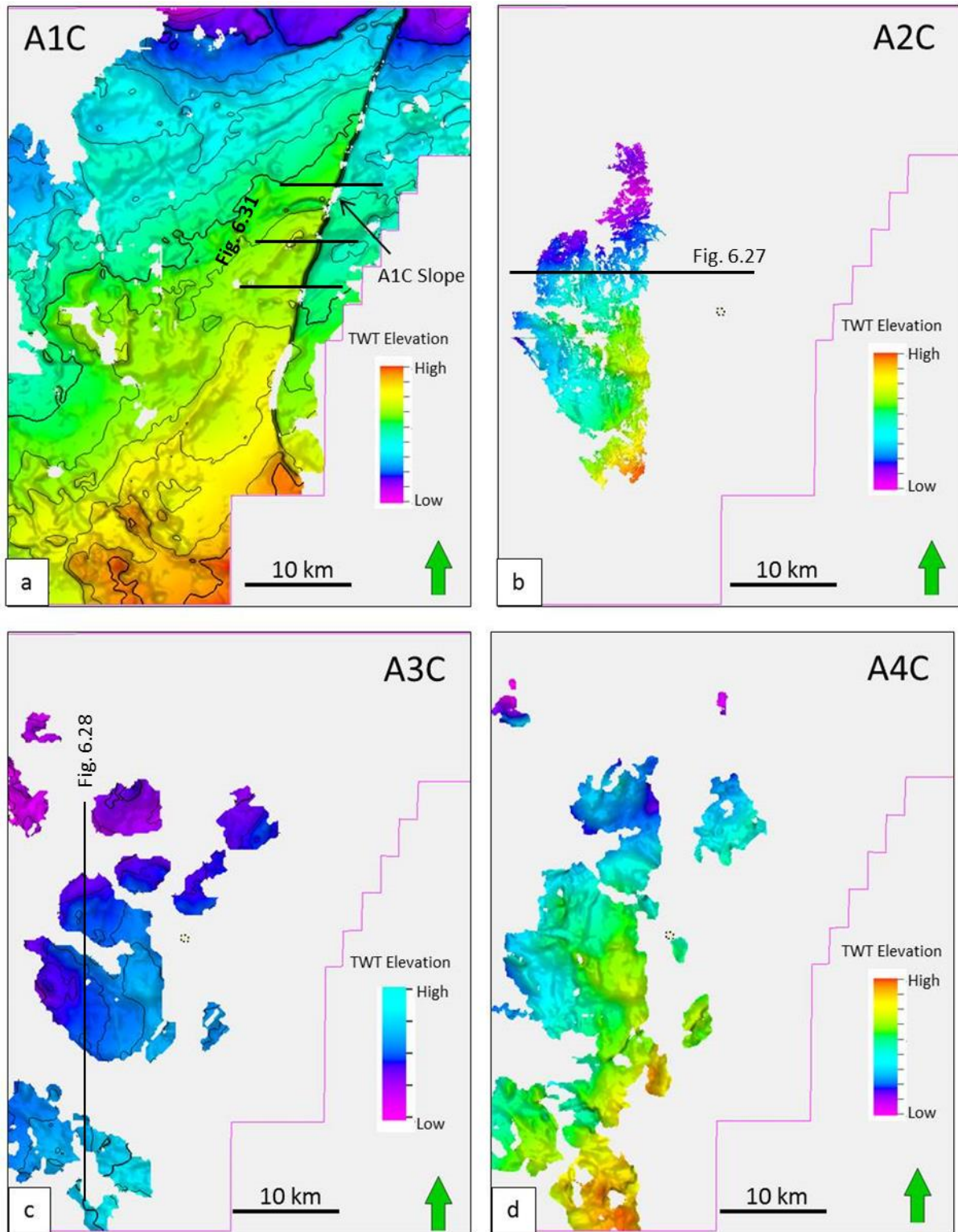
Fig. 6.26: Two-way-travel-time (TWT) structure maps of the stringers in the Birba area.
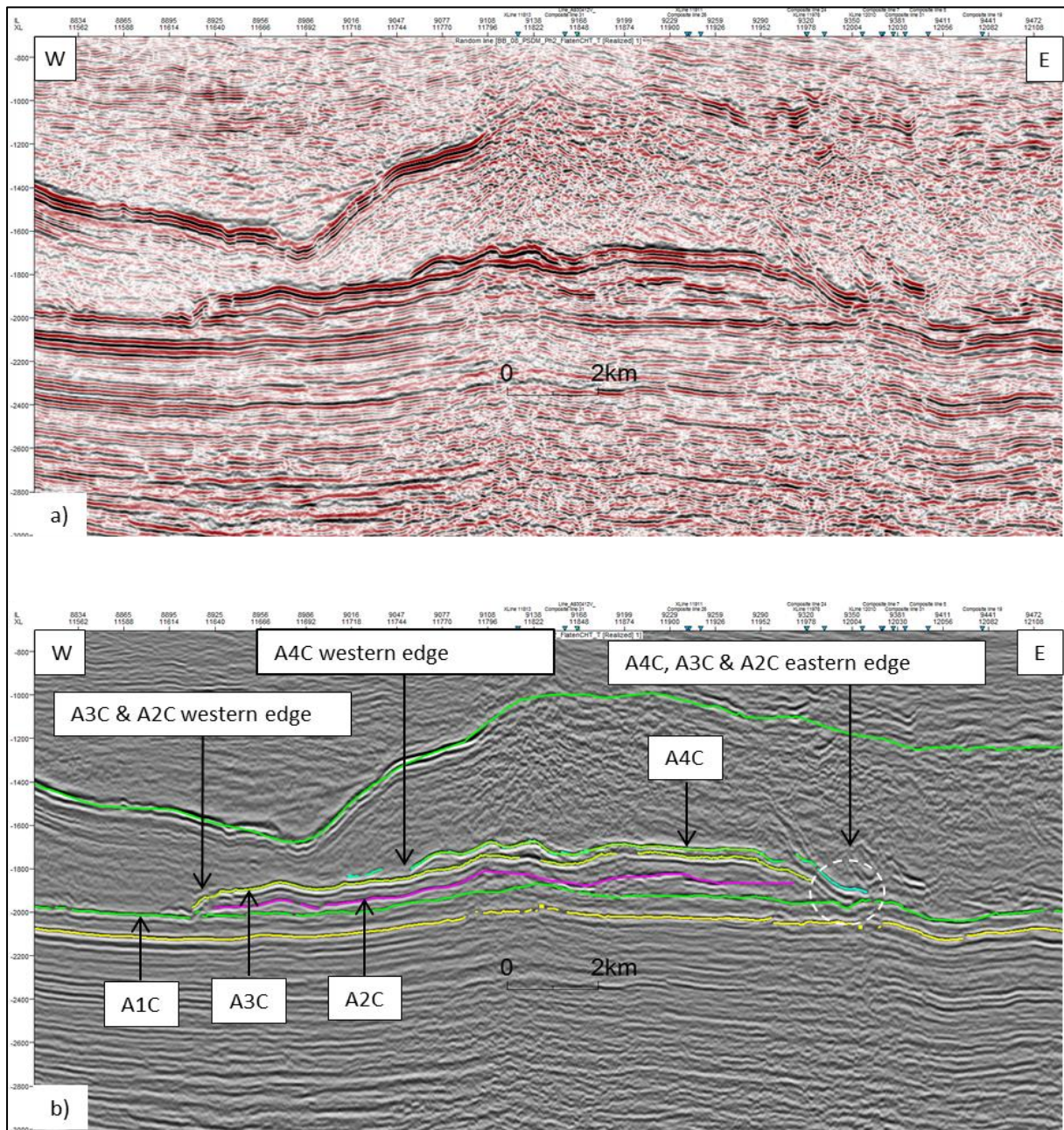
Fig. 6.27: NE–SW seismic line south of the MB-4 displays the western and eastern edges of the A2C, A3C, and A4C stringers. Note the downlapping geometry and the discontinuity of the stringers. Note that the A1C stringer is more continuous and forms the basement hard boundary for the upper stringers (see Fig. 6.26b for location).
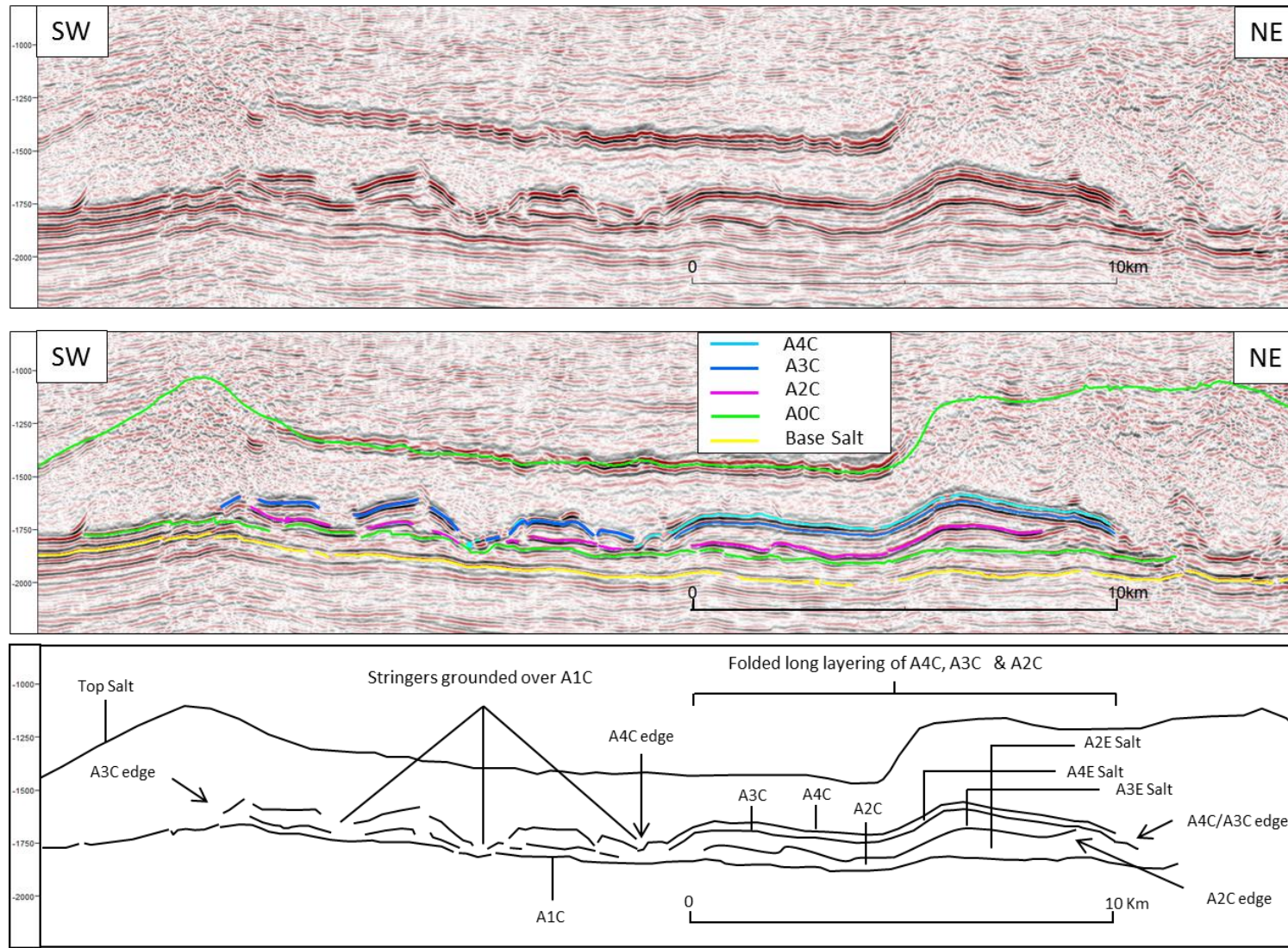
Fig. 6. 28: Geometry of the A2C, A3C, and A4C stringers south of the MB-4. Note the shape of the isolated stringers. The stringers are largely discontinuous below the subsided Top Salt area (see Fig. 6.26c for location).
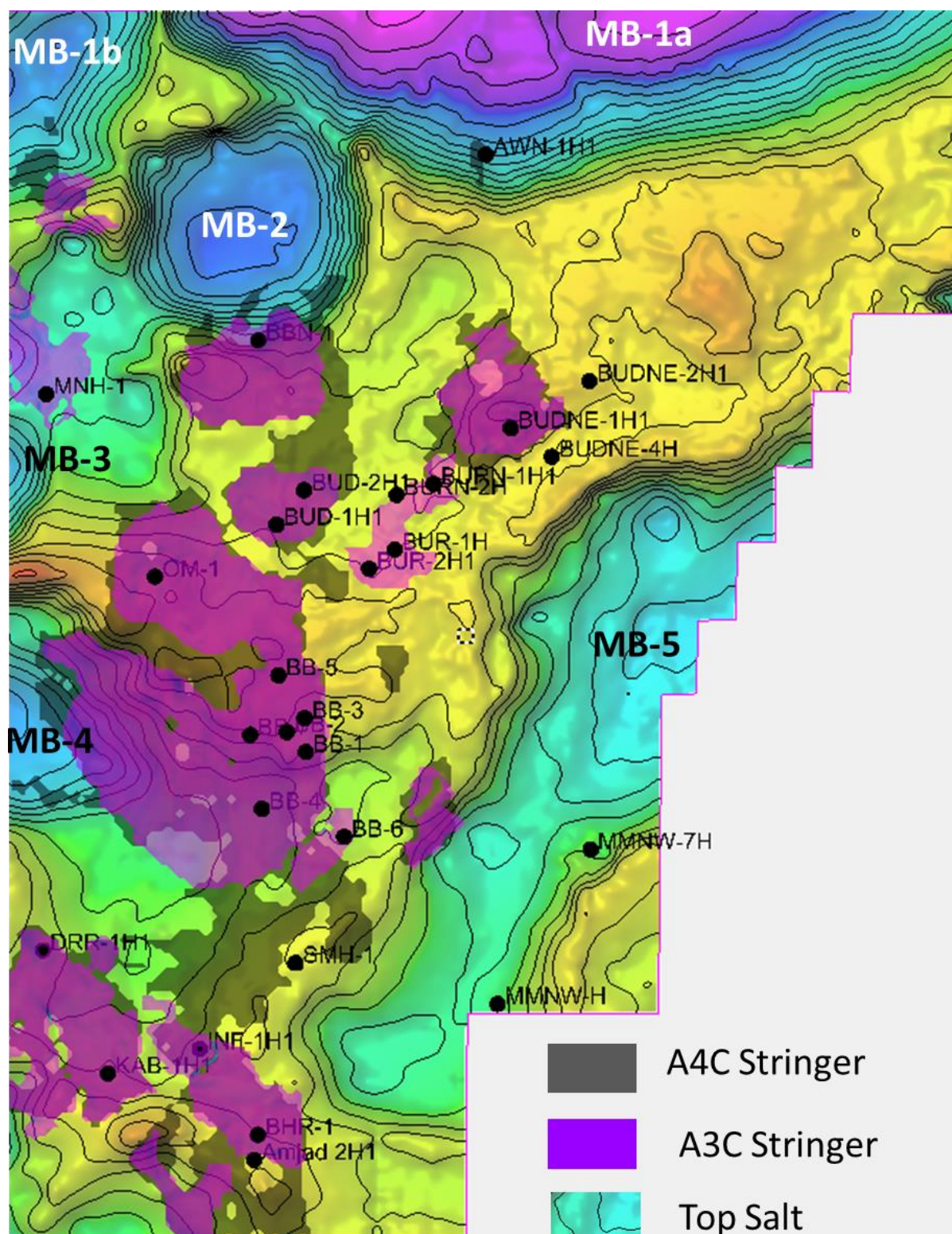
Fig. 6. 29: A4C and A3C stringers superimposed with the Top Salt surface. Note the distribution of the two stringers in different areas of the Top Salt. The stringers are discontinuous and not observed under minibasins and at the eastern side of the Structural High Region north and east of BUDNE-2H1.
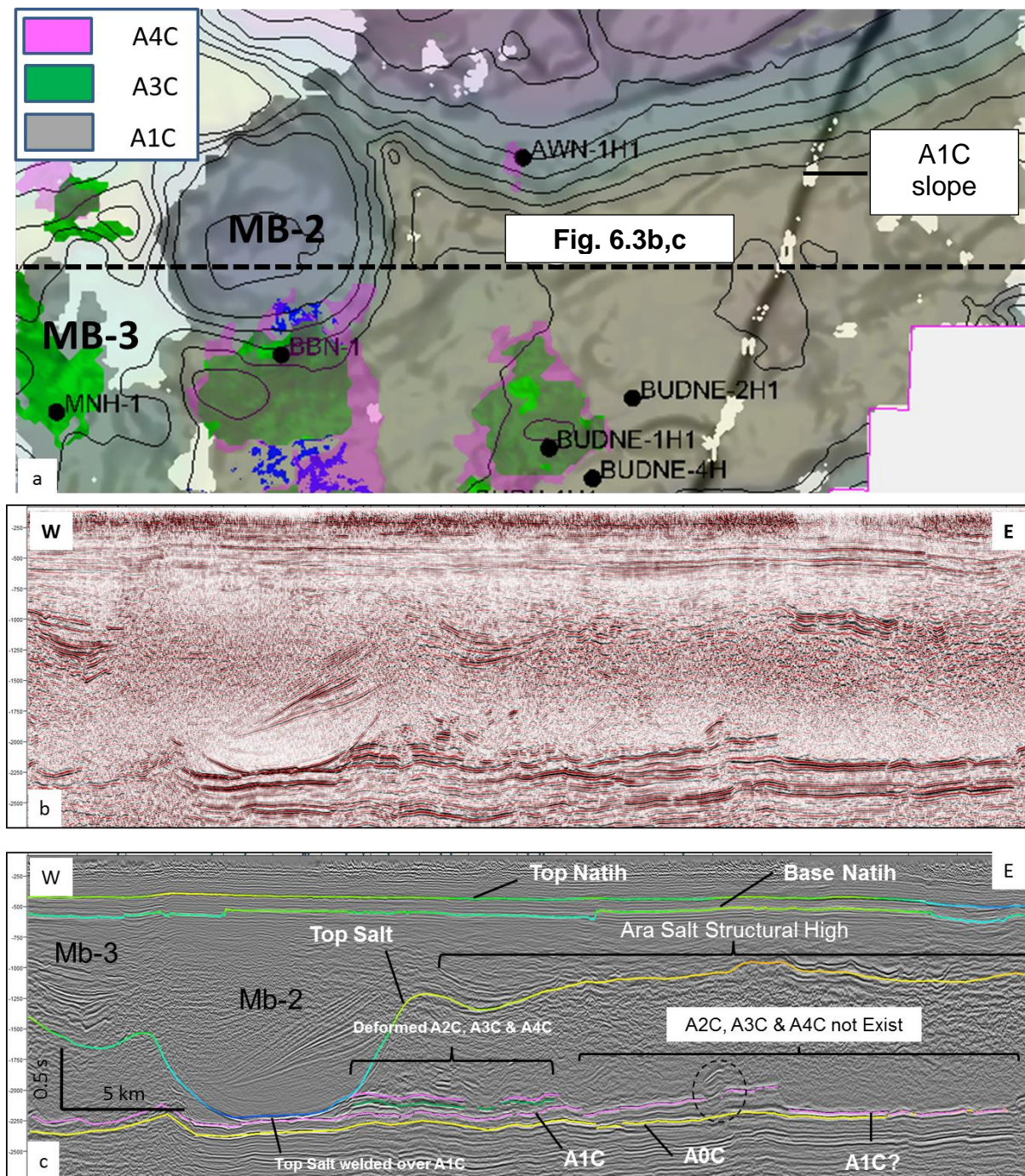
Fig. 6.30: (a) Zoom-in on the northern part of Fig. 6.29. (b, c) Uninterpreted and interpreted seismic profile passing through the MB-2 and MB-3 to the west and the deeper part of A1C to the east. Note that A4C-A2C stringers are not found in the eastern region. The A1C is interpreted only from seismic data to be continuous east of the slope.

6.8   Stratigraphic features of the Ara stringers in the Birba area

The A1C stringer in the eastern side of the Birba area has an eastward steeply dipping slope striking NE–SW (Fig. 6.26a and Fig. 6.31). This geometry is also observed in the Base Ara salt and the underlying pre-salt section, forming similar geometry of a basin slope (Fig. 6.31). The A1C is thicker to the east towards the edge of the slope (Fig. 6.31). In the downslope area, the thickness of the A1C stringer is significantly reduced, and small-scale fragments are observed above it. These could be either remnants of stringers that were deformed during salt subsidence or simply downslope basin deposits.

The absence of displacement in the underlying stratigraphy below the A1C reduces the possibility to interpret the structure as a half graben. Therefore, the A1C structure has been interpreted to be the platform margin with steep slope dipping to the east (Fig. 6.31).

Basinward deep marine facies is expected to form east of the slope. This is also indicated in well MMNW-7 (Fig. 6.25). The decrease in thickness of the A1C above the slope from more than 100 m to about 10 m downslope indicates that the carbonate factory is active in the shallow areas in the platform margin and very weak in the basin side (Fig. 6.31). If this interpretation is valid, then good carbonate reservoirs which are perfectly sealed by salt are expected to be found along the strike of the platform margin.

The A4C and A3C stringers are not found in BUDNE-2 and BUDNE-4 in the eastern side of the study area (Fig. 6.26). In spite of the presence of weak seismic loops above the A1C stringer, the A4C and A3C stringers were not encountered (Fig. 6.24). This has been interpreted to be related to an eastward stratigraphic thinning

and termination of the A4C and A3C carbonates (Fig. 6.32). The N-S A1C slope and the N–S elongation of the A2C, A3C, and A4C stringers support the east-west lateral stratigraphic facies changes (Fig. 6.26).

The A3C and A4C stringers form overlapped dome shapes south of the MB-4 (Fig. 6.33). Dome-1 and Dome-2 have steep slopes in the northern side where the A3C and A4C stringers terminate at the A1C level (Fig. 6.33a,b). Similarly, the A3C–A5C stringers display vertical build-up at OM-1H1 (Fig. 6.33e). These have been interpreted here as open marine carbonate build-up.

The A3C and A4C stringers in general are mostly conformable in thickness. However, the A4C grounding and welding over the A3C is found in areas near minibasins (Fig. 6.33f). This could be related to squeezing of the salt between the stringers during subsidence.
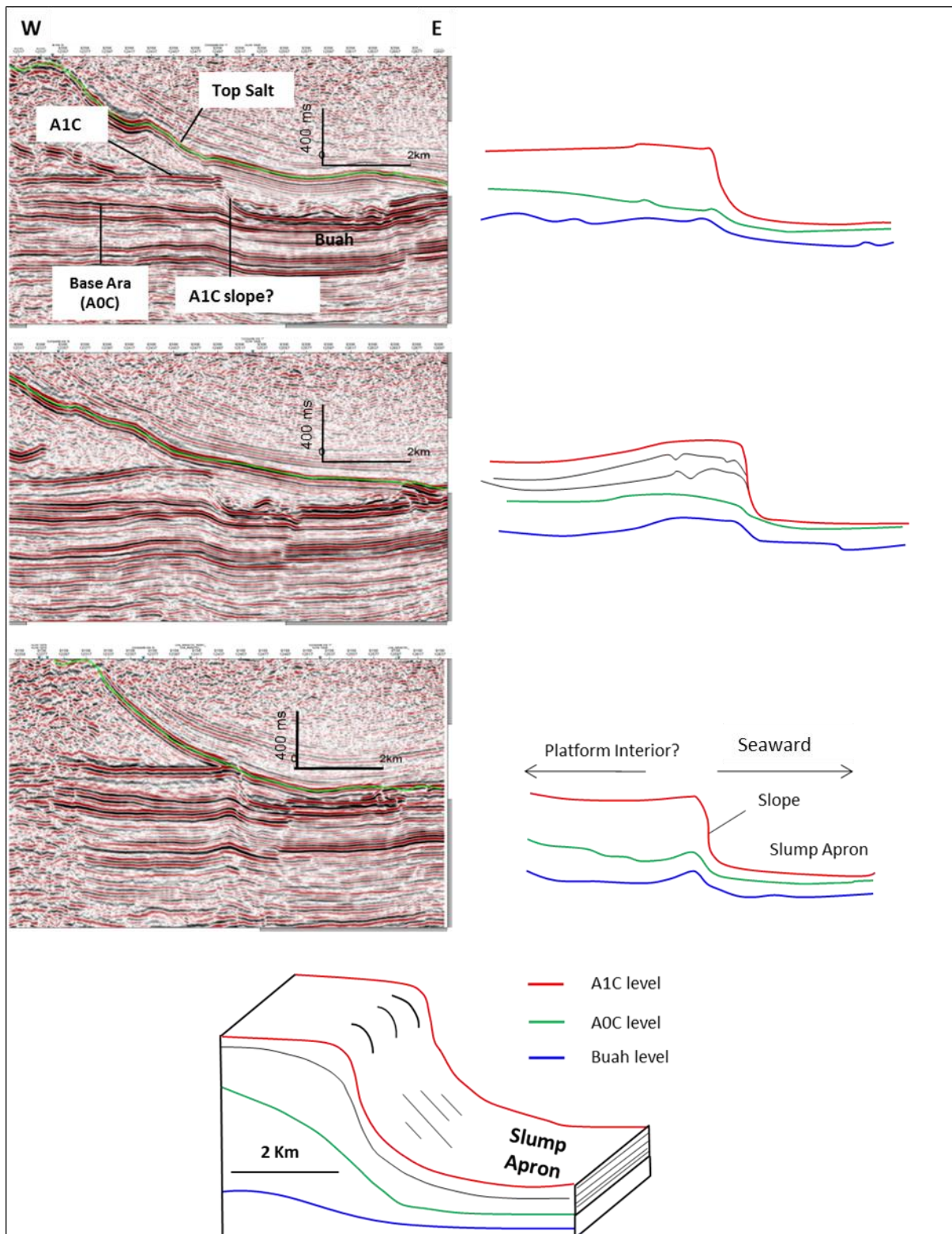
Fig. 6.31: The geometry of the A1C slope in the eastern side of the study area (see Fig. 6.26a). The A1C steep geometry is interpreted to be a platform margin and thus the eastern side is the basin facies. Note the thickness of the A1C in the platform margin and the small thickness in the basin side.
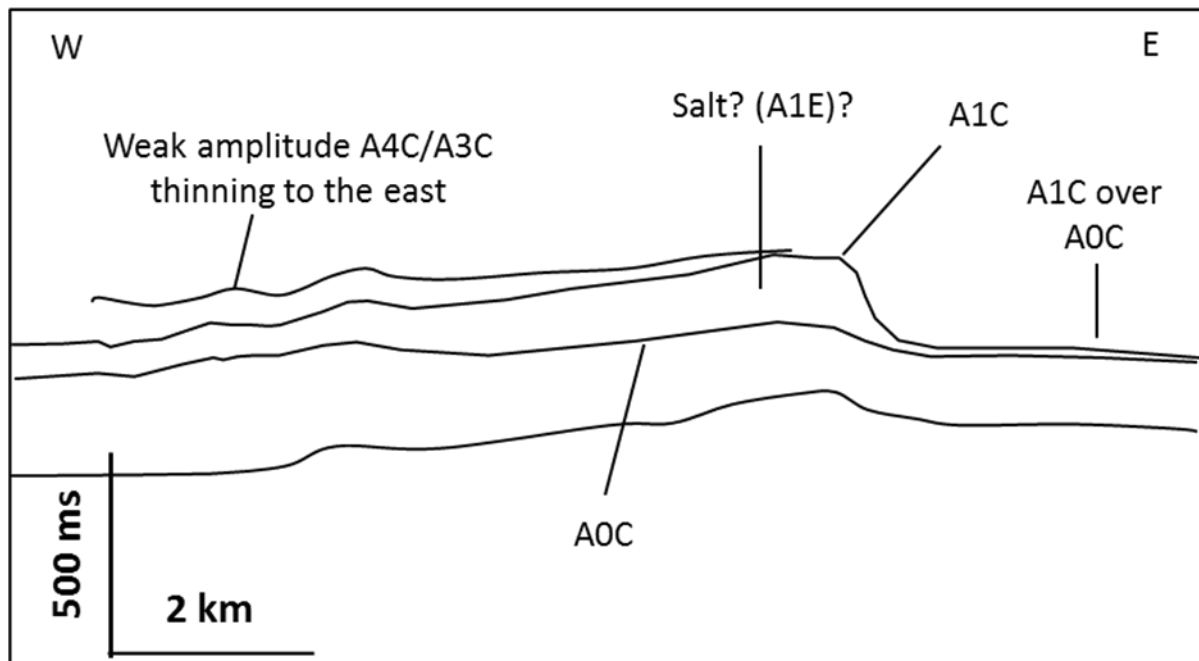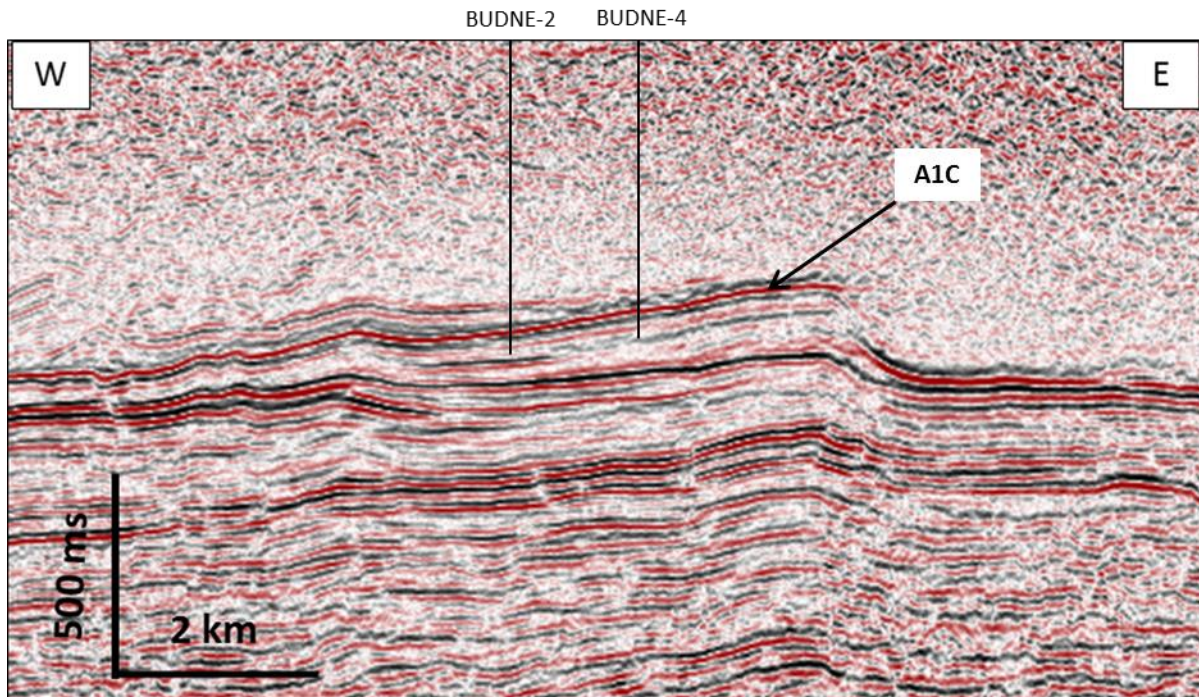
Fig. 6.32: E–W seismic profile in the NE region of the Birba study area (see Fig. 6.7 for location). Note the SE thinning of the weak seismic character at the A3C and A4C level. Well BUDNE-2H1 and BUDNE-4H1 show a very thin carbonate layer (~2 m) in the first well and no A4C/A3C stringers in the second well.
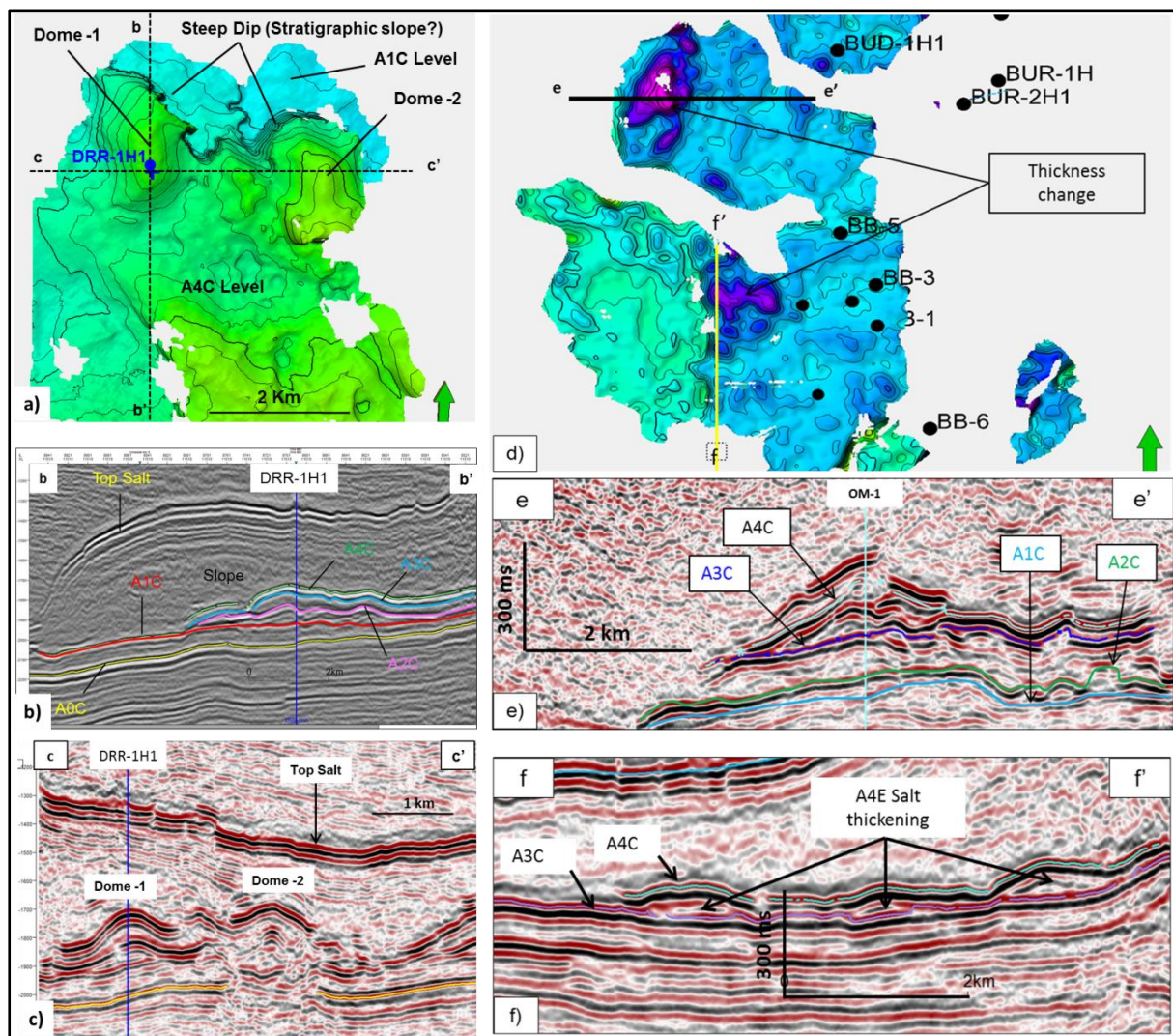
Fig. 6.33: (a) 3D TWT surface displays dome shapes in the A4C stringer. (b) N–S seismic profile passing through Dome-1 and DRR-1H1. Note the discontinuity of the A4C and the continuity of the A1C stringer from south to north. (c) E–W seismic line passing though Dome-1 and Dome-2. Note the shape of the domes and their location below the minibasin. (d) A4C–A3C time thickness map. Two major thickening areas identified (purple colours). (e) Profile passing through the OM-1 displays the thickness change between the A4C and A3C stringers. The complex dome shape is similar to reef structures. (f) Welding of the A4C stringer over the A3C stringer with variable thickness change of the A4E salt interval.

6.9   Discussion

6.9.1 Salt tectonics in the Birba area

Three syn-kinematic growth units in the overburden have been interpreted from seismic profiles (Fig. 6.9 to Fig. 6.13).

- Syn-kinematic Unit-1 directly overlies the Ara Salt found within deeper minibasins (e.g., MB-1, MB-4, and MB-5; Fig 6.9). This unit belongs to the Early Cambrian Nimr Group (Al-Siyabi 2005). The mechanism of down-building simply means the subsidence of salt by sediment load creates minibasins at the middle while the two sides of the salt remain at the same level (Jackson et al. 1990; Hudec 2007). This mechanism is the most important in the case of salt tectonics driven by sediment load. The structural high region, or salt wall, in the northeast of the study area has almost constant salt thickness (Fig. 6.7).

- Syn-kinematic Unit-2 overlies Syn-kinematic Unit-1 and contributes to the sinking of the minibasins that were filled by Syn-kinematic Unit-1 as well as producing new minibasins in the Ara elevated regions (e.g., MB-3; Fig 6.9 and Fig 6.10).

- The extensional faults in the overburden created syn-extensional growth units due to salt rise (e.g., west of Profile E; Fig. 6.13), which also add new load over the Ara salt, causing a third phase of salt flow. Syn-kinematic Unit-3 is a localised kinematic unit formed by faults displaced from the Top Mahwis unconformity up to the base Natih (Fig. 6.15). A summary of the evolution of salt tectonics in the Birba area is shown in Figure. 6.34.
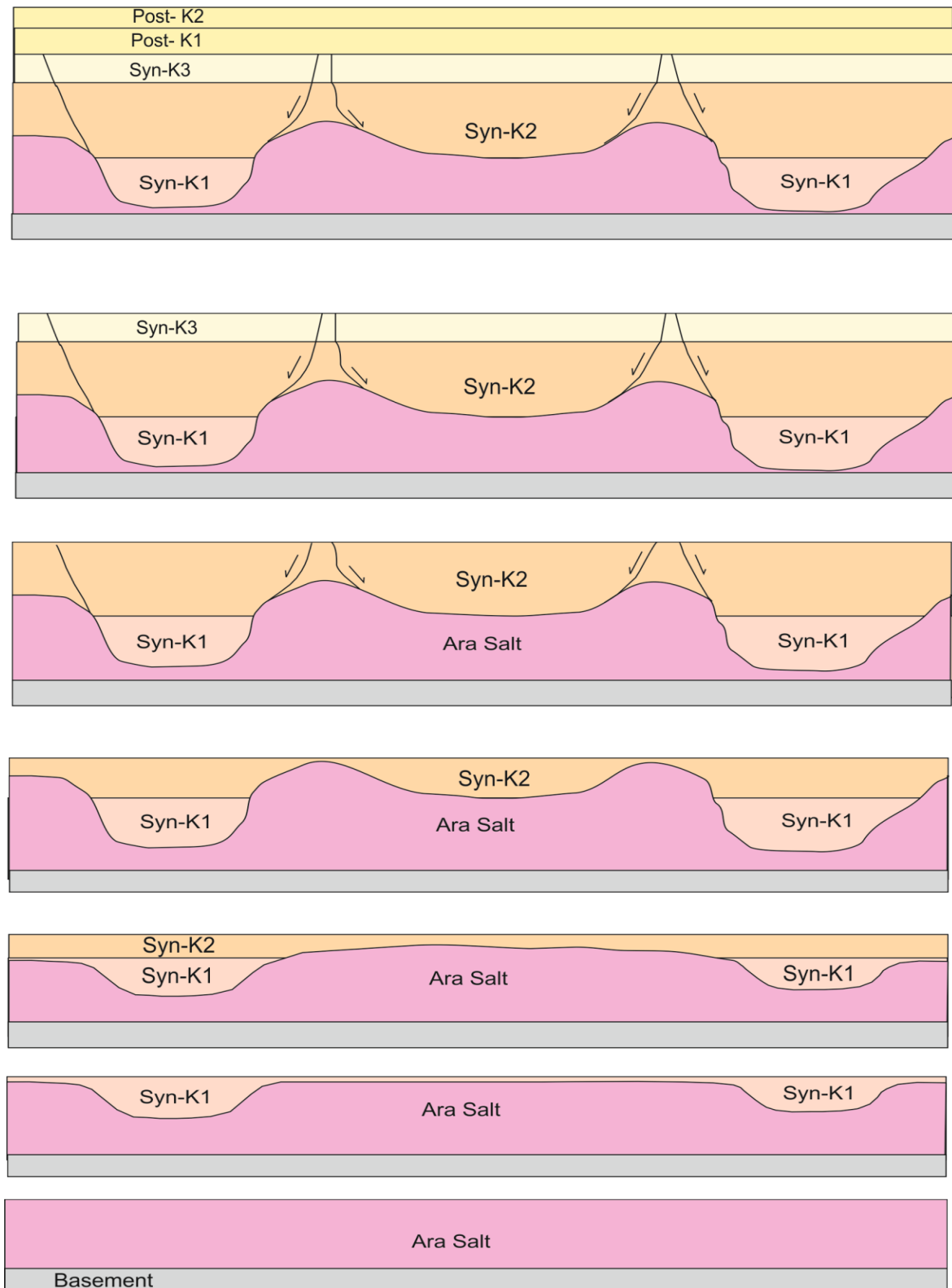
Fig. 6.34: Schematic 2D model for post-salt evolution in the Birba area summarised from seismic profiles (Fig. 6.9 to Fig. 6.13).

6.9.2 Detailed evolution of minibasins

The evolution of minibasins can be more complex depending on the source of sediment influx and the subsidence direction of the salt layer (Fig. 6.14). The syn-kinematic indicators within the MB-2 were used as an example to demonstrate the minibasin developments in the study area. The results indicate the complexity of the basin filling wedges and thus the complexity of the internal salt dynamics. Three strong indicators were mapped within the minibasin, followed by construction of thickness maps for each package (Fig. 6.14). The thickness maps of the three units revealed a change in the maximum thickness of the units from middle (Fig. 6.14b) to the east (Fig. 6.14c) and finally to the north (Fig. 6.14d). Unit-2 displays upward thickening with a dip of approximately 30° (Fig. 6.14h). It is not geologically possible to deposit syn-kinematic units with such geometry. However, if the top of Unit-3 is flattened, Unit-2 indicates downward thickening with a magnitude of 5° to 10°, which is more geologically reasonable (Fig. 6.14f). The evolution of the kinematic filling units within the MB-2 can be summarised in three stages (Fig. 6.35):

1. The minibasin initially filled almost equally from all directions while Top Salt was displaced downwards, forming a synclinal basin shape (Fig. 6.35b; see also Fig. 6.14b).

2. The eastern flank of the basin was displaced more than others due to the eastward sediment influx resulting in the deposition of the Syn-kinematic Unit-2 (Fig. 6.35c; see also Fig. 6.14c).

3. A third salt displacement event took place in the north to northwest of the MB-2 with the rising of a salt diapir in the east, resulting in the rotation of Unit-1 and Unit-2, and deposition of Syn-kinematic Unit-3 (Fig. 6.35d; see also Fig. 6.14d).

W   E
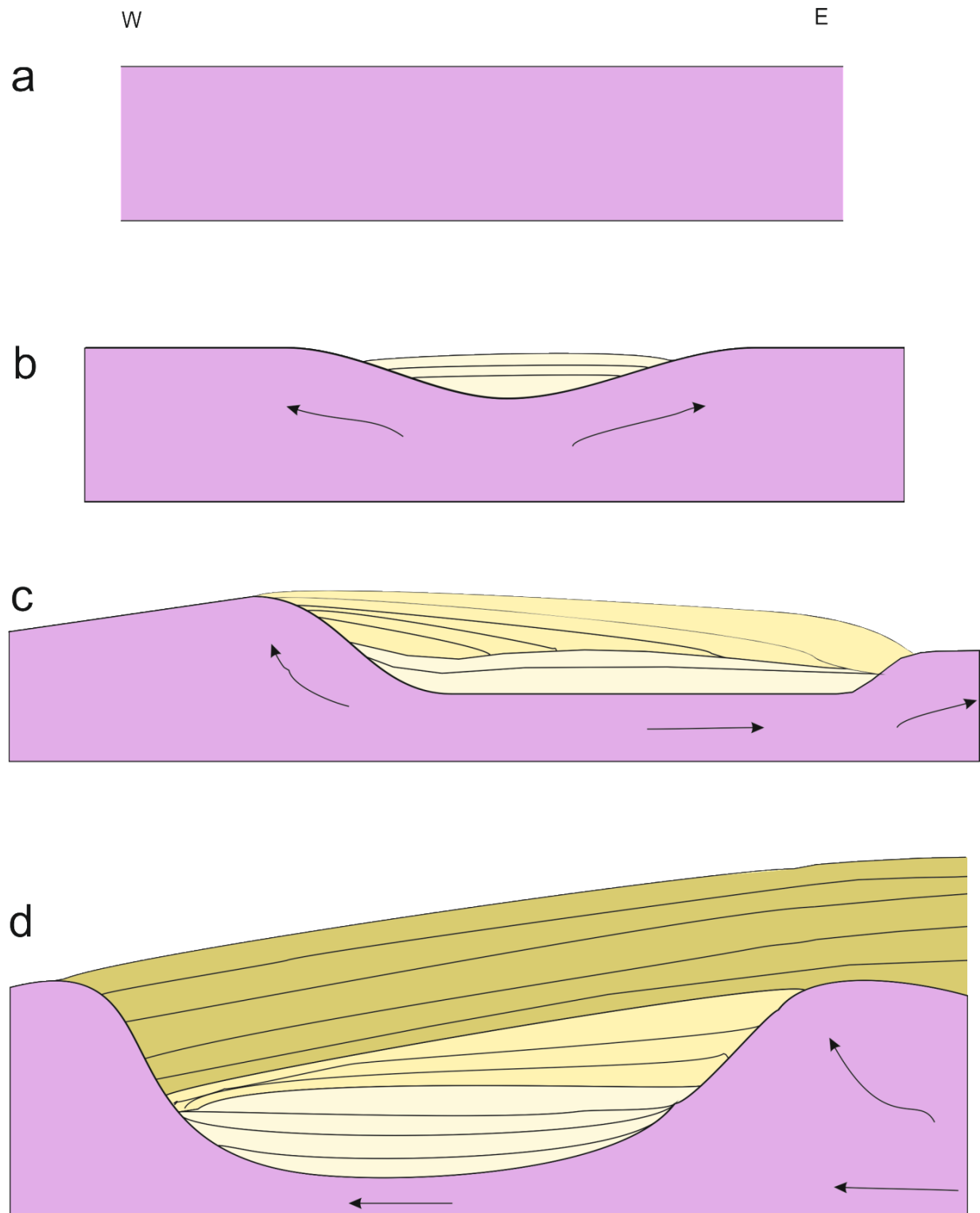
Fig. 6.35: Schematic model of basin fill units over the MB-2 (see Fig. 6.14). (a) Ara salt before sediment influx. (b) Deposition of Unit-1 forming thickening strata in the middle and onlapping at the syncline flanks. (c) Deposition of Unit-2 and downward salt depression resulting in an eastward thickening wedge. (d) Westward salt movement resulted in the formation of the flank of the MB-2, which rotates Unit-2, and the deposition of N–NW thickening wedge of Unit-3.

6.9.3   Depositional model of the carbonate stringers in the Birba study area

Defining platform geometries and stratigraphic features on seismic data is an important and primary method for understanding the depositional environment of the basins. However, generating platform geometry and later depositional facies models for the Ara stringers based on the geometry of the stringers observed from seismic data is challenging. This is because of the influence of halokinesis of the Ara salt on the carbonate stringers resulted in significant deformation such as folding, faulting, and lateral displacement (Al-Siyabi 2005). By superimposing the A1C and the upper stringers, the initial depositional environment of the lower part of the basin (A1C-A4C) can be summarised (Fig. 6.36 and Fig. 6.37).

- The A1C stringer is thickening to the east until the edge and thinning downslope of the basin, indicating a platform margin trending N–S (Fig. 6.31).

- The western part of the basin displays a gradual deepening of the A1C, indicating deeper deposits and lack of A2C–A4C stringer deposits (Fig. 6.27).

- The carbonate stringers are well distributed in the middle of the study area (Fig. 6.26). Therefore, this area is the shallow marine carbonate factory of the stringers.

- The A4C and A3C stringers are thinning and terminating towards the east (Fig. 6.32). Similarly, the A2C–A4C stringers are not stratigraphically extended towards the western part of the basin (Fig. 6.27).
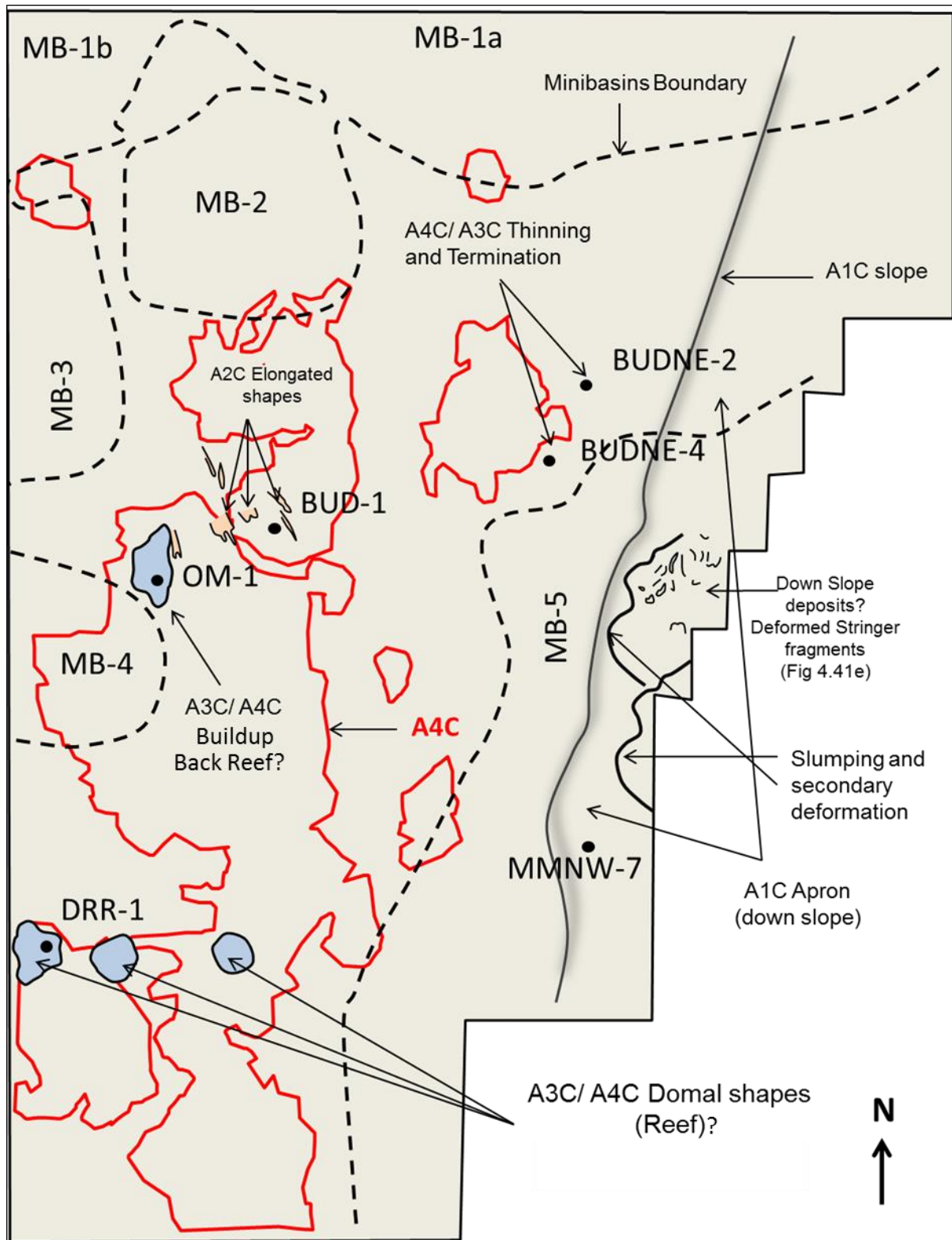
Fig. 6.36: Summary map of the stratigraphic features in the Birba 3D seismic area. The red boundary is the current extent of the A4C stringer.
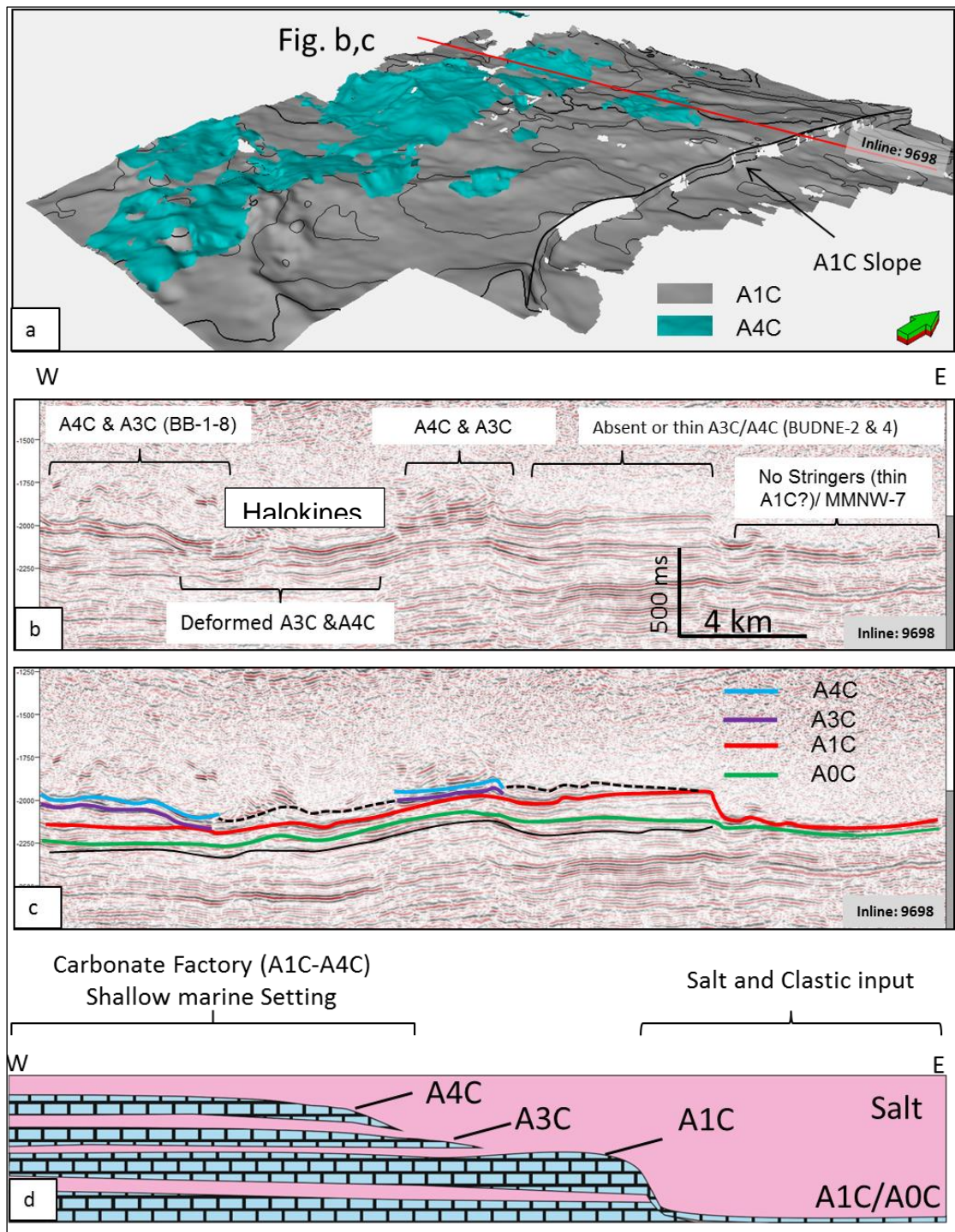
Fig. 6.37: (a) The A1C stringer surface (grey) overlain by the A4C surface (blue). (b–c) East-west seismic profile through the A1C platform margin. Note the termination of the A4C and A3C stringers in the eastern side (right dash line) and the deformation-related discontinuity in the western side (left dash line). (d) The depositional model of the Ara stringers in the northern part of the study area.

6.10 Conclusions

- Five large minibasins have been identified in the Birba study area. The formation of these minibasins is more complex than expected, where the overburden sediment switched its depocentre direction because of the changes in location of the salt subsidence zones and the change in sediment influx. These changes in minibasins generated variable movement of the salt and hence complex internal deformations during the creation of the minibasins.

- The calibration and identification of at least five intra-salt carbonate stringers was done by well-to-seismic tie of 28 wells in the Birba area. The lower four stringers are observed both on seismic and well data. These are A1C, A2C, A3C, and A4C. The upper stringer, A5C, is rarely found, and it is significantly discontinuous.

- The A1C is deposited regionally, maintains its thickness in a large area, and is only observed to thin and probably terminates beyond the platform margin to the eastern side of the study area.

- The thickness of the halite intervals (A1E–A4E) is variable due to both early stratigraphic deposition and tectonics.

- The carbonate stringers in the Birba area have complex stratigraphic and structural geometries. Because of such complex geometries, the stratigraphic features can easily be misinterpreted as tectonically derived features.

Chapter 7: Structural description and kinematic evolution of the carbonate stringers in the South Oman Salt Basin

Abstract

The structure and kinematic evolution of the carbonate stringers in the South Oman Salt Basin is described in this chapter using 3D time migrated seismic reflection data. Four intra-salt carbonate layers known as the A1C–A4C stringers, which are encased within a 1.5–2 km-thick salt and have been subjected to a significant differential subsidence, are examined here. To understand the kinematics of the Ara carbonate stringers during halokinesis, the geometry of the stringers was studied beneath major salt structures such as salt diapirs, salt walls, minibasins, and around the flanks of minibasins. The amount of displacement of Top Salt at different parts of the basin was used herein as a tool to test the internal kinematics of the stringers. The results indicate that differential loading alone was sufficient to significantly deform, fragment, drag, and fold the layered stringers within the salt. The kinematics of the carbonate stringers during salt halokinesis were documented during three main stages: (a) During the early stages of subsidence, the upper stringer (e.g., A4C) beneath the subsided region was exposed to lateral extension earlier than the underlying stringers (A3C and A2C). With more subsidence, the lower stringers were consequently ruptured. (b) During the moderate to late stage of subsidence, the stringers beneath the depocentre of the minibasins were broken into smaller stringer fragments, while the stringers around the flanks of the minibasins were folded. (c) During the welding and late stage of halokinesis, more salt was evacuated from the depocentres, which resulted in fragmentation and lateral displacement of the stringers in areas of subsidence and vertical displacement and uplift of stringer fragments into high elevations (up to 2 km) within the salt walls.

The results from this chapter highlight the significance of sub- and intra-salt faulting on initially breaking the stringers and subsequently creating large-scale gaps. The

study contributes to the understanding of pore pressure prediction of the stringers and can be used as an initial step for classifying and predicting overpressured stringers from hydrostatic stringers.

7.1   Introduction

In the South Oman Salt Basin (SOSB), large carbonate bodies, so-called rafts, floaters, or stringers, are encased in salt and form substantial hydrocarbon plays (Al-Siyabi 2005; Peters et al. 2003; Li et al. 2012a). Understanding when and how these intra-salt stringers break and how they redistribute fluids is of practical importance for hydrocarbon exploration and production. Apart from being exploration targets, the stringers can also pose drilling hazards, and non-target stringers are always avoided during operations because they contain overpressured fluids (Williamson et al. 1997; Koyi 2001; Al-Siyabi 2005; Schoenherr et al. 2007, 2008; Kukla et al. 2011). For well engineers, it is important to have an estimate of the pore fluid pressure within the stringers in order to avoid taking "kicks" during drilling.

The SOSB is an intracontinental basin formed by *down-building* in the absence of significant extension or contraction and without significant surface or basal slope (Al-Marjeby and Nash 1986; Al-Siyabi 2005; Li et al. 2012a; Peel 2014). However, the internal salt deformations in the SOSB are found to be more complex because of the complex evolution of the salt.

Salt tectonics in the basin can be summarised to have been formed in least three stages: passive as down-building, reactive, and finally active salt tectonics (Loosveld et al. 1996; Hudec and Jackson 2007; Reuning et al. 2009). Hence, the early structural geometries and the kinematic evolution of the internal salt stringers remain a challenge. Recent numerical modelling simulating the stringers in the SOSB

revealed that the carbonate stringers can break soon after the onset of salt tectonics and can deform in different ways (Li et al. 2012a). If extension along the inclusion dominates, the carbonate stringers are broken by tensile fractures and boudinage at relatively shallow depth.

7.1.2 Aims of this chapter

The aims of this chapter are

- To understand the kinematic evolution of the intra-salt stringers from the early to the late stages of tectonics under salt subsidence and thickening, by selecting local areas where the regional salt structure is less deformed to represent an early deformation stage of the stringers, and areas from highly deformed regional structures to represent the late-stage deformation of the stringers (Fig. 7.1).

- To carry out detailed structural descriptions of the deformed A1C–A4C carbonate stringers underneath regional salt structures (e.g., salt minibasins, salt walls, and salt flanks) (Fig. 7.1).

- To use the geometries of the stringers to understand the kinematics and dynamics of the salt during halokinesis.

- To compare the structural styles of carbonate stringers in the SOSB with the Z3 anhydrite stringer in the Southern North Sea.

Initial stage before halokinesis

Salt   Stringers

Early stage of halokinesis

Intermediate stage of halokinesis

Salt wall   Minibasin   Salt wall

Late stage of halokinesis

Salt wall   Salt wall

Minibasin Flank →   Minibasin   ← Minibasin Flank
                         Depocentre

welding
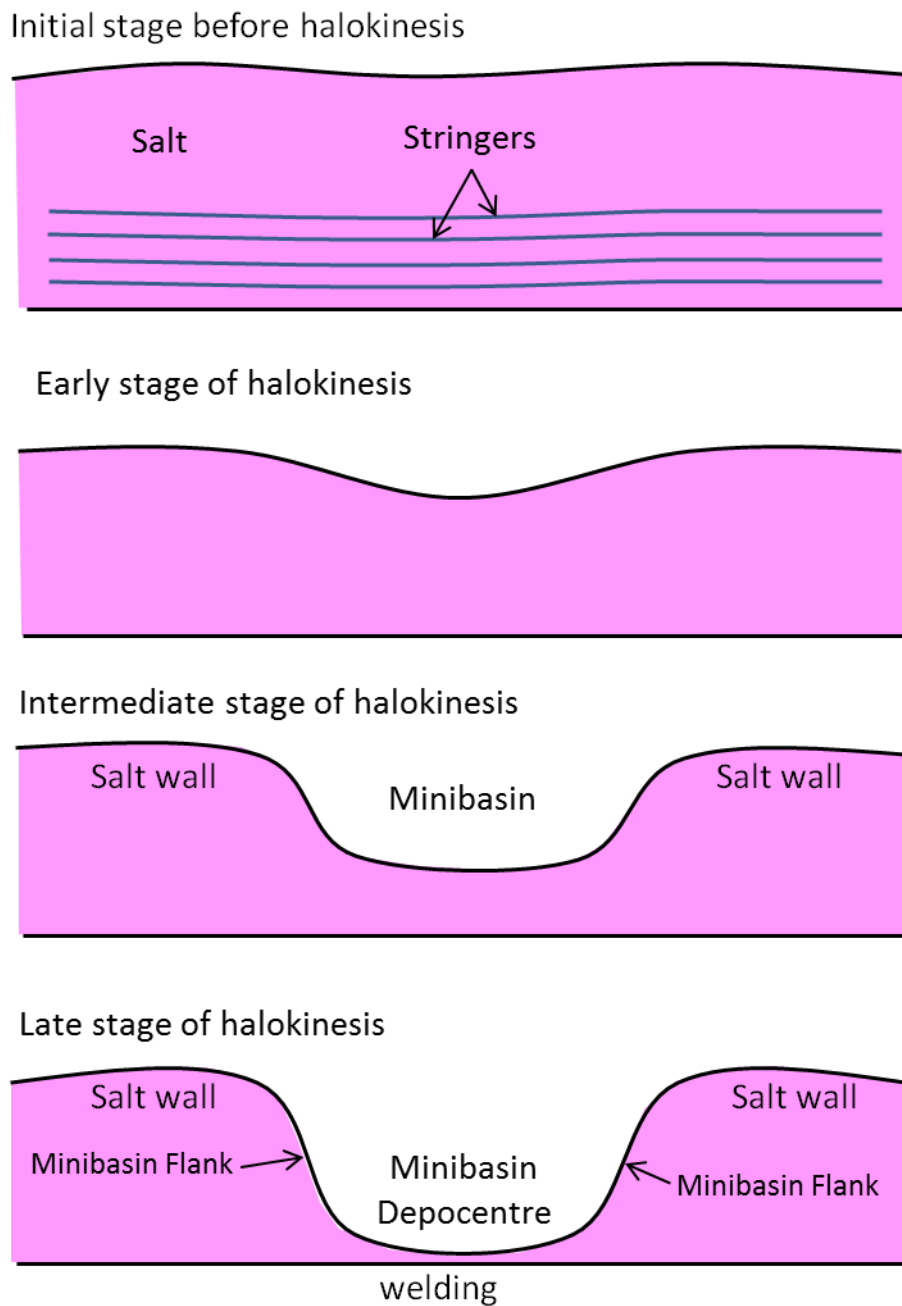
Fig. 7.1: 2D Schematic showing the evolution of a minibasin in the SOSB. The stringers inside the salt will be described at each stage of subsidence and beneath all the regional structures.

7.2   Regional structural description of Top Salt and stringers

The overall distribution and morphology of the salt structures in the Birba area are summarised here to provide a regional framework for the intra-salt structures (Fig. 7.2a). The basin can be simplified into three regional layers (Fig. 7.2b): (1) sub-salt layers characterised by extensional faults; (2) the salt layer, which is highly variable in thickness, largely because of evaporite mobility and variously associated with minibasins, diapirs, and salt walls; and (3) the thick clastic overburden deposited above the salt layer known as the Haima Supergroup, which was deposited during halokinesis in the basin (Al-Siyabi 2005; Reuning et al. 2009). The differential loading of the thick clastic overburden Haima Supergroup onto the mobile Ara salt caused passive diapirism (down-building) until the clastic overburden sediments grounded on the sub-salt strata (Al-Siyabi 2005; Reuning et al. 2009).

The seismic interpretation of the Top Salt surface revealed three main regional salt structures: (1) salt minibasins, where the salt is extremely thinned or welded; (2) salt walls; and (3) salt flanks (Fig. 7.2a, b). Five salt minibasins (MB-1 to MB-5) and a large irregular salt wall with an average height of 1.7 km (Fig. 7.2a) have been found.

The degree of subsidence of the minibasins varies significantly. For example, the MB-1 and MB-2 are completely welded with the A1C (Fig. 7.3a). The deformation of the stringers in this minibasin indicates the configuration of the stringers at the late stages of halokinesis. The salt walls have relatively simple external morphologies, and are defined by relatively flat crests and dipping flanks (20°–50°) (Fig. 7.2). The salt walls are up to 2 km tall, 20 km wide, and 60 km long (Fig. 7.2a). Minibasins, on the other hand, are circular to sub-circular in shape. The random shapes of minibasins, the irregularity of salt walls, and the significantly thick syn-kinematic units

in the overburden support the down-building mechanism of the basin (Peters et al. 2003; Al-Siyabi 2005; Li et al. 2012a).
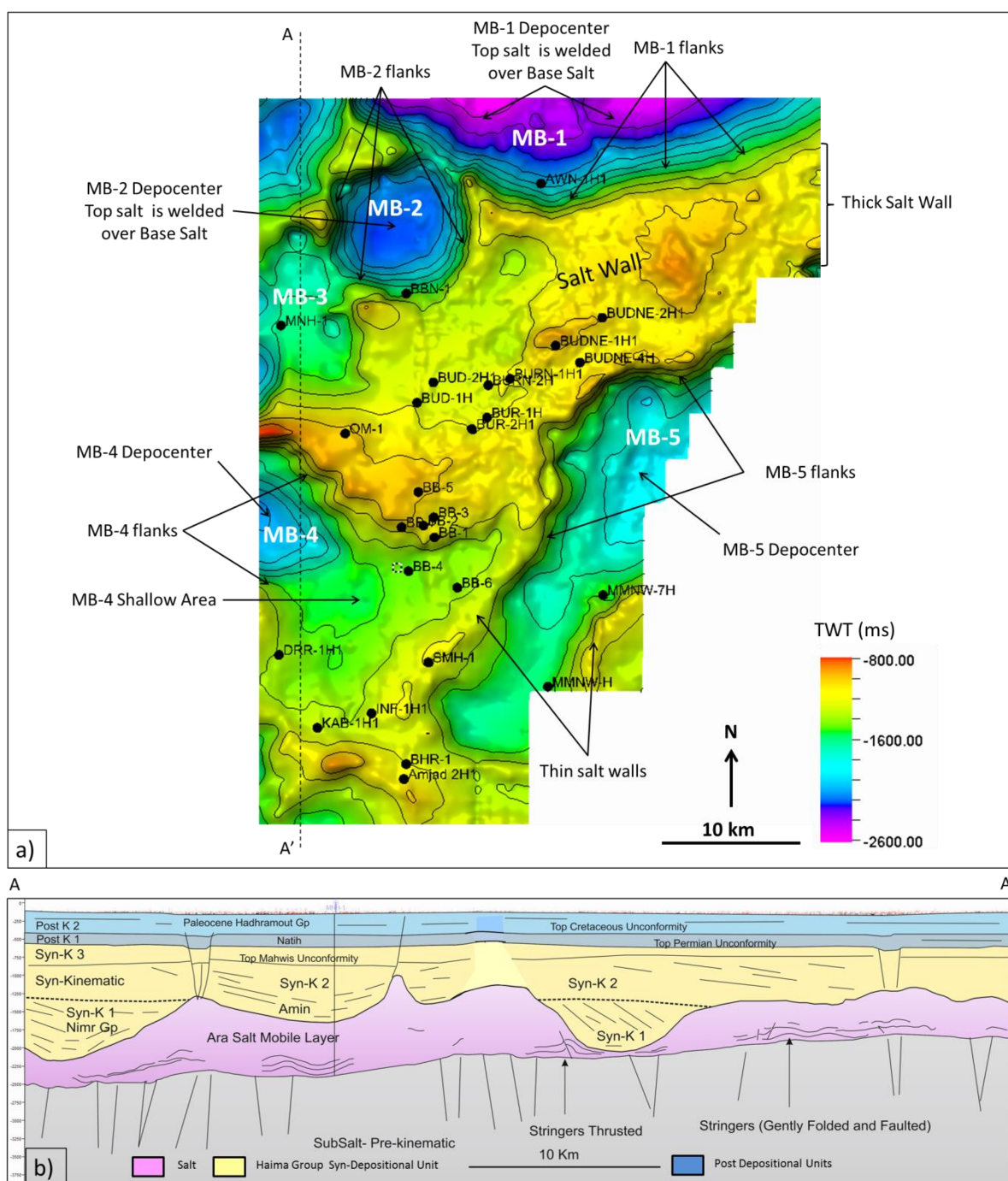
Fig. 7.2: Two-way-travel-time map of the Top Salt surface shows the most important regional salt structures. Note the irregular shapes of the minibasins and the salt walls. Note also the degree of subsidence of the minibasins.
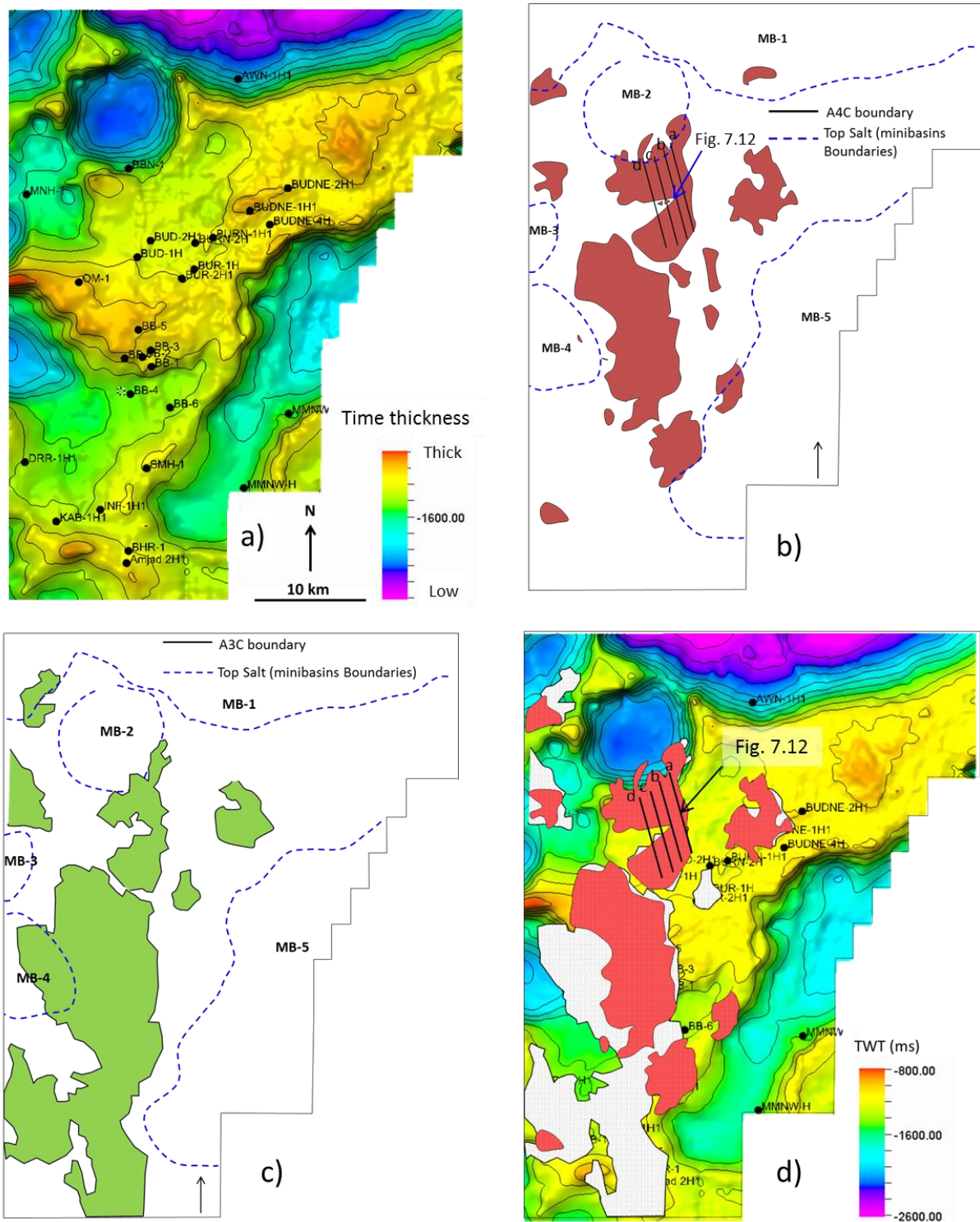
Fig. 7.3: Distribution and extent of the upper stringers. (a) Ara salt time thickness (Top Salt to A0C). (b) A4C stringer surface. (c) A3C stringer surface. (d) The A4C and A3C stringers are superimposed on the Top Salt surface.

7.3   Deformation of the stringers beneath regional structures

The degree of subsidence of the salt minibasins varies significantly (Fig. 7.2). For example, the northern MB-1 and MB-2 are highly subsided and welded with a maximum subsidence recorded within the MB-1 (Fig. 7.3a). However, areas to the south of MB-4 and MB-5 are less subsided. In this section, the intra-salt structures are first analysed qualitatively: (1) beneath areas of shallow subsidence (e.g., east of the MB-4 and south of the MB5); (2) beneath areas of moderate subsidence (e.g., south of the MB-4); and (3) within and around areas of high subsidence, where Top Salt is completely welded (e.g., MB1, MB2, and MB-4). Such qualitative description allowed the understanding of the kinematic evolution of the stringers during the early to the late stages of salt tectonics.

7.3.1   Deformation of the stringers in the area east of MB-4

In Fig. 7.2.a, the salt section has undergone relatively low subsidence in the area east of the MB-4. Hence, this area can be used to analyse the stringers at the early stages of subsidence.

Four linear discontinuities are observed within the A4C stringer surface, with lengths of 5 km to 6 km and widths of 100 m to 200 m (Fig. 7.4a). These linear gaps become wider towards the west, where the Top Salt is more subsided (Fig. 7.4a). Profiles B, C, and D (Fig. 7.4a) are used to demonstrate the propagation of these gaps from areas of less subsidence in the east towards areas of high subsidence in the west, close to the MB-4.

The profiles across these gaps show that the A4C stringer is either laterally disconnected by small-scale gaps (Fig. 7.4a) or welded over the A3C stringer to form two thickening zones of the A4E salt interval on each side of the welded points (Fig.

7.4b). The profiles show that the A4C stringer is laterally displaced, while the underlying A3C and A2C stringers are more continuous (Fig. 7.4d). The continuity of the underlying A3C stringer, in spite of the brittle deformation in the overlying A4C stringer, may reflect the effect of the decollement of the A4E salt layer in between, suggesting that the A3C stringer does not necessarily deform during the deformation of the A4C stringer.
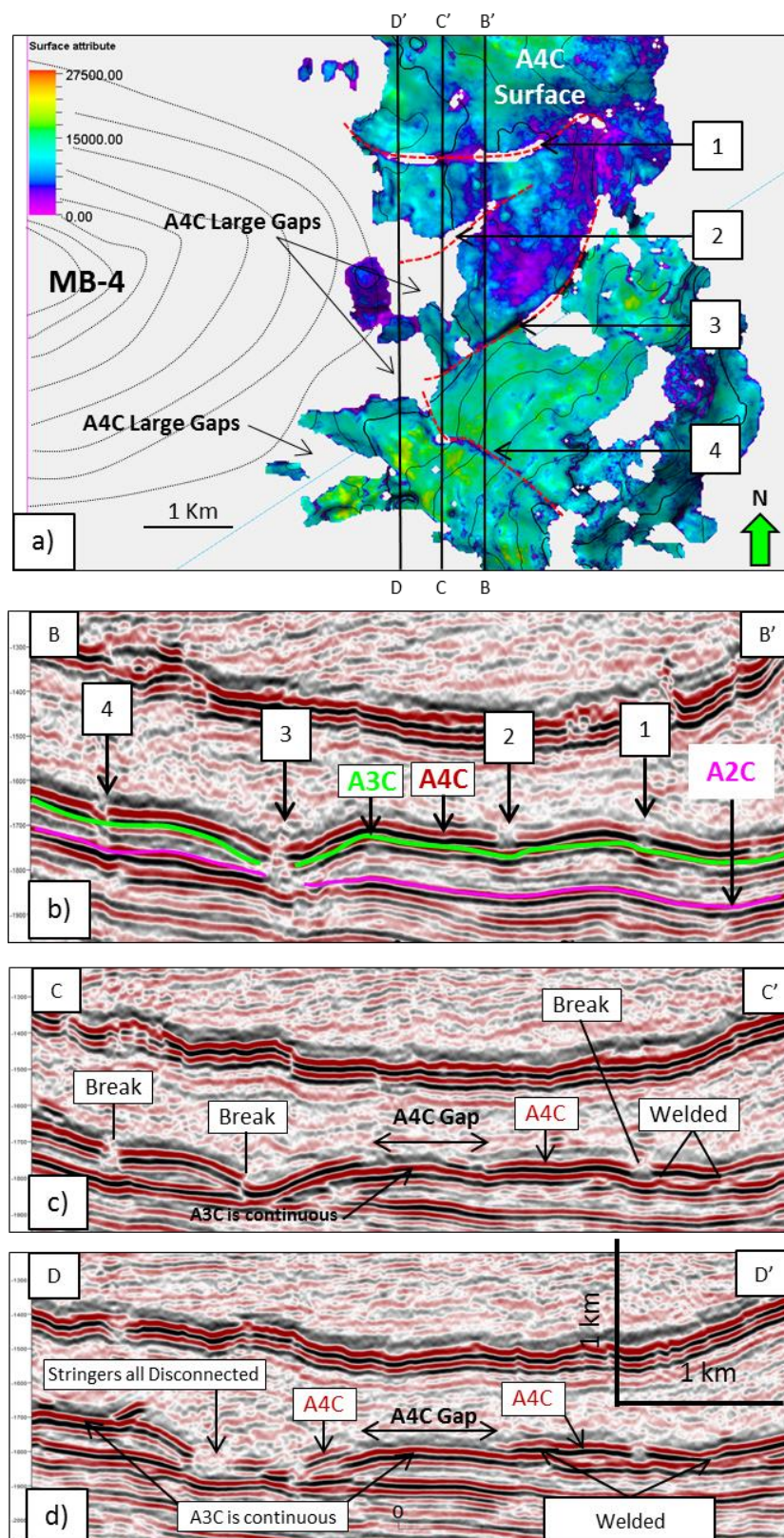
Fig. 7.4: (a) RMS seismic attributes of the A4C stringer in the area west of the MB-4. Note the annotated linear gaps (1–4). (b,c,d) Seismic profiles showing the discontinuities of the upper A4C stringer. The green reflector is the A3C surface. Note that the A3C and A2C stringers are more continuous than the A4C as in (b and c), until they eventually break towards the west, as in profile d (d).

7.3.2 Deformation of the stringers at the middle and at the flanks of the MB-4

The minibasin MB-4 has an E–W strike, and the minibasin front propagates towards the east (Fig. 7.5). The central part of the minibasin is located in the western part of the study area. Here, the A4C stringer is discontinuous, about 2 km far from the centre of the MB-4 and does not extend further west (Fig. 7.5a). However, the lower A2C and A3C stringers are more continuous and extend further west beneath the depocentre of the MB-4 (Fig. 7.5a). Beneath the centre of the MB-4, the stringers have been significantly fragmented into smaller blocks and are laterally disconnected and surrounded by salt (Fig. 7.5b). On seismic profiles, it is difficult to correlate these fragments to their stringers (A4C–A2C) due to the smaller sizes and disconnections of the broken stringer parts (Fig. 7.5b,c).

Additionally, the A3C and A2C stringers beneath the northern flank of the MB-4 have been both folded (Fig. 7.5c). The cores of these anticlines have been filled by salt that was mobilised from the welding zone (Fig. 7.5d,e). The proximal limbs of the stringer anticlines, which are the limbs closer to the minibasin flanks, have almost similar dip magnitude and direction with the limb of the Top Salt (Fig. 7.5d,e). The A3C, and A2C stringers were bent beneath the minibasin during subsidence and were dragged to greater depths than their regional stratigraphic position by displacing the salt below (Fig. 7.5e). This indicates that the salt layers beneath the A3C carbonate stringer have been evacuated during halokinesis to form these anticlines. These structures could represent important structural traps. However, these anticlines might be thrusted during progressive subsidence with further salt flow to the core (Fig. 7.5d,e).
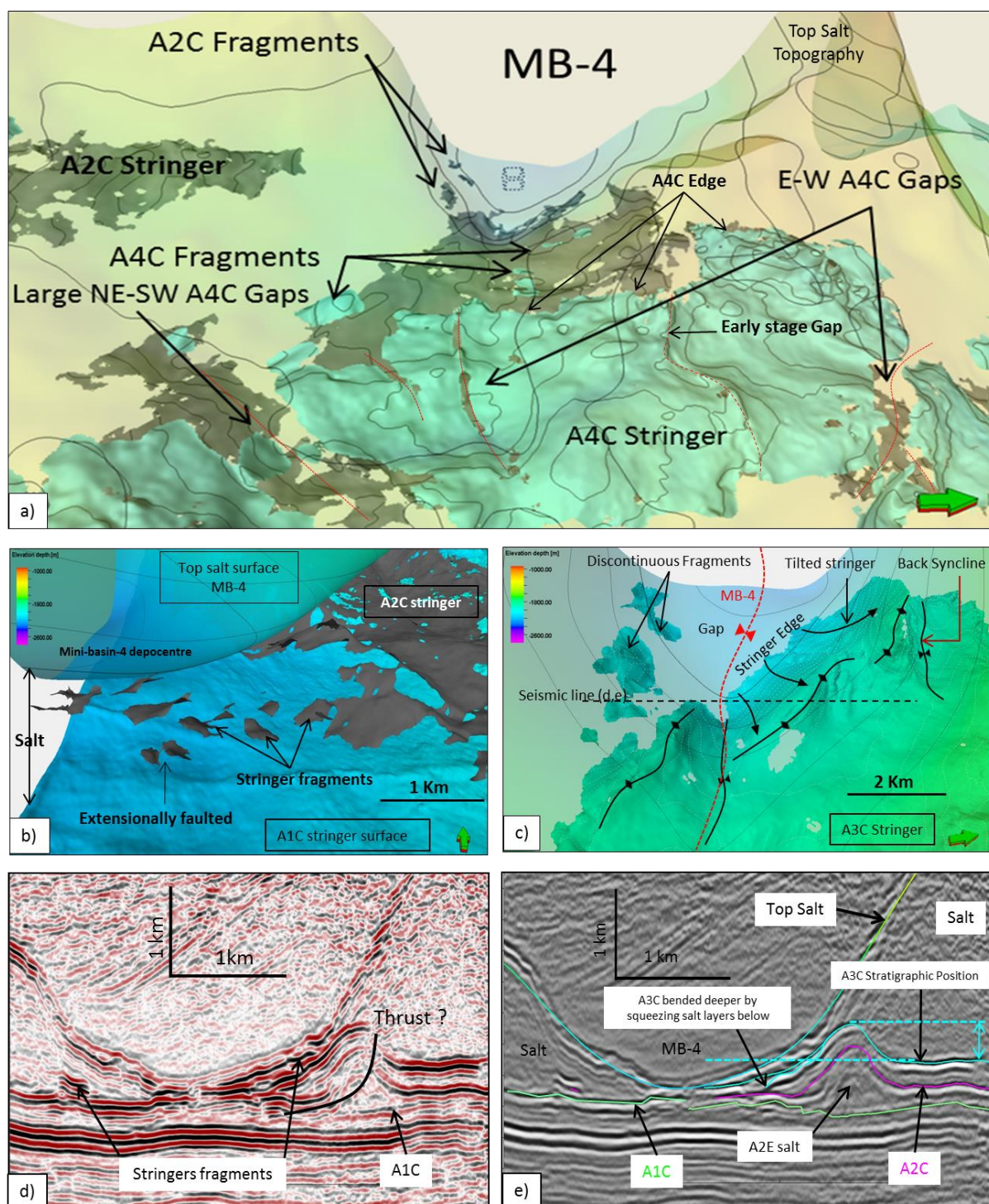
Fig. 7.5: (a) 3D TWT surfaces of the A2C stringer (grey) and A4C stringer (blue) east of the MB-4. (b) 3D visualizations of the A2C stringer (dark grey), A1C stringer (blue), and Top Salt (contoured surface) beneath the depocentre of the MB-4. Note the disconnected smaller fragments beneath the centre of the minibasin. (c) 3D visualizations of the A3C stringer with Top Salt surface. (d, e) Seismic profile across the MB-4 (see (c) for location) shows the geometries of the anticline structure.

7.3.3 Deformation of the stringers beneath the flanks of the MB-2

The MB-2 has a circular shape with a diameter of 8 km, and the Top Salt is completely welded at its centre. Thus, no stringer fragments have been recorded beneath the minibasin (Fig. 7.6a). However, the A4C and A3C stringers occur south of the minibasin, forming three structural styles around the flanks of the MB-2 (Figs. 7.3 and 7.6):

1. The A4C and A3C stringers are folded similar to a dome shape or a bulge fold, with the A3E salt at the core of the dome shape (Fig. 7.6a). In addition, the fold limbs of both A4C and A3C stringers are faulted (Fig. 7.6c).

2. The stringers are only folded from the proximal part, parallel to the Top Salt limb, while the distal part is flat, forming a monocline structure (Fig. 7.6a). The folded stringers are likely the response of the subsidence of the overburden that dragged part of the stringers downwards during salt evacuation.

3. The third structural style is manifested where the stringers are flat and sharply discontinuous against the flank of the minibasin (Fig. 7.6a).
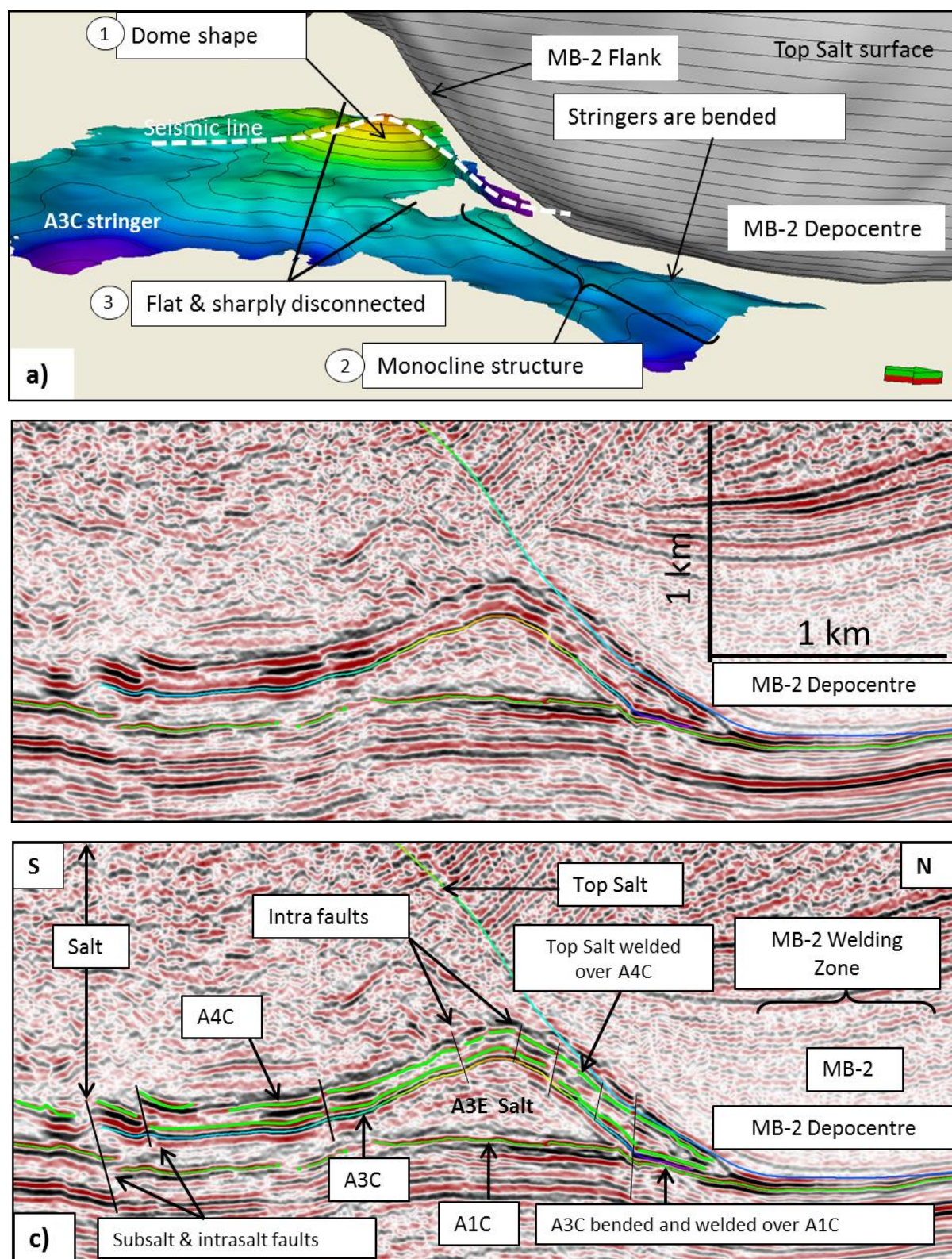
Fig. 7.6: The A4C and A3C stringers around the flanks of the MB-2. (a) 3D visualizations of the Top Salt surface (grey) and the A3C stringer surface (coloured). Here, the stringer is either folded into dome and monocline structures or sharply fragmented at the edge of the Top Salt. (b) Uninterpreted and (c) interpreted seismic profile across the dome showing the folded A3C and A4C stringers with intra-salt extensional faults largely concentrated at the hinge and at the northern limb of the fold structure.

7.3.4 Deformation of the stringers beneath the flanks of the MB-1

At the depocentre of the MB-1, the Top Salt is deeply subsided and completely welded over the A1C (Fig. 7.7a). The internal structural geometries of the stringers that are distributed beneath the southern flank of the MB-1 can be grouped into five zones based on their structural styles and their positions within the salt (Fig. 7.7c):

1. Highly fragmented, faulted, and overlapping small-scale fragments of stringers (less than 500 m) are found in the lower section close to the minibasin welding zone (Fig. 7.7b). This zone shows a chaotic seismic character and the stringers are poorly imaged.

2. At larger distances from the MB-1, large-scale layered stringers are extensionally faulted and gently rotated towards the minibasin welding zone (Fig.7.7b).

3. Close to the Top Salt limb, the stringers are steeply rotated, with dip direction and magnitude similar to Top Salt (Fig.7.7b). The stringers in this zone are stretched and rarely folded. On the 3D display, the stringers are disconnected and are highly irregular in shape (Fig.7.7c). Along the strike of the flank of the MB-1, the stringers and the Top Salt limb have similar dip directions (Fig.7.7c).

4. At the top of the salt dome, the stringers are either horizontal or gently folded and parallel to the Top Salt geometry. A similar structure is also found within the core of the salt dome (Fig. 7.7b).

5. Most distally from the minibasin, some of the stringers are rotated in opposite directions within the salt layer.

290
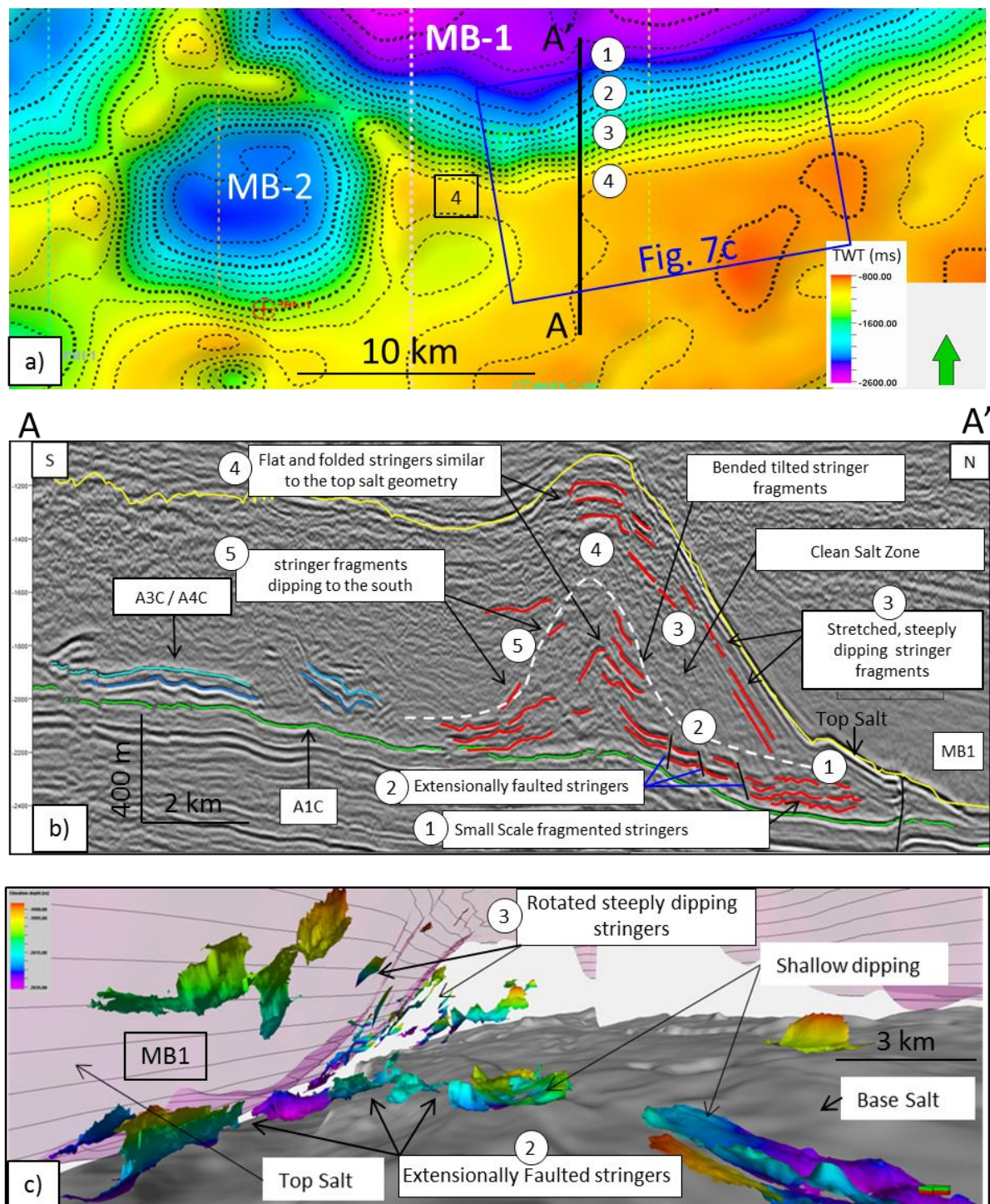
Fig. 7.7: (a) Top Salt surface in the northern part of the study area. (b) Profile crosses the MB-1 depocentre in the north, the limb of the minibasin, and the salt wall in the south. (c) Interpreted seismic profile; see (a) for the location of the profile. (c) 3D visualization of the stringer fragments; see (a) for the location. Note the distributions and geometries of the fragments.

7.4   Faults within the Ara Group evaporites

The faults that penetrated the stringers are clearly observed on seismic sections and base maps. A seismic line was selected to summarise the main four types of faults (Fig. 7.8): sub-salt to intra-salt extensional faults, faults formed entirely within the stringers, post-salt to intra-salt extensional faults, and intra-salt thrust faults.

7.4.1 Sub-salt to intra-salt extensional faults

Sub-salt faults are mostly extensional faults that propagate upwards and penetrate the lower stringers. The variance attribute was computed over the A1C stringer and was used to characterise the fault styles (Fig. 7.9b). The A1C stringer is largely affected by the pre-salt faults. Most of the sub-salt faults do not extend to penetrate the upper A3C and A4C stringers due to the presence of salt intervals (Fig. 7.9b). However, the sub-salt faults can be reactivated to penetrate all the stringers and can even reach the post-salt section in areas where the salt is welded and the stringers are all grounded with no salt layers in between (e.g., Fig. 7.6c and Fig. 7.9a). The faults penetrated the post-salt Haima Supergroup in areas where Top Salt is welded over the basal Ara.

Since the salt has been evacuated from underneath the minibasin, faults easily propagate upwards in these regions. Such faults might result in leakage of hydrocarbon traps of the pre-salt and the stringers into the post-salt Haima Supergroup. Another example is shown in Fig. 7.9c,d, where an extensional fault propagated upwards, penetrating both the A1C stringer and an overlying discontinuous stringer block that belongs to the A2C stringer. The fault plane is observed in the A0C (Base Salt), the A1C, and in the A2C stringer block. The discontinuous A2C block seems to be grounded over the A1C stringer and hence faulted.
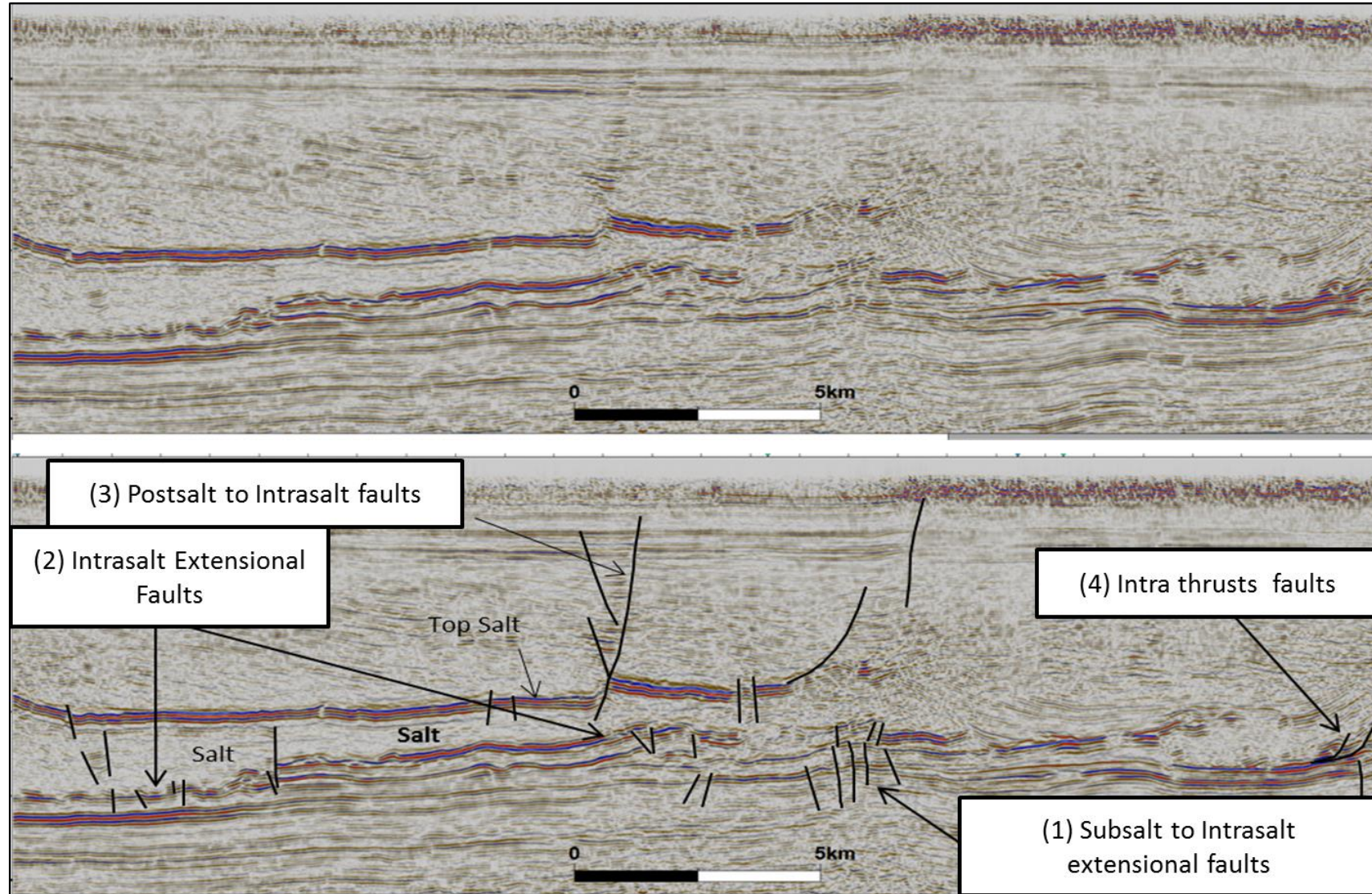
Fig. 7.8: The four types of faults within the Ara Group evaporites: (1) faults that extend from sub-salt into the salt section, (2) intra-extensional faults, (3) faults that propagate downwards from the post-salt section into the Ara salt, and (4) intra-thrust faults.
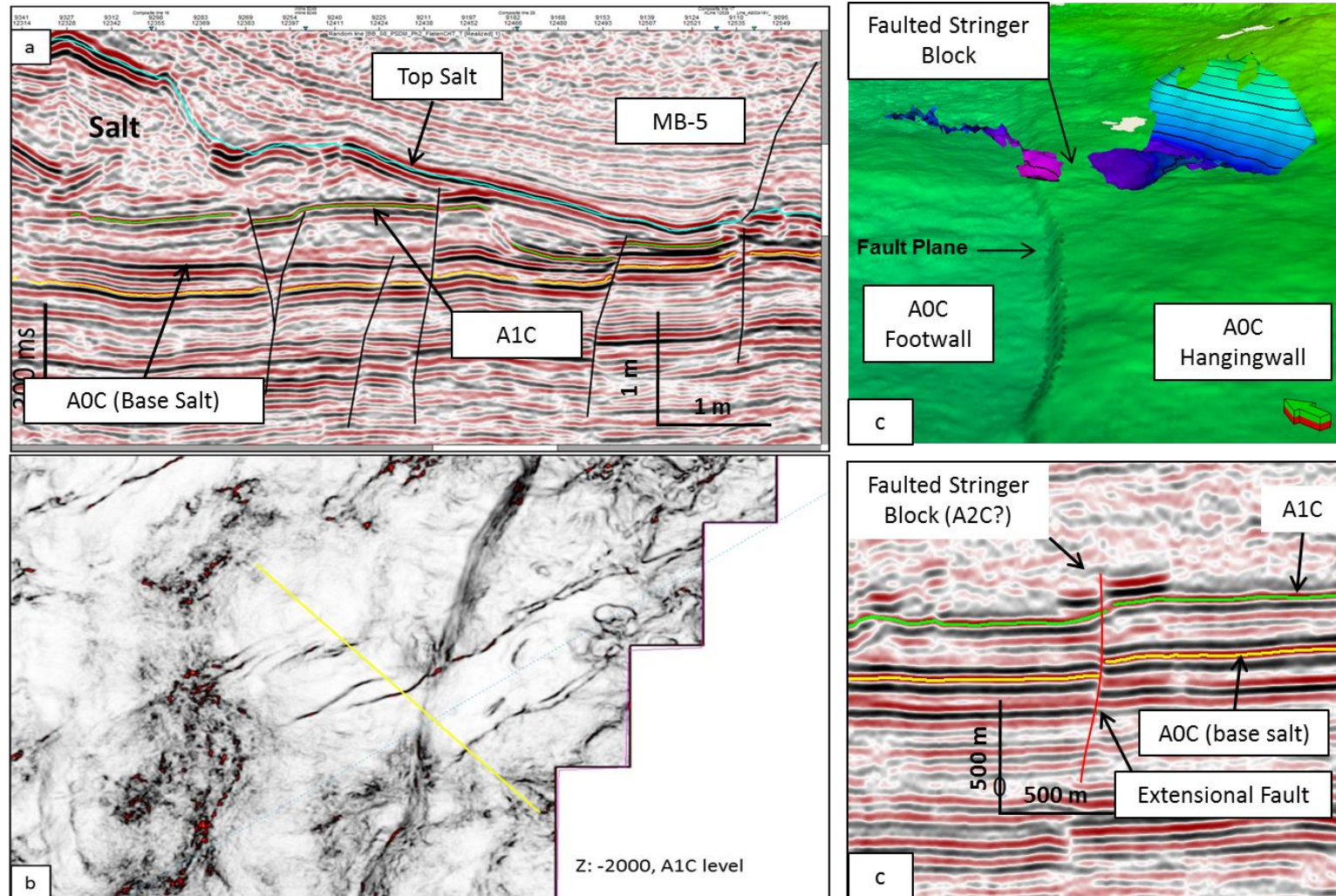
Fig. 7.9: Examples of sub-salt faults that extend upwards and penetrate the stringers. (a) The A1C is largely faulted by sub-salt faults. Note that some faults can penetrate the overburden, as shown to the right of the profile, where the salt is welded; see (b) for the location of the seismic line. (b) Variance surface of the A1C stringer. Note the style of the extensional faults. (c and d) Sub-salt fault reactivated upwards to fault the A1C stringer and an overlain grounded stringer block.

7.4.2 Intra-salt extensional faults

Intra-salt extensional faults are faults that formed within the Ara salt and cut the competent carbonate stringers. These faults are common beneath the flanks of minibasins, where the stringers are tilted and collapsed by extensional faults into smaller blocks (Fig. 7.10a,b). If the stringers are in contact with the flank of the Top Salt, the faults can extend further up to penetrate the overburden (Fig. 7.6c). Such faults can act as conduits for fluids to flow into the overburden.

7.4.3 Intra-salt thrust faults

In the Birba study area, thrusts are rarely found within the Ara Group evaporites. Only few examples have been observed. An obvious example of thrust fault is seen in the southern part of the study area (Fig. 7.10a). The A2C and A3C stringers have been thrusted by shallow dipping reverse faults that detached within the A2E salt (Fig. 7.10b). Profiles across the fault strike display maximum displacements at the middle and minimum displacements at the fault tips (Fig. 7.10a, c).

7.4.4 Post-salt to intra-salt extensional faults

Overburden faults can penetrate the underlying salt section and detach within the salt. The stringers are affected by post-salt faults largely in the welded areas. Alternatively, the faults might penetrate any stringer fragments that are roofed to the Top Salt level.
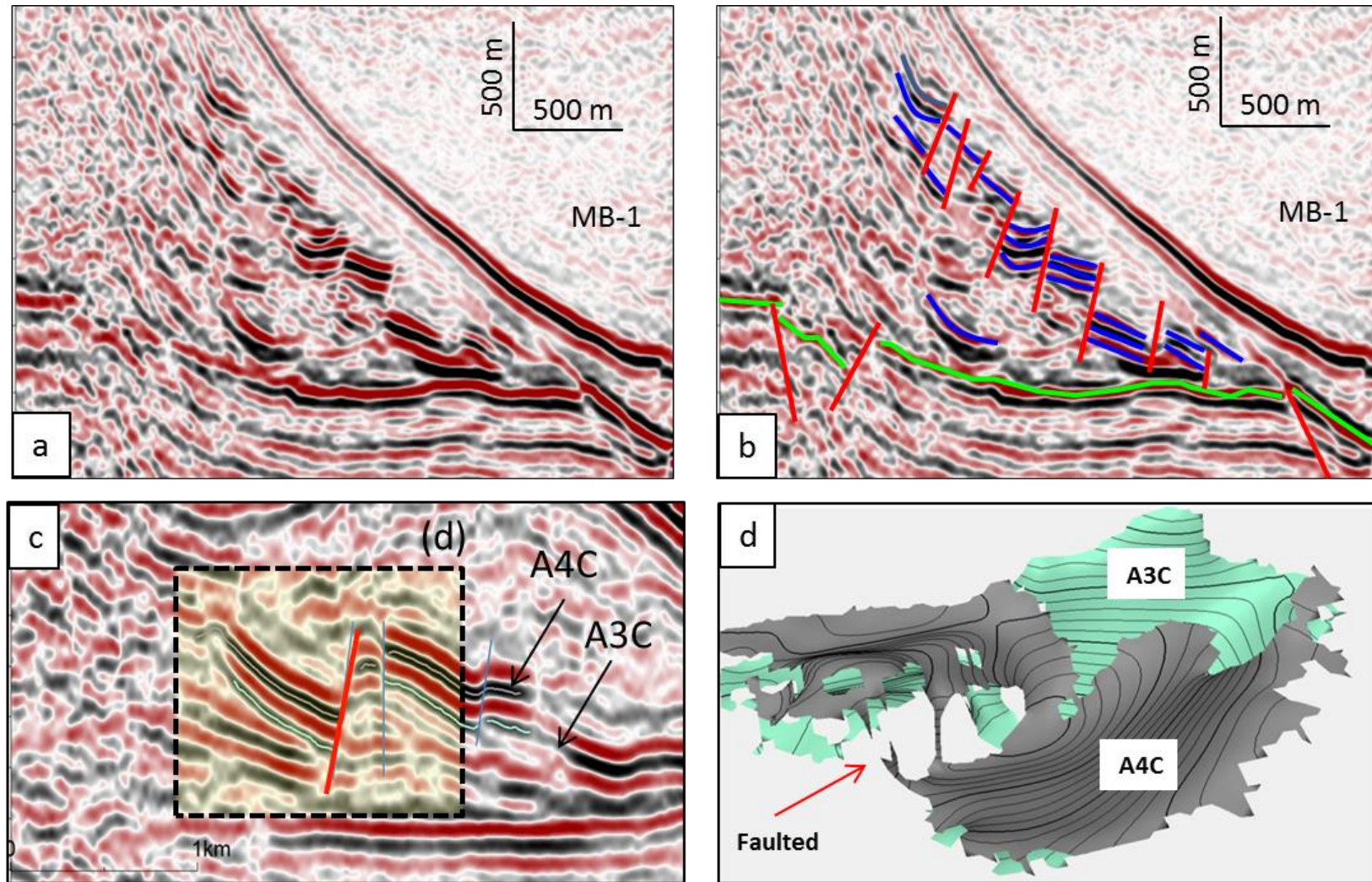
Fig. 7.10: Intra-salt extensional faults from south of the MB-1. (a, b) E–W profile through the MB-1 shows intra-extensional faults. Note that the stringers are all rotated parallel to Top Salt. (c) Zoomed-in view of the faulted A4C and A3C stringers. (d) 3D visualization of the faulted stringer blocks.
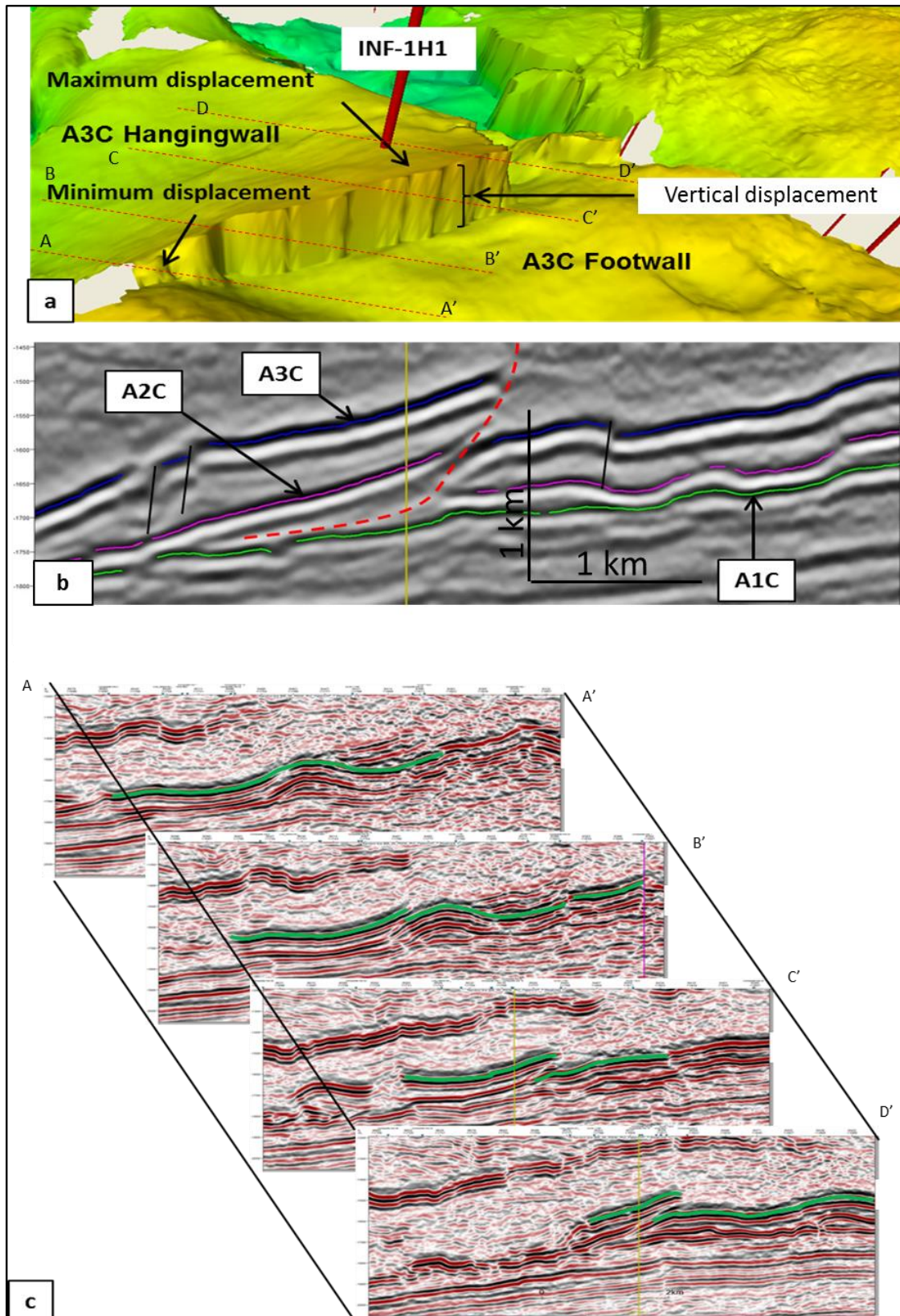
Fig. 7.11: (a) Thrust fault cutting the A3C and A2C stringers. Note that the fault plane is curved, with maximum displacements at the middle. (b) The thrust is detached within the A2E salt interval. Note also the back thrust fault in the footwall. (c) Along-strike profiles show the displacement changes from the fault tips (minimum displacement, A-A') to the middle (maximum displacement, D-D').

7.4.5 Gaps-derived faults

An example of stringer gaps that formed in areas of thick salt section with no significant thinning or subsidence is found to the south of the MB-2 beneath the salt wall (Fig. 7.3b,d). In map view, the gap is open towards the west and narrows to the east, forming a "V" shape structure. Seismic profiles at the tip of the gap show that the stringers were initially faulted by sub-salt extensional faults that extended upwards intersecting the A1C, A2C, A3C, and A4C stringers (Fig. 7.12a). A westward shift of the profiles shows that the stringers are intensively faulted and deformed by intra-salt extensional faults (Fig. 7.12b,c). The faulted stringer blocks have been intensively deformed into smaller fragments (Fig. 7.12c). Profiles towards the west at the middle of the gap show that the faulted zone is replaced by salt and the smaller faulted blocks have been displaced away by the salt, resulting in a large-scale gap (Fig. 7.12d).
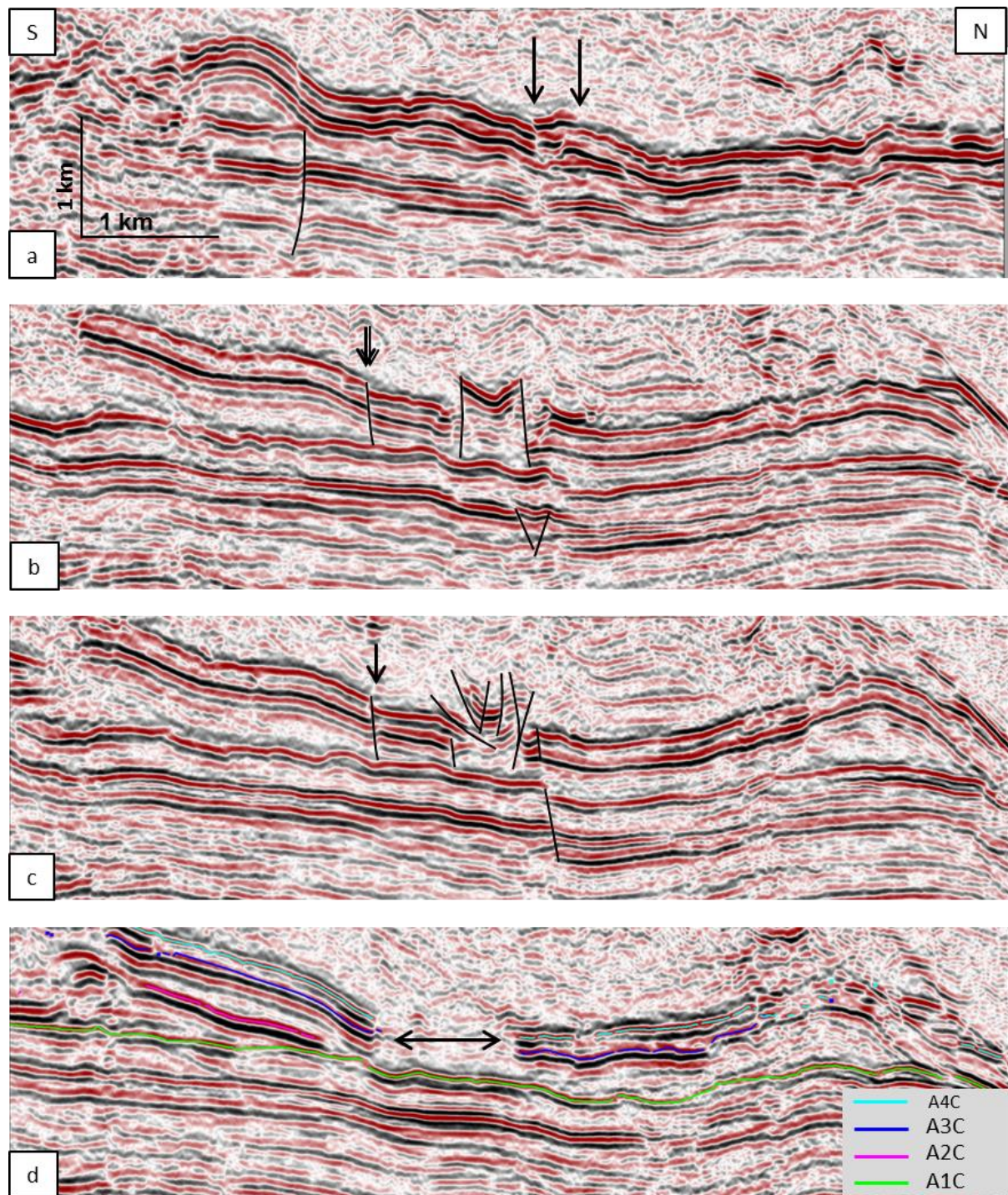
Fig. 7.12: Profiles across a gap in the northern part of the study area (see Fig. 7.3b,d for location). (a) Sub-salt extensional faults extended upwards and faulted the A4C–A1C stringers. (b) Two faults uplifted the A3C/A4C blocks at the middle of the section, forming a horst structure. Note the normal fault to the south which might indicate a future weakness zone. (c) Complex faulting of the middle zone. (d) Large-scale gap separating the stringers and filled by salt.

7.5   Discussion

In this chapter, the A4C–A1C intra-salt stringers have been structurally described in their context beneath regional salt structures. The structural evolution of the stringers can be related to the degree of halokinesis represented by each hosting salt structure. The deformation style of the stringers can be subdivided into three stages:

Stage 1: Early deformation stage

Shallow subsidence of the Top Salt in areas east of the MB-4, (Fig. 7.2a) has been interpreted as being representative of the structural configuration of the stringers during the early stages of subsidence (Fig. 7.4). Four linear lateral extensional gaps were observed within the upper A4C stringer surface, with lengths of 5 km to 6 km and widths of 100 m to 200 m (Fig. 7.4a). The underlying A3C and A2C stringers are more continuous than the upper A4C stringer. However, profiles towards the MB-4 where the salt becomes thinner display greater lateral extension in the A4C stringer and early small-scale gaps within the underlying A3C stringer (Fig. 7.4c,d and Fig. 7.13e). With increasing subsidence, all the stringers would be anticipated to experience lateral breakages, with gaps separated by salt (e.g., Fig. 7. 13). In this case, the A4C stringer reduces the time needed to deform the lower stringers (A3C and A2C stringer) by acting as a barrier that prevents the overlying thick A5E–A6E salt movements to deform the lower stringers. The A4C stringer deforms first, followed by the underlying stringers at later stages of subsidence (Fig. 7.13).

In areas where the salt section is thick and has not been subjected to significant subsidence due to salt depletion, the carbonate stringers nonetheless experience structural breaks and gaps by sub-salt and intra-salt faulting (Fig. 7.12). This faulting

fragments the stringers into smaller blocks, facilitating their motion even by a modest salt flow leaving a structural gap (Fig. 7.12d).

Stage 2: Intermediate deformation stage

The stringers beneath a subsided minibasin that has experienced significant salt depletion are suggested to deform internally by extensional failure in the early stage of subsidence, as seen earlier in this chapter. However, beneath the flanks of the minibasins, the stringers are dragged and folded (e.g., Figs. 7.5c,d,e and Fig. 7.6).

Folds around the minibasins have been created beneath the southern flank of the MB-2 and the northern flank of the MB-4. To the south of the MB-2, the A4C and A3C stringers are folded and the A3E salt interval is the core of the anticline (Fig. 7.6). On the northern side of MB-4, the A3C and A2C stringers are folded with the A2E salt intervals, forming the core of the anticlines (Fig. 7.5c,d,e).

These anticlines are interpreted to have formed by outward viscous drag during halokinesis, similar to bulge folds (Jackson et al. 1994). The hinge of the anticline structure might be thrusted when more salt flows inwards towards the core of the anticlines (Fig. 7.5d). In addition, the limbs of the fold structures are collapsed and faulted by extensional faults during the late stages of subsidence (Fig. 7.6 b,c and Fig. 7.10a,b).
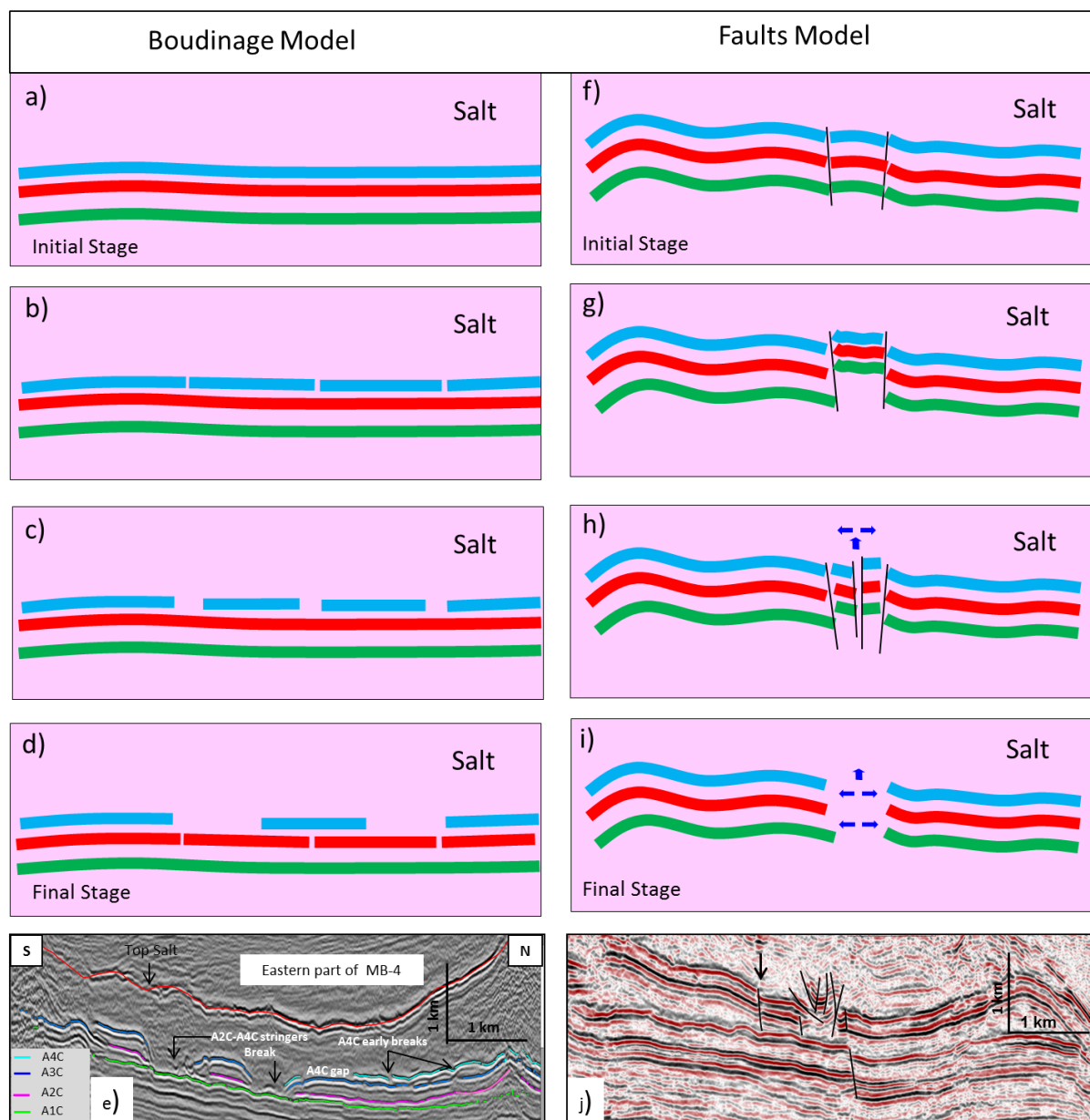
Fig. 7.13: Schematic showing the proposed structural evolution of the stringer gaps in areas of subsidence (boudinage model) and areas of thick salt structures by faults (faults model). (a–e) The lateral extension model (left) observed south of the MB-4 where the Ara salt has shallow subsidence (see also Fig. 7.4). (f–j) The faulted model (right) suggests that early gaps can be derived from fault activities (see also Fig. 7.12).

Detailed description of the formation of bulge folds

The kinematical evolution of the stringers beneath the minibasin depocentres and minibasin flanks has been qualitatively analysed using N–S profiles perpendicular to the strike of the MB-4 (Fig. 7.14). The profiles that pass through the eastern shallow part of the minibasin (i.e., profiles a, b, c in Fig 7.14) were used to characterise the early stages of stringer deformation. On the other hand, the profiles that transect the depocentre of the minibasin (i.e., profiles e and f in Fig 7.14) were employed to represent the late stages of stringer deformation.

In the eastern shallow side of the basin, where the salt section is thick, seismic profiles show that the A3C, A2C, and A1C stringers are flat (Fig 7.15a). Halite intervals between the stringers (A3E, A2E) are laterally constant in this configuration (Fig 7.16a). As the Top Salt is grounded over the A3C stringer, the upper A3C and A2C stringers are gently folded (Fig 7.15b). With additional Top Salt displacements, the stringers are then folded to form syncline structures at the middle just below the hinge of the minibasin (Fig 7.15c). The synclinal structures form by evacuating the A2E and A3E salt layers underneath (Fig 7.16c). Such salt evacuation from the centre of the minibasin has the chance to create two anticlines at the flanks of the minibasin (Fig 7.16c). Bulge folds in this case are caused by pressure when the underlying A3E salt is flowing against the upper competent stringers, similar to the flow of the viscous salt upwards from a diapir stem (Jackson et al. 1994).

Dynamic bulges can lift strata above the regional surface; such structures are common in northern Iran (Ala 1974; Talbot 1979). A bulge structure is likely to subside again if the salt source layer is exhausted (Jackson et al. 1994). Further subsidence leads to breakage of the stringer just below the hinge of the minibasin

(Fig 7.15d). More overburden subsidence causes the stringers to break into smaller fragments at the middle of the basin, while the A3E and A2E halite intervals continue to thicken the core of the stringer anticlines at the flanks of the minibasin (Fig 7.15d). At this stage, the inner limbs of the anticlines are tilted parallel to the Top Salt limb until they eventually weld with each other (Fig. 7.6b,c, Fig. 7.15e, and Fig. 7.16d). Within the depocentre of the minibasin, the stringers are broken into smaller fragments (Fig 7.15e). The final stage of subsidence causes the stringers that are beneath the flanks of the minibasin to be fragmented and intensively faulted into smaller blocks and finally transported away with the flowing salt (Fig 7.15f).
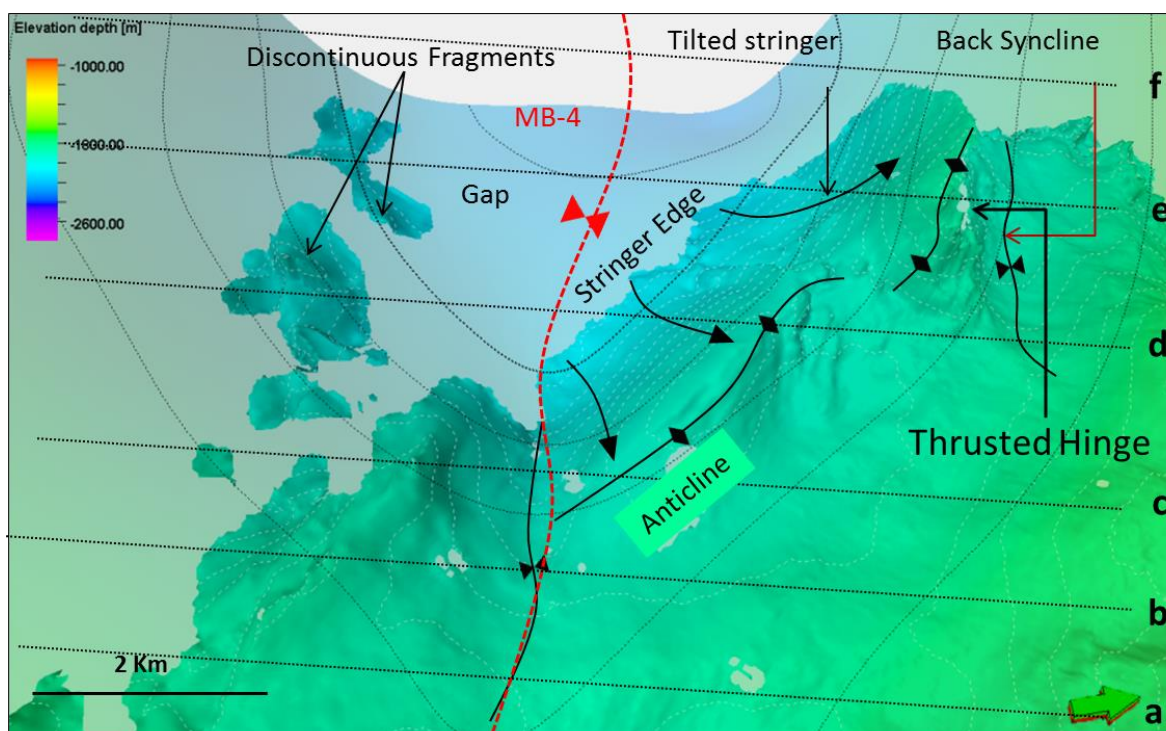
Fig. 7.14: 3D visualization of the A3C stringer beneath the MB-4. The Top Salt is shown as contours. Profiles (a–f, see Fig. 7.15) are used to investigate the kinematic behaviour of the stringers from the minibasin shallower regions (e.g., profile a and b) towards the basin depocentre (e.g., profile e and f).
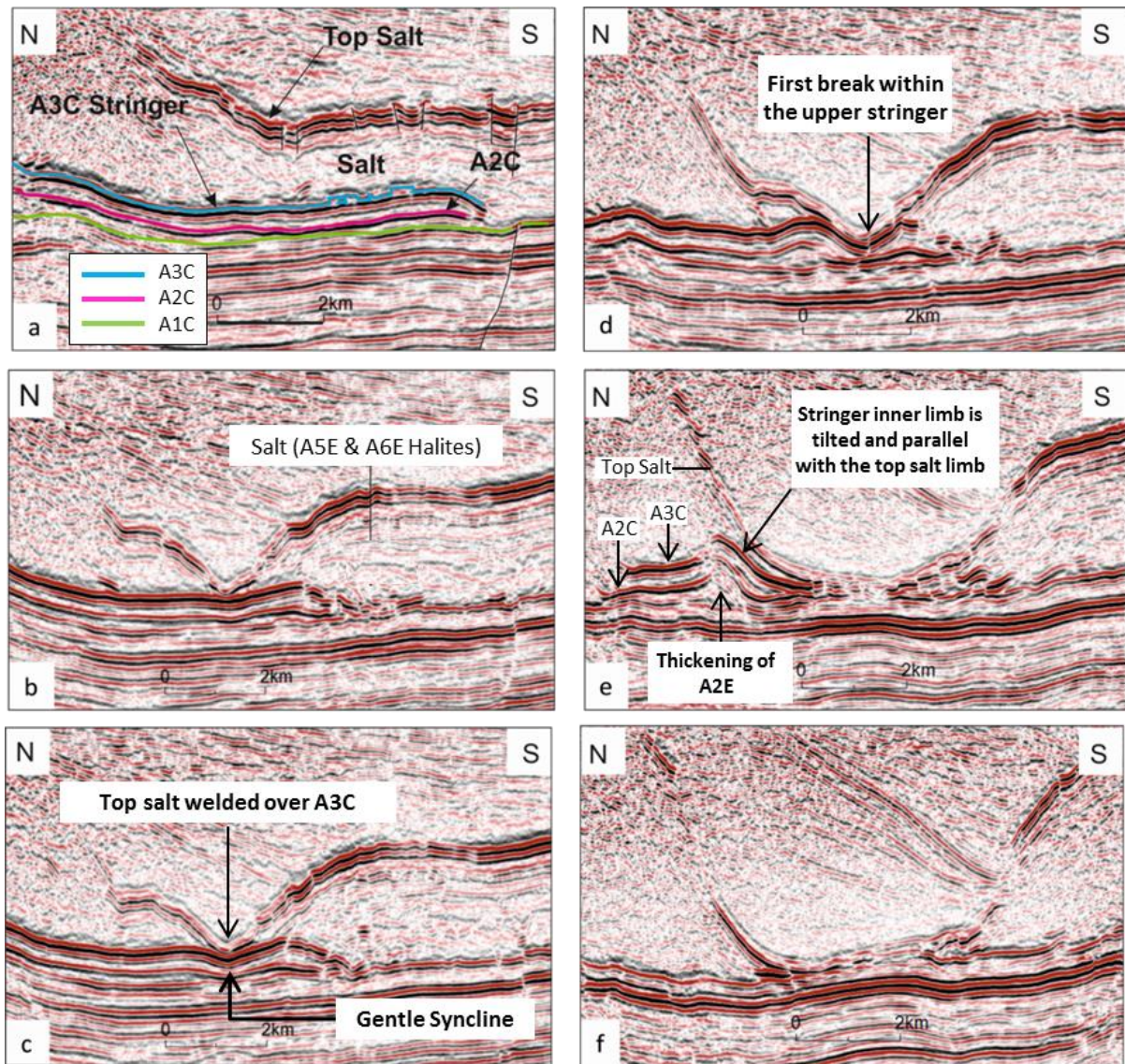
Fig. 7.14 (continued)
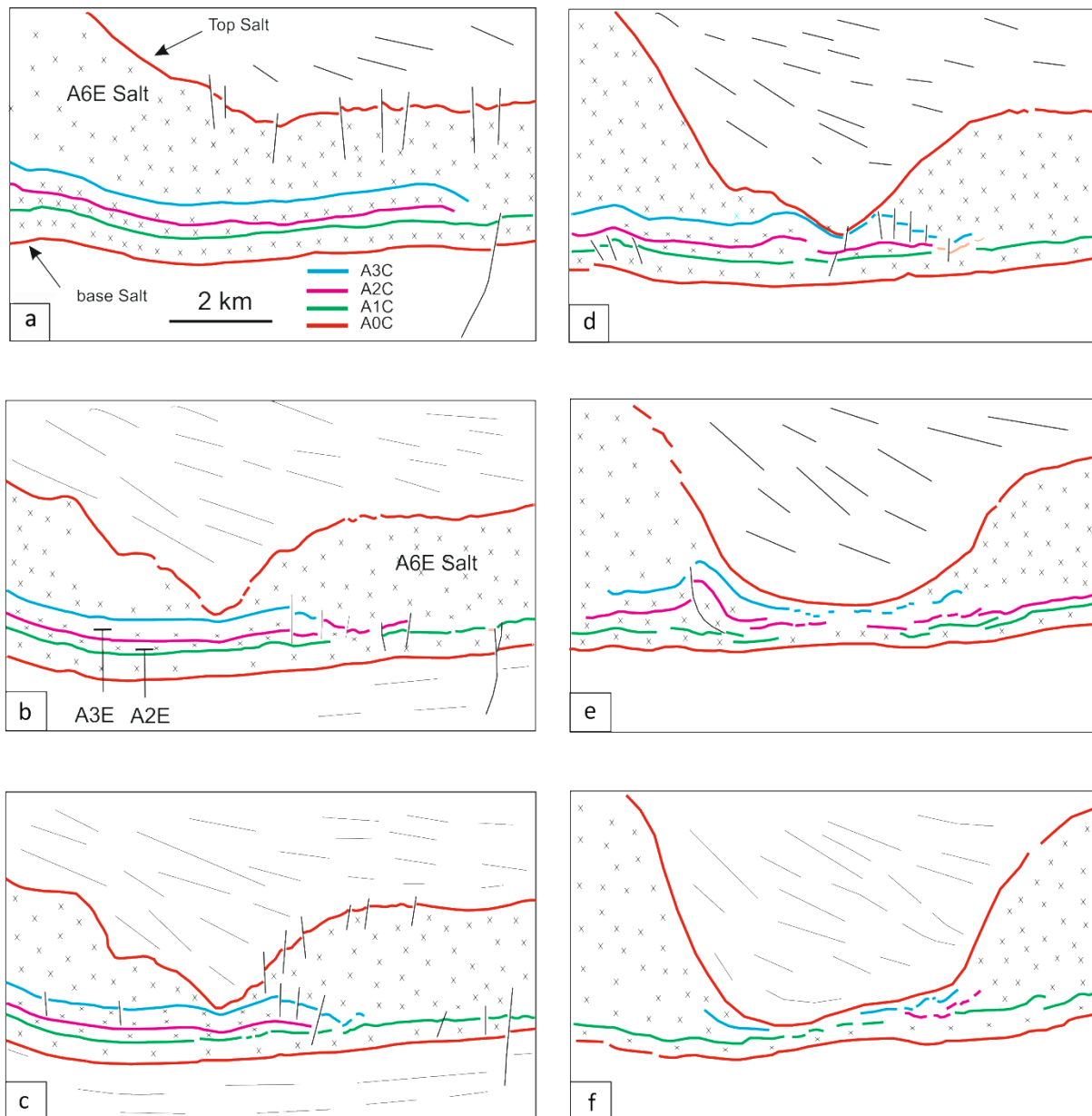
Fig. 7.15: (a–d) N–S uninterpreted and interpreted profiles perpendicular to the MB-4. (e–f) Crosslines from the eastern shallow part of the minibasin to the western, deeper part of the basin where the Top Salt is welded over the carbonate stringers.
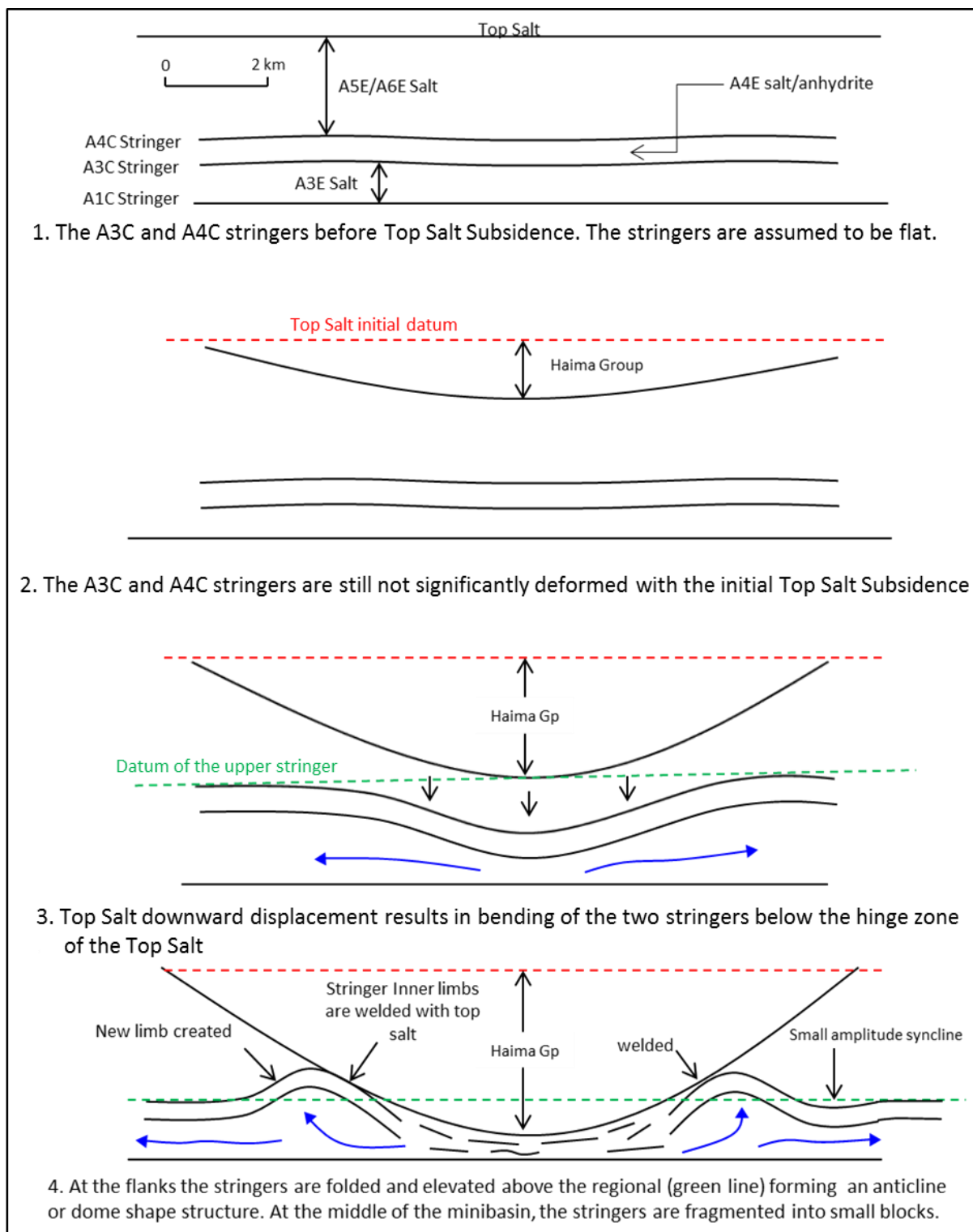
Fig. 7.16: Schematic showing the evolution of the fold near the minibasins and the fragmentation of the stringers beneath the minibasin maximum subsidence. The A4C and A3C stringers are used as examples. The A1C stringer is used as the base hard mechanical boundary. The green datum represents the regional occurrences of the upper stringer.

Stage 3: Late deformation stage

The lateral extension of the stringers during salt subsidence in Stage 1 and Stage 2 (Fig. 7.4c,d and Fig. 7.13) continues to break the stringers into smaller blocks and separate them away from each other by salt flow (Fig.7.5b). The deformed stringer fragments are carried away by salt into higher elevations (e.g., Fig. 7.7c).

7.6   Conclusions

- Analysing the structural styles of the carbonate stringer based on Top Salt displacement and their occurrences within salt structures (e.g., minibasin, salt flanks, dome shapes) is an important method for seismic interpreters to predict deformational styles of the stringer.

- Differential loading of thick clastic pods and salt diapirs led to folding and fragmentation of the carbonate stringers into isolated stringers that float within the Ara salt.

- Structural styles of the stringers within the Ara salt include boudinage lateral extension, extensional and thrust faults, bending faults, and buckled folds.

- The analysis of these stringers contributes to the understanding of the petroleum system of the stringers in the South Oman Salt Basin.

Chapter 8: Summary and conclusions

8.1   Comparison of intra-salt kinematics from the two case study areas

Two case studies have been used to analyse and understand the kinematic evolution of the intra-salt stringers during salt tectonics. The kinematics of the Z3 Stringer in the North Sea in areas of regional salt thinning and thickening were summarised in chapters 4 and 5, while the structural evolution and kinematics of the Ara carbonate stringers in the SOSB were discussed in chapter 7. The important factors that control the variable structures and kinematics of the intra-salt are discussed next (and summarised in Table 8.1):

- Mechanical properties of the stringers: In the Southern North Sea, the anhydrite layer is observed to have a density of ~3000 kg/m3, and is encased by the Zechstein salt, with a density of ~2000 kg/m3 (Fig. 8.1b). The dolomite and limestone stringers in the South Oman Salt Basin have densities of ~2700 to 2800 kg/m3 and are separated by halite intervals (Fig. 8.1a). The variation in the density of the anhydrite as compared to the carbonates thus implies differences in their rheology and behaviour during regional tectonics (see Urai et al. 2008). For example, during shortening, the Z3 anhydrite stringer under domes, pillows, and anticline structures commonly forms buckle folds, with a fold tightness that ranges from gentle to isoclinal. In contrast, the anhydrite stringer forms boudins beneath subsided regions, and also undergoes brittle deformation at the late stages of tectonics, suggesting that early subsidence is not enough to generate boudin structures. In many cases, during shortening, the Z3 Stringer is hardly broken by Top Salt downward displacement (e.g., Syncline-2, Syncline-4) but instead folded with variable fold amplitudes and wavelengths. The Z3 Stringer only shows evidence for lateral stretching and tensile fracturing at extreme thinning of the Top Salt

(e.g., Syncline-1). Hence, the anhydrite layer behaves more in a ductile manner than most other brittle rocks and does not deform extensionally under low to modest subsidence of the overburden. On the other hand, the carbonate stringers in the South Oman Salt Basin are rarely folded. When subjected to shortening, these stringers tend to form thrust structures (Fig. 8.1a; Fig. 7.11). The carbonate stringers in areas of extension (i.e., beneath minibasins) are extensively fragmented and extensionally faulted at early stages of subsidence (sensu Hansen et al. 2004).

- *Regional salt tectonics:* The southern North Sea has aligned, elongated, generally trending NW–SE, regional buckle folds (Coward and Stewart 1995) (Fig. 4.2). Synclines and anticlines induced internal local extension and internal local contraction, respectively. The regional shortening of the basin generated higher intra-salt shortening within regional anticlines, as represented by the folds of the Z3 Stringer. Beneath the hinge zone of the regional synclines, lateral extension, boudinages, and large-scale lateral displacements of the stringer were observed (Fig. 4.5; Fig. 4.6; Fig. 4.10; Fig. 4.12). At the flanks of these synclines, flat to gentle, passive flow folds with a vergence direction away from the regional strike of the syncline were also observed (Fig. 8.1b; see also Fig. 4.17 and Fig. 5.15a, b). Under contractional anticlines, open to isoclinal folds with upright and inclined fold axes were formed (Fig. 5.14).

In the SOSB, differential loading of massive clastic sediments over the salt resulted in the development of minibasins and irregular salt walls with variable shapes and trends. Since the sediment load is the primary factor controlling salt movement, the subsidence regions of synclines and minibasins were

created first and resulted in extensional deformation to the stringers. Unlike the Z3 Stringer, the fold structures of the Ara carbonate stringers are only well-developed in the flanks of the minibasin at later stages and have been created by salt flowing beneath minibasins into the core of their anticlines rather than by salt shortening (Fig. 7.15 and Fig 7.16).

- *Stratigraphic position of the stringers in the salt layer:* The Z3 Stringer is situated in the upper half of the Zechstein salt and is bounded by two thick salt intervals (Fig. 8.1a). In general, such stratigraphic position allows the stringer to form well-developed fold structures in areas of contraction. However, locally, the stringer anticlines have lower fold amplitudes than synclines because salt is thicker below the stringer than above (Fig. 5.9g,h; Fig. 5.12h; and Fig. 5.14c). On the contrary, the stringers in the SOSB were deposited in the lower part of the salt layer. This stratigraphic position allowed the stringers to be affected by the pre-salt faults.

- *Multi-layered stringers vs. single stringer:* The presence of multi-layered stringers controls the distribution of strain within the stringers during tectonics. In the SOSB, the upper stringers were largely affected by tectonics during down-building and subsidence, more than the lower stringers (Fig 7.13 and Fig. 7.12). The sub-salt faults in the SOSB can propagate upaward and penetrate the lower stringers (i.e., A1C and A2C), especially when the stringers were grounded and not separated by a salt layer (Fig. 7.9). On the other hand, faults are rarely associated with the Z3 Stringer due to the thick salt (Z2 halite) below the stringer. The stringer instead is boudinaged in extensional regions due to salt movement.
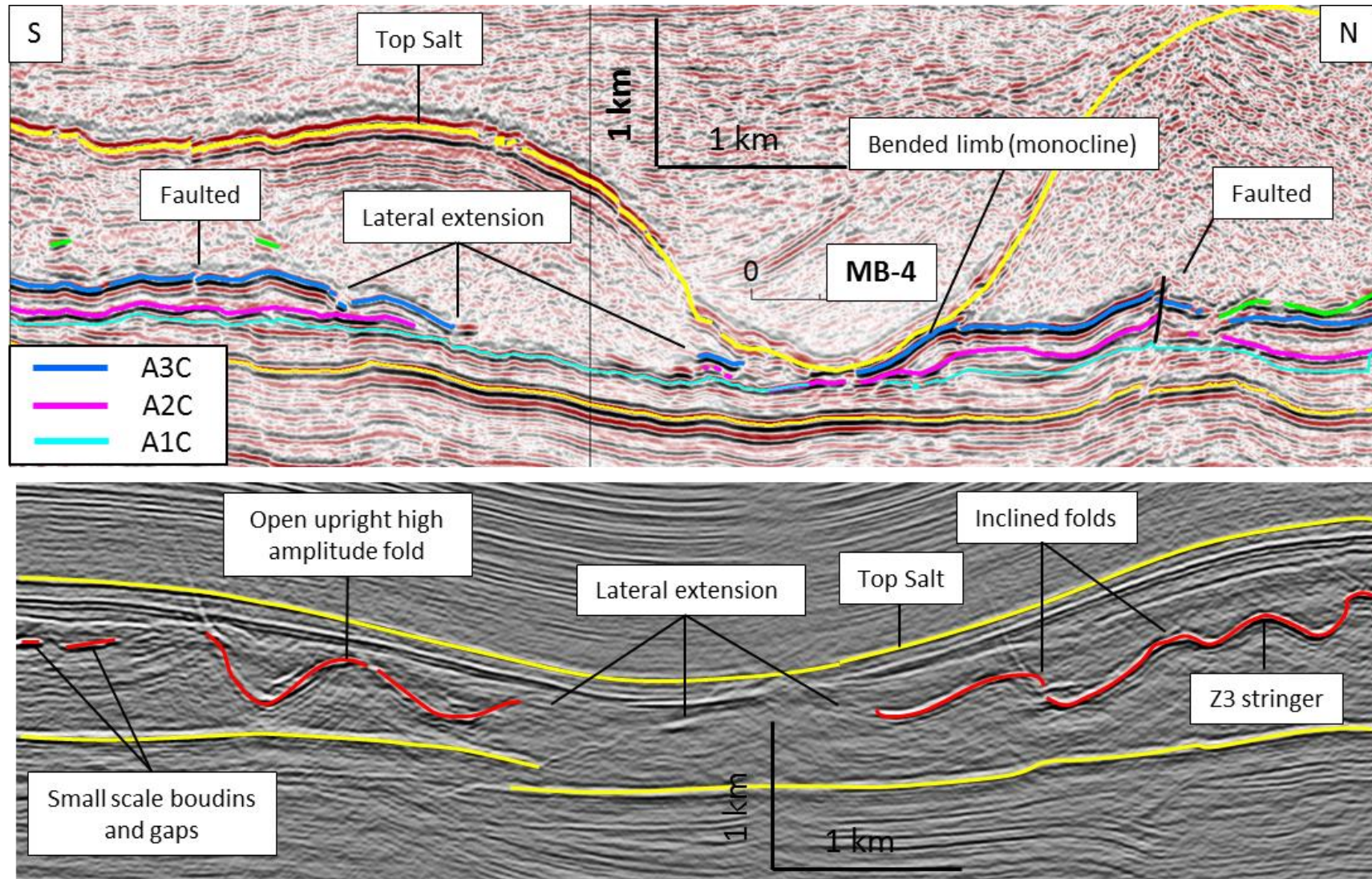
Fig. 8.1: Seismic profiles comparing the intra-salt structural styles of the SOSB (top image) and of the Silverpit Basin (bottom image). Note the well-developed folding and vergence of the Z3 Stringer.

Table 8.1 Summary of the main differences between the two case study areas.

Basin/Elements	Silverpit Area (SNS)	Birba Area (SOSB)
Stringer(s)	Dominantly anhydrite	Dominantly dolomite and limestone
Number of stringers	Single layer	Multi-layered separated by halites
Thickness of the stringer(s)	23–25 m	~10–200 m
Average thickness	24 m	60 m
Evaporite media (salt)	Halite	Halite
Original thickness of the salt	~1 km	~2 km
Salt thickness above the stringer(s)	~200–300 m	~1500–1700 m
Salt thickness below the stringer(s)	~700–800 m	Layers 10–300 m thick, total ~200 m
Dominant structural styles	Folding	Lateral extension
Secondary structural styles	Lateral extension and boudinage	Bending and faulting
Stringer shortening	Very high	Low
Salt tectonics driver mechanism	Downdip contraction zone of an updip dip extension and inversion	Differential loading
Salt tectonics grade	Early to intermediate	Late
Salt tectonics structures	Anticlines, synclines, size of pillows	Minibasins and salt walls

8.2   Internal salt flow pattern in the Silverpit area

After analysing the internal deformation of the Z3 Stringer, the most important question is how the halite intervals respond internally to the regional deformation. Three models are suggested here (Fig. 8.2):

1. The Zechstein salt has a similar trend and is harmonic with the Z3 Stringer folds but possibly with small differences in fold magnitude with increasing distance from the stringer (Fig. 8.2b). This is supported by the internal imaging of seismic data within the Z2 and Z3 halites, and may have formed due to the buckling of the basin.

2. The halite layers are horizontal as when they were deposited. The competent contrast between the Z3 Stringer and the incompetent halite causes the stringer to fold in a viscous medium (Fig. 8.2c).

3. The internal salt layers are more complex than expected and strongly concordant with the Z3 Stringer (Fig. 8.2d). This is supported by data from boreholes and mining galleries (Schléder et al. 2008) (Fig. 1.1).

The second model suggests that the stringer could cross the layers, penetrate, and sink into the halite intervals. The salt in this case is less deformed (Fig. 8.2c). The third model suggests that the salt suffered complex deformation, mixing without crossing the boundary of the Z3 Stringer unless the stringer is broken, allowing the lower Z2 salt interval to flow into the overlain Z3 halite (Fig. 8.2d).

Based on observations from the Gorleben salt dome (Bornemann 1991) (Fig. 1.2), the interpretation in this study is close to that of model 1 (Fig. 8.2b) where the thin layers within the Z2, Z3, and Z4, to some extent, have similar geometry. The observation also agrees with what has been observed from seismic profiles (Fig.

315

8.3). Although some of these reflections within the salt can be interpreted as noise or multiples, the presence of less dense salt (potash and polyhalite salts), or any thin competent materials (shale, anhydrite) which have different densities than halite, can generate some acoustic impedance (see Raith et al. 2015). The interpretation also strongly agrees with what has been observed from other salt domes (e.g., Seidl 1921) (Fig. 8.3d).

a) Example of folded and discontinuous Z3 anhydrite
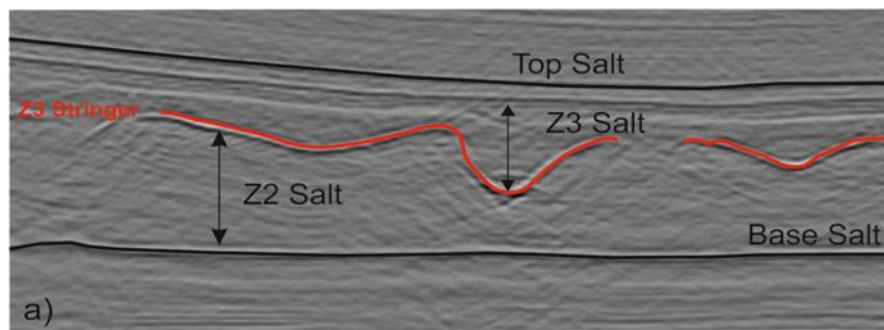
(b) The Z3 Stringer represents the internal pattern of salt
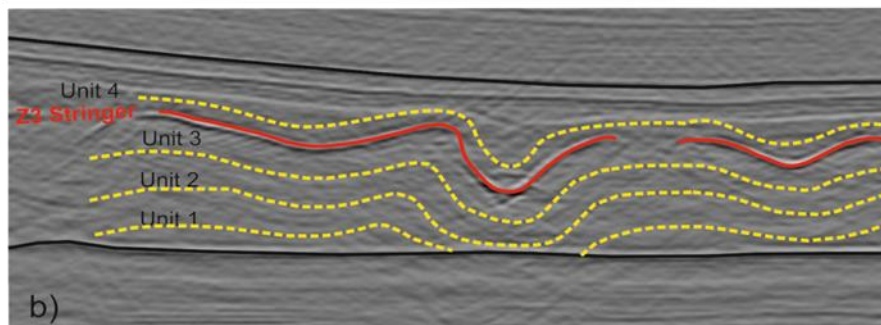
(c) The Z3 Stringer sinks and crosses vertically the halite units
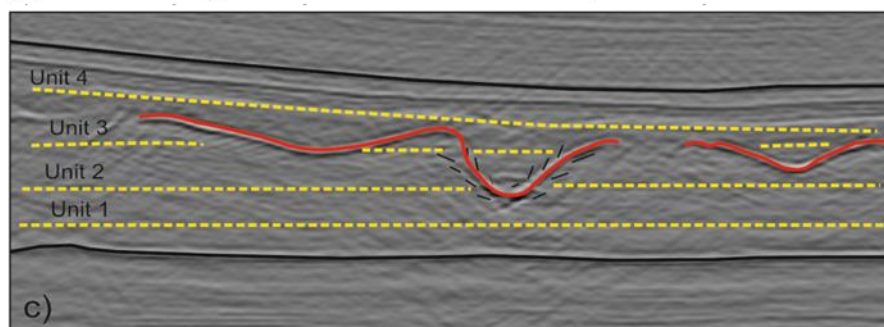
(d) The salt deformed more complex than the Z3 Stringer
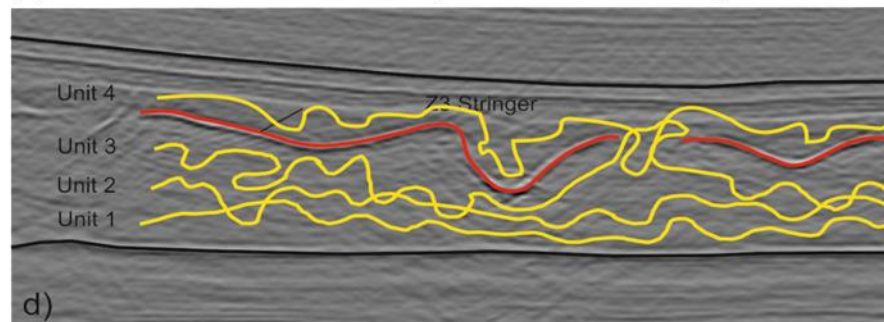
Fig. 8.2: Suggested internal salt patterns within the Zechstein. (a) The folding and discontinuity of the Z3 Stringer within the Z2–Z3 halite intervals. (b) Model 1: The internal salt patterns have a similar shape to that of Z3 Stringer. Units (1–4) are drawn to show the internal dynamic of the salt. (c) The salt units are presumably flat and the Z3 Stringer is folded or sinks within the Zechstein salt. (d) The internal salt layers are highly complex and shortened, disharmonic with the Z3 Stringer. The Z2–Z3 halites can mix with each other when the Z3 Stringer is discontinuous.

317
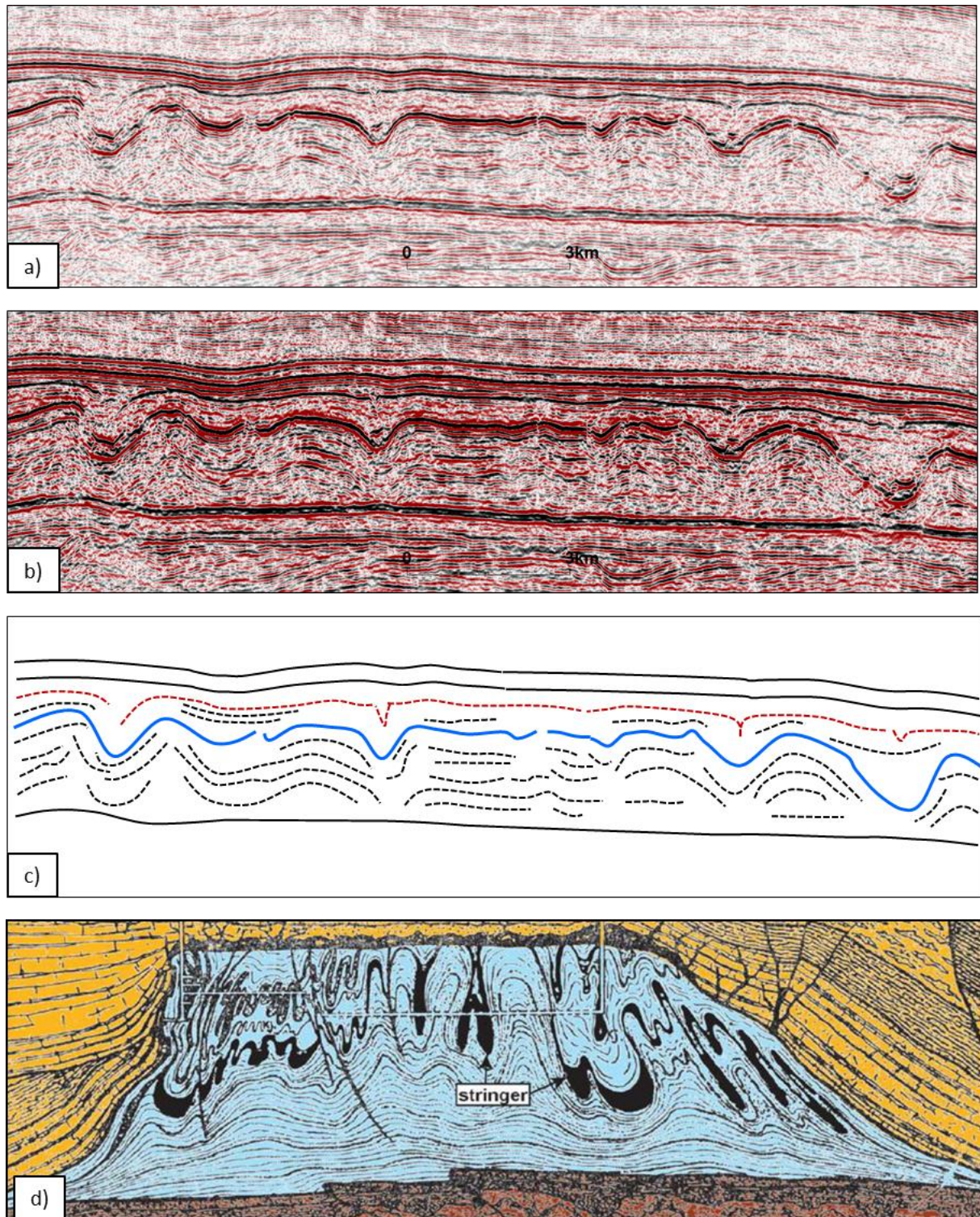
Fig. 8.3: (a) 2D seismic profile across the Cavendish field. (b) The same seismic profile but with increased amplitude gain to show the details of the internal pattern of the salt and to highlight the internal geometry of the salt. (c) The internal salt layering of the Z2 and Z3 halite intervals interpreted by tracing the internal reflectors on seismic profiles. (d) Schematic cross-section across a salt dome structure (after Seidl 1921). Note the continuity of the stringer and the internal layers, which have a similar pattern to that of the stringer, with fold magnitudes reducing away from the middle of the stringer. The interpretation agrees with the observation of the Zechstein layering in the Gorleben salt dome.

8.3   Implications of the research

8.3.1   Implications of the SOSB stringers for the petroleum system

The SOSB is an important and unusual hydrocarbon-producing basin. Self-charging limestone and dolomite stringers encased within the salt of the SOSB represent a unique intra-salt petroleum system (Al-Siyabi 2005; Schoenherr et al. 2009). However, the complexity of the deformations of the stringers makes the prediction of stringer geometries in the subsurface challenging. The reservoirs and the structural traps are scattered in the salt within isolated, commonly overpressured carbonate blocks.

There are two suggested charge models: (1) self-charging petroleum system (Frewin et al. 2000) (Fig. 8.5a), where the stringer combines both source rock and reservoir facies, and (2) pre-salt charge model, suggesting hydrocarbon migration from the sub-salt layers through faults in areas where the stringers are welded to the pre-salt section (Al-Siyabi 2005) (Fig. 8.5 b). Sub-salt charge situations could be the case in areas beneath minibasins, where the stringers are completely welded, as well as in areas where the stringers are folded and consequently grounded and penetrated by pre-salt faults (Fig. 8.4). In such cases, there are better chances for the reservoirs within the stringers to be charged, as they could contribute to the intra-stringer charge volume (Fig. 8.4c). However, the stringers might break, and the broken blocks that contain hydrocarbon can flow in all directions within the salt (Fig. 8.4d).

The best examples of structural traps are the four-way-closure traps and dome shapes. Such structures are commonly formed around minibasins (Fig. 8.5c). However, if the limbs of the dome are welded with the Top Salt and

followed by active faulting during the formation of the fold structure, hydrocarbon might leak to the overburden or may result in uncommercial accumulation. Similarly, with the outer limb of the fold structure, the migration pathway might be deviated into attached stringer fragments or smeared by faults, leaving the crest of the dome structure uncharged. When the hinge zone of the folded stringers is faulted by intra-extensional faults, these faults might also transfer fluids into an attached adjacent stringer block (Fig. 8.5c).

8.3.1   Implications of the SOSB stringers to pore pressure prediction

Drilling through the carbonate stringers and floaters in the SOSB is considered one of the major risks that need to be highly considered in the pre-drilling and during drilling operations (Al-Siyabi 2005; Kukla et al. 2011; Strozyk 2017). The stringers in the SOSB are isolated in salt and frequently contain low-permeable dolomites that are characterised by high initial production rates because of overpressures of more than 22 kPa/m (Kukla et al. 2011; Strozyk 2017). Such pressure requires heavy mud weight to overbalance the well and avoid any kick from stringer reservoirs.

The interpretation in this study suggests that the stringers that are surrounded by salt are mostly overpressured. This is because the perfect sealing by the salt and the generation of the pressure by source rock maturation within the stringer itself led to high pressure regimes. In this case, the high rate of subsidence does not form an important element for pressure build-up within the stringers, as it has been suggested by some studies (e.g., Kukla et al. 2011).

In addition, this study suggests that salt contraction regions can contribute to the overpressure of the stringers by squeezing the stringer in a similar process as a thrust front (e.g., Platt 1990). If the stringer is grounded with the pre-salt rock, which is always hydrostatic (see Al-Siyabi 2005), the stringer is interpreted to be hydrostatic because of the potential connection with the pre-salt layers.

In summary, the A2C, A3C, A4C, A5C and the floaters within the salt are all considered to be overpressured, and thus a mud weight of over 22 kPa is required. If the A1C is not underlain by a salt interval, then it is considered to have hydrostatic pressure.
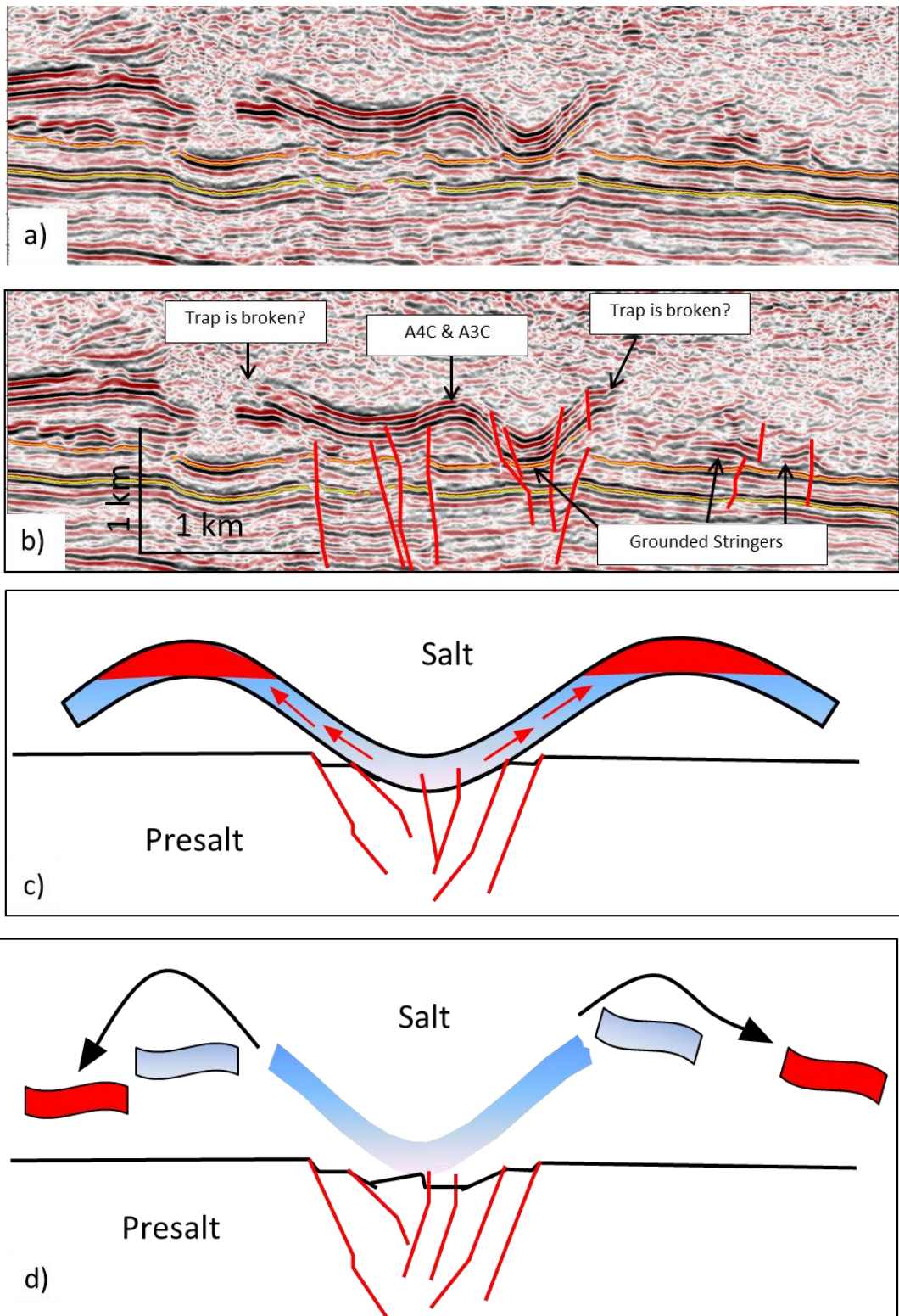
Fig. 8.4: (a–b) A possible example of hydrocarbon charge by self-charge and pre-salt charge by faults when the stringers are grounded and faulted. (c–d) New proposed scenarios. (c) The classic hydrocarbon transportation to the hinge of the anticline. (d) The stringer is broken and the reservoir is carried away by salt. Note that the hydrocarbon might flow downwards during salt movement.
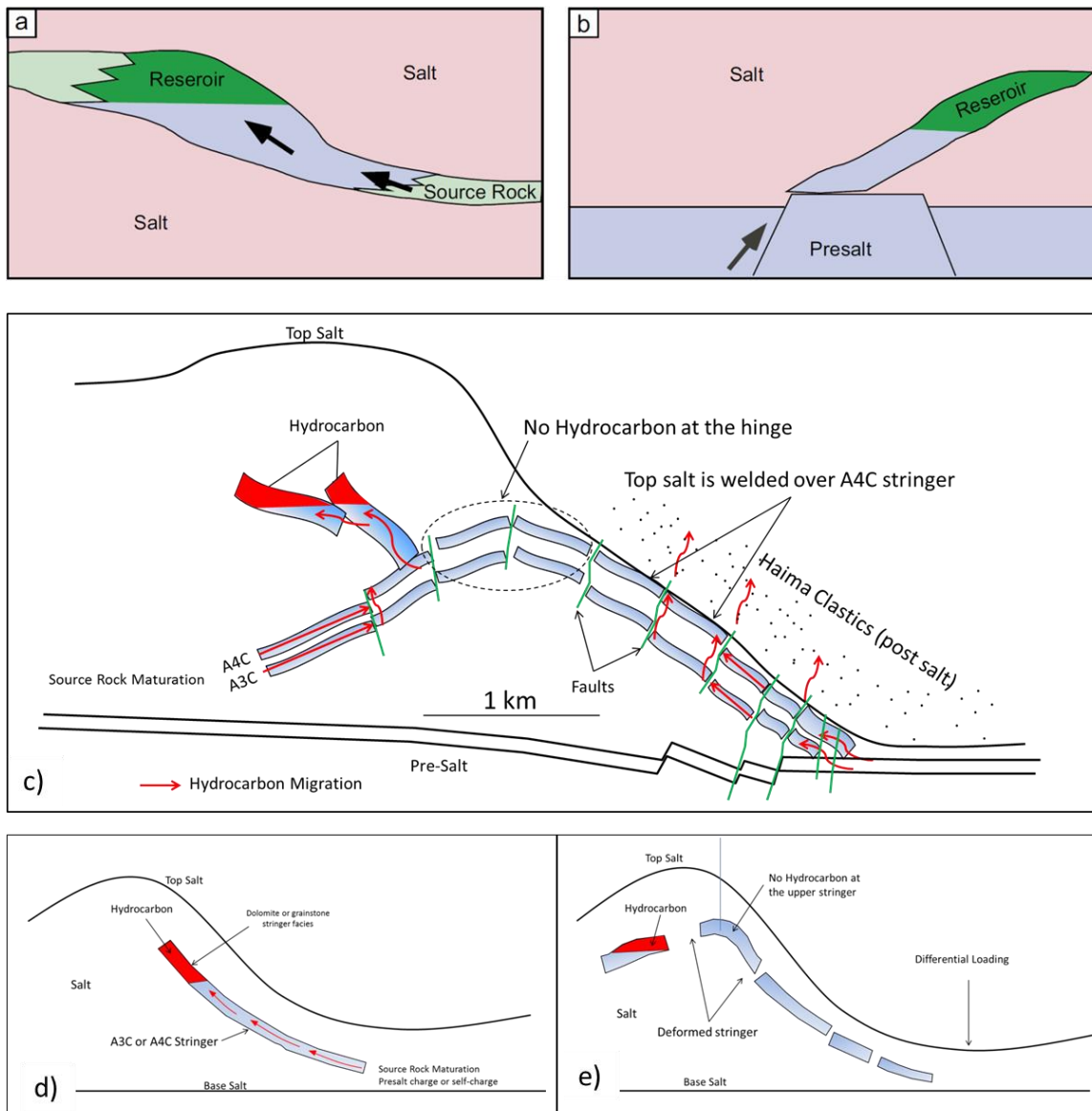
Fig. 8.5: Traps and charge of the Ara carbonate stringers. (a) Stringers are self-charging. (b) Charge is supplied from the underlying pre-salt sequence. (c–d) Newly proposed 2D schematic of possible petroleum system examples. (d) Bulge folds (see similar structure in Fig. 7.6) show possible hydrocarbon leakages by faults from the welded stringer limbs into the overburden. Note that attached blocks of stringers may transmit hydrocarbons (left). (e) Tilted unbroken stringer layer; hydrocarbons are expected to migrate to the top. (e) Stringer is faulted or boudinaged. Note the upper block that contains hydrocarbons has been carried away by salt.

8.4   Conclusions

The main conclusions from this thesis are the following:

1. Regional salt structures in the Southern North Sea and South Oman Salt Basins are characterised by intra-salt layers called stringers. The lithology of the stringers includes anhydrites and carbonate rocks. These salt stringers have a high acoustic impedance contrast that contradicts the reflectivity of the surrounding salt. Hence, they are seismic markers for understanding the internal salt dynamics of regional salt structures.

2. Stringers are deformed largely in response to regional basin deformation. Shortening of basins by regional compressional events is a major driver mechanism for salt tectonics. For example, bulk shortening of the Silverpit Basin resulted in the formation of detached anticlines and synclines with highly deformed intra-salt deformation experienced by the Z3 Stringer. When compressed, salt stringers respond to the applied stress by either being deformed in a ductile manner, as when a ductile layer is overlain by thick overburden, or in a brittle manner, by being fractured and displaced. Because of regional tectonics, salt stringers can display complex structures such as normal and thrust faults, bending faults, synclines, anticlines, boudinages, and non-cylindrical buckled folds.

3. The degree of deformation of the stringers is related to the rheology of the encasing regional salt layer. Stringers are easily folded and more resistant to brittle deformation in areas where the encasing salt is thick. Deformation in the form of boudinaging, lateral stretching, and fragmentation of stringers is common in areas where the encasing salt has witnessed a high rate of

subsidence. In addition, the shortening intensity of the regional anticlinal structures is directly proportional with the tightness of the intra-salt folding and inversely proportional to the internal fold wavelengths.

4. Analysing the structural styles of salt stringers is an important tool for seismic interpreters to predict deformational styles of the stringers and understanding regional tectonics. The analysis of these stringers will contribute to the understanding of the complexity of intra-salt petroleum systems in several salt basins around the world.

References

Abe, S., Urai, J.L. and Kettermann, M., 2013. Fracture patterns in nonplane strain boudinage—insights from 3-D discrete element models. *Journal of Geophysical Research: Solid Earth 118*(3), pp. 1304–1315.

Adamuszek, M., Schmid, D.W. and Dabrowski, M., 2011. Fold geometry toolbox–Automated determination of fold shape, shortening, and material properties. *Journal of Structural Geology 33*(9), pp. 1406–1416.

Ala, M., 1974. Salt diapirism in southern Iran. *American Association of Petroleum Geologists Bulletin 58*(9), pp. 1758–1770.

Al-Barwani, B. and McClay, K.R., 2008. Salt tectonics in the Thumrait area, in the southern part of the South Oman Basin: implications for mine-basin evolution. *GeoArabia 13*, pp. 77–108.

Allen, M., Griffiths, P., Craig, J., Fitches, W. and Whittington, R., 1994. Halokinetic initiation of Mesozoic tectonics in the southern North Sea: a regional model. *Geological Magazine 131*, pp. 559–561.

Al-Marjeby, A. and Nash, D., 1986. A summary of the geology and oil habitat of the Eastern Flank hydrocarbon province of South Oman. *Marine Petroleum Geology 3*, pp. 306–314.

Al-Siyabi, H.A., 2005. Exploration history of the Ara intrasalt carbonate stringers in the South Oman Salt Basin. *GeoArabia 10*(4), pp. 39–72.

Amthor, J.E., Ramseyer, K., Faulkner, T. and Lucas, P., 2005. Stratigraphy and sedimentology of a chert reservoir at the Precambrian-Cambrian boundary: The Al Shomou Silicilyte, South Oman Salt Basin. *GeoArabia 10*, pp. 89–122.

Andresen K.J., Huuse M., Schødt N.H., Clausen L. and Seidler L., 2011., Hydrocarbon plumbing systems of salt minibasins offshore Angola revealed by three-dimensional seismic analysis, *American Association of Petroleum Geologists Bulletin, 95*, pp. 1039–1065.

Bauerle, G., Bornemann, O., Mauthe, F. and Michalzik, D., 2000. Origin of stylolites in Upper Permian Zechstein anhydrite (Gorleben salt dome, Germany). *Journal of Sedimentary Research 70*(3).

Bäuerle, G., Bornemann, O., Mauthe, F. and Michalzik, D., 2000. Turbidite, Breccien und Kristallrasen am Top des Hauptanhydrits (Zechstein 3) des Salzstocks Gorleben. *Zeitschrift der Deutschen Geologischen Gesellschaft* 99–125.

Behlau, J. and Mingerzahn, G., 2001. Geological and tectonic investigations in the former Morsleben salt mine (Germany) as a basis for the safety

assessment of a radioactive waste repository. *Engineering Geology 61*, pp. 83–97.

Bergbauer, S., 2002. *The use of curvature for the analysis of folding and fracturing with application to the Emigrant Gap Anticline, Wyoming.* PhD thesis, Stanford University.

Bernitsas, N., J. Sun, and C. Sicking, 1997. Prism waves—An explanation for curved seismic horizons below the edge of salt bodies. In: *59th Annual International Conference and Exhibition, EAGE, Extended Abstracts, E38.*

Bons, P.D., Druguet, E., Hamann, I., Carreras, J. and Passchier, C.W., 2004. Apparent boudinage in dykes. *Journal of Structural Geology 26*, pp. 625–636

Borchert, H. and Muir, R.O., 1964. *Salt Deposits. The Origin, Metamorphism and Deformation of Evaporites.* D. Van Nostrand Company, Ltd., London, New York, Toronto.

Borgos, H., Gramstad, O., Dahl, G., Le Guern, P., Sonneland, L., and Rosalba, J., 2007. Automated Horizon and Geobody Extraction Using 3D Seismic Waveform Sequences. In: *Proceedings 69th EAGE Conference and Exhibition 2007.*

Bornemann, O., 1991. Zur Geologie des Salzstocks Gorleben nach den Bohrergeb-nissen. *BfS-Schriften 4*, pp. 1–67.

Burliga, S., 1996. Kinematics within the Klodawa salt diapir, central Poland. In: Alsop, G.I., Blundell, D.J., Davison, I. (eds.), *Salt Tectonics.* Geological Society Special Publication 100. Geological Society, London, pp. 11–21.

Carter, N., Horseman, S., Russell, J. and Handin, J., 1993. Rheology of rocksalt. *Journal of Structural Geology 15*, pp. 1257–1271.

Cartwright, J.A. and Jackson, M., 2008. Initiation of gravitational collapse of an evaporite basin margin: The Messinian saline giant, Levant Basin, Eastern Mediterranean. *Geological Society of America Bulletin 120*, pp. 399–413.

Cartwright, J., Jackson, M., Dooley, T. and Higgins, S., 2012. Strain partitioning in gravity-driven shortening of a thick, multilayered evaporite sequence. *Geological Society, London, Special Publications 363*, pp. 449–470.

Cavalca, M. and P. Lailly, 2005. Prismatic reflections for the delineation of salt bodies. *75th Annual International Meeting, SEG, Expanded Abstracts*, pp. 2550–2553.

Chaves, M. U., Oliver, F., Kawakami, G., and Di Marco, L., 2011. Visualization of Geological Features Using Seismic Volume Rendering, RGB Blending and Geobody Extraction. In: *Proceedings 12th International Congress of the Brazilian Geophysical Society 2011*.

Chemia, Z., Koyi, H. and Schmeling, H., 2008. Numerical modelling of rise and fall of a dense layer in salt diapirs. G*eophysical Journal International 172*, pp. 798–816.

Clark, I.R. and Cartwright, J.A., 2009. Interactions between submarine channel systems and deformation in deepwater fold belts: Examples from the Levant Basin, Eastern Mediterranean sea. *Marine and Petroleum Geology 26*, pp. 1465–1482.

Coelewij, P.A.J., Haug, G.M.W. and Kuijkv, H., 1978. Magnesium-salt exploration in the Northeastern Netherlands. *Geologie en Mijnbouw 57* (4), pp. 487–502.

Cohen, H. and Hardy, S., 1996. Numerical modelling of stratal architectures resulting from differential loading of mobile substrate. In: Alsop, G.I., Blundell, I., Davison, I. (Eds.), *Salt Tectonics.* Geological Society, London, Special Publications 100, pp. 265–274.

Coward, M. and Stewart, S., 1995. *Salt-influenced structures in the Mesozoic-Tertiary cover of the southern North Sea, United Kingdom.*

Daniilidis, A. and R. Herber, 2015. *Fractured Anhydrite as a Geothermal Source in a Low Enthalpy Context (Southern Permian Basin, Netherlands).*

Davies, R.J., Stewart, S.A., Cartwright, J.A., Lappin, M., Johnston, R., Fraser, S.I. and Brown, A.R., 2004. 3D seismic technology: Are we realising its full potential? *Geological Society, London, Memoirs 29,* pp. 1–10.

Davison, I., 2009. Faulting and fluid flow through salt. *Journal of the Geological Society 166*, pp. 205–216.

Davison, I., Alsop, I. and Blundell, D., 1996. Salt tectonics: some aspects of deformation mechanics. *Geological Society, London, Special Publications 100*: pp. 1–10.

Davison, I., Anderson, L., Nuttall, P., 2012. Salt deposition, loading and gravity drainage in the Campos and Santos salt basin. In: Alsop, G.I., Archer, S.G., Hartley, A.J., Grant, N.T., Hodgkinson, R. (eds.), *Salt Tectonics, Sediments and Prospectivity, vol. 363.* Geological Society, London, Special Publications, pp. 159–174.

Davison, I., Bosence, D., Alsop, G.I. and Al-Aawah, M.H., 1996. *Deformation and sedimentation around active Miocene salt diapirs on the Tihama Plain, northwest Yemen.* Geological Society, London, Special Publications 100, pp. 23–39.

Demercian, S., Szatmari, P. and Cobbold, P.R., 1993. Style and pattern of salt diapirs due to thin-skinned gravitational gliding, Campos and Santos basins, offshore Brazil. *Tectonophysics 228*, pp. 393–433.

DeVasto, M. A., Czeck, D. M. and Bhattacharyya, P., 2012. Using image analysis and ArcGIS® to improve automatic grain boundary detection and quantify geological images: *Computers and Geosciences 49*, pp. 38–45.

Dooley, T.P., Jackson, M.P., Cartwright, J.A. and Hudec, M.R., 2008. Modeling of strain partitioning during gravity-driven deformation of layered

evaporates and overburden. *AAPG Annual Convention and Exhibition, Abstracts Volume 17*, p. 46.

Dooley, T. P., Jackson, M. P. A. and Hudec, M. R., 2007. Initiation and growth of salt-based thrustbelts onpassive margins: results from physical models. *Basin Research 19*, pp. 165–177.

Escher, B.G. and Kuenen, P.H., 1928. Experiments in connection with salt domes. *Leidse Geologische Mededelingen, 3*(1), pp. 151–182.

Evans, D.J. and Chadwick, R.A. (eds.), 2009. *Underground Gas Storage: Worldwide Experiences and Future Development in the UK and Europe.* Special Publications, Geological Society, London 313.

Fiduk, J.C. and Rowan, M.G., 2012. *Analysis of folding and deformation within layered evaporites in Blocks BM-S-8 & -9, Santos Basin, Brazil.* Geological Society, London, Special Publications 363, pp. 471–487.

Fleuty, M.J., 1964. The description of folds. *Geological Association Proceedings 75*, pp. 461–492.

Fokker, P.A., Urai, J.L. and Steeneken, P.V., 1995. Production-induced convergence of solution mined caverns in magnesium salts and associated subsidence. In: *Proceedings of the Fifth International Symposium on Land Subsidence.* The Hague, The Netherlands, A.A. Balkema, pp. 281–289.

Fossen, H., 2010. *Structural Geology.* Cambridge: Cambridge University Press.

Frewin, N., S. Indrelid, I. Kowalewski, B. Carpentier, A. Huc, F. Gelin and Albercht, P., 2000. Accurate charge risking of unconventional source rock/reservoir in South Oman. *GEO 2000 Abstracts in GeoArabia 5*(1), p. 89.

Fulda, E., 1928. Die Geologie der Kalisalzlagerstätten. Das Kali, II. Teil. *Enke's Bbliothek für Chemie und Technik unter berücksichtiging der Volkswirtschaft 7*, pp. 24–136.

Gaullier, V. and Vendeville, B.C., 2005. Salt tectonics driven by sediment progradation. Part II: Radial spreading of sedimentary lobes prograding above salt. *American Association of Petroleum Geologists Bulletin* 89, pp. 1081–1089.

Ge, H., Jackson, M.P.A. and Vendeville, B.C., 1997. Kinematics and dynamics of salt tectonics driven by progradation. *American Association of Petroleum Geologists Bulletin 81*(3), pp. 398–423.

Geluk, M., 2000. Late Permian (Zechstein) carbonate-facies maps the Netherlands. *Geologie en Mijnbouw 79*, pp. 17–28.

Geluk, M., 2007. *Triassic. Geology of the Netherlands.* Royal Netherlands Academy of Arts and Sciences, pp. 85–106.

Geluk, M, Van Wees, J.D., Grönloh, H. and Van Adrichem Boogaert, H.A. 1997. Prace Panstw. *Inst. Geolog. CLVII: 63.*

References

Gemmer, L., Beaumont, C. and Ings, S.J., 2005. Dynamic modelling of passive margin salt tectonics: effects of water loading, sediment properties and sedimentation patterns. *Basin Research 17*(3), pp. 383–402.

Gemmer, L., Ings, S. J., Medvedev, S. and Beaumont, C., 2004. Salt tectonics driven by differential sediment loading: stability analysis and finite-element experiments. *Basin Research 16*, pp. 199–218.

Ghosh, S.K., 1988. Theory of chocolate tablet boudinage. *Journal of Structural Geology 10*, pp. 541–553.

Goscombe, B.D. and Passchier, C.W., 2003. Asymmetric boudins as shear sense indicators: an assessment from field data. *Journal of Structural Geology 25*(4), pp. 575–589.

Goscombe, B.D., Passchier, C.W. and Hand, M., 2004. Boudinage classification: end member boudin types and modified boudin structures. *Journal of Structural Geology 26*, pp. 739–763.

Grujic, D. and Mancktelow, N.S., 1995. Folds with axes parallel to the extension direction: an experimental study. *Journal of Structural Geology 17*, pp. 279–291.

Hale, D., Hill, N.R. and Stefani, J., 1992. Imaging salt with turning seismic waves. *Geophysics 57*(11), pp.1453–1462.

Hansen, D.M., Shimeld, J.W., Williamson, M.A., Lykke-Andersena, H., 2004. Development of a major polygonal fault system in Upper Cretaceous chalk and Cenozoic mudrocks of the Sable Subbasin, Canadian Atlantic margin. *Marine and Petroleum Geology 21*, pp. 1205–1219.

Harris, L.B., Yakymchuk, C. and Godin, L., 2012. Implications of centrifuge simulations of channel flow for opening out or destruction of folds. *Tectonophysics 526*, pp. 67–87.

Heward, A.P., 1990. Salt removal and sedimentation in Southern Oman. In: Robertson, A. H. F., Searle, M. P. and Ries, A. C. (eds.) *The Geology and Tectonics of the Oman Region*. Geological Society, London, Special Publications 49, pp. 637–652.

Hodgson, N.A., Farnsworth, J., Fraser, A.J., 1992. *Salt-related tectonics, sedimentation and hydrocarbon plays in the Central Graben, North Sea, UKCS.* Geological Society, London, Special Publications 67, pp. 31–63.

Hudec, M.R. and Jackson, M., 2007. Terra infirma: Understanding salt tectonics. *Earth-Science Reviews 82*, pp. 1–28.

Hudec, M.R., Jackson, M.P. and Schultz-Ela, D.D., 2009. The paradox of minibasin subsidence into salt: Clues to the evolution of crustal basins. *Geological Society of America Bulletin 121*, pp. 201–221.

Hughes, M. and Davison, I., 1993. Geometry and growth kinematics of salt pillows in the southern North Sea. *Tectonophysics 228*, pp. 239–254.

Humphris Jr., C.C., 1979. Salt movement in continental slope, northern Gulf of Mexico. *American Association of Petroleum Geologists Bulletin 63*, pp. 782–798.

Hunsche, U. and Hampel, A., 1999. Rock salt—the mechanical properties of the host rock material for a radioactive waste repository. E*ngineering Geology 52*, pp. 271–291.

Ings, S. J. and Beaumont, C., 2010. Shortening viscous pressure ridges, a solution to the enigma of initiating salt 'withdrawal' minibasins. *Geology 38*, pp. 339–342.

Ings, S., Beaumont, C., Gemmer, L., 2004. Numerical modeling of salt tectonics on passive continental margins: preliminary assessment of the effects of sediment loading, buoyancy, margin tilt, and isostasy. In: Post, P.J., Olson, D.L., Lyons, K.T., Palmes, S.L.,Harrison, P.F., Rosen, N.C. (Eds.), *Salt Sediment Interactions and Hydrocarbon Prospectivity: Concepts, Applications, and Case Studies for the 21st Century.* Gulf Coast Section of the Society of Economic Paleontologists and Mineralogists 24th Annual Research Conference Program with abstracts, pp. 36–68.

Jackson, C.A.-L., Jackson, M.P.A., Hudec, M.R., Rodriguez, C.R., 2015. Enigmatic structures within salt walls of the Santos Basin—Part 1: Geometry and kinematics from 3D seismic reflection and well data. *Journal of Structural Geology 75*, pp. 135–162.

Jackson, M.P.A., 1985. *Natural Strain in Diapiric and Glacial Rock Salt, with Emphasis on Oakwood Dome, East Texas.* Bureau of Economic Geology, The University of Texas at Austin, Texas.

Jackson, M.P.A., 1995. Retrospective salt tectonics. In: M.P.A. Jackson, M.P.A, Roberts, D.G. and Snelson, S. (eds.), *Salt tectonics: a global perspective*, AAPG Memoir 65, pp. 1–28.

Jackson, M.P.A., Cornelius, R.R., Craig, C.H., Gansser, A., Stöcklin, J. and Talbot, C.J., 1990. Salt diapirs of the Great Kavir, Central Iran. *Geological Society of America Memoirs 177*, pp. 1–150.

Jackson, M.P.A. and Talbot, C.J., 1989. Anatomy of mushroom-shaped diapirs. *Journal of Structural Geology* 11(1/2), pp. 211–230.

Jackson, M.P.A. and Talbot, C.J., 1991. A glossary of salt tectonics. *Geological Circular - Bureau of Economic Geology*, University of Texas at Austin, pp. 91–4.

Jackson, M.P.A. and Vendeville, B.C., 1994. Regional extension as a geologic trigger for diapirism: *Geological Society of America Bulletin 106*, pp. 57–73.

Jackson, M.P., Vendeville, B.C., and Schultz-Ela, D.D., 1994. Structural dynamics of salt systems: Ann*ual Review of Earth and Planetary Sciences 22*, p. 93–117.

References

Jaeger, J.C. and Cook, N.G.W., 1979. *Fundamentals of Rock Mechanics* (3rd Ed.), Chapman & Hall, London.

Ji, S., Huang, T., Fu, K. and Li, Z., 2011. Dirty salt velocity inversion: The road to a clearer subsalt image. *Geophysics*.

Jones, I.F., 2008. A modeling study of preprocessing considerations for reverse-time migration. *Geophysics 73*(6), pp. T99–T106.

Jones, I.F. and I. Davison, 2014. Seismic imaging in and around salt bodies. *Interpretation 2*(4), pp. SL1–SL20.

Kaus, B.J.P. and Podladchikov, Y.Y., 2001. Forward and reverse modelling of the three-dimensional viscous Rayleigh–Taylor instability. *Geophysical Research Letters 28*, pp. 1095–1098.

Kehle, R.O., 1988. The origin of salt structures. In: Schreiber, B.C (ed.), *Evaporites and Hydrocarbons.* Columbia University Press, New York, pp. 345–404.

Kent, P.E., 1979. The emergent Hormuz salt plugs of southern Iran. *Journal of Petroleum Geology, 2*(2), pp. 117–144.

Kettermann, M., 2009. *The analogue modelling of boudins*, BSc Thesis, RWTH Aachen University.

Koyi, H., 1996. Salt flow by aggrading and prograding overburdens. In: Alsop, G.I., Blundell, D.J., Davison, I. (eds.), *Salt Tectonics.* Geological Society, London, Special Publications, pp. 243–285.

Koyi, H.A., 2001. Modeling the influence of sinking anhydrite blocks on salt diapirs targeted for hazardous waste disposal. *Geology 29*, pp. 387–390.

Kukla, P.A., Reuning, L., Becker, S., Urai, J.L. and Schoenherr, J., 2011. Distribution and mechanisms of overpressure generation and deflation in the late Neoproterozoic to early Cambrian South Oman Salt Basin. *Geofluids, 11*(4), pp. 349–361.

Kupfer, D. H., 1968. Relationship of internal to external structure of salt domes, in J. Braunstein, ed., *Diapirism and diapirs*, Tulsa, OK, American Association of Petroleum Geologists 8, pp. 78–89.

Li, S., Abe, S., Reuning, L., Becker, S., Urai, J.L. and Kukla, P.A., 2012a. Numerical modelling of the displacement and deformation of embedded rock bodies during salt tectonics: A case study from the South Oman Salt Basin. *Geological Society, London, Special Publications 363*, pp. 503–520.

Li, S., Abe, S., Urai, J. and van Gent, H. eds., 2009. Sinking of carbonate and anhydrite stringers in rock salt: insights from numerical simulations. *EGU General Assembly Conference Abstracts.*

Lisle, R.J. 1994. Detection of zones of abnormal strains in structures using Gaussian curvature analysis: *American Association of Petroleum Geologists Bulletin v. 78*(12), pp. 1811–1819.

Lisle, R.J. and Toimil, N.C., 2007. Defining folds on three-dimensional surfaces: *Geology 35*(6), pp. 519–522.

Loosveld, R., Bell, A. and Terken, J., 1996. The tectonic evolution of interior Oman. *GeoArabia 1*, pp. 28–51.

Marshak, S., 2004. Arcs, oroclines, salients, and syntaxes—The origin of map-view curvature in fold-thrust belts. *Thrust Tectonics and Petroleum Systems: American Association of Petroleum Geologists Memoir 82*, pp. 131–156.

Mattes, B. and Morris, S.C., 1990. Carbonate/evaporite deposition in the Late Precambrian—Early Cambrian Ara Formation of Southern Oman. *Geological Society, London, Special Publications 49*, pp. 617–636.

McClay, K.R., Dooley, T., Lewis, G., 1998. Analog modeling of progradational delta systems. *Geology 26*, pp. 771–774.

Mogaji, K., Aboyeji, O., and Omosuyi, G., 2011. Mapping of lineaments for groundwater targeting in the basement complex region of Ondo State, Nigeria, using remote sensing and geographic information system (GIS) techniques: *International Journal of Water Resources and Environmental Engineering 3*(7), pp. 150–160.

Mohr, M., Kukla, P., Urai, J. and Bresser, G., 2005. Multiphase salt tectonic evolution in NW Germany: seismic interpretation and retro-deformation. *International Journal of Earth Sciences 94*, pp. 917–940.

Oudmayer, B. and De Jager, J. (eds.), 1993. *Fault reactivation and oblique-slip in the Southern North Sea.* Geological Society, London, Petroleum Geology Conference series. Geological Society of London.

Paton, G., Elghorori, A. and McArdle, N., 2012. March. Adaptive Geobodies: Extraction of Complex Geobodies from Multi-attribute Data Using a New Adaptive Technique. *GEO 2012*.

Peel, F.J., 2014. How do salt withdrawal minibasins form? Insights from forward modelling, and implications for hydrocarbon migration. *Tectonophysics 630*, pp. 222–235.

Peters, J., Filbrandt, J., Grotzinger, J., Newall, M., Shuster, M. and Al-Siyabi, H., 2003. Surface-piercing Salt Domes of interior North Oman, and their significance of the Ara Carbonate "stringer" hydrocarbon play. *GeoArabia 8*, pp. 231–270.

Platt, J.P., 1990. Thrust mechanics in highly overpressured accretionary wedges. *Journal of Geophysical Research 95*, pp. 9025–9034.

Podladchikov, Y., Talbot, C. and Poliakov, A.N.B., 1993. Numerical-models of complex diapirs. *Tectonophysics 228*, pp. 189–198.

Raharimahefa, T., and Kusky, T.M., 2009. Structural and remote sensing analysis of the Betsimisaraka Suture in northeastern Madagascar. *Gondwana Research 15*(1), pp. 14–27.

References

Raith, A F., Strozyk, F., Visser, J., and Urai, J. L. (2015). Evolution of rheologically heterogeneous salt structures: a case study from the northeast of the Netherlands, Solid Earth Discuss., 7, 1877-1908.

Reuning, L., Schoenherr, J., Heimann, A., Urai, J.L., Littke, R., Kukla, P.A. and Rawahi, Z., 2009. Constraints on the diagenesis, stratigraphy and internal dynamics of the surface-piercing salt domes in the Ghaba salt basin (Oman): a comparison to the Ara formation in the South Oman salt basin. *GeoArabia 14*, pp. 83–120.

Richter-Bernburg G., 1980. Salt domes in northwest Germany, *Centres de Recherches Exploration-Production, Bulletin, Elf Aquitaine 4*, pp. 373–393.

Roberts, A., 2001. Curvature attributes and their application to 3D interpreted horizons. *First Break 19*, pp. 85–100.

Rowan, M.G., 1995. *Structural styles and evolution of allochthonous salt, central Louisiana outer shelf and upper slope.*

Rowan, M.G., 2002. Salt-related accommodation in the Gulf of Mexico deepwater: withdrawal or inflation, autochthonous or allochthonous? *Gulf Coast Assoc. Geol.Soc. Trans. 52*, pp. 861–869.

Rowan, M.G. and Fiduk, J.C., 2015. *Internal Deformation in Layered Evaporite Sequences: Evacuation and Diapirism Versus Contraction and Inflation.* AAPG Annual Convention and Exhibition.

Rowan, M.G., Peel, F.J., Vendeville, B.C., 2004. Gravity-driven Foldbelts on Passive Margins, vol. 82. *AAPG Memoir*, pp. 157–182.

Rowan, M.G. and Vendeville, B.C., 2006. Foldbelts with early salt withdrawal and diapirism: physical model and examples from the northern Gulf of Mexico and the Flinders Ranges, Australia. *Marine and Petroleum Geology 23*, pp. 871–891.

Schléder, Z., Urai, J.L., Nollet, S. and Hilgers, C., 2008. Solution-precipitation creep and fluid flow in halite: a case study of Zechstein (Z1) rocksalt from Neuhof saltmine (Germany). *International Journal of Earth Sciences 97*(5), pp. 1045–1056.

Schoenherr, J., Littke, R., Urai, J.L., Kukla, P.A. and Rawahi, Z., 2007. Polyphase thermal evolution in the Infra-Cambrian Ara Group (South Oman Salt Basin) as deduced by maturity of solid reservoir bitumen. *Organic Geochemistry 38*, pp. 1293–1318.

Schoenherr, J., Reuning, L., Kukla, P.A., Littke, R., Urai, J.L., Siemann, M., Rawahi, Z., 2009. Halite cementation and carbonate diagenesis of intra-salt reservoirs from the Late Neoproterozoic to Early Cambrian Ara group (South Oman Salt Basin). *Sedimentology 56*(2), pp. 567–589.

Schoenherr, J., Urai, J.L., Kukla, P.A., Littke, R., Schleder, Z., Larroque, J.M., Newall, M.J., Al-Abry, N., Al-Siyabi, H.A. and Rawahi, Z., 2007. Limits to the sealing capacity of rock salt: A case study of the infra-Cambrian Ara Salt from

the South Oman salt basin. *American Association of Petroleum Geologists* Bulletin *91*(11), pp. 1541–1557.

Schreiber B.C. (ed.) 1988. *Evaporites and hydrocarbons.* Columbia University Press, New York.

Schröder, S., Grotzinger, J.P., Amthor, J.E. and Matter, A., 2005. Carbonate deposition and hydrocarbon reservoir development at the Precambrian–Cambrian boundary: the Ara Group in South Oman. *Sedimentary Geology, 180*(1), pp. 1–28.

Schwerdtner, W.M. and Van Kranendonk, M., 1984. Structure of Stolz diapir; a well exposed salt dome on Axel Heiberg Island, Canadian Arctic Archipelago. *Bulletin of Canadian Petroleum Geology 32*(2), pp. 237–241.

Seidl, E., 1921. *Schürfen, Belegen und Schachtabteufen auf deutschen Zechsteinsalzhorsten. Archäologische Lagerstätten – Forschung 26*, Berlin (Geol. L.-A.).

Shan, G. and Biondi, B., 2008. Angle-domain common-image gathers for steep reflectors. In: *2008 SEG Annual Meeting*, Society of Exploration Geophysicists.

Sheriff, R.E., 1975. Factors affecting seismic amplitudes. *Geophysical Prospecting 23*, pp. 125–138.

Sleep, N.H. and Fujita, K., 1997. *Principles of Geophysics.* Blackwell Science, USA.

Smith, D.B., 1996. Deformation in the late Permian Boulby halite (EZ3Na) in Teesside, NE England. *Geological Society Special Publications 100*, pp. 77–88.

Stewart, S., 2007. *Salt tectonics in the North Sea Basin: a structural style template for seismic interpreters*. Special Publication, Geological Society of London 272.

Stewart, S. and Allen, P., 2005. 3D seismic reflection mapping of the Silverpit multi-ringed crater, North Sea. *Geological Society of America Bulletin 117*, pp. 354–368.

Strozyk, F., 2017. The internal structure of the Zechstein salt and related drilling risks in the northern Netherlands. In: J.I. Soto, Flinch, J.F., Tari, G. (Eds), *Permo-Triassic salt provinces in Europe, North Africa and the Atlantic margins: Tectonics and hydrocarbon potential.* Elsevier.

Strozyk, F., van Gent, H., Urai, J. and Kukla, P., 2012. 3D seismic study of complex intra-salt deformation: An example from the Upper Permian Zechstein 3 Stringer, Western Dutch offshore*. Geological Society, London, Special Publications 363*, pp. 489–501.

Strozyk, F., Urai, J.L., van Gent, H., de Keijzer, M. and Kukla, P.A., 2014. Regional variations in the structure of the Permian Zechstein 3 intrasalt

stringer in the northern Netherlands: 3D seismic interpretation and implications for salt tectonic evolution. *Interpretation 2*(4), pp. SM101–SM117.

Talbot, C., 1979. Fold trains in a glacier of salt in southern Iran: Journal of *Structural Geology 1*(1), pp. 513–1118.

Talbot, C.J., 1992. Centrifuged models of Gulf of Mexico profiles. *Marine and Petroleum Geology 9*, pp. 412–432.

Talbot, C.J., 1998. Extrusions of Hormuz salt in Iran. *Geological Society, London, Special Publications 143,* pp. 315–334.

Talbot, C.J. and Aftabi, P., 2004. Geology and models of salt extrusion at Qum Kuh, central Iran. *Journal of the Geological Society of London 161*, pp. 321–334.

Talbot, C. and Jackson, M., 1987. Internal kinematics of salt diapirs. *American Association of Petroleum Geologists Bulletin 71*: pp.1068–1093.

Taylor, J., 1990. *Upper Permian—Zechstein. Petroleum Geology of the North Sea: Basic Concepts and Recent Advances,* Fourth Edition, pp. 174–211.

Terken, J.M.J. and Frewin, N.L., 2000. The Dhahaban petroleum system of Oman. *American Association of Petroleum Geologists Bulletin 84*, pp. 523–544.

Thomson, K., Owen, P. and Smith, K., 2005. Discussion on the North Sea Silverpit Crater: impact structure or pull-apart basin? *Journal of the Geological Society 162*, pp. 217–220.

Trusheim, F., 1960. Mechanism of salt migration in northern Germany. *American Association of Petroleum Geologists Bulletin 44*, pp. 1519–1540.

Underhill, J.R., 2004. Earth science: an alternative origin for the 'Silverpit crater'. *Nature 428*(6980).

Underhill, J.R., 2009. Role of intrusion-induced salt mobility in controlling the formation of the enigmatic 'Silverpit Crater', UK Southern North Sea. *Petroleum Geoscience 15*, pp. 197–216.

Urai, J., Schléder, Z., Spiers, C. and Kukla, P., 2008. Flow and transport properties of salt rocks. *Dynamics of Complex Intracontinental Basins: The Central European Basin System*, pp. 277–290.

Van Adrichem Boogaert, H. and Kouwe, W., 1993. Stratigraphic nomenclature of the Netherlands, revision and update by RGD and NOGEPA: *Mededelingen Rijks Geologische Dienst 50*.

van Gent, H., Strozyk, F., Urai, J., de Keijzer, M. and Kukla, P. eds., 2012. The large scale structures of the Late Permian Zechstein 3 intra-salt stringer, northern Netherlands. In: *EGU General Assembly Conference Abstracts.*

van Gent, H., Urai, J.L. and De Keijzer, M., 2011. The internal geometry of salt structures–A first look using 3D seismic data from the Zechstein of the Netherlands. *Journal of Structural Geology 33*, pp. 292–311.

Van Keken, P.E., 1993. *Numerical modeling of thermochemically driven fluid flow with non-Newtonian rheology: applied to the Earth's lithosphere and mantle*. PhD thesis. Faculty of Geosciences, Utrecht University, Utrecht.

Vendeville, B.C., 2005. Salt tectonics driven by sediment progradation, Part 1 — mechanics and kinematics. *American Association of Petroleum Geologists Bulletin 89*, pp. 1071–1079.

Vendeville, B.C. and Jackson, M.P.A., 1992a. The rise of diapirs during thin-skinned extension. *Marine and Petroleum Geology 9*, pp. 331–353.

Vendeville, B.C. and Jackson, M.P.A., 1992b. The fall of diapirs during thin-skinned extension. *Marine and Petroleum Geology 9*, pp. 354–371.

Vendeville, B.C., Jackson, M.P.A. and Weijermars, R., 1993, December. Rates of salt flow in passive diapirs and their source layers. In: *Rates of geological processes: Gulf Coast Section SEPM 14th Annual Research Conference*, pp. 269–276.

Wagner, B. H. and Jackson, M.P., 2011. Viscous flow during salt welding. *Tectonophysics 510*(3), pp. 3092326.

Walker, I. and Cooper, W., 1987. The structural and stratigraphic evolution of the northeast margin of the Sole Pit Basin. In: *Petroleum Geology of North West Europe.* Graham & Trotman, London, pp. 263–275.

Wall, M., Cartwright, J., Davies, R. and McGrandle, A., 2010. 3D seismic imaging of a Tertiary Dyke Swarm in the Southern North Sea, UK. *Basin Research 22*, pp. 181–194.

Warsitzka, M., Kley, J. and Kukowski, N., 2013. Salt diapirism driven by differential loading – Some insights from analogue modelling. *Tectonophysics 591*, pp. 83–97

Weijermars, R., Jackson, M. and Vendeville, B., 1993. Rheological and tectonic modeling of salt provinces. *Tectonophysics 217*, pp. 143–174.

Williamson, M., Murray, S., Hamilton, T. and Copland, M. eds., 1997. A review of Zechstein drilling issues. *Offshore Europe 97 Conference.*

Williams-Stroud, S.C. and Paul, J., 1997. Initiation and growth of gypsum piercement structures in the Zechstein Basin. *Journal of Structural Geology 19*, pp. 897–907.

Wong, T.E., Batjes, D.A., de Jager, J. and van Wetenschappen, K.N.A. (eds.), 2007. *Geology of the Netherlands.* Royal Netherlands Academy of Arts and Sciences Amsterdam.

Worrall, D.M. and Snelson, S., 1989. Evolution of the northern Gulf of Mexico, with emphasis on Cenozoic growth faulting and the role of salt. In: Bally, A.W.,

References

Palmer, A.R. (Eds.), *The Geology of North America: An overview*. Geological Society of America, v. A, pp. 97–138.

Wu, S.A., Bally, A.W., and Cramez, C., 1990. Allochthonous salt, structureand stratigraphy of the northeastern Gulf of Mexico, Part II: Structure. *Marine and Petroleum Geology 7*, 334–370.

Zhuo, L. and C. Ting, 2011. Subsalt steep dip imaging study with 3D acoustic modeling. *73rd EAGE Conference & Exhibition*.

Zirngast, M., 1996. The development of the Gorleben salt dome (northwest Germany) based on quantitative analysis of peripheral sinks. In: Alsop, G.I., Blundell, D.J., Davison, I. (Eds.), *Salt Tectonics, vol. 100*. Geological Society, London, pp. 203–226. Special Publications.

Zulauf, J. and Zulauf, G., 2005. Coeval folding and boudinage in four dimensions. *Journal of Structural Geology 27*, pp. 1061–1068.

Zulauf, G., Zulauf, J., Bornemann, O., Kihm, N., Peinl, M. and Zanella, F., 2009. Experimental deformation of a single-layer anhydrite in halite matrix under bulk constriction. Part 1: Geometric and kinematic aspects. *Journal of Structural Geology 31*(4), pp. 460–474.

Zulauf, J., Zulauf, G., Hammer, J. and Zanella, F., 2011. Tablet boudinage of an anhydrite layer in rock-salt matrix: Results from thermomechanical experiments. *Journal of Structural Geology, 33*(12), pp. 1801–1815.

Zulauf, G., Zulauf, J., Hastreiter, P. and Tomandl, B., 2003. A deformation apparatus for three-dimensional coaxial deformation and its application to rheologically stratified analogue material. *Journal of Structural Geology 25*, pp. 469–480.

Appendices

Appendix 2.1: Summary chart of the velocities, thicknesses and formation tops of the internal Zechstein intervals. The data were manually collected from the completion report of well 43-19-2.

	Formation	Top (m)	Base (m)	Thickness (m)	Average DT (us/ft)	Inverse DT (ft/us)	Inverse DT (km/s)
			Data For well to seismic Calibration				
			Well: 43-19-2				
Z5?	Z5?	2226	2269	43	70	0.0181818	4.3542944
Z4 Group	Aller Potash Member	2269	2297	28	75	0.0133333	4.0640081
	Aller Halite Formation	2297	2330	33	68	0.0147059	4.4823619
	Roter Salton Formation	2330	2359	29	90	0.0111111	3.3866734
Z3 Group	Leine Potash Member	2359	2424	65	83	0.0120482	3.6722965
	Z3 Halite (Leine Halite Fm)	2424	2591	167	70	0.0142857	4.3542944
	Z3 Anh (Haupt-anh Fm)	2591	2614	23	55	0.0181818	5.5418293
	Stassfurt Potash Member	2614	2649	35	75	0.0133333	4.0640081
Z2 Group	Z2 Halite (Stassfurt Halite Fm)	2649	3191	542	70	0.0142857	4.3542944
	Z2 Polyhalite	3191	3263	72	55	0.0181818	5.5418293
Z1 Group	Z1/Z2 Carbonate Units	3263	3302	39	50	0.02	6.0960122

Appendix 5.1: Interlimb angles of the Z3 Stringer folds below the domains A1D, A2D, A3D, A4D S1D, and S4D in the Cavendish 3D seismic survey.

Interlimb Angles of the Z3 Stringer Folds in (°)						
A1D	A2D		A3D	A4D	S1D	S4D
62	67	132	63	66	107	113
64	69	132	64	67	109	113
66	94	132	66	67	110	128
67	95	133	66	69	125	128
68	96	133	68	88	131	134
69	98	135	94	88	132	134
69	99	135	94	88	132	134
78	101	136	94	88	133	134
78	103	137	94	88	134	136
79	104	138	94	88	134	136
81	105	140	94	88	139	141
84	105	141	94	88	139	141
85	106	141	95	89	141	143
85	107	145	95	89	141	143
86	108	148	96	90	142	144
86	110	148	96	90	142	144
86	110	148	96	90	145	147
86	110	149	96	90	145	147
88	110	153	98	92	145	147
88	111	159	98	92	146	148
88	113	163	98	92	150	152
88	115		98	92	150	152
90	116		100	94	150	152
90	117		100	94	150	152
91	118		101	95	151	155
91	118		101	95	152	155
91	119		101	95	153	155
91	119		101	95	153	155
91	119		101	95	154	156

91	120		101	95	154	156
92	120		102	96	154	156
92	120		102	96	154	156
93	122		103	97	155	157
93	122		103	97	155	157
94	123		104	98	156	158
94	123		104	98	156	158
96	123		106	100	160	162
96	125		106	100	160	162
100	125		110	104	161	163
100	125		110	104	162	164
100	126		110	104	163	166
100	126		110	104	164	166
101	126		111	105	165	167
101	128		111	105	165	167
116	129		114	120	173	175
116	129		115	120	173	175
117	131		143	137	174	176
62	67		63	66	107	113
119	131		143	137	175	177
88.551	121.942029		98.5102	94.3878	147.367	150